The development of high strength multi-component Al-based die-cast alloys

A thesis submitted for the degree of
Doctor of Philosophy

by

Qing Cai

Supervision: **Isaac T.H Chang, Zhongyun Fan**

BCAST
Brunel University
Uxbridge, UB8 3PH
United Kingdom

August 2020

Copyright

Abstract

High-pressure die casting (HPDC) has drawn great attention in recent decades, because of its good surface finish, high productivity and excellent mechanical properties. In recent years, many scientific investigations have been performed on multi-component alloys, including high entropy alloys, metallic glass or high-order eutectic alloys. These multi-component alloys have excellent mechanical properties as compared with many conventional alloys. Thus, in this thesis, aluminium die-cast alloy compositions were designed with the concept of multi-component eutectic systems (e.g. Al-Si-Mg and Al-Cu-Si-Mg). The CALPHAD modelling was used to design the alloys compositions with the required phase constitution (e.g. various volume fraction of eutectic mixture). The microstructural evolution during solidification for these newly developed aluminium alloys was studied using a combination of DSC, XRD, SEM, TKD, TEM. The mechanical properties were obtained from the standard tensile testing and Vickers hardness test.

Experimental results confirmed that the new Al-Si-Mg-Mn alloys have bimodal microstructure. It consists of α-Al, α-AlFeMnSi, binary eutectic (Al+Mg_2Si) and ultrafine quaternary eutectic (Si+α-Al+Mg_2Si+π-AlFeMnSiMg). The high strength is induced by the formation of the multi-scale eutectic mixture and fine α-AlFeMnSi particles. The microstructure of quaternary Al-Cu-Si-Mg eutectic alloy consisted of four phases, including α-Al, Al_2Cu, Si, and $Al_4Cu_2Mg_8Si_7$ coexisted together in a cellular microstructure with an ultrafine lamellar eutectic mixture as well as in the nano-scaled anomalous eutectic at the intercellular region. The Al-Cu-Si-Mg hypoeutectic alloys were investigated with Cu content ranging from 5wt% to 10wt%. The microstructure of these alloys comprised of the multi-scale eutectic mixture, from coarse binary to ultrafine quaternary eutectic. It was found that the yield strength and elongation can be tailored by controlling the volume fraction of the eutectic mixture.

Optimised solution heat treatment conditions of newly developed aluminium die-cast alloys were developed. They are 540°C/10min for Al-Si-Mg-Mn alloys and 500°C/30(60) min for Al-Cu-Si-Mg alloys. The effects of solution time and temperature on the expansion of porosity were assessed. There is no apparent porosity expansion under short solution treatment or the prolonged solution time with lower temperatures.

The short solution treatment in Al-Si-Mg-Mn alloys enables the dissolution of Mg and spheroidisation of eutectic Si and Mg_2Si phases, thereby minimising the growth of α-Al grains. The π-AlFeMnSiMg in the final quaternary eutectic reaction transforms into nano-scale body-centred α-AlFeMnSi phase after the short solution treatment due to the reaction with the dissolved Si and Mg in the α-Al matrix. The peak ageing hardness was dominated by solution temperature, and the highest peak hardness was obtained under the short T6 heat treatment with the highest solution treatment temperature. The coherent β'' precipitate with needle-like morphology was found after the short T6 heat treatment.

The solution treatment in Al-Cu-Si-Mg alloys for 30/60 min at 500 °C dissolves sufficient quantity of Cu (~3wt%), and spheridises the Al_2Cu and $Al_5Cu_2Mg_8Si_7$ phases. A large number of θ' precipitates and Q'' coexist inside the α-Al matrix after T6 heat treatment, contributing to the exceptional mechanical strength. In addition, the T5 heat treatment of Al-Cu-Si-Mg alloys were also studied. Due to the various Cu content in the α-Al matrix, the alloys were strengthened by β'' in Al5Cu alloy, β'' and θ' in Al6.6Cu alloy, and θ' and Q'' in Al10.6Cu alloy.

Depending on the alloy composition, these newly developed aluminium die-cast alloys exhibit mechanical properties that are comparable and even exceed those in existing aluminium die-cast alloys under similar T6 heat treatment.

Acknowledgement

I would like to thank my supervisor Prof. Isaac T.H chang and Prof. Zhongyun Fan for providing me with the opportunity to pursue the PhD degree. My sincere thanks to Brunel University London for financial support, which enables me to focus on my research. During the four years of PhD journey, I would like to express my deepest gratitude towards my principal supervisor Prof. Isaac T. H. Chang for his excellent supervision, smart guidance and constant patient, especially during the writing up of my PhD thesis. His valuable experience and precious advice helped me to improve my scientific understanding of solidification and overcome many barriers to the research challenges during my PhD studies. I am also indebted to my co-supervisor Prof. Zhongyun Fan for his scientific advice and philosophical guidance in the new and exciting world of heterogeneous nucleation and multi-component eutectic solidification. More importantly, the research spirit developed by Prof Zhongyun Fan has instilled in me to think creatively and be more ambitious to achieve remarkable goals for specific purposes.

Secondly, I would like to thank my colleagues for technical help in my work during my PhD studies. Dr. Chamini Mendis, Dr. Feng. Wang and Mr. Shihao Wang help me on the operation of transmission electron microscopy and interpretation of TEM data. Dr. Yijie Zhang, Mr. Jon Gadd and Dr. Xiangzhen Zhu provide the technical assistance on the high-pressure die casting and processing of liquid metal. Mr. Stephen Cook, Mr. Peter Lloyd, Mr. Warren Lee and Miss. Sam Melvin provide laboratory support. I would like to thank staff members at Experimental Techniques Centre (ETC), Brunel University London for their help on the training of electron microscopes and BCAST administrative team for their administrative support. Besides, I would like to thank Dr. Vivian Tong at National Physical Laboratory (NPL) London for her help to characterise the eutectic orientation relationship with TKD.

Thirdly, I would like to show my gratitude to Prof Shouxun Ji, Prof. Hamid. Assadi, Prof. Hari Babu Nadendla, Dr. Yan Huang, Dr. Zaidao Li, Dr. Xixi Dong, Dr. Dan Luo, Dr. Ning Hou, Dr. Guangyu Liu, Dr. Junhai Xai, Miss. Jiao Fang, Miss. Susanna Venditti, Miss. Chrysoula Tzileroglou, Mr. Onuh. Adole and Mr. Vincenzo.DeStefano who have accompanied during my PhD journey.

Lastly, I offer my best wishes to my parents as well as my girlfriend, Miss Li, who give me a lot of love and power to overcome many difficulties and achieve every small target. Their accompany and inspiration will guide me and make me achieve more in the future.

Publication List

[1] Q. Cai, C.L. Mendis, I.T.H. Chang, Z. Fan, Microstructure evolution and mechanical properties of new die-cast Al-Si-Mg-Mn alloys, Mater. Des. 187 (2020) 108394.
[2] Q. Cai, C.L. Mendis, I.T.H. Chang, Z. Fan, Effect of short T6 heat treatment on the microstructure and the mechanical properties of newly developed die-cast Al-Si-Mg-Mn alloys, Mater. Sci. Eng. A. 788(2020) 139610.
[3] Q. Cai, C.L. Mendis, I.T.H. Chang, Z. Fan, Microstructure and mechanical properties of new die-cast quaternary Al-Cu-Si-Mg alloys, Mater. Sci. Eng. A. 800(2021) 140357.
[4] Isaac Chang, Qing Cai, From simple binary to complex multi-component eutectic alloys, Prog. Mater. Sci. (2020) Submitted.

Nomenclature

Abbreviation or Symbol	Description
ΔG_v	volume free energy
L_m	heat fusion
ΔT	undercooling
T_m	melt temperature
r	embryo radius
ΔG	Gibbs free energy
r^*	the critical value of embryo radius
I_{hom}	the rate of homogeneous nucleation
Q	the activation energy for diffusion
K	Boltzmann's constant
ΔG^*	Gibbs free energy at r*
$\sigma_{\alpha L}$	surface tension between nucleus (α) and liquid (L)
$\sigma_{\alpha W}$	surface tension between nucleus (α) and substrate (W)
σ_{LW}	surface tension between substrate (W) and liquid (L)
ΔG_{het}	the free energy of heterogeneous nucleation
I_{hom}	the nucleation rate of heterogeneous nucleation
ΔT_k	the dynamic supercooling
v_g	the growth velocity of the crystal
C_s	local composition of the solid
C_L	the liquid composition
f_s	the fraction of the solid
λ	the lamellar spacing
R	the solidification rates
τ_{L-N}	the solid solution hardening
G	the shear modulus
f_m	the force
c	the atomic fraction of the solute
b	the Burgers vector
ε_L	the combination of size and modulus misfit
σ_y	the yield strength

σ_0	the friction stress or resistance to dislocation motion
d	the grain size
λ_{Ol}	the average spacing between precipitates
$\Delta\tau$	the increment of yield stress
r_p	the average radius of precipitates
f	the volume fraction of precipitates
υ	the Poisson's ratio
G	the shear modulus
t_{max}	disintegration time
D_s	the diffusion coefficient of Si or Mg_2Si
γ	the interfacial energy
T	the solution treatment temperature
φ	atomic diameter
ρ	the diameter of eutectic phases
R	final radius of the particle
R_0	initial radius of the particle
R_{gas}	gas content
V	molar volume
C_0	equilibrium concentration of structures in the matrix
D	diffusion coefficient
$\Delta\sigma_i$	intrinsic strength
$\Delta\sigma_{GB}$	grain boundary strengthening
$\Delta\sigma_{eutectic}$	eutectic phases strengthening (volume fraction, morphology and size distribution)
$\Delta\sigma_{ss}$	solute solution strengthening
$\Delta\sigma_{ppt}$	precipitation hardening
δ	lattice mismatch
DSC	differential scanning calorimetry
OM	optical microscope
SEM	scanning electron microscopy
EBSD	electron backscatter diffraction
FIB	focused ion beam
TEM	transmission electron microscope
TKD	transmission Kikuchi diffraction

XRD	X-Ray diffraction pattern
HPDC	high pressure die casting
BCC	body centred cubic
FCC	face-centred cubic
SADP	selected area diffraction patterns

Table of Contents

Chapter 1 Introduction

1.1 Background

For decades, there is a great number of studies on the development of aluminium alloys, including wrought alloys and casting alloys for lightweight and structural engineering applications. The high pressure die casting, low pressure die casting, sand casting and so on are common methods usually applied for the fabrication of aluminium shaped components. Among them, high pressure die casting (HPDC) has gained more attention, accounting approximately 60% of lightweight alloys in automotive components [1]. However, with the growth of the automotive and aerospace industries, currently registered die-cast alloys cannot meet the increasing demand of higher materials specifications. It is essential and challenging for the development of new die-cast aluminium alloys with excellent strength and toughness. In recent years, a lot of research work is focusing on multi-component alloys, such as bulk metallic glass, multi-component eutectic alloys or high entropy alloys [2–4]. These alloys show exceptional mechanical properties, which are several times better than those in conventional alloys. Therefore, multi-component alloys are a potential and promising choice for the development of future alloys. However, expensive and/or high melting point elements are usually selected for the production of metallic glasses or high entropy alloys, leading to less castability and the increased material cost. Consequently, the widespread use of this type of multi-component alloys is prohibited.

Concerning economic and castability factors, the multi-component eutectic alloys are more affordable for the development of die-cast alloys. The eutectic alloys usually have a lower melting point and better castability with less expensive alloying elements. There are several investigations on non-aluminium alloy systems, such as titanium and ferrous alloys. But, only a few studies have been reported on aluminium based multi-component alloys, but their mechanical properties are based on the compression test. Thus, there is an urgent need to apply this new approach of designing aluminium die-cast alloys with multi-component systems.

1.2 Research objectives

The overall aim of this research project is to develop high-performance multi-component aluminium die-cast alloys with a bimodal or multimodal hierarchical microstructure consisted of soft primary α-Al dendrites together with a hard ultrafine

nano-sized eutectic mixture, to provide a combination of high strength and good ductility. This is achieved by the following objectives:

Objective 1: to study the ternary (e.g. Al-Si-Mg) eutectic solidification with the addition of minor elements (e.g. Fe and Mn) and the mechanical properties of the of Al-Si-Mg-Mn alloys

Objective 2: to investigate the solidification behaviour of quaternary eutectic (e.g. Al-Cu-Si-Mg) alloy and the fracture behaviour under the compression test

Objective 3: to study the solidification mechanism of the quaternary Al-Cu-Si-Mg hypoeutectic alloys and the tensile mechanical properties

Objective 4: to study the microstructure evolution (including pores and eutectic phases) of the designed alloys after solution treatment, and to optimise the solution treatment time and temperature for both Al-Si-Mg-Mn and Al-Cu-Si-Mg alloy systems

Objective 5: to investigate the precipitation of the alloys (e.g. Al-Si-Mg-Mg and Al-Cu-Si-Mg) and the mechanical properties after T6 or T5 heat treatment

1.3 Outline of the thesis

The thesis is divided into eight chapters. Chapter 2 introduces the aluminium alloys classification, solidification mechanisms, strengthening mechanisms as well as the operating principles/equipment of high pressure die casting (HPDC) and existing aluminium die-cast alloys. In addition, it includes a summary of the development of multi-component alloys from previous studies. Chapter 3 describes the starting materials and methodologies used in the fabrication and characterisation of these newly developed multi-component aluminium alloys. Chapter 4 presents the results and discussions on the development of new aluminium die-cast alloys based on ternary Al-Si-Mg alloy system using a combination of CALPHAD modelling, suction casting/HPDC processing and characterisation of thermal stability, microstructure and mechanical properties. Chapter 5 is focussed on the studies of the solution and artificial ageing treatment of these newly developed Al-Si-Mg-Mn alloys in terms of annealed microstructure and resultant mechanical properties. Chapter 6 consists of two parts, and the first part is the study of the solidification behaviour and compression properties of Al-Cu-Si-Mg quaternary eutectic alloy. The second part was concerned

with the study of newly developed-Cu-Si-Mg hypoeutectic alloys in terms of solidified microstructure and resultant mechanical properties. Chapter 7 presents results and discussions on the effect of solution and artificial ageing treatments to the microstructure and mechanical properties of newly developed Al-Cu-Si-Mg hypoeutectic alloys. In Chapter 8, the main conclusions of the project are summarised, and the suggestions for future work are presented.

Chapter 2 Literature review

2.1Casting Aluminium Alloy Classification

2.1.1 Designation, temper and characteristics of cast aluminium alloys

Aluminium alloys are one of the most widely used engineering alloys in the world. They exhibit low density ~2.7 g/cm^3 (one-third of steel), low melting temperature (<660 °C) and high thermal conductivity (~200 W/mK). The demand for aluminium alloys has been increasing with the growth of the automotive industry worldwide. The exploitation of the low-density property of aluminium alloys in automotive components has enabled a considerable weight saving of cars, leading to the reduction of CO_2 emission and fuel consumption. Consequently, the number of aluminium alloys used in the passage cars has doubled in the last decades [5] as the automotive industry is required to comply with strict environmental regulations.

The aluminium alloys can be divided into two types, which are cast and wrought aluminium alloys. Generally, about 85% of aluminium alloys were used as wrought alloys in the form of plates, sheets, foils and so on. These alloys are based on α-Al solid solution phase that exhibits good ductility for excellent deformation formability and can be age-hardenable to enhance mechanical properties. Cast aluminium alloys are also a very important material in the car industry. They are processed into shaped components using manufacturing methods such as sand casting, permanent mould casting, high-pressure and low-pressure die casting. Currently, the most widely used aluminium alloys are based on Al-Si, Al-Si-Mg and Al-Si-Mg-Cu systems, because of excellent castability and good mechanical properties [6]. The remainder of this chapter focuses on aluminium casting alloys.

Currently, there is no universally accepted system of nomenclature to classify aluminium casting alloys. The Aluminium Association of the United States and United Kingdom have developed their own classification system, and details are described below. Table 2-1 shows a four-digit numerical system describing the aluminium and aluminium alloys by United States Aluminium Association [7]. In terms of the unalloyed aluminium group (1xx.x), the first two digits represent the purity of aluminium. For example, 150.x indicates that the purity of aluminium is 99.5%. Moreover, the last

decimal digit with 0 and 1 indicates the product is used to denote castings or ingot, respectively. However, in group 2xx.x to 9xx.x, there is no specific meaning of composition similar to the group (1xx.x). The two digits identify the different aluminium alloys. The last decimal digit is the product form.

Table 2-1 Four-digit system for aluminium alloys

	Current designation	Former designation
Aluminium, 99% or greater	1xx.x	
Grouped by major elements :		
Cu	2xx.x	1xx
Si with added Cu/Mg	3xx.x	3xx
Si	4xx.x	1-99
Mg	5xx.x	2xx
Zn	7xx.x	6xx
Sn	8xx.x	7xx
Other elements	9xx.x	7xx
Unused series	6xx.x	

The alloys classified by the United Kingdom is different from those by the United States. They are classified without specific order but have been assigned the prefix LM [8]. Most casting aluminium alloys in the British system are classified into four alloys (LM2, LM4, LM6 and LM21), which are based on Al-Si-Fe, Al-Si-Cu, Al-Si and Al-Si-Cu-Mg, respectively. The detailed compositions and designation can be found in [8].

The condition of castings, according to the United Kingdom system, is indicated by the following suffixes:

M as-cast
TB solution treated and naturally aged
TB7 solution treated and stabilised
TE artificially aged after casting
TF solution treated and artificially aged
TF7 solution treated, artificially aged and stabilised
TS thermally stress-relieved

If there are no suffixes of the alloy, it means the alloys are in an ingot form.

The castability plays a dominated role in the development of aluminium casting alloys with preferable microstructures and dimension stability [9]. The castability is characterised by several factors, including fluidity, mould-filling volume shrinkage, hot

tearing resistance, pore formation and surface quality [10–13]. Although the mould design or casting operation has some influence on these factors, the alloy composition plays a more important role. These factors are discussed below.

Fluidity depends on the alloy composition, which is usually measured by pouring the metal into the spiral mould. The filling length of the metal was compared with some other alloys, and the fluidity is assessed. The fluidity affects melt characteristics, such as viscosity, surface tension and freezing range. Volumetric shrinkage is one of the defects in castings, which is affected by a combination of alloy composition, mould design and casting. This defect is in the form of large isolated voids or interconnected porosity. It is well known that Al-Cu, Al-Mg and Al-Zn alloys are most prone to the hot tearing, while Al-Si alloys show the best hot tearing resistance. It is because Al-Cu, Al-Mg and Al-Zn alloys have large solidification temperature ranges [14,15].

Die soldering is the problem which usually occurs in high-pressure die casting. The affinity of iron and aluminium melt causes the metal casting to stick to the steel mould, leading to the formation of an intermetallic compound layer at the mould/casting interface [16]. Thus, the alloy composition needs to be modified in order to prevent die soldering.

2.1.2 Alloys based on Al-Si system

Al-Si alloys are the most important of aluminium casting alloys, due to its excellent fluidity, good corrosion resistance and low coefficient of expansion. The eutectic composition of Al-Si binary alloy has shown to be Al-12.6%Si (wt%), with solidification temperature 577 °C and a maximum solubility of 1.65 wt%.

However, the eutectic Si phase shows either plate-like or needle-like morphology. Such faceted morphology is formed under a slow cooling rate (10-100 K/s) or without any chemical modification (such as Na, P or Sr). The unmodified eutectic Si can act as crack initiation during tensile testing resulting from stress concentration [17], which is detrimental to the elongation at fracture, thus restricting the application of the Al-Si alloys. In recent decades, a lot of research studies have been performed on the modification of Al-Si eutectic alloys to understand the effect of chemical and physical intervention on the Si morphology [18]. It is reported that the addition of chemical modifiers can generate twin defects in the Si crystals, reorientating the growth, therefore the eutectic Si can be bent, split and curved into finer particles [19]. The Sr,

Na, Sb, Zr, Gd, Na or P elements have been investigated for its chemical modification effect on the eutectic Si phase. Sr and Na are two popular alloying elements in Al-Si alloys. The addition of a concentration level of 0.01~0.03wt% of either Sr or Na, is able to refine and decrease the aspect ratio of the eutectic Si phase. As a result, the strength and elongation can be improved [20].

The widely used Al-Si based alloys include Al-Si alloys (LM20, LM2, LM6), Al-Si-Mg alloys (LM25) and Al-Si-Cu (LM24). The Al-Si based alloys with modified elements for Si have excellent ductility and good dimensional stability that have found applications where the strength is not the primary requirement. For example, these alloys are usually applied in domestic cookware, pump castings and particular automobile castings. A large quantity of sand or permanent castings are based on Al-Si-Mg alloys (LM25, A356 or A357). These alloys contain 0.3-0.5wt% Mg, having a good age-hardening response, and usually used in cylinder heads, wheels and engine support. After T6 heat treatment, the eutectic Si in Al-Si-Mg alloys become spherodised and β'' precipitate formed after peak ageing treatment (8-12 hours at 170 °C) [21,22]. Moreover, iron-contained intermetallic phases are unavoidable in Al-Si or Al-Si-Mg alloys as a result of Fe impurity in the alloys. In Al-Si alloys, the brittle β-AlFeSi phase with large plate-like shape forms, which needs to be controlled and minimised [23]. The addition of Mn has been studied, and it was found to be beneficial for these alloys as they form fine α-AlFeMnSi phase when Mn:Fe ratio is maintained at least 0.5:1 [24].

2.1.3 Alloys based on Al-Cu system

The Al-Cu based alloys were widely used for aluminium castings, but some of them has been superseded due to poor castability. The major disadvantages of Al-Cu based casting alloys are poor hot-tearing resistance and corrosion resistance [14,25]. Most Al-Cu casting alloys contain additional elements (such as Mg, Si, Ag) and have a good age-hardening response.

Al-(4-6wt%)Cu based alloys have excellent yield strength under as-cast or T6 heat treatment condition. The highest strength of Al-Cu based casting alloy is Al-4.7Cu-0.7Ag-0.3Mg which is usually applied in the aerospace industry and has a yield strength of 480 MPa and tensile strength of 550 MPa after T6 heat treatment [8]. Because of the cost of Ag, the Al-Cu based alloy with Ag has limited applications. In recent years, Al-Cu-Mg-Zr alloy was developed and fabricated via selective laser melting [26]. The addition of Zr can provide Al_3Zr intermetallics and grain refinement.

The yield strength and ultimate tensile strength is 446 MPa and 451 MPa, respectively. Moreover, greater yield strength of 453 MPa has been achieved in Al-Cu-Li-Zn alloy after peak ageing [27].

2.1.4 Alloys based on Al-Mg system

The castability of Al-Mg alloys is less favourable than Al-Si alloys, because of oxidation of Mg during pouring and holding of the melt. However, the Al-Mg alloys have high corrosion resistance and excellent machinability. During the casting of Al-Mg alloys, the beryllium is usually added, resulting in the formation of an oxide film at the surface. The Mg content of Al-Mg alloys is usually 4-10wt% and most sand casting Al-Mg alloys have Mg content 7-8wt%, and Zn or Si is usually added in the Al-Mg alloy for improving ageing hardening response. Al-Mg alloys with 5-6wt% Mg, ~0.5wt% Mn and ~2.2wt%Si are usually processed by high-pressure die casting [24]. These alloys have a very high elongation at fracture of 15% with good strength. However, Al-Mg alloys with lower Mg (<5wt%) are usually used in wrought alloys [28].

2.2 Solidification behaviour of aluminium casting alloys

2.2.1 Solidification of hypoeutectic or hypereutectic alloy

Most cast aluminium alloys are designed based on hypoeutectic or hypoeutectic composition. The microstructure of these casting alloys mainly consists of primary phases, eutectic structures and secondary intermetallics. The solidification commences with the development of primary phases. The nucleation affects the size and distribution of these primary phases, which play an important role in the mechanical properties of the alloys.

2.2.1.1 Homogeneous nucleation

Nucleation can be divided into two categories, which are homogeneous nucleation and heterogeneous nucleation. The homogeneous nucleation in casting alloys needs to consider both temperature and composition. Before solidification, the temperature of the melt drops and the nucleation will occur if the melt temperature is below T_m. The undercooled melt provides a driving force. The embryo forms in the undercooled melt, leading to the ordered atoms in the melt and decreasing the volume free energy (ΔG_v), Which can be written as

$$\Delta G_v = \frac{-L_m \Delta T}{T_m} \qquad 2\text{-}1$$

Where L_m is heat fusion, and ΔT is undercooling. However, the interfacial energy can increase with the decrease of volume free energy. The change of free energy caused by interfacial energy and volume free energy can be described as follows [29]:

$$\Delta G = 4\pi r^2\sigma + \frac{4}{3}\pi r^3 \Delta G_v \qquad 2\text{-}2$$

where ΔG is Gibbs free energy, r is the embryo radius, and σ is the surface tension of the interface between the nucleus and its surroundings. It is shown in Fig 2-1 (a) that there is a critical value of r^* ($r^* = {2\sigma \cdot T_m}/{L_m \cdot \Delta T}$) in which the nucleus has the highest volume free energy ΔG_v. The free energy will decrease with further growth of the nucleus. When the liquid undercools to a temperature below T_m, nucleus grows. The embryo sizes occur in the range of cluster size presenting in the liquid. The rate of nucleation I_{hom} can be calculated as follows:

$$I_{hom} = \frac{nkT}{h} exp - \left(\frac{\Delta G^* + Q}{kT}\right) \qquad 2\text{-}3$$

$$\Delta G^* = \frac{16\pi\sigma^3 {T_m}^2}{3(L_m \cdot \Delta T)^2} \qquad 2\text{-}4$$

where n is the total number of atoms, h is Planck's constant, Q is the activation energy for diffusion, T is temperature, K is Boltzmann's constant and ΔG^* is Gibbs free energy at r*. The ΔG^* are decided by undercooling, and therefore it can be found that the nucleation rate is very sensitive to the undercooling. The relationship between nucleation rate (I_{hom}) and undercooling (ΔT) is shown in Fig.2-1 (b). Although there are some specific conditions whereby the impurities level can be minimised after careful preparation to provide a condition for near homogeneous nucleation, the homogeneous nucleation rarely occurs in nature.

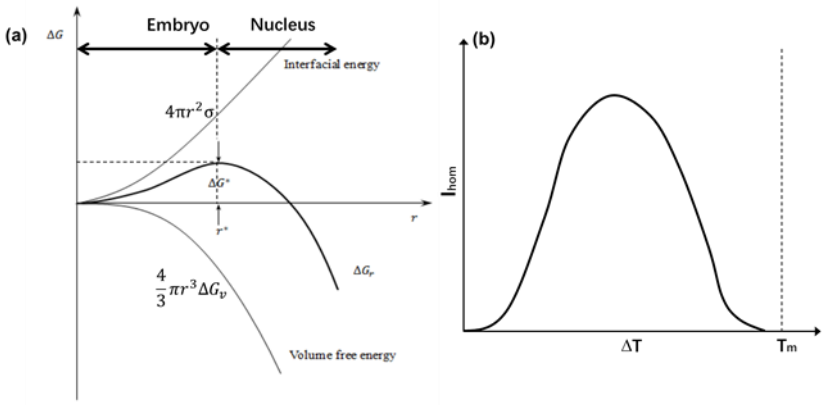

Fig.2-1 (a) Schematic illustration of the free-energy barrier to nucleation (b) the relationship between undercooling and nucleation rate

2.2.1.2 Heterogeneous nucleation

Heterogeneous take place in almost all the solidification process, which occurred with much lower undercooling compared with homogeneous nucleation. This classic heterogeneous nucleation was developed by Turnbull et al. [30], in which a spherical cap forms on a planar substrate shown in Fig.2-2. $\sigma_{\alpha L}$, $\sigma_{\alpha W}$ and σ_{LW} are surface tension between nucleus (α) and liquid (L), nucleus (α) and substrate (W) as well as substrate (W) and liquid (L). Because of the presence of substrate, the free energy for nucleation decreases and the driving force of nucleation is lower than homogeneous nucleation. The free energy of heterogeneous nucleation can be written as

$$\Delta G = \left(4\pi r^2 \sigma_{\alpha L} + \frac{4}{3}\pi r^3 \Delta G_v\right)\left(\frac{2-3cos\theta+cos^3\theta}{4}\right) \quad 2\text{-}5$$

In a certain system, θ is a constant value, thus from $^{dG}/_{dr} = 0$, the critical value of nucleation radius r^* can be obtained

$$r^* = -\frac{2\sigma_{\alpha L}}{\Delta G_v} \quad 2\text{-}6$$

The critical value of r^* in heterogeneous nucleation is same as that in homogeneous nucleation. The free energy of heterogeneous nucleation ΔG_{het} at r^* can be written as

$$\Delta G_{het} = \Delta G_{hom}\left(\frac{2-3cos\theta+cos^3\theta}{4}\right) = \Delta G_{hom} f(\theta) \quad 2\text{-}7$$

It should be noted that the free energy barrier under heterogeneous nucleation is modified by an additional term of $f(\theta)$ and $f(\theta)$ is below 1. If θ is 0°, ΔG_{het} becomes 0, which indicates it is entirely wet between the substrate and the liquid. If θ is 180°, $\Delta G_{het} = \Delta G_{hom}$ and the substrate makes no contribution to nucleation. Under no extreme condition, θ is in the range of 0° to 180°. Thus f(θ) is below 1. As a result, ΔG_{het} is smaller than ΔG_{hom}. The nucleation is much easier under heterogeneous nucleation.

The nucleation rate is expressed in the same way as for homogeneous nucleation

$$I_{hom} = \frac{nkT}{h} exp - \left(\frac{(2+cos\theta)(1-cos\theta^2)}{4kT}\Delta G^* + \frac{\Delta G_D}{kT}\right) \quad 2\text{-}8$$

The classical nucleation theory reveals that contact angle θ plays a very important role for nucleation.

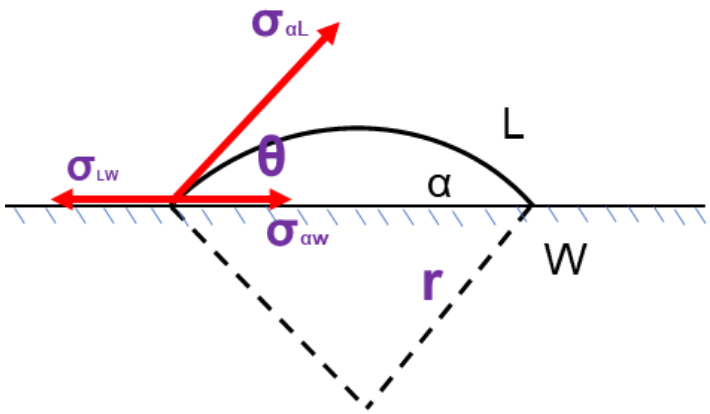

Fig.2-2 Schematic illustration of the cap-shaped nucleus

2.2.1.3 Growth of primary phase

After nucleation, the crystals start to grow, and the final size and morphology have significant effects on the mechanical properties of the alloys. The crystals show different shape after solidification, which is determined by the structure between the solid and liquid interface. The interface between the solid and liquid can be divided into two types, which are smooth interface and rough interface. Microscopically, the smooth interface is an ideal surface with a spreading of a single layer of atoms, while the rough interface is rugged and it has some transitional layers of atoms. On the macro level, the smooth interface structure can lead to broken-line shape, due to different orientations of fact plans, and there are no fact plans on the crystals with a rough interface.

The style of crystal growth is determined by the interfacial structure of the crystals. The first style is continuous growth, which occurs on the rough interface. There are some vacancies of atoms on the rough interface. Hence, the atoms in the liquid can fill these vacancies, and the crystal grows into the liquid. The dynamic supercooling (ΔT_k) has a linear relationship with the growth velocity of the crystal (v_g) under this style. The second style is two-dimensional nucleus. It appears on the surface of the crystal with a smooth interface. A nucleus grows parallel to the basal plane to form an expansion layer. After that, another stage forms and repeat the growth. The relationship between ΔT_k and v_g is $v_g = u_2 exp(\frac{-b}{\Delta T_k})$. u_2 and b are constant value. It can be found that high growth velocity (v_g) needs large dynamic supercooling (ΔT_k). Lastly, the crystal growth starts on the screw dislocation. If there is a screw dislocation on the smooth surface,

there are some screw stages and atoms in the liquid can fill the vacancies. The relationship between ΔT_k and v_g is $v_g = u_3 \Delta T_K{}^2$.

Apart from the interfacial structure of the crystals, the temperature field on the front of the solid/liquid interface also affect the crystal growth. Under a positive temperature gradient, the temperature in the liquid is higher than the solid. Because of the higher temperature in the liquid, the occasional hump part can be retarded. The growth of the crystal is in the form of a flat move. However, if the temperature gradient is not positive, the hump structure in the solid/liquid interface can grow into the liquid and form a dendritic structure with secondary or tertiary dendrites.

The different grain structures can usually be observed from the microscope in the castings or ingots. There are usually three regions of grain structure in the ingot without grain refinement or alloy modification. In an out layer of the castings, the fine and random orientated equiaxed grains can be observed, and it is because of the high cooling rate and subtracts for nucleation provided by the wall of the mould. After the formation of out layer, the temperature of the mould increases, leading to a slower cooling rate. The columnar grains form with a preferred orientation, and the growth direction is towards the centre of the casting. Further solidification causes a decrease in the temperature gradient, which prohibit the growth of columnar grains. In the meantime, there are some nucleus in the liquid and grow in all directions, and the equiaxed grains form at the centre of the casting. This is so-called the columnar-to-equiaxed (CET) transition. The castings with more equiaxed grains are less susceptible to hot tearing, and the feeding can be enhanced, leading to the improvement of the distribution of porosities [31].

There are a lot of work investigating the mechanism CET. It can be divided into two groups. One is because of the heterogeneous nucleation of equiaxed grains in the last liquid [32,33]. Another explanation is the fragments of dendrites from mould walls or upper liquid-air surface [34]. Superheat, alloy composition and fluid flow can affect CET. It is reported that increasing the superheat can increase the columnar length and suppress CET, which is because of a larger temperature gradient [35–37]. Moreover, alloy composition has a great effect on CET, resulting from the melting temperature, kinetics of dendrite growth [37] and nucleation rate [35,36,38]. Lastly, the convention created by nature or electromagnetic results in modifications of temperature field and concentration field, and finally, the columnar region can be shifted and minimised [39].

2.2.2 Solute segregation during solidification

The prediction of solidification and other properties in aluminium alloys is very critical. In the simulation of alloy solidification, Lever rule and Scheil-Gulliver model are two popular approaches to describe the phase fraction as a function of temperature [40]. The assumption of the Lever rule is that the diffusion in the liquid or solid is very fast at any time, and the solidifying phases are always maintained at the equilibrium state. However, Scheil-Gulliver model assumes there is no diffusion in the solid phase while the solute redistribution in the liquid is infinitely fast. The analytical solution of the Scheil equation can be written as [41]:

$$\mathrm{k} = \frac{C_S}{C_L} \qquad 2\text{-}9$$

where C_s is the local composition of the solid, C_L is the liquid composition. C_s is expressed as:

$$\mathrm{C}_s = kC_0(1 - f_s)^{k-1} \qquad 2\text{-}10$$

where K is the partition coefficient, C_0 is the base composition and f_s is the fraction of the solid. The formula 2-10 is restricted to a single phase with one constant partition coefficient. The model was later developed for multi-component alloys with various partition coefficients derived from CALPHAD databases. Some casting processes have high cooling rate and are under no-equilibrium condition. Hence, Scheil-Gulliver model is more suitable to predict these solidifications [42].

The original Scheil-Gulliver model did not consider the back diffusion of the elements in the solid [43] as well as different solidification conditions. Thus, Scheil-Gulliver model has limited application. For decades, the improvement of Scheil-Gulliver model has been investigated by many researchers. Yoo developed an analytical model of binary alloys based on Scheil-Gulliver model, taking into consideration of dendrite arm coarsening [43]. It is found that there is a lower limit of initial concentration affecting eutectic formation. Chen et al. proposed that the scheme of solute back diffusion in the multi-component system with partial equilibrium assumption agrees well with experiment results [44]. Ilbagi et al. extend Scheil-Gulliver model in Al-Ni alloys with various cooling rate, and the fractions of Al_3Ni_2 and Al_3Ni was predicted with consideration of peritectic reaction [42]. In addition, Zhao et al. have investigated step size and cut-off limit of the residual liquid amount on the solidification simulation based on Scheil-Gulliver model in Al-Mg-Zn system [40]. It was found that a proper step size and cut-off limit value needs to be selected for accurate prediction of phase constitution, which depends on the system.

2.2.3 Eutectic solidification

2.2.3.1 Nucleation in the eutectic solidification

Similar to some other solidification process, eutectic solidification consists of nucleation and growth process. The nucleation of one eutectic phase at the temperature below the eutectic temperature is the initial state, following by the nucleation on the second eutectic phase. Thus, the exceptional orientation relationship is usually found in the eutectic microstructure, which is the origin of the nucleation process. Many investigations have been done on the early stage of eutectic solidification. Cantor studied crystallography of Al-Al_2Cu, Al-Al_3Ni and Al-ζ(AlAg) eutectic alloys which solidified in a vertical annular furnace with chilled nucleation base [45]. It is found that the at the nucleation surface there are random orientations in Al-Al_2Cu, Al-Al_3Ni alloys indicating random nucleation of eutectic phase, while the Al-ζ(AlAg) nucleus epitaxially with preferred orientation relationship. Moreover, Bhat studied eutectic nucleation in hypoeutectic Al-Cu alloy under directional solidification with various holding time at high temperatures [46]. There is no orientation between primary α-Al dendrite and eutectic structure, and the eutectic structure grows from Al_2Cu precipitates. A similar phenomenon was found by Kim as well, who studied the Al-Al_2Cu droplets in Al matrix [47]. In addition, the nucleation process in the Al-Si binary alloy is also studied. Shankar et al. studied the nucleation behaviour of hypoeutectic Al-Si alloy with iron impurity [48]. The iron impurity plays an important role in heterogeneous nucleation of eutectic phases, which can form β-AlSiFe precipitates or β-AlSiFe secondary phase depending on the amount of Fe impurities. The eutectic Si nucleates on these particles and grows as flaks. After that, the surrounding liquid is enriched with aluminium. Eventually, eutectic aluminium nucleates and grows on the edges or tips of these flak eutectic Si phases. However, Nafisi et al. proposed that apart from some impurities, some small Si particles, which results from localised Si enrichment, can also provied heterogeneous nucleation of eutectic Si [49]. In addition, Zarif et.al studied the effects of P and Sr on the nucleation of Al-Si alloys, and found that P addition contribute to the heterogeneous nucleation of eutectic Si, but Sr does not promote nucleation [50]. It is because unlike Sr-contained phases, AlP phase having an excellent match with Si can be nucleation sites for eutectic phases.

2.2.3.2 Growth of eutectic alloys

The solidification behaviour of eutectic or alloys is initiated by nucleation stage and completed with the growth stage. Undercooling also plays a key role in the driving force

for growth as well as growth behaviour. The undercooling in the eutectic growth mainly consists of curvature undercooling (ΔT_d), constitutional undercooling (ΔT_c) and kinetic undercooling (ΔT_k), in which kinetic undercooling can be negligible (~0.01 °C). Based on the liquid-solid interface, eutectic can be divided into three groups: (1) metallic-metallic; (2) metallic-nonmetallic; and (3) nonmetallic-nonmetallic. Eutectic aluminium alloys cover the metal-metal group (e.g. α-Al-Al_2Cu, α-Al-Ag_2Al, α-Al-Al_3Ni, α-Al-Mg_2Si). There are many types of eutectic morphology, such as lamellar structure, fibrous, needle-like. The morphology of eutectic mainly depends on the interfacial energy. It has been calculated that if the volume fraction of one eutectic phase is lower than 27.6%, the total area of rod phases is smaller than that of lamellar interfaces. Thus, the morphology shows fibrous, since it has lower interfacial energy. Here, the metallic-metallic group of lamellar eutectic is taken as an example to reveal the binary eutectic growth mechanism. At equilibrium condition of the metallic-metallic eutectic solidification, the solid-liquid interface is usually a rough surface as discussed in Chapter 2.2.1.3. The temperature at the interface is approximately 0.02 °C lower than the eutectic temperature. The temperature on the surface is almost the same. At the initial stage, one of the eutectic nucleates (α phase), which is called the leading phase. After that, another eutectic phase (β phase) nucleates and grows along the leading phase (α phase). During the eutectic growth, there is a short lateral diffusion of chemical species between these eutectic mixtures to maintain the composition of each phase, as shown in Fig.2-3. The growth of β phase is accompanied by absorption of A atoms and rejection of excessive B atoms. At the same time, B atoms are absorbed by α and α reject excessive A atoms. This transverse diffusion process leads to the formation of the lamellar structure with uniform interlamellar spacing.

There is an orientation relationship between the eutectic phases. The lamellar spacing is related to the undercooling, and the relationship developed by Hunt and Chilton [51] can be written as

$$\lambda = \frac{k}{\sqrt{R}} \qquad 2\text{-}11$$

where λ is the lamellar spacing, k is a constant and R is the solidification rates. Therefore, a high solidification rate results in a finer lamellar structure according to equation 2-11. The constant k is related to the alloy composition or different alloy system.

Moreover, it is usually observed that the lamellar spacing of eutectic alloys is not uniform with sudden decrease or increase of lamellar spacing. Jackson et al. reported

that lamellar faults play a critical rule in changing the lamellar spacings [52]. Ourdjini et al. found that there is a limited range of eutectic spacings under a constant growth velocity [53]. The minimum and maximum spacings were calculated based on a self-consistent interface shape, and the results agree well with experimental results. Besides, Carlberg et al. studied Ag-Cu, Al-Zn, Al-Cu eutectic alloys with unidirectional solidification [54]. It was found that the distribution of lamellar spacing was sinusoidal shaped, and Al-Zn has the fastest adjustment of the lamellar spacing due to the roughest solidification front.

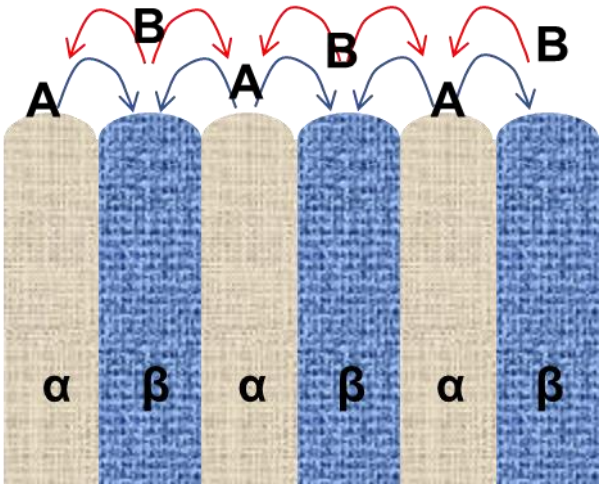

Fig.2-3 Transverse diffusion of lamellar eutectic growth

Lastly, some ternary eutectic systems were also investigated. It is found that the eutectic pattern and morphology depends on the eutectic systems. The solidification of Sn-Pb-Cd was investigated by Gregory et al. and the orientation relationship was characterised, showing coupled growth of three phases [55]. The ternary Sn-Pb-Cd system has ABCA eutectic pattern and the lamellar interfaces have low energies, which are closed-packed planes. Bottin-Rousseau et al. studied near eutectic In-In_2Bi-Sn alloy, and this alloy shows ABAC pattern having a wide stability range of lamellar spacing under a constant growth rate [56]. Moreover, Hotzer et al. studied the Relationship between growth velocity and microstructure evolution of ternary Al-Ag-Cu alloy [57]. The microstructure shows a chain-like structure with alternating Ag_2Al and Al_2Cu embedded in the Al matrix. With the increase in growth rate, the phases fractions adjust quickly, but there is no change of eutectic pattern. In addition, some other ternary eutectic systems have been studied (such as Al-Cu-Si [58], Al-Cu-Ni [59] and Mg-Cu-Zn [60]) and it was found that these ternary eutectic alloys have a bimodal eutectic structure, and the coupled growth of three phases in these alloys can not be

found. Lastly, there is only a little literature reporting the quaternary eutectic alloys and the available systems and growth mechanism have not been widely investigated.

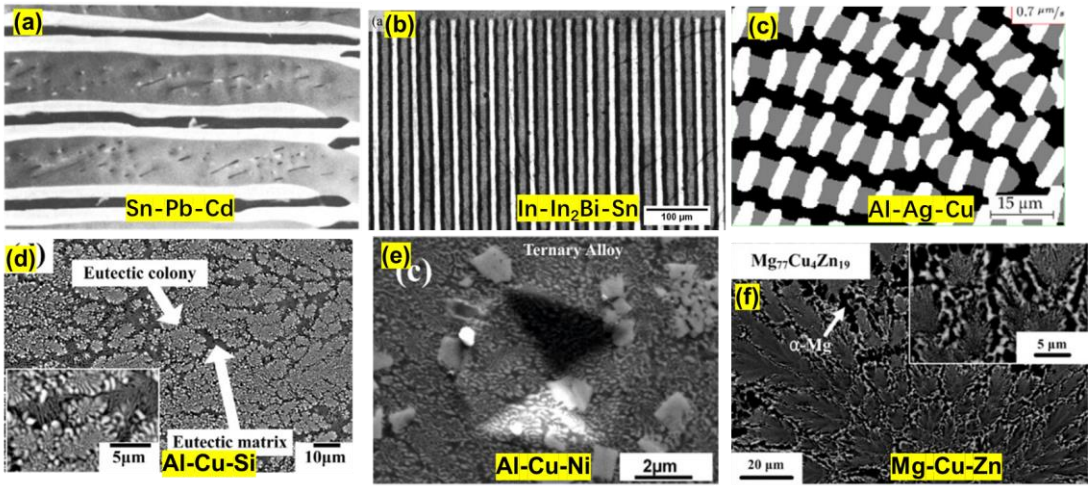

Fig.2-4 The microstructure of ternary eutectic alloys (a) Sn-Pb-Cd [55] (b) In-In_2Bi-Sn [56] (c) Al-Ag-Cu [57] (d) Al-Cu-Si [58] (e) Al-Cu-Ni [59] (f) Mg-Cu-Zn [60] (the web version of the images)

2.2.3.3 Anomalous eutectic solidification

Anomalous eutectic is usually observed in the undercooled eutectic solidification, with typical features such as flake, complex regular and quasi-regular as shown in Fig. 2-5 [61]. This formation mechanism has been usually studied via EBSD, mainly in many binary eutectic systems, such as Ag-Cu [62], Co-Ge [63], and Ni-Sn [64]. Many investigations have been done to reveal the mechanism of anomalous eutectic formation. Some models have been proposed to explain its formation. Coupled or decoupled growth with remelting/fragmentation is one of the most popular models to explain its formation [65–67]. Li et al. found that anomalous eutectic formed in Ni-Sn eutectic alloy with various degree of undercooling [68]. There exists a critical undercooling (130 K), and if the undercooling is larger than the critical value, α-Ni grows as a primary phase into the undercooled melt and β-Ni_3Sn nucleates heterogeneously, forming anomalous eutectic structure. Conversely, if the undercooling is smaller than the critical value, α-Ni and β-Ni_3Sn eutectic mixture exhibits a lamellar morphology, and develop into dendritic morphology, due to the negative temperature gradient in the liquid during eutectic solidification. Wei et al. have extended the mechanism that the anomalous eutectic formation induced by remelting/fragmentation depends on the alloy system [69]. Ag-Cu, Ni-P and Pd-P were selected which represents solid solution-solid solution, solid solution-intermetallic

compound and intermetallic compound-intermetallic compound systems, respectively. It was found that no remelting occurred in the intermetallic phases, but only in the solid solution phases remelted. The calculated results show that for these eutectic systems with larger equilibrium solute distribution coefficients or small solidus slopes, the solid solution phases are supersaturated with more solute, and thus, they are more prone to be remelted.

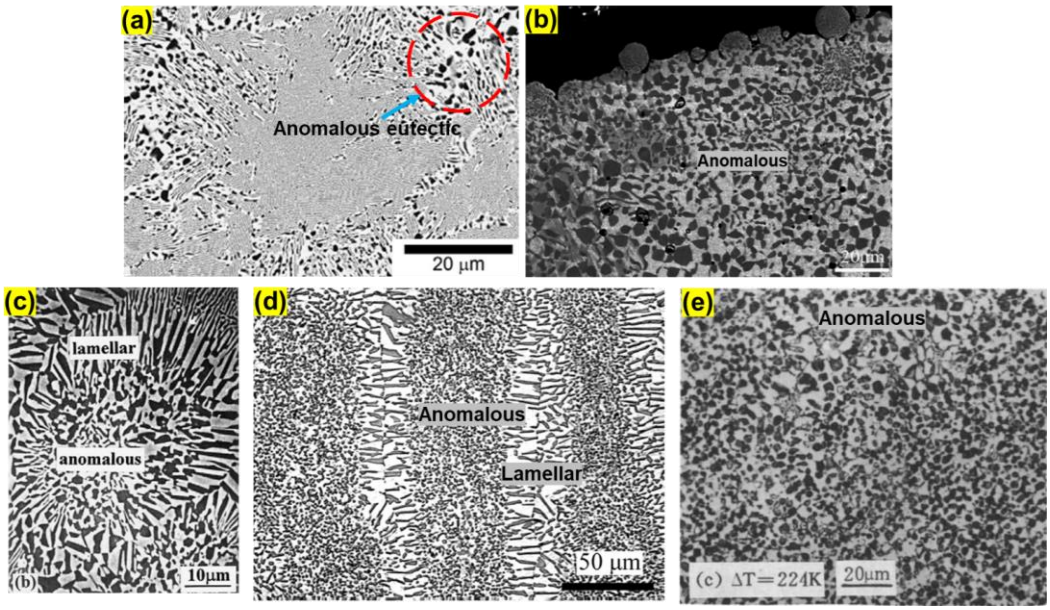

Fig.2-5 The microstructure of anomalous eutectic at high undercoolings: (a) Ag-39.9 at.%Cu [62] (b) Ni-32.5 wt.%Sn [64] (c) Co-29.7 wt.%Ge [63] (d) Ag-39.9 at.%Cu [69] (e) Co-34.2 wt.%Sn [70]

Recently, Mullis and Clopet calculated and found that the volume fraction of anomalous eutectic caused by remelting is much smaller than the experimental results [62]. Based on this finding, a new model has been proposed that there is a kinetic shift of the eutectic point during rapid solidification. Under rapid solidification, the location (sloid/liquid) of a eutectic point is affected by the growth velocity [71]. As shown in Fig. 2-6, in Ag-Cu alloy the local eutectic point shift to Cu corner with increasing growth velocity. Thus, during the growth of cellular eutectic, there is a diffusion layer in front of eutectic, which need to approach local eutectic composition with respect to a kinetic eutectic point. The boundary will be riched in Cu. Thus, at the last solidification process, the residual liquid is enriched with Cu. The heterogeneous nucleation of Cu-rich phases is the main factors contributing to the anomalous eutectic.

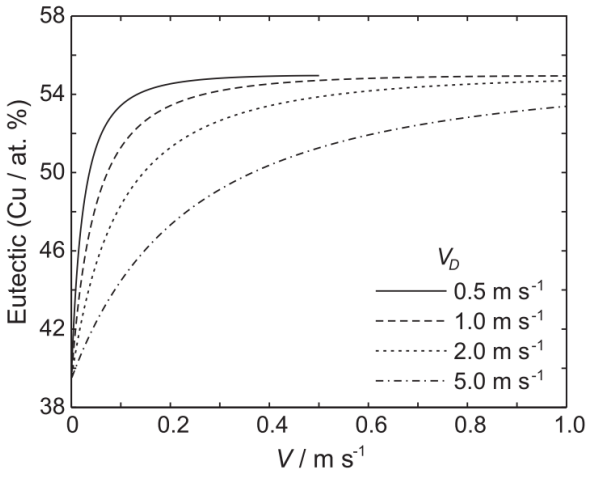

Fig.2-6 Kinetic shift of eutectic point versus growth velocity V with various diffusion speed V_D [62]

2.2.3.4 Divorced (decoupled) eutectic solidification

The eutectic growth can be divided into two types, based on their growth mechanism. They are cooperative growth and divorced growth or decoupled growth. The divorced eutectic grows with no exchange of solute and no trijunction. There are several mechanisms causing divorced eutectic growth.

Firstly, Xiao et al. simulated solidification of binary and off-eutectic alloys via a modified diffusion-limited aggregation model [72]. It was found that oscillations in lamellae width have an influence on the morphology of eutectic and server oscillations can break orientational symmetry leading to divorced eutectic. The eutectic morphology in Mg-Al alloys under high pressure die casting and gravity casting was studied by Dargusch [73]. It is found that a high cooling rate is able to obtain fine α-Mg grains, and the eutectic solidified inside these narrow interdendritic regions. Thus, growth of eutectic phases becomes restricted in these small spaces and divorced eutectic morphology forms. A similar phenomenon was also reported by Cao et al [74].

Furthermore, divorced eutectic morphology is also found in ternary systems. Wang et al. investigated the formation of eutectic in undercooled Pb-Sb-Sn alloy [75]. The microstructure of Pb-14%Sb-10%Sn alloy consists of pseudobinary eutectic (Pb+Sb) and ternary eutectic (Pb+Sb+SbSn). Because of great differences of a lattice structure among these three phases, coupled growth is hard to maintain, leading to divorced eutectic morphology. The divorced eutectic was also found in $(Co_{76}Sn_{24})Nb$ alloy [76]. The addition of Nb in Co-Sn alloy contributed to a great difference in growth velocity of

α-Co and β-Co_3Sn_2 and divorced eutectic takes place. Lastly, the ultrasonic field can also trigger the growth of divorced eutectic, due to cavitation effect and acoustic streaming [77,78]. The cavitation effect and acoustic streaming can promote the nucleation of eutectic phases and suppress the coupled growth, respectively.

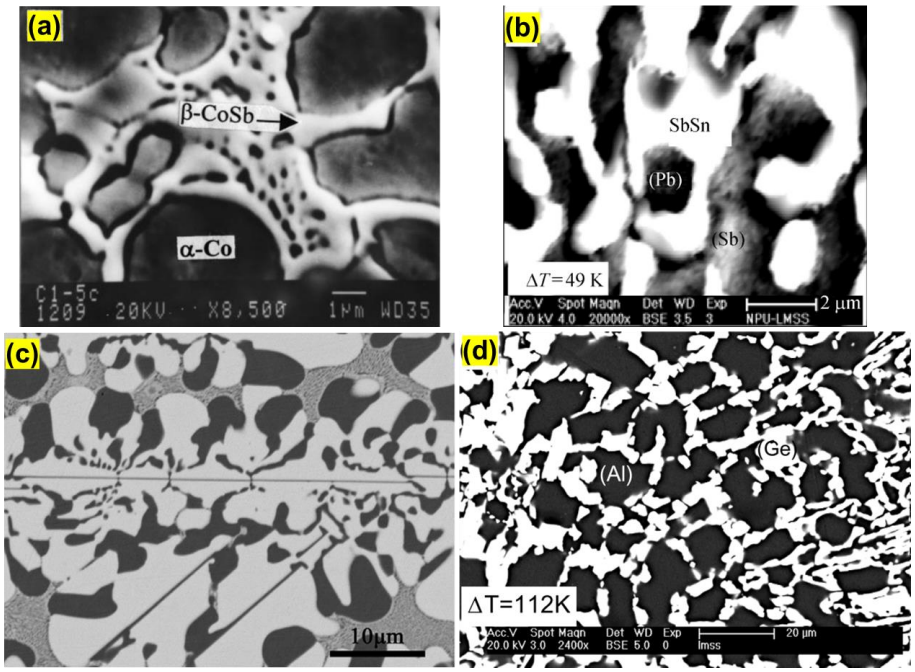

Fig.2-7 Microstructure of divoreced eutectic (a) Co-20%Sb [74] (b) Pb-14%Sb-10%Sn [75] (c) ($Co_{76}Sn_{24}$)Nb [76] (d) Al-50%Ge [78]

2.2.4 Cellular to dendritic eutectic microstructure

Cellular eutectic morphology can usually be observed in binary or ternary eutectic alloys under directional solidification, suction casting and et al. The main factor contributing to the cellular eutectic growth is the impurities and third element in binary eutectic alloy. The impure Al-Al_2Cu and Al-Al_3Ni eutectic alloys under directional solidification were studied by Lawson et al [79]. The elongated cells in longitudinal section and equiaxed cells in the transverse section were found, and inside one cell, there was a constant orientation relationship between the eutectic phases. Similar microstructure in binary eutectic alloys was also found by Moura et al. who studied Sn-0.7wt%Cu alloy [80]. Cellular eutectic alloys were also found in ternary Al-Cu-Ag [81] and quaternary Ni28Al28Cr28Mo6Fe10 (at%) alloys [82]. It is proposed that under eutectic solidifications, some additional elements can lead to the solid-liquid interface instability [83], due to the solute built-up during solidification. In addition, the cellular spacing decreases with an increase of cooling rate, and the mechanism is similar to the grain refinement of rapid solidification [84]. The development of the eutectic cell is

usually accompanied by the coupled growth of two eutectic phases, following the nucleation of one eutectic phase (leading phase) and the growth of another eutectic phase on the leading phase. Thus, the heterogeneous nucleation of eutectic leading phase has great impact on microstructure of the eutectic cells [85,86]. At the certain undercooling range, increasing the undercooling is able to get higher heterogeneous nucleation rate of the eutectic phase, resulting in more eutectic cells and decreased cell spacing.

Furthermore, the transition of eutectic structure from cellular to dendrite occurs in the eutectic alloys. Goetiznger et al. studied Ni-21.4%Si alloy without the influence of impurities, and dendritic eutectic morphology was found in the undercooled Ni-Sn alloy [87]. The negative thermal gradient from a planar interface to the liquid is responsible for the instability of the liquid/solid interface, and the dendritic structure forms with branches for the effective dissipation of excessive heat. Besides, Li et al. took into consideration of kinetic effect and thermal undercooling on the dendrite formation [88]. The thermal undercooling caused by negative thermal gradient has the largest proportion contributing to dendrite formation at low undercooling, while at large undercooling, kinetic effect undercooling also plays an important role. In addition, Zhao et al. studied the undercooled solidification of high-purity Ag-Cu eutectic alloy, and the cellular eutectic cannot form without negative temperature field [89]. It is because the eutectic phase composition and high thermal diffusion coefficient can suppress dendritic eutectic and contribute to the cellular structure. To be detailed, the compositions of eutectic phases in Ag-Cu alloy have large variations, and more solute needs to diffuse away, resulting in lower growth. Also, the Ag-Cu melt has large thermal diffusion coefficient. The high thermal diffusion and lower growth of the cells restrain the development of the branches of the cells.

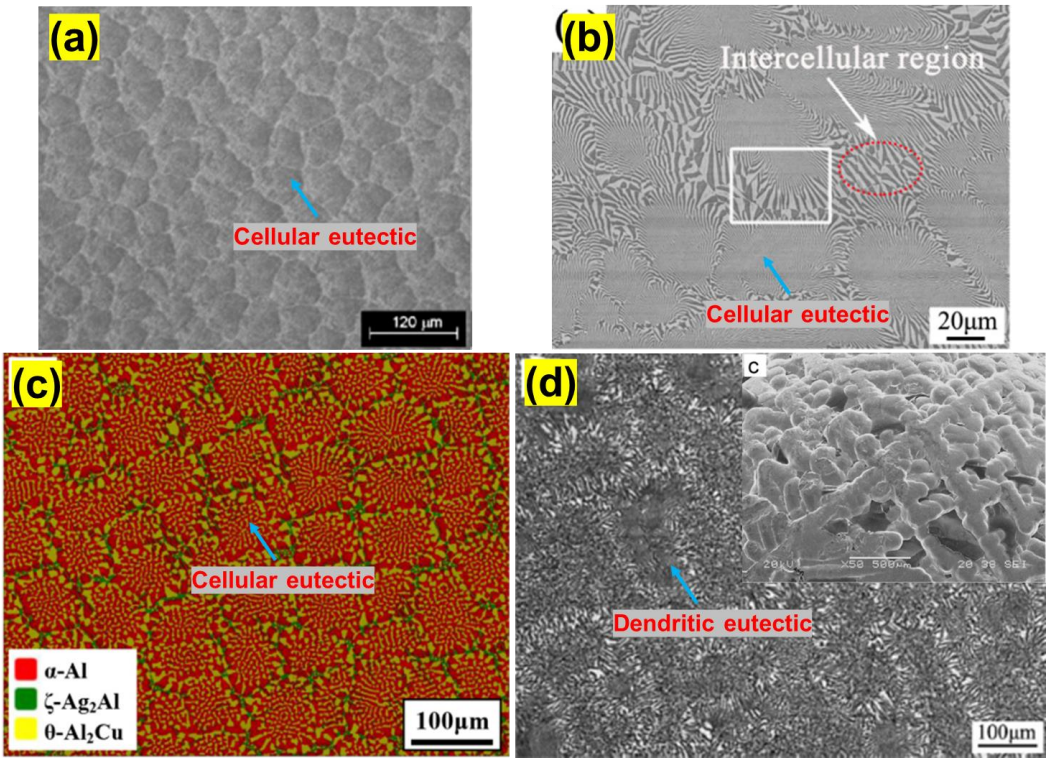

Fig.2-8 Cellular eutectic structure of Sn-0.7wt%Cu alloy [90] (a), Ni28Al28Cr28Mo6Fe10 (at%) alloy [91] (b), Al-21.5 wt%Cu-27wt%Ag eutectic alloy [83] (c); dendritic eutectic structure of Ag-39.9at%Cu [92] (d)

2.3 Traditional strengthening mechanisms employed in the development of high strength cast aluminium alloys

The majority of commercial aluminium alloys are binary, ternary or even multi-component alloys fabricated by melting. Alloys exhibit better physical or mechanical properties than pure element. This is because various strengthening mechanisms can be operated in a given alloy. They include solid solution strengthening, precipitate strengthening, and grain boundary strengthening, which contribute to obstacles that hinder the dislocation motion, thereby increasing the resistance of plastic deformation.

2.3.1 Solution strengthening

A solute solution contains one or more solute (minor) elements inside a solvent metal, maintaining its original crystal structure. The solid solution can be divided into two types, based on the roles of solute atoms. They are referred to as either substitutional solid solution or interstitial solid solution. The so-called substitution solid solution is that the solute atoms substitute the solvent lattice atoms in random or order manners. However, the interstitial solid solution is formed when the solute atoms distribute inside

the gap of solvent lattice. It should be noted that from a macroscopic point of view, the solute atoms homogeneously distribute, but from a microscopic point of view, these atoms are inhomogeneous.

Different elements have different solubility. There are three main factors affecting the solubility, which are atomic size, relative valence and electronegativity difference [93]. The first factor is that the primary solidarity will be restricted, provided the difference in atomic size between solvent and solute is 13-15%, owing to the large lattice distortions [94]. Secondly, Hume-Rothery proposed that it is more likely for the metal with a lower valence to dissolve into the metal with higher valence [93]. Lastly, it is also found that electronegativity difference also plays a role in the solubility [95]. It is concluded that intermetallic compounds are more porn to form if more electronegative is the solute and the more electropositive is the solvent metal [96].

In aluminium alloys, different atoms have different solubility. For example, Si has a low solubility of ~1.65wt% in aluminium, while 5.65wt% of Cu can be dissolved in aluminium. Zander et al. have investigated non-hardenable aluminium alloys and proposed solid solution hardening model, taking into consideration of the size and modulus misfit parameters between solute and solvent elements [97]. The solid solution hardening (τ_{L-N}) is expressed as:

$$\tau_{L-N} = \frac{(2wf_m^4C^2)^{1/3}}{2b^{7/3}(Gb)^{1/3}} \quad 2\text{-}12$$

$$f_m = \frac{Gb^2}{120}\varepsilon_L \quad 2\text{-}13$$

where w is the range of the force, G is the shear modulus, f_m is the force, c is the atomic fraction of the solute, b is the Burgers vector and ε_L is the combination of size and modulus misfit.

It can be found that the solid solution hardening is proportional to $c^{2/3}$ and ${\varepsilon_L}^{4/3}$. Furthermore, Ryen et al. investigated Al-Mg and Al-Mn binary alloys with minor impurities of Si or Fe [98]. The linear relationship between concentration and strength were found at a given strain rate, and Mn provides a more effective solution strengthening rate than Mg.

2.3.2 Grain boundary strengthening

Grain refinement has been a hot topic for decades. The cast alloys or wrought alloys with fine grain size have many advantages. For example, it has better fluidity and

feeding, better distribution of porosity, improved surface finish and better mechanical properties. Among them, better mechanical properties can be greatly improved with the decrease of grain size from hundreds of micrometre to hundreds of nanometres. It is proposed that finer grain size can lead to more grain boundaries. Meanwhile, the grains in the alloys have different orientations. Thus, grain boundaries can act as obstacles inhibiting the dislocation movement that leads to dislocation pile-ups near grain boundaries during deformation. The relationship between grain size and yield stress is described as the Hall-Petch equation [99]

$$\sigma_y = \sigma_0 + kd^{-1/2} \qquad 2\text{-}14$$

Where σ_y is the yield strength, σ_0 is the friction stress or resistance to dislocation motion, k is the constant and d is the grain size. k is affected by orientation texture concerning the distributions of grain boundaries [96].

This equation has a good agreement with the experimental results obtained from coarse-grained microstructure, and it shows that the yield stress increases with decreasing grain size. It is also desirable in the eutectic alloys, where finer interlamellar spacing contributes high strength. Furukawa et al. reported that there is a decrease in the slope on the Hall-Petch equation when the grain size decreases to 150 nm in torsion-strained samples [100]. The grain boundaries increase dramatically with the decrease of grain size, and at these grain boundaries, there are a lot of extrinsic dislocations. During the impingement of indenter, the participation of these extrinsic dislocations moves in these non-equilibrium grains, which changes the slope (k). Moreover, it was found that even a negative slope occurs in the Hall-Petch equation. Carlton et al. proposed the statistical absorption of dislocations by grain boundaries, accounting for this inverse Hall-Petch effect [101]. It is because with decreasing the grain size, the alloys have more grain boundaries and more dislocations will be absorbed by the grain boundaries during deformation. As a result, the decrease in grain size has a negative effect on yield strength.

2.3.3 Precipitation strengthening

The precipitation strength involves the dispersion of fine precipitates to impede the motion of dislocation, thereby increasing the strength of the alloy. Based on the interaction between the precipitates and dislocations, the precipitation strengthening mechanism can be divided into two groups, that involve non-deformed precipitates and deformed/sheared precipitates. The balance of force between line tension (T) and obstacle, as shown in Fig.2-9. The force meets the maximum level when $sin\,\theta$ is 1 or

θ is 90°. The hard particle acts as an obstacle to block the motion of incoming dislocation. The dislocation can bypass the hard precipitates when the applied stress exceeds 2T where T is the line tension force of dislocation. Orowan loops or cross slip forms as shown in Fig.2-9 [102]. The precipitation strengthening based on Orowan loop mechanism can be expressed by λ_{Ol} and $\Delta\tau$, as shown below [103,104]

$$\lambda_{Ol} = (\frac{2\pi}{3f})^{1/2} r_p \quad 2\text{-}15$$

$$\Delta\tau = \frac{\mathrm{Gb}}{2\pi\lambda\sqrt{1-\upsilon}} \ln\frac{r_p}{r_o} \quad 2\text{-}16$$

Where λ_{Ol} is the average spacing between precipitates, $\Delta\tau$ is the increment of yield stress, r_p is the average radius of precipitates, f is the volume fraction of precipitates, r_o is the radius of dislocation core, υ is the Poisson's ratio, G is the shear modulus, and b is the magnitude of the Burgers vector.

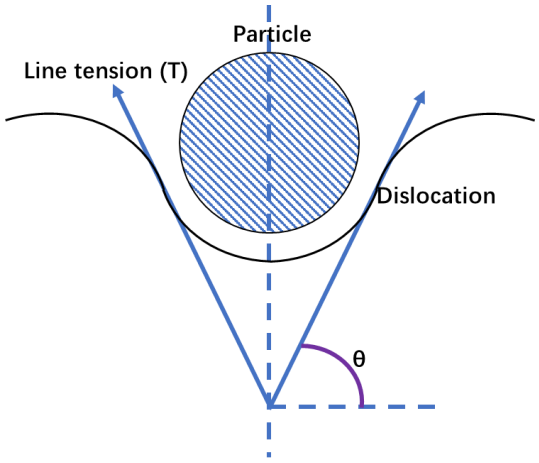

Fig.2-9 The illustration of non-deformable precipitate impeding dislocation motion

From the above equations, it can be found that smaller size and higher volume fraction of precipitates can lead to higher strength. The bypass of dislocation of precipitates by Orowan looping is shown in Fig.2-10. The process undergoes four stages. Firstly, the force is approaching the precipitates. Secondly, the dislocation approaches the precipitates and bends around it. Thirdly, two dislocation segments on sides of the particles are elastically attracted having same Burgers vector and opposite line directions [101]. Lastly, the dislocation bypasses the precipitate forming a loop. During the process, the precipitates remain unchanged, and the resistance force is greater than 2T. Fig.2-11 shows the dislocation pass through the precipitate when the maximum force reaches before the θ is 90°. The precipitates are sheared and pass through the precipitates.

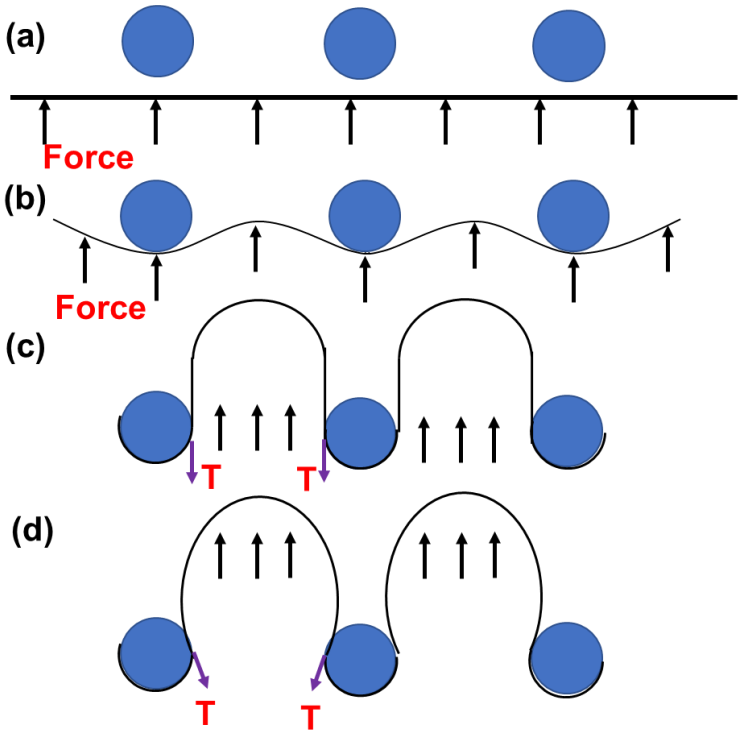

Fig.2-10 The bypass of dislocation through the precipitates

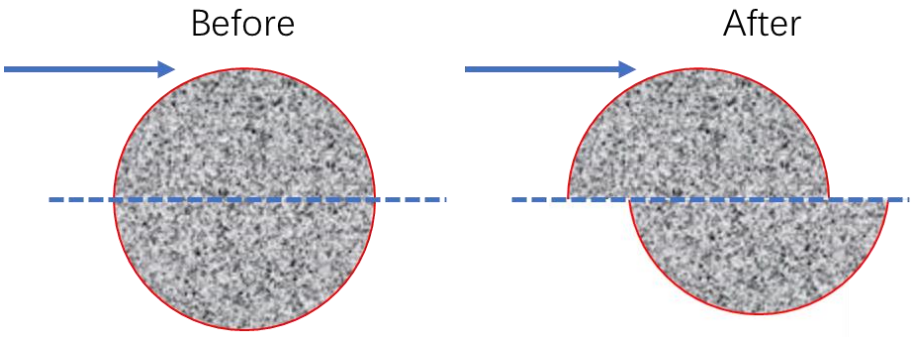

Fig.2-11 Dislocation motion through deformed precipitates

The peak ageing hardness or strength is determined by the size and distribution of precipitates as well as their coherency/semi-coherency. The shearing process is more difficult if the size of the precipitates increases. As a result, the dislocations pass the precipitates in the form of Orowan mechanism and the strength decreases. The highest strength is obtained with an equal probability of bypassing and shearing precipitates, shown in Fig.2-12.

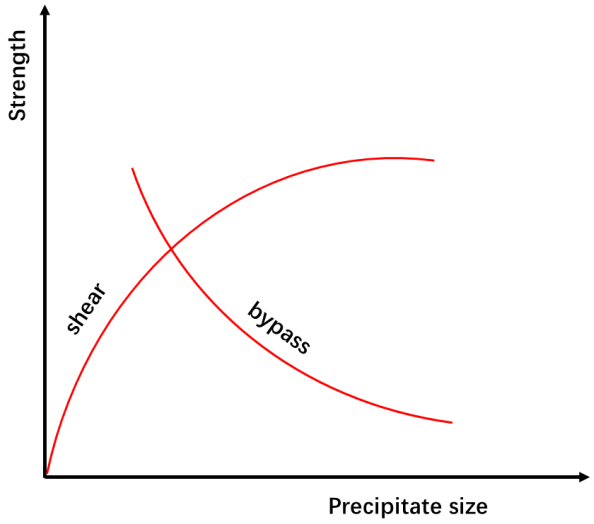

Fig.2-12 Relationship between precipitate size and strength [105]

The types of precipitates and precipitation sequence in various alloy systems are different. For example, A356 and A357 alloys (Al-Si-Mg), which are widely used in structure components, have excellent ageing hardening response after solution treatment. The precipitation sequence in these two alloys are [106,107]

SSSα→GP zones (needles or spheres)→β'' (needles)→β' (rods)→β(plates, Mg_2Si or non-stoichiometric Mg_xSi_y)

Moreover, Al-Cu alloys are widely applied in aerospace industries [108]. The classical precipitation sequence in Al-Cu binary is [108,109]

SSSα→GPI→ GPII→θ''→θ'

It is reported that in Al-Si-Mg alloy, the attracting of Mg around Si clusters causes GP zones, following the transmission to β'' [106]. The structure of GPI in Al-Cu alloy is a single Cu layer lies on $\{002\}_\alpha$ plan, while GPII has two Cu layers on $\{002\}_\alpha$ plan with a distance of 0.808 nm [106]. All the GP zones are coherent with Al matrix.

The peak ageing time of Al-Si-Mg alloy is between 12-24 hours at an ageing temperature of 180 °C [110] or between 18-24 hours at an ageing temperature of 160 °C [111]. Over-ageing treatment leads to the coarsening of the precipitates, and the hardness decreases. β'' forms at peak ageing treatment in Al-Si-Mg alloys and it is coherent along $<001>_{Al}$ axes, but the rhombohedral cross-section of β'' has large misfit with Al matrix [112]. Besides, the peak ageing time in Al-Cu alloys also depends on the ageing temperature. Liu et al. studied the precipitation in Al-Cu alloys [113] and the peak ageing time is about 24 hours at 165 °C. The majority of precipitates are plate-

like θ'. The interface of θ' around the rim of the plates is semi-coherent, while the rest of the interfaces are coherent [108].

Furthermore, apart from Al-Si-Mg or Al-Cu alloys, the mechanical properties and precipitation of some other alloys were also studied. For example, It is found that Al-Si-Cu-Mg alloys (Al-Si based) have much higher strength than ternary Al-Si-Mg alloys [114]. The maximum yield strength of ~415 MPa was obtained after ageing for 24 hours at 150 °C. Under peak ageing condition, there are mainly three types of precipitates in Al-Si-Cu-Mg alloys, which are β'', θ', Q'' [115,116]. It is apparent that two combinations of precipitates (β''+θ' and θ'+Q'') exist in the alloy under peak ageing condition. The precipitates and mechanical properties of Al-Cu based multi-component alloys were also studied. Liu et al. found that Al-5Cu-0.3Mg-0.3Si (wt%) alloy has θ'+Q'' precipitates after peaking at 180 °C for 10 hours [117]. Five types of precipitates of T1 (Al_2CuLi), θ'(Al_2Cu), θ'', δ' (Al_3Li) and σ ($Al_5Cu_6Mg_2$) coexists in Al-3.7Cu-1.5Li (wt%) alloy after ageing for 24 hours at 165 °C [118]. It is more complex of the precipitation in multi-component systems, and the combination of precipitates leads to high strength. In addition, the morphology and orientation of precipitates or dispersoid particles also have an influence on the strength. Nie reported that in magnesium alloys with the same volume fraction and number density of precipitates, plate precipitate contributes to the highest yield strength, compared with rods or spherical particles [119]. The reason is that the plate-shaped precipitates forming on prismatic plans have the smallest inter-particle spacings, based on Orowan equation.

2.4 Recent development of high strength alloys based on ultrafine eutectic microstructure

The mechanical properties of eutectic alloys can be greatly improved with the refined interlamellar spacing based on Hall-Petch theory [99]. The strength of eutectic alloys can be increased by reducing the interlamellar spacing due to increasing interface density, leading to an increasing amount of obstacles to dislocation motion. For example, the binary eutectic alloy of Al-33%Cu is one kind of most common binary eutectic Al alloys that have been investigated in details. Under rapid solidification condition, the interlamellar spacing of α-Al and Al_2Cu decreases. Srivastava et al. studied the effect of cooling rate on the as-solidified microstructure of Al-33%Cu alloy fabricated by suction casting using 2-5 mm diameter water-cooled copper mould [120]. It was found that the average interlamellar spacing of Al-33%Cu eutectic alloy decreased with increasing cooling rate. The smallest interlamellar spacing of 200 nm

was obtained when the melt was solidified at a cooling rate of 600K/s using a 2 mm diameter water-cooled copper mould. It is reported by Park et al. that Al-Cu binary eutectic alloy with an interlamellar spacing of ~200 nm has high ultimate fracture strength of ~1.2 GPa and low plastic strain of ~2% under compression test [121].

Although the alloys with ultrafine eutectic microstructure have excellent strength, the low plasticity and toughness are main factors that hinder their adoption to engineering applications. The properties of these alloys depend on the crystal structure, length scale and volume fraction of each constituent phase [58]. In recent decades, a lot of investigations have been carried out to improve the plasticity of nanostructured eutectic alloys without compromising the strength. Two design strategies have been adopted. One approach involves the formation of a composite microstructure consisting of the soft dendritic primary phase and interdendritic ultrafine eutectic mixture, which based on hypoeutectic alloy composition. The other approach is to modify the single homogeneous eutectic matrix into the bimodal eutectic mixture, comprising of a hierarchy of different length scales and morphologies of eutectic phases.

2.4.1 Hypoeutectic ternary and multi-component alloys

Most of the mechanical properties of ultrafine ternary eutectic alloys are based on compressive strength and ductility. Hence, these alloys are believed to have a low tensile ductility to meet the engineering applications in the automotive industries. Recently, this design strategy of introducing soft micron-sized grains as a primary phase embedded into a nano-/ultrafine matrix has been developed successfully in Ti-based and Ni-based ultrafine eutectic alloys to improve tensile ductility. It is believed that good ductility can be achieved via introducing soft primary phases. The microstructures of ultrafine hypoeutectic Ti-16.6%Nb-6%Co-5.1%Cu-6.5%Al (at%) alloys reported by Okulov et al. are shown in Fig.2-13 [122]. The microstructure consisted of soft β-Ti(Nb, Al) dendrites with a volume fraction of 90-95% and β-Ti(Co,Cu)-TiCo ultrafine eutectic. The tensile yield strength and elongation of Ti-Nb-Co-Cu-Al hypo-eutectic alloy are about 1.1GPa and 11% respectively, which is higher than that of many ternary Ti-based alloys. The improved mechanical properties are due to the high density of slip bands in the soft dendrites during deformation and dissipation of excessive stress though high strength ultrafine eutectic mixture. Li et al. fabricated $(Fe_{0.5}Co_{0.5})_{90}$-$(Mo_{0.1}C_{0.2}B_{0.5}Si_{0.2})_{10}$ multiphase composites with a microstructure, consisting of nano-lamellar phase strengthened α-(Fe,Co) dendritic

cores surrounded by a network of refinement phases of ultrafine eutectics [123]. When the volume fraction of FeCo dendrites reach 95%, the compressive yield strength and strain to failure are 1153MPa and 18.62% respectively.

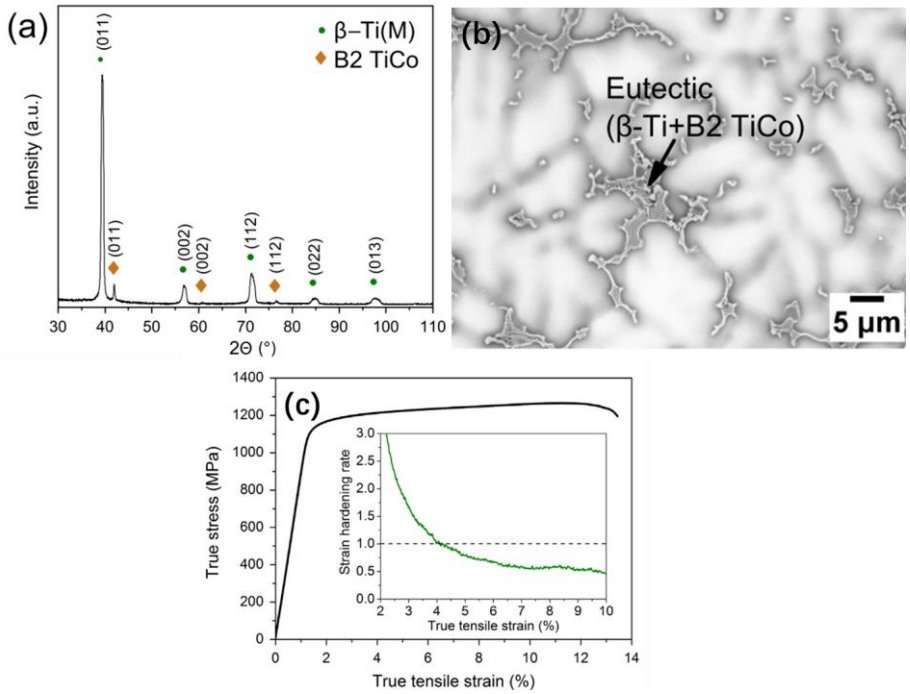

Fig.2-13 XRD pattern (a), SEM backscattered image (b) and tensile properties (c) of Ti-16.6%Nb-6%Co-5.1%Cu-6.5%Al(at%) hypoeutectic alloy [122]

More recently, hypoeutectic alloys with quaternary or even quinary recipe were developed, which enable to improve the strength and ductility further. Kang et al. prepared $(Ti_{70.56}Fe_{29.44})_{90}Co_{10}$ ternary, $(Ti_{63.5}Fe_{26.5}Co_{10})_{87.8}Nb_{12.2}$ quaternary, $(Ti_{63.5}Fe_{26.5}Co_{10})_{82}Nb_{12.2}Al_{5.8}$ quinary alloys via semi-solid sintering (SSS), which is shown in Fig.2-14 [124]. The additional elements of Nb and Al contribute to a novel bi-modal microstructure that comprised of coarse Ti2(Fe,Co) phase surrounded by the ultrafine eutectic matrix containing β-Ti and Ti(Fe,Co) lamellae. The compressive yield strength and plasticity of quinary alloy are 2050 MPa and 19.7%, respectively. It can be noted that introducing soft dendrite which is beneficial to the plasticity, and the high-order eutectic mixture which surrounds the dendrites provides the strength is able to yield a combination of good ductility without compromising the strength of the alloy. Similar results were found by Liu et al. who studied $Ti_{62}Nb_{12.2}Fe_{13.6}Co_{6.4}Al_{5.8}$ alloy [125]. The microstructure of the alloy consists of solid solution β-Ti dendrites and ultrafine eutectic (TiFe+ β-Ti), and it has more favourable mechanical properties. However,

there are only a few investigations on multi-component ultrafine hypoeutectic aluminium alloys.

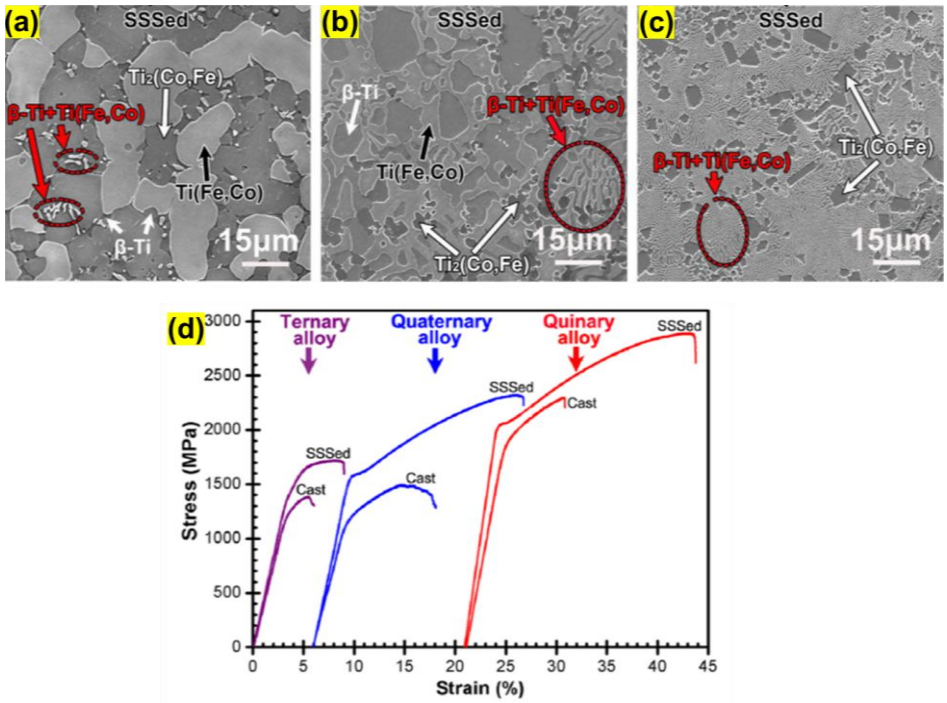

Fig.2-14 $(Ti_{70.56}Fe_{29.44})_{90}Co_{10}$ ternary (a), $(Ti_{63.5}Fe_{26.5}Co_{10})_{87.8}Nb_{12.2}$ quaternary (b), $(Ti_{63.5}Fe_{26.5}Co_{10})_{82}Nb_{12.2}Al_{5.8}$ quinary (c) alloys via semi-solid sintering (SSS) and their mechanical properties (d) [124]

2.4.2 Ternary and multi-component eutectic/near-eutectic alloys

A unique eutectic microstructure can be generated by modifying the binary eutectic composition with the addition of different elements to form high-order eutectic alloys. Recent reports on the study of Al-13%Cu-6%Si (at%) eutectic alloy have demonstrated superior compressive mechanical properties due to the presence of a bi-modal microstructure shown in Fig.2-15 (a), containing microstructural length scale hierarchy in the eutectic microstructure to dissipate the shear stress effectively and suppress the localisation of deformation [121]. The compressive fracture strength and strain to failure of Al-13%Cu-6%Si (at%) eutectic alloy were found to be 0.8±0.05 GPa and 11±2%, which exhibits significantly increased plasticity with a limited reduction of fracture strength as compared with Al-33%Cu (wt%) binary eutectic alloy. The similar bimodal eutectic structure was also found in quaternary $Mg_{56}Al_{30}Li_7Cu_7$ alloy under rapid solidification condition [126]. It can be noted that the ternary or quaternary alloys exhibit better mechanical properties, especially ductility, as compared to their binary

counterparts. During the compression test, the bimodal eutectic microstructure can lead to the rotation of the cellular structure, resulting from the interaction of primary and secondary bands [127]. Consequently, it is more effective to dissipate the excessive stress.

Tiwary et al. found that the ternary eutectic Al-10Cu-1.3Ni (wt%) alloy with a bi-modal microstructure consisting of a fine eutectic matrix (Al+Al_2Cu) with an interlamellar spacing of 40nm-90nm and Al_7Cu_4Ni intermetallic (size of 1.5-2.5μm) has high strength at elevated temperatures [59]. The microstructure is shown in Fig.2-15 (b). It is reported that the compressive fracture strength and plasticity at room temperature and 300 °C are 1 GPa and 9%, 0.5 GPa and 12.5%, respectively.

The ultrafine ternary eutectic microstructure with different microstructures has been observed in other alloy systems such as $(Ti_{70.5}Fe_{29.5})Sn_9$ with better compressive plasticity (~15%) and higher compressive strength (~2261 MPa), as compared to its binary Ti-Fe counterparts [128]. The microstructure of $(Ti_{70.5}Fe_{29.5})Sn_9$ ternary eutectic consisted of a heterogeneous distribution of ultrafine phase mixtures of β-Ti(Nb) solid solution surrounded by alternating plate-like shaped Ti_3Sn and α-Ti phases (shown in Fig.2-15 (e)), which has outstanding strength of ~1.1 GPa and large plasticity of ~36% [129]. However, in some Fe-based ternary eutectic alloys, the addition of Al shifts the composition to the off-eutectic point slightly and increases the growth undercooling [130]. This can lead to the formation of a few solution hardened dendrites and reduced interlamellar spacing. The microstructure of the Fe-based multi-model structure is shown in Fig.2-15 (c,f). Consequently, these ultrafine ternary eutectic alloys exhibit a combination of good plasticity and high strength in compression [130–132].

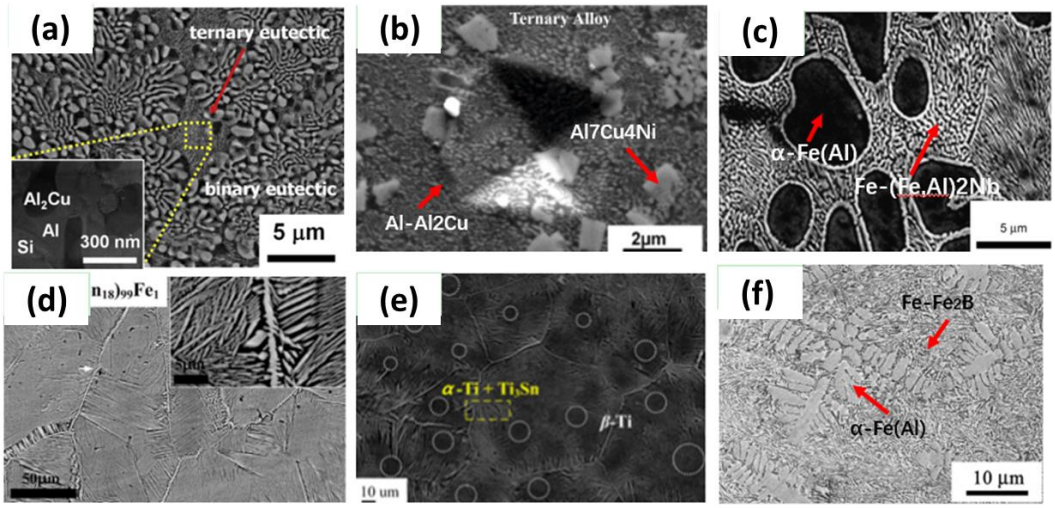

Fig.2-15 The bi-modal microstructure of ternary eutectic (a) Al-Cu-Si [121] (b) Al-Cu-Ni [59] (c) Fe-Nb-Al [131] (d) Ti-Sn-Fe [133] (e) Ti-Sn-Nb [129] (f) Fe-B-Al [130]

2.5 High pressure die casting (HPDC)

Aluminium is an attractive engineering material due to its unique physical and chemical characteristics. It has one-third of the density and modulus of steels, exhibiting high thermal conductivity and electrical conductivity, and high corrosion resistance. Since the application of the Hall-Heroult method of electrolytic reduction as an industrial process for the production of pure aluminium from its ores, aluminium alloys have gained wide acceptance in engineering industries and its commercial applications continue to increase [134]. Aluminium production rises from just over 45,000 tons in 1992 to more than 25 million tons today. This is driven by the need for a lightweight vehicle in automotive industries to reduce fuel consumption. Fig.2-16 illustrates the growth of aluminium alloys used per vehicle over the past 50 years based on Ducker Worldwide cited by Drive Aluminium [135].

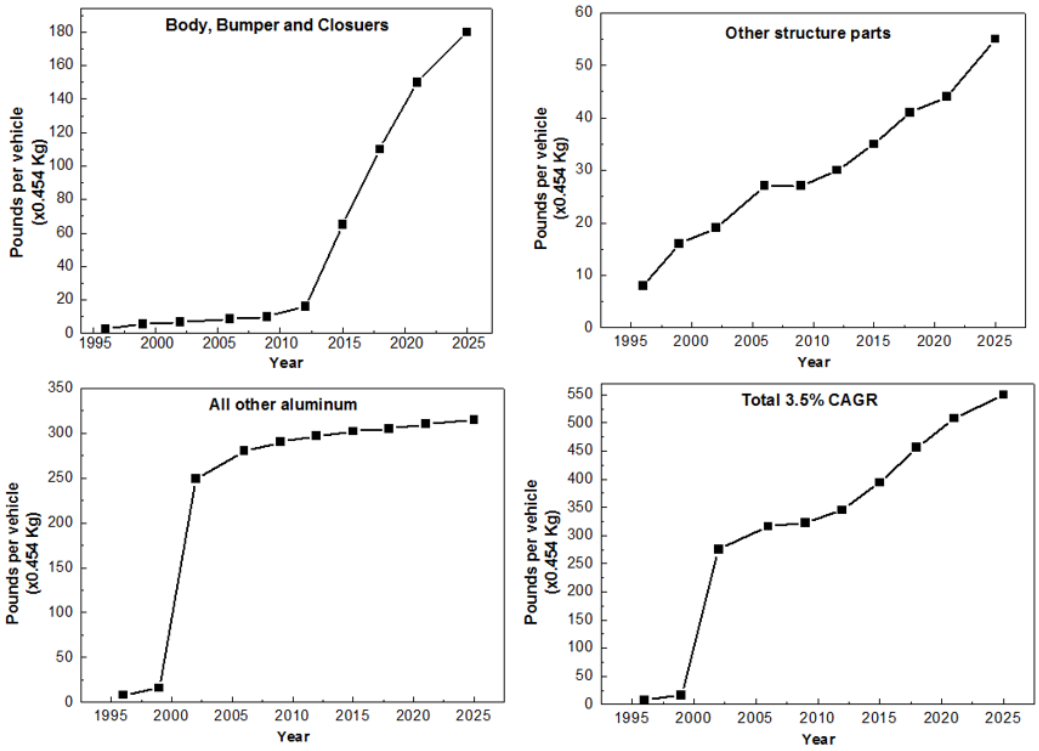

Fig.2-16 Average weight of aluminium alloy used in automobile vehicles [134]

The casting process has always been the main processing method for the fabrication of aluminium alloy parts. Among all the casting process, high pressure die casting is widely applied in the automotive industry, which is about 60% [1]. There are some advantages of HPDC contributing to its wide application. Firstly, it has very high productivity that each injection process takes about 60 seconds [136]. Secondly, it can produce a thin wall and complex parts [137]. In addition, excellent surface quality and good mechanical properties can be achieved via this process, due to the high pressure and fast cooling rate [137]. Fig.2-17 shows some examples of aluminium castings produced by high pressure die casting.

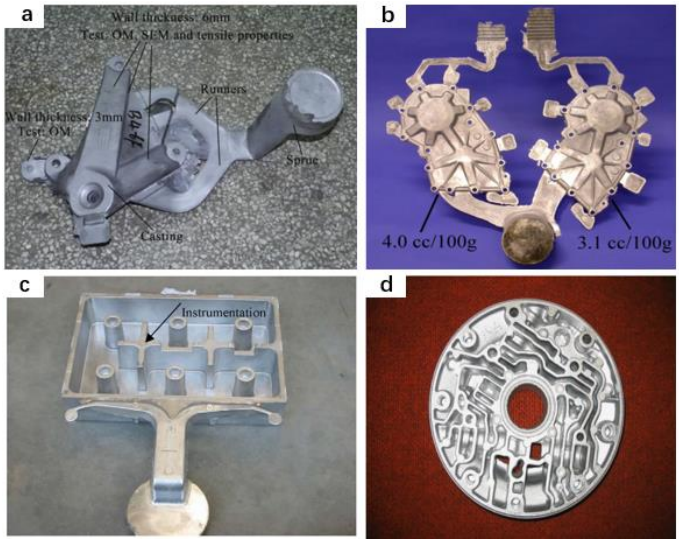

Fig.2-17 Aluminium castings produced by high pressure die casting: (a) casting of alloy Al11wt%Si2wt%Cu1wt%Fe with filling and overflow system [138] (b) twin cavity casting of alloy ADC12 [139] (c) the filter box of Al12wt%Si alloy [140] (d) the pump cover casting of alloy ADC12 (1700 g weight, 215 mm diameter) [139]

2.5.1 High pressure die-cast process

Fig.2-18 shows a high pressure die casting injection system. From the image, there are mainly three parts of the HPDC system, which are vacuum system, casting mould and injection system and pressure system which provides a force for the injection. The vacuum system is alternative, and without it, the castings can still meet the designed properties in some cases.

The casting process can be divided into three stages. In the first stage, the molten alloy fills into the short sleeve, and the plunge starts to move at slow velocity to avoid turbulence and a large quantity of air entrapment. In the second stage, the plunge moves at high speed suddenly. Thus the filling of the die cavity is at high speed, and the premature solidification can be avoided. At this stage, any entrapment of air in the injection chamber and die cavity, can result in the presence of gas porosities in complex die castings, leading to poor mechanical properties. At the third stage, the die is fully filled by the melt, and the high pressure on the plunger is kept until the end of solidification. Moreover, air entrapment can be minimised by using a vacuum system [139]. The HPDC equipped with the vacuum system is a so-called vacuum assisted high pressure die-cast (VPDC). In addition, the second process plays a very important on the final quality of the castings, such as surface finish and porosity level. The parameters of stage two, which affects the casting quality, are discussed below.

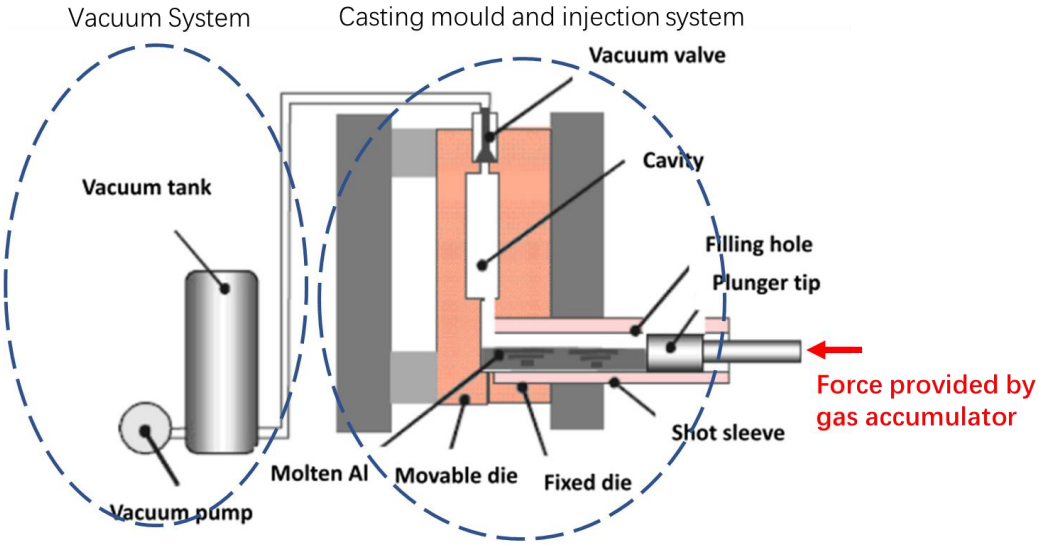

Fig.2-18 A schematic illustration of hydraulic injection system [141]

Several investigations on the relationship between the casting quality and vacuum system have been carried out. Niu et al. studied the porosity distribution and mechanical properties of Al-(5-18%)Si (wt%) alloys produced by vacuum assisted high pressure die casting process [142]. The study shows that the volume of gas porosity and pore sizes can be significantly reduced with a vacuum system, which is because of less air in the shot sleeve and mould during the injection. As a result, the mechanical properties of as-cast components are improved. For example, the tensile strength and elongation in Al5%Si (wt%) alloy improved by 6.6% and 15%, respectively.

Hu et al. studied Al-Mg-Si-Mn alloy processed by vacuum assisted die casting, and the result shows that porosity and oxide inclusions can be mitigated, resulting in the increase of fatigue limits from 57 MPa to 75 MPa [143]. Moreover, Dong et al. reported that the application of the vacuum system during. HPDC process is able to minimise the deviation of tensile ductility under as-cast and T6 state [136].

2.5.2 Process parameters of high pressure die casting

Although the application of vacuum system to HPDC can improve the quality and mechanical properties of as-cast components, the capital investment of VHPDC is huge, hindering its wide usage in the casting industries. The high pressure die casting without a vacuum system has gained more attention, due to the low cost. The process parameters play a vital role in the quality of HPDC products. Fig.2-19 illustrates the

detailed HPDC process without a vacuum system. It can be seen that there are several important parameters, including injection temperature, plunge velocity 1, gate velocity or plunge velocity 2, mould temperature and intensive pressure. The effects of these parameters on casting quality are discussed below.

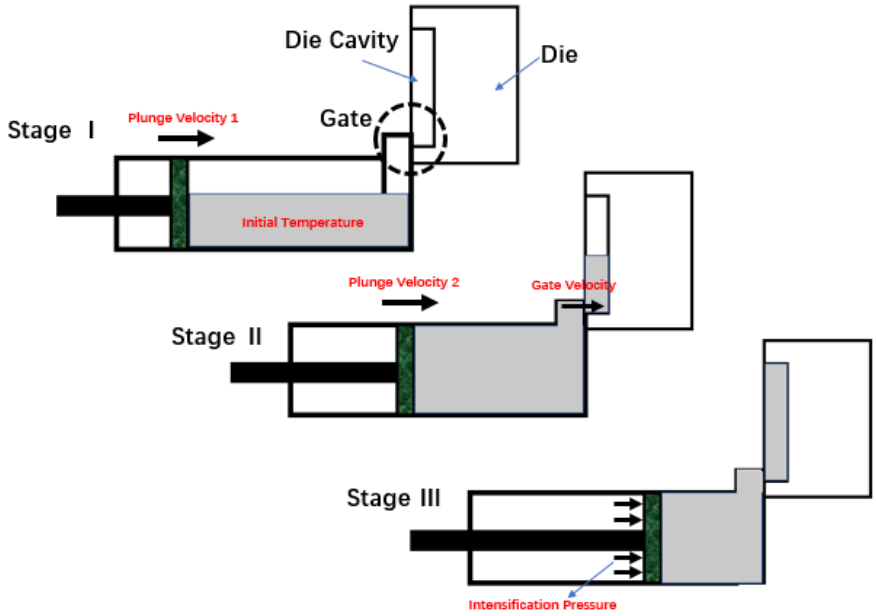

Fig.2-19 Process of high pressure die casting and its parameters [144]

2.5.2.1 Injection temperature

The injection temperature is related to the susceptibility of die soldering. If the melt is maintained at low temperature in the short sleeve, an amount of iron-containing intermetallic phase can form because of the significant heat loss of the casting. During final solidification in the die cavity, less Fe remains in the liquid and the intermetallic layer are easy to form. Thus the soldering reactions can occur in the die cavity [145]. Moreover, a large amount of intermetallic phases which form in the shot sleeve is detrimental to the fluidity of the alloy, thus degrading the surface quality of the casting. However, high injection temperature can prohibit the formation of initial phases such as dendrite α-Al, which is usually formed in the shot sleeve. Therefore high volume fraction of finer α-Al dendrites can solidify in the steel mould at high cooling rate. Outmani et al. found that the as-solidified microstructure consisted of much smaller α-Al dendrite phase together with, fibrous morphology of eutectic Si, and smaller block-like intermetallic compounds [146] as the injection melt temperature increased to 680 °C. In addition, Yang et al. investigated the melt superheating on Al-Mg-Si-Mn alloy and found that the α-$Al_{12}(Fe,Mn)_3Si$ phase has the same composition with or without

melt superheating. But with melt superheating, more refined α-$Al_{12}(Fe,Mn)_3Si$ particles form, owing to the suppress of its solidification in the shot sleeve [147].

2.5.2.2 Plunge velocity and gate velocity

Previously, some studies show that during stage 1, there is a critical plunger speed which can raise the wave of the melt caused by plunger motion to the ceiling of the shot sleeve to avoid it rolling over. If the plunger moves at speed greater than the critical value, the wave will reflect against the sleeve ceiling and might roll over, resulting in air entrapment. However, if the speed is lower than the critical speed, the wave will reflect against the end wall of the short sleeve and trap the air in front of the plunger. Fig 2-20 shows these two scenarios of plunge speed in stage 1. More recently, Hernández at al. have carried out detailed and systematic studies of wave dynamics in stage 1 as a function of process variables of plunger motion parameters, an initial filling fraction of the liquid in the shot sleeve and shot sleeve dimensions, so as to minimise air entrapment [148]. The optimum process parameters in stage 1 have been identified by taking into consideration of non-hydrostatic and viscous effects using analytical and numerical models [148,149]. Hernández and Faura used two-dimensional finite element model and a simpler model based on a shallow-water approximation to analyse the flow of melt in the shot sleeve and found that the initial filling fraction and dimension of plunger have a close relationship with the plunge speed [146,148].

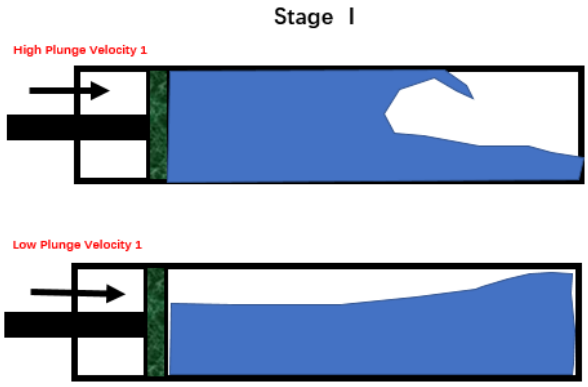

Fig.2-20 Different plunge speed in stage 1 [148]

The melt velocity during stage 2, which is decided by plunge velocity 2 or gate velocity, is one of the most important features controlling the casting quality. The cavity filling time significantly reduces with increasing gate velocity. If the gate speed is too high, it may make the surface finish worse and increase the porosity caused by air entrapment

[144]. Gunasegaram et al. showed that the increased gate velocity from 1.0 m/s to 1.6 m/s led to increased strength by 6% and ductility of die-cast A380 alloy by 30% [150]. Verran et al. investigated that the plunge velocity 1 (0.14-0.29 m/s) has effects on the density of the castings, which is not a linear relationship [151]. Chiang et al. found that in Al-Si die casting alloys, the compaction of the melt into the die with increased plunge velocity can lead to higher heat transfer and a significant reduction of silicon particle size, thereby, improving the hardness [152].

2.5.2.3 Intensive pressure

Intensive pressure is applied once the die cavity is completely filled, hindering the formation of porosity and expansion of entrapped air, thus improving the strength [144]. Syrcos et al. showed that increasing the intensive pressure in Al-Si-Cu alloy from 120 bar to 280 bar can increase the density from 2.74 g/cm^3 to 2.745 g/cm^3, while improving the casting quality with lower porosity [153]. Verran also found that the highest density of die casting can be achieved at a certain intensive pressure. When the pressure exceeds this critical pressure (24.3 MPa), there is no chance of the density [151]. Furthermore, Outmani et al. found that in Al-Si-Cu die casting alloys, high intensive pressure contributes to more fragmentation of α-Al dendrites, leading to the development of homogeneous microstructure and reduced level of porosity, giving improved mechanical properties and density [146].

2.5.2.4 Die temperature

The die temperature is controlled by the internal cooling system and has a great influence on the cooling rate during HPDC operation [154]. The decreased die temperature is beneficial for decreasing the solidification time of the casting. Chiang et al. found that die temperature is one of the important factors on the mean particle size of silicon and hardness value of Al-Si alloys [152]. The Si particle size decreased while the hardness increased with decreasing die temperature. With reduced die temperature, the time of solidification can be decreased. Thus, coarse Fe-rich intermetallic compound particles can be suppressed, and finer lamellar eutectic can be achieved [155]. Die temperature is a very important factor contributing to die soldering. It is because the lower die temperature enables the die to be protected by a lubricant. A high die temperature can lead to direct contact between the die and the molten metal, resulting from wash-off of the lubricant. Therefore, the mould is more susceptible to die soldering [156].

2.5.3 Casting defects

2.5.3.1 Hot tearing

One of the most detrimental and common defects in HPDC is hot tearing, which results from the lack of liquid feeding in solid skeleton during solidification [157]. The phenomenon is very complex, and it can be influenced by intrinsic material properties (including interfacial energy/ viscosity of the liquid and high-temperature strength of alloy) and process parameters (e.g. solidification path, the orientation of neighbouring solid grains, casting temperature and cooling rate) [15,158]. Normally, the alloy that has a wide solidification temperature range, such as Al-Cu and AZ91 (Mg-Al) alloys whose solidification temperature range exceeds 100 °C exhibits low hot tearing resistance. It is because the alloys with a large temperature interval from solidus to liquidus take a long time of coexisting solid and liquid. It is more vulnerable for the grains to separate, resulting from shrinkage. Consequently, hot tearing occurs induced by insufficient feeding of the thin film of liquid between the interdendritic regions [14]. In addition, the grain size and morphology play an important role in hot tearing. The equiaxed grains are stronger and more resistant to hot tearing because of more surface area of grains per volume compared with dendrites, resulting in a more homogeneous distribution of liquid around solid grains [15,159]. A fine-grain microstructure exhibit higher strength due to the restriction of dislocation motion or grain boundary sliding, thereby leading to enhanced hot tearing resistance [15]. Kimura et al. added Ti-B as a grain refiner in the die-cast Al-4.5wt%Mg alloy [160]. This caused a reduction in the susceptibility of hot cracking because of a large number of grain boundaries. The addition of iron increases high-temperature strength of the alloy. Zak et al. have revealed the improvement in castability and hot tearing resistant of die-cast Al-14wt%Si alloy with the addition of Fe (1.8wt%) and Cr (0.3wt%) [161]. This is because α-AlFeMnSiCr with compact, star-like morphology is beneficial for the high-temperature mechanical properties of the alloy. The mould temperature and pouring temperature also has impacts on the susceptibility of hot tearing. High pouring temperature and mould temperature can alleviate the tendency of hot tearing due to the reduction of mush zone [162].

2.5.3.2 Die soldering

Die soldering is one of many casting defects in which molten melt sticks onto the surface of the steel mould, causing considerable economic and production loss [163–165]. Especially, in the die casting process, the die lifetime expectancy and casting

quality are severely affected by microcavities and microcracks formed near the die surface [166]. Shankar testified that the die soldering in die casting process is a diffusional process that the iron and aluminium atoms diffuse into each other, giving rise to the formation of intermetallic particles [167]. Chen et al. identified two growth modes of intermetallics: a sudden built-up of one thick layer and gradual built-up of thick layer [168]. Han et al. proposed a critical soldering temperature which is dependent on the elements of die material and casting alloy composition. However, it was suggested that die soldering could be prevented by applying surface coatings containing elements such as titanium, chromium and manganese [169]. Many investigations have been focused on the modification of alloy composition and the replacement of die material to improve the soldering resistance during die casting. Zhu et al. revealed that Anviloy 1150 (W4wt%Mo4wt%Ni2wt%Fe) was the die material having the best soldering resistance, compared with H13, Mo-785, Ti-6Al-4V and Ni-718. In general, H13 is the most common die or tooling material used in the manufacturing industries [16]. However, the typical secondary die casting Al-Si alloys usually contain iron impurities ranging from 0.2wt% to 0.8wt%, which can hinder soldering on the H13 steel mould [161].

2.5.4 Commerical die-cast alloys

2.5.4.1 Die-cast alloy systems

A great number of alloys have been created over the years and of which 23 are developed for die casting processes. The compositions of these alloys are shown in Table 2-2. These alloys contain major alloying elements such as silicon(Si), copper(Cu), magnesium(Mg) and iron(Fe). Furthermore, the alloys can be classified into five groups: Al-Si-Cu, Al-Si-Mg, Al-Si-Mg-Cu, Al-Si and Al-Mg. Major alloying elements are chosen to control castability and develop the required properties that meet standard specifications [23,170,171].

Table 2-2 Composition of registered aluminium die-cast alloys used to cast shaped components [134]

	Composition, wt-%												
											Others except Al		
Alloy	Si	Fe	Cu	Mn	Mg	Cr	Ni	Zn	Sn	Ti	Each	Total	Al
343.0	6·7–7·7	1·2	0·5–0·9	0·5	0·1	0·1	...	1·2–2·0	0·5	...	0·1	0·35	Remainder
360.0	9·0–10·0	2·0	0·6	0·35	0·4–0·6	...	0·5	0·5	0·15	...	...	0·25	Remainder
A360.0	9·0–10·0	1·3	0·6	0·35	0·4–0·6	...	0·5	0·5	0·15	...	...	0·25	Remainder
361.0	9·5–10·5	1·1	0·5	0·25	0·4–0·6	0·2–0·3	0·2–0·3	0·5	0·1	0·2	0·05	0·15	Remainder
364.0	7·5–9·5	1·5	0·2	0·1	0·2–0·4	0·25–0·5	0·15	0·15	0·15	...	0·05*	0·15	Remainder
369.0	11·0–12·0	1·3	0·5	0·35	0·25–0·45	0·3–0·4	0·05	1·0	0·1	...	0·05	0·15	Remainder
380.0	7·5–9·5	2·0	3·0–4·0	0·5	0·1	...	0·5	3·0	0·35	...	...	0·5	Remainder
A380.0	7·5–9·5	1·3	3·0–4·0	0·5	0·1	...	0·5	3·0	0·35	...	...	0·5	Remainder
B380.0	7·5–9·5	1·3	3·0–4·0	0·5	0·1	...	0·5	1·0	0·35	...	...	0·5	Remainder
383.0	9·5–11·5	1·3	2·0–3·0	0·5	0·1	...	0·3	3·0	0·15	...	...	0·5	Remainder
384.0	10·5–12·0	1·3	3·0–4·5	0·5	0·1	...	0·5	3·0	0·35	...	...	0·5	Remainder
A384.0	10·5–12·0	1·3	3·0–4·5	0·5	0·1	...	0·5	1·0	0·35	...	...	0·5	Remainder
385.0	11·0–13·0	2·0	2·0–4·0	0·5	0·3	...	0·5	3·0	0·3	...	...	0·5	Remainder
390.0	16·0–18·0	1·3	4·0–5·0	0·1	0·45–0·65	...	...	0·1	...	0·2	0·1	0·2	Remainder
B390.0	16·0–18·0	1·3	4·0–5·0	0·5	0·45–0·65	...	0·1	1·5	...	0·2	0·1	0·2	Remainder
392.0	18·0–20·0	1·5	0·4–0·8	0·2–0·6	0·8–1·2	...	0·5	0·5	0·3	0·2	0·15	0·5	Remainder
393.0	21·0–23·0	1·3	0·7–1·1	0·1	0·7–1·3	...	2·0–2·5	0·1	...	0·1–0·2	0·05†	0·15	Remainder
413.0	11·0–13·0	2·0	1·0	0·35	0·1	...	0·5	0·5	0·15	...	...	0·25	Remainder
A413.0	11·0–13·0	1·3	1·0	0·35	0·1	...	0·5	0·5	0·15	...	...	0·25	Remainder
C443.0	4·5–6·0	2·0	0·6	0·35	0·1	...	0·5	0·5	0·15	...	...	0·25	Remainder
515.0	0·5–1·0	1·3	0·2	0·4–0·6	2·5–4·0	...	...	0·1	...	...	0·05	0·15	Remainder
516.0	0·3–1·5	0·35–1·0	0·3	0·15–0·4	2·5–4·5	...	0·25–0·04	0·2	0·1	0·1–0·2	0·05‡	...	Remainder
518.0	0·35	1·8	0·25	0·35	7·5–8·5	...	0·15	0·15	0·15	...	...	0·25	Remainder

* 0·02–0·04%Be; † 0·08–0·15%V; ‡ max. 0·1%Pb.

Al-Si-Cu alloys are the most common aluminium alloys based on composition around Al-Si alloys with various amount of copper, together with some other minor alloying elements such as zinc and magnesium. The microstructure of Al-Si-Cu alloys mainly consists of binary eutectic (α-Al+Si), ternary (Al+Si+Al_2Cu) and α-Al grains. The excellent castability and good mechanical properties can be achieved in Al-Si-Cu alloys, although corrosion resistance of the alloys is not good enough [146], compared with other Al alloys. Al-Si-Mg alloys have good castability, and good corrosion resistance, but fair machinability. The eutectic phases (Si or Mg_2Si) and iron-contained intermetallics (α-AlFeMnSi or π-AlFeMnSiMg) contribute to the strength. In general, it has lower elongation and tensile strength, as compared to Al-Si-Cu alloys [172]. Al-Si-Cu-Mg alloys have outstanding wear resistance, low thermal expansion, high thermal conductivity, and very good castability, but fair corrosion resistance, low ductility and poor machinability [173]. The microstructure is more complex than some other ternary or binary alloys. Apart from eutectic Si or Al_2Cu phases, Q phase can also form, which is very thermodynamically stable. Thus, the Al-Si-Cu-Mg alloys have excellent mechanical properties at elevated temperatures [174]. In addition, the T6 heat treated Al-Si-Cu-Mg alloys have excellent ageing hardening response, forming Q'' and θ' precipitates at peak ageing condition [175]. Al-Si alloys are widely used in the engineering industries, due to the fact that silicon reduces the thermal expansion coefficient, increases corrosion and wear resistance, improves the castability [146,176]. Silicon is fairly inexpensive and one of the few elements that can be added into

aluminium without sacrificing the low density. The good surface finish and castability can be easily achieved in Al-Si alloys because of fair narrow freezing range and outstanding fluidity. Hypereutectic Al-Si alloys containing Si concentration in excess of 12wt%, exhibit good wear resistance, thermal conductivity and good fluidity. This group of alloys is commonly used in linerless engine block and pistons [161]. In comparison, hypoeutectic Al-Si alloy has high ductility, good corrosion resistance, and good machinability, but low strength, fair castability [23]. Al-Mg alloys have good corrosion resistance, high strength, high ductility, excellent machinability and good fatigue properties. This group of alloys has poor castability due to wide solidification temperature range and unavoidable oxidization inclusions [177]. It is best suited for simply shaped castings, where excellent corrosion resistance is needed [155].

2.5.4.2 Effects of alloying elements in commercial die-cast alloys

2.5.4.2.1 Copper

Copper is a common element in die-cast alloys, which provides many functions. Copper is easily dissolved in α-Al matrix and can form intermetallic phases such as Al_2Cu, Al_2CuMg, $Al_{20}Cu_2Mn_3$, Al(MnCuFe)Si and $Al_5Cu_2Mg_8Si_7$ [178,179]. Aluminium die-cast alloys with dissolved Cu have the largest increase in strength and exhibit high ductility. If Al-Cu die-cast alloys undergo spheroidization at 500°C for 6 hours, the transformation of Al_2Cu phases from plate to small particles can occur [180]. Zhang et al. studied the chemical compositions of die-cast Al-10Si-yCu-xMn (x=0.5-1.5 and y=0.2-0.8wt%) alloys, and he found that the yield strength (YS) and ultimate tensile strength (UTS) tested at various temperatures (eg. 20 °C, 150 °C, 300 °C), increased with increasing copper content. This is due to the fact that Cu content increases the matrix strength, improving the resistance of dislocation movement and formation of slip bands [181]. Shabestari et al. also investigated the effect of Cu in Al-Si alloy. They observed that copper contributed to the formation of Al_2Cu precipitates in the matrix and, thus enhanced the strength [182]. The microstructure and properties of die-cast AlSi9Cu2-4Fe (wt%) alloys were studied by Fabrizi et al [183]. The result showed that the volume fraction of microporosity and intermetallic phases increased while the SDAS decreased with increasing copper. When copper is in solid solution, it has less impact on its corrosion resistance, while it is present as Al_2Cu, it is more susceptible to intergranular corrosion. Badawy et al. found that Al-Cu alloys have less corrosion

inhibition efficiency in neutral solutions because the intermetallic particles enhance galvanic corrosion [25].

2.5.4.2.2 Magnesium

Magnesium is the principal alloy element in die-cast alloys 515, 516, and 518 grades. In some alloys, such as 390 and 360, Mg is also added as an alloying element. The reasons for the limited concentration of Mg could be attributed to the strong reaction tendency of Mg with some other elements to form intermetallic and inclusions. It can be found that in Al-Si, Al-Si-Cu and Al-Si-Cu-Mn die-cast alloys which contain Mg in the range between 0.1 and 0.5wt%. This amount is sufficient to react with other alloying elements to produce intermetallic phases, such as π-$Al_8FeMg_3Si_6$, Mg_2Si, Al_2CuMg, $Al_5Mg_8Si_6Cu_2$, AlCuMgSi, which either maintain the alloy strength or enhance its yield strength [184–186]. Some of these intermetallic phases are unstable at elevated temperatures, and they can be dissolved back into α-Al after a short period of heat treatment [172,183,187]. Mg addition (eg. 0.1%-0.3%) can counteract the formation of microporosity in Al-Si-Cu die-cast alloys, while Cu addition increases the amount of microporosity [183]. Mohamed et al. found that in Al-10.8wt%Si-2-3wt%Cu-0.2-0.3wt%Mg die-cast alloys, $Al_5Mg_8Si_6Cu_2$ which is insoluble after solution or ageing process can increase the alloy strength [178]. At a high level of Mg in Al-Mg die casting alloys, the eutectic phase or some complex intermetallic phases can form to give high strength and good toughness [188,189]. In addition, Al-Mg-Si-Mn die-cast alloys have gained much attention in recent years because of its lightweight, excellent surface finish, high strength and good ductility, which can be applied in high-integrity shaped automotive components subjected to cyclic stress, such as sub-frame and door frame [190]. Hu et al. studied the effect of Mg content in $AlMgSi_2Mn$ die-cast alloy and found that the yield strength and hardness increased by 11% and 9% respectively, while the elongation decreased dramatically from 8.31% to 4.52% [143] with increasing Mg contents from 5.7%-7.2%. The amount, morphology and distribution of Mg_2Si and dissolution of Al_3Mg_2 are vital to the strengthening of these alloys [155,191]. Recently, Al-Mg_2Si-Mg-Zn based alloy with Mg content up to 11% has been developed, exhibiting yield strength and ultimate tensile strength of 300 MPa and 420 MPa, respectively under solution and ageing conditions [192]. The eutectic phases and solution strengthening with Zn and Mg contribute to the high strength of this alloy. However, the addition of Mg results in the formation of inclusion cluster, which can degrade machining performance and castability [141,177].

2.5.4.3 Effects of minor elements in commercial die-cast alloys

Meanwhile, minor alloying elements are chosen to control the solidification behaviour through the modification of the eutectic structure and refinement of primary phases and/or grain size, as well as controlling specific phase transformation [176]. During casting, the impurities cannot be avoided easily, which influence the castability and form insoluble phases.

2.5.4.3.1 Manganese (Mn) and Iron (Fe)

Mn and Fe are two common elements found in aluminium die casting alloys. They can form intermetallic compounds with silicon and aluminium such as $Al_{15}(Fe,Mn)_3Si_2$, $(Fe,Mn)Al_6$. Mn addition to aluminium die casting alloys can modify the morphology of Fe-rich compounds from equiaxed structure to Chinese script and compact morphology. Generally, the Mn content should not be less than half of the iron content in commercial die-cast aluminium alloys [193], which can prevent the formation of Al_3Fe, Al_8Fe_2Si or Al_5FeSi phases. Zhang et al. found that in Al-10wt%Si-0.49-1.37wt%-Cu-0.17-0.78wt%Mn die casting alloys, the addition of 0.78wt%Mn gives rise to the highest yield strength and ultimate tensile strength of 190MPa and 308MPa at room temperature and 94MPa and 111MPa at 300C°, respectively. This is because increasing Mn content leads to the formation of iron/manganese-contained particles [181]. Mohamed et al. found that Fe or Mn should be less than the critical level (0.75%), hindering serious loss of ductility in Al-Si die casting alloys [178]. The length scale and kind of Fe-rich particles is also related to the solidification conditions, which has an impact on mechanical properties [194]. At long solidification time, the volume fraction of α-AlFeMnSi particles can be reduced, and β-AlFeSi phases can form, which is detrimental to the mechanical strength [138,164]. The effect of iron and manganese in die-cast Al-Si alloys containing 0.1% Cr, which is used to modify the morphology of eutectic Si was also studied. It was found that the volume fraction of intermetallic phases of α-Alx(Fe/Mn)ySiz increased with increasing Fe and Mn contents. Furthermore, AlFeMnCrSi intermetallic particles can also form in alloys with 0.5% Mn [179], which can sink to the bottom of the sleeve as sludge, thereby increasing the die soldering tendency and deteriorating the castability [161]. Taghaddos et al. investigated the effect of iron on the fluidity in 413 aluminium die-cast alloy and revealed that although increasing Fe content can mitigate the susceptibility of die soldering, the fluidity can be degraded. With decreasing melt holding time from 60 min

to 0 min and the modification of 0.5% Mn, the fluidity can be improved around 11% [195].

2.5.4.3.2 Nickel (Ni)

The strength of die casting Al-Si alloy at both room temperature and elevated temperature can be increased slightly with Ni addition. Nickel can also increase the ductility, provided that it acts as a Fe corrector [134]. Recently, Yang et al. studied the effect of Ni in Al-Mg-Si-Mn alloy and found that the Ni-rich phases showed a combination of dendrite and lamellar morphology [172]. When Ni content reached to 2.06wt%, no Al_3Ni phases were found, and Ni was associated with Fe to form AlFeMnSiNi intermetallic phases. Increasing the amount of Ni from 0.01% to 0.05% is detrimental to the ductility but can slightly increase the strength [196].

2.5.4.3.3 Chromium (Cr)

Chromium is usually used as a Fe corrector too. With the addition of Cr in Al-Si die casting alloys, the Fe-rich phases can be transformed from β-Al_8Fe_2Si to α-$Al_{15}(Fe,Mn,Cr)_3Si_2$ which has higher micro-hardness, increasing the wear-resistant and strength [161]. Furthermore, in Cr modified Al-Si die casting alloys, it can be found that the eutectic silicon particles are much smaller than conventional hypereutectic Al-Si alloys. Timelli et al. also investigated the effect of Cr in Al-Si-Cu die casting alloys and it can be found that the morphology of α-$Al_{15}(Fe,Mn,Cr)_3Si_2$ particles were polyhedral, star-like and blocky. The volume fraction and size of intermetallic phase increased with increasing Cr addition from 0.057% to 0.15% [197]. In Al-Mg die casting alloys, the addition of 0.1% Cr tend to form coarse particles and increase both strength and creep resistance.

2.5.4.3.4 Zinc (Zn)

A solid solution is formed in Al-Zn alloys with a Zn concentration of approximate 1wt%. Al-Zn based alloys have an outstanding wear resistance and mechanical properties because of non-equilibrium solidification phases or Zn-rich intermetallic phases. In economic terms, aluminium alloys with the addition of Zn yield some benefits, such as good corrosion resistance and energy savings in processing due to lower melting temperature [190,196]. Recently, Shin et al. have successfully fabricated Al-Zn based casting alloys without melt modification or post-heat treatment with an ultimate tensile strength of up to 470MPa [198]. Ji et al. designed and fabricated Al-Mg_2Si-Mg-Zn

based alloy with a yield strength of 300 MPa, ultimate tensile strength of 420 MPa after heat treatment [192]. This is because after solution treatment at 490°C, AlMgZn intermetallic compounds can be dissolved in α-Al and subsequently they are precipitated after ageing treatment at 180 C°, leading to the improvement in mechanical properties. However, in Al-Si die casting alloys, Zn addition of up to 3wt% has the tendency to decrease the high-temperature strength and decrease hot tearing resistance.

2.5.5 Effect of heat treatment in aluminium die casting alloys

The widely used commercial die-cast aluminium alloys such as A380, LM24 and A360, have a yield strength below 200 MPa with an elongation from 2-6%. Recently, many investigations have been done to improve the mechanical properties further, for example, alloy modification with Zr or Sc [189], and the extra addition of Zn or Cu [186]. However, the as-cast yield strength of existing die-cast alloys is still below 250 MPa. Hence, heat treatment is another possible way of developing the die-cast alloys with high yield strength over 250 MPa and acceptable elongation. It should also be noted that most of the die-cast alloys are Al-Si based alloys with the addition of Mg (0.1-0.6%) or Cu (0.6-4%) and have a good ageing response.

The blistering of HPDC alloys after solution heat treatment is the inherent problem. The reasons are as follows. The high pressure die casting is a two-stage solidification which has a high injection speed of the liquid, resulting in the entrapment of the gas. During the solidification, these gas pores are compressed by the high pressure (100~380 bar) applied by the injecting piston. Consequently, during the solution treatment at high temperature, the α-Al grains become soft, and the expansion of the pores occur. It is reported that the lower temperature and shot solution treatment time are able to obtain an adequate supersaturated solid solution without any blistering [199,200]. Moreover, the reduced solution time provides the opportunity to increase productivity and reduce cost while maintaining the mechanical properties close to its maximum level [201].

There are only a few works reporting T6 heat treatment of die-cast alloys. The T6 heat treatment process of A360 and A380 was optimised by R. Lumley et al [202]. It was found that the blistering and dimensional change can be eliminated with a maximum temperature of 525 °C for 15 min, shown in Fig.2-21. Yield strength of 320 MPa and

elongation of 2.5% was achieved in A360 with an ageing treatment of 180 °C for 2 hours. Yang et al. reported that A380 alloy can achieve yield strength of 282 MPa and elongation of 4.2% after T6 heat treatment (525 °C for 15 min then 170 °C for 24 h). The microstructure of A380 after T6 is shown in Fig.2-22 (a,b). The coexisting of Q' and minor θ' precipitates shown in Fig.2-22 (c,d) were reported by Lumley in Al8.6Si1.3Cu0.5Mg (wt%) alloy at peak ageing condition (150 °C and 220 °C), and the yield strengths are both over 310 MPa [202]. It can be found that the T6 heat treatment with shot period solution treatment is effective to promote dissolution and facilitate the homogenization of eutectic phases [203]. Thus, the great improvement of strength and good elongation can be achieved. Niklas et al. found that the yield strength and ultimate tensile strength increased with increasing solution temperature and time during the heat treatment of AlSi10MgMn die-cast alloy [204]. However, the heat treatment degraded the elongation because of the increased porosity after long and high-temperature solution treatment [204]. The effect of solution heat treatment time and temperature on microstructure and tensile properties of AlSi7MgMn was studied by Timelli et al [205]. It was revealed that a solution heat treatment of 15 min at 475 °C was sufficient to spheroidise the eutectic silicon and increase the interparticle distance of eutectic silicon. In addition, the yield strength and ultimate tensile strength and elongation of the alloy increased remarkably from 125MPa to 250MPa, 260MPa to 325MPa and 10% to 17%, respectively after the solution treatment for 15 min at 525 °C following artificial ageing for 4 hours at 180 °C [205]. Srivastava et al. studied the energy absorption of AlSi4MgMn and AlSi9MgMn die cast alloys. The best energy absorption capacity for these alloys was obtained after solution treatment at 480 °C for 40 min and artificial ageing at 180 °C for 4 hours. This is due to the transformation of silicon particles from continuous morphology to spheroidized Si morphology [206]. Kasprzak et al. studied the effect of heat treatment on micro-hardness in Al-Si die casting alloys and it can be noted that T5 (cooled from elevated temperature and artificially aged at 200 °C for 2 hours) temper conditions are able to produce a hardness above 74 HRB [207]. Emma et al. studied the change of microstructure in Al-Si-Cu-Mg die casting alloys [173]. In these alloys, β-Mg_2Si, θ-Al2Cu, π-$Al_8Mg_3FeSi_6$ or Q-$Al_5Cu_2Mg_8Si_7$ phases are dominant phases found in the solidified microstructure. However, during solution treatment, β-Mg_2Si and θ-Al2Cu phases can easily be dissolved into the α-Al matrix, while π-$Al_8Mg_3FeSi_6$ and Q phases are harder to be dissolved or transformed in the solid-state [208]. Many different precipitates in different combinations have been observed at the peak-aged condition of Al-Si-Cu-Mg, which contributes to the highest strength as compared with ternary alloy systems. Examples

of precipitates that can be present in the peak-aged condition are: β"(Mg_2Si), θ"(Al_2Cu) and Q"($Al_5Mg_8Si_6Cu_2$). It is apparent that there are two possible combinations of precipitates. Precipitation of β"(Mg_2Si) and θ"(Al_2Cu), or alternatively θ"(Al_2Cu) and Q"($Al_5Mg_8Si_6Cu_2$), depending on the Cu concentration [186].

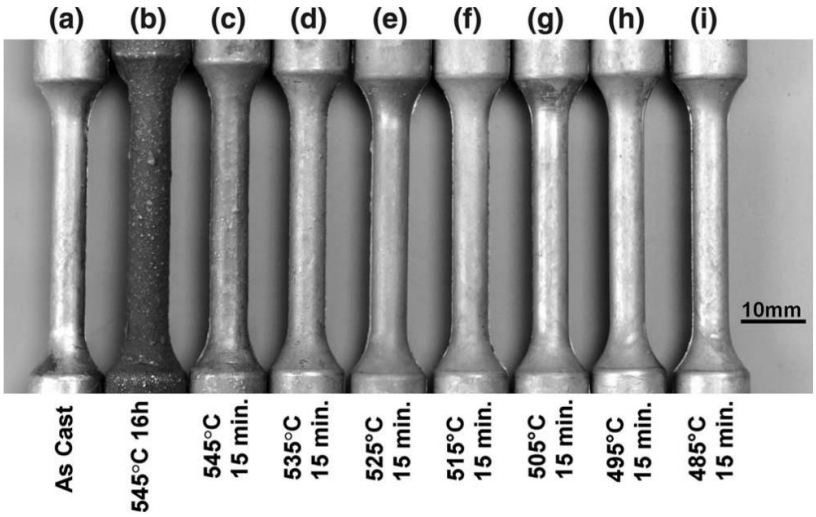

Fig.2-21 Surface of the tensile testing sample after heat treatment with various temperatures for 15 min [199]

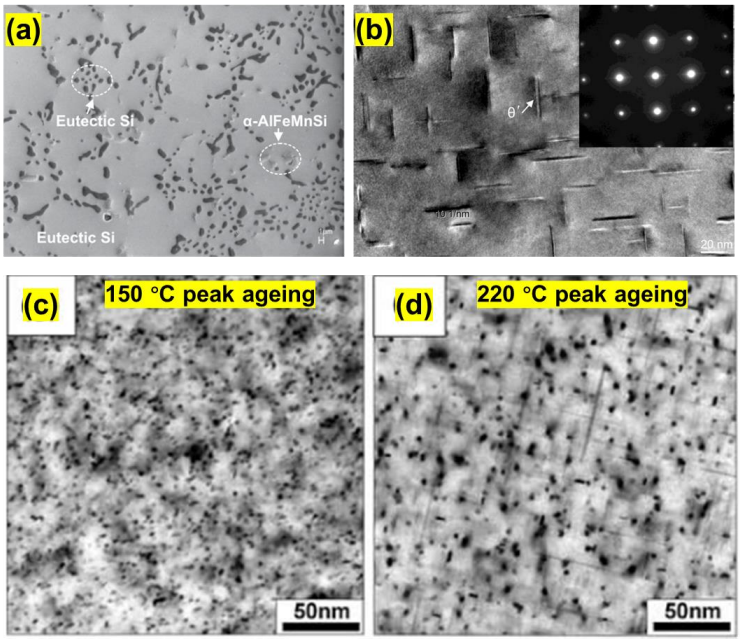

Fig.2-22 (a) spheroidized eutectic Si and (b) θ' precipitates in the matrix of A380 alloy [186]; the precipitation at peak ageing condition in Al8.6Si1.3Cu0.5Mg (wt%) alloy (a) at 150 °C and (b) 220 °C [202]

Al-Mg die-cast alloys are also widely applied in the industry because of its high strength and good ductility after heat treatment [160]. Hu et al. studied the effect of age treatment on AlMgxSi$_2$Mn (x=5.7~7.2wt%) die casting alloys [143]. After age treatment, the yield strength and tensile strength of AlMg5.5Si2Mn alloy increased by 14% and 29%, respectively. Yan et al. found that the yield strength and ultimate tensile strength of Al-10Mg-3.5Zn-2.7Si (wt%) die-cast alloy can increase to 320 MPa and 420 MPa, respectively after solution treatment for 30 min at 490 °C and ageing treatment for 60 min at 180 °C [209]. This is because $Mg_{32}(Al, Zn)_{49}$ intermetallic phase in the as-cast microstructure can be easily dissolved into α-Al phase, and the $MgZn_2$ phases can be precipitated after ageing treatment [203]. The microstructure of Al-10Mg-3.5Zn-2.7Si (wt%) alloy after the shot T6 heat treatment is shown in Fig.2-23.

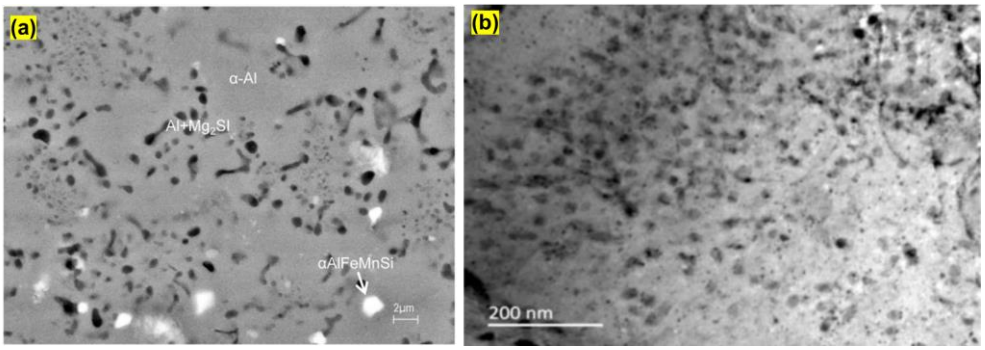

Fig.2-23 (a) eutectic structure after heat treatment (b) the $Mg_{32}(Al, Zn)_{49}$ precipitate in the matrix [209]

2.5.6 Mechanical Properties of Al HPDC alloys

Table 2-3 shows the mechanical properties of commercial die-cast alloys with different compositions which are widely applied in industry. For commercial die-cast aluminium alloys, the yield strength and tensile strength are normally below 250 MPa and 325MPa, respectively, while the elongation is between 1% and 7%.

Table 2-3 Mechanical properties of different commercial die-cast alloys [134,141,143,197,210,211]

Alloy	Tensile Strength /MPa	Yield Strength /MPa	Impact Strength /J	Shear Strength /MPa	Hardness /HB	Elongation /%in50mm
413	295	145	-	170	80	2.5
383	310	150	4	-	75	3.5
B390	317	250	-	-	120	1
A360	317	170	-	180	75	3.5
A380	325	160	4	185	80	3.5
383/384	310-330	150-165	-	-	-	2.5-3.5
A413	290	130	-	170	80	3.5
K-Alloy	295	-	-	-	80	5
361	250-290	120-150	-	-	75-95	5-7
A360	270-300	140 - 160	-	-	-	3-6
516	290-315	170-190	-	-	-	4-6
518	310	190	-	-	-	4

Table 2-4 shows the mechanical properties of die-cast alloys, which were reported in the recent 10 years. It can be found that Al-Si binary and Al-Mg alloys have excellent ductility. The more addition of Mg (>7wt%) in Al-Mg alloys can cause the decrement of ductility. The addition of Cu has positive effects on the strength, although it can decrease the ductility considerably with over 3wt% Cu. The maximum addition of Mn in die-cast alloys was found to be below 0.85wt%. Moreover, the Mg, Zn and Cu in the alloys allow good ageing hardening response. Thus high yield strength can be achieved after T6 heat treatment.

Table 2-4 Recent work on the development of die-cast aluminium alloys

Alloy composition(wt%)	Temper	Tensile Strength/MPa	Yield Strength /MPa	Elongation/%
Al10Si1.2Cu0.7Mn [143]	As-cast	267	167	11.1
	Nature ageing	331	206	9.8
Al10Si0.4Mg0.55Fe0.2-0.85Mn [209]	As-cast	230	150	6-7
Al7Si0.7Mn0.3Mg [184]	As-cast	260	125	10
	T6	315	240	12.5
Al9Si3Cu [205]	As-cast	325	140	6
Al10Si0.5Cu0.2-0.8Mn [197]	As-cast	275-285	140-150	9-7
Al10Si1.0-1.5Cu0.8Mn [181]	As-cast	275-300	150-180	7.5-6
Al5.5Mg2Si0.57Mn [192]	As-cast	324	183	8.31
	Age-treated	369	236	8.47
Al6Mg2Si0.57Mn [192]	As-cast	324	190	7
Al7Mg2Si0.57Mn [192]	As-cast	315	205	4.5
Al11.0Mg2.9Si3.5Zn0.6Mn [137]	As-cast	350	250	3.5
	T6	430	340	3.3
Al10Mg2.7Si3.5Zn0.5Mn[172]	As-cast	350	240	2.0
	T6	420	320	4.5

Chapter 3 Experimental procedures

3.1 Materials and melt preparation

Pure aluminium, Al-50wt%Cu, pure magnesium, Al-50wt%Si, pure Fe (99.97%) and Al-20wt%Mn were used as starting materials with compositions of commercial purity which is listed in Table 3-1. During the experiment, each element was supplied at a specified ratio with additional burning loss of melting. A melt of 6 kg was prepared each time in a clay-graphite crucible using electric resistance furnace for high pressure die casting. Moreover, 1 Kg of starting alloy ingot was prepared by gravity casting with a steel mould (inner size: Φ14 diameter x 20 mm length). Nominal eutectic composition of the ingot for suction casting was prepared via melting appropriate amounts of Al (99.99%), Al-50wt%Si, Cu (99.99%) and Pure Mg using electric resistance furnace.

Table 3-1 Master alloys used for casting

Master alloys	Elements (wt%)											
	Al	Cu	Mg	Si	Mn	Fe	Zn	Pb	Ni	Sn	Ti	Cr
Al	Bal.	0.001	0.001	0.06	0.001	0.12	0.001	0.001	-	-	-	-
Al20wt% Mn	Bal.	-	0.01	0.05	21.8	0.23	-	-	-	-	-	-
Al50wt% Si	Bal.	-	-	49.9	-	0.28	-	-	-	-	-	-
Al50wt% Cu	Bal.	49.2	0.12	0.19	0.09	0.38	0.05	0.02	0.02	0.02	0.01	0.04
Pure Mg	0.04	0.001	Bal.	0.013	0.02	0.002	0.00	-	0.001	-	-	-

The melt temperature was controlled between 700 °C and 720 °C in an electric resistance furnace or induction furnace. Pure Mg ingots were preheated to 200 °C and were carefully added to the melt. After half-hour homogenisation, argon gas was input into the melt by a commercial rotatory degasser at 500 rpm for 5 min, and the top of the melt was covered by commercial granular flux. The melt was subsequently homogenised in the furnace for around 15 min before casting. The alloy composition of each alloy was analysed using a mushroom casting with Φ60x10 mm testing part made by a steel mould.

3.2 Material precessing

3.2.1 Suction casting

An Edmund BuhlerMAM-1 compact arc melting system with a suction casting configuration was used to prepare the quaternary Al-28wt%Cu-6wt%Si-2.2wt%Mg

eutectic alloy using the initial alloy ingot prepared in section 3.1. The weight of each eutectic alloy for arc melting was maintained to an average value of 3 g. A water-cooled copper mould (shown in Fig.3-1) was used to fabricate suction cast sample of 3 mm diameter and 30 mm long. Initially, the chamber was flushed three times with argon gas and then evacuated down to a based pressure of -0.7 bar atmosphere prior to backfilling with argon gas to 0.2 bar atmosphere. This was followed by arc-melting a piece of oxygen gettering material such as Zr to reduce the oxygen content in the chamber prior to melting the aluminium alloys. The melting of the aluminium alloys was performed using arc current setting of 3 from the unit for 30 seconds before the suction casting was performed by opening the valve connecting the chamber to the evacuated suction tank that maintained a pressure of -1 bar atmosphere. Once the unit has been cooled down, the suction cast sample was extracted from the copper mould. The microstructure of each sample was taken from the middle part of the suction cast rod.

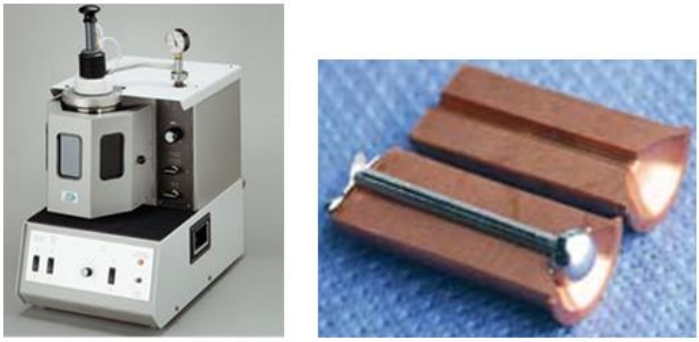

Fig.3-1 (a) An Edmund Buhler MAM-1 compact arc melting unit and (b) a water-cooled copper mould used for suction casting

3.2.2 High pressure die casting

A Frech 4500 kN HPDC machine shown in Fig.3-2 (a) was used for making standard tensile testing samples from the initial alloy ingots. The melt was dosed and poured into the shot sleeve with a temperature of 60°C above the liquids temperature that was measured using a K-type thermocouple. For each HPDC run, the total mass of melt was about 750 g with an initial injection speed of ~2.3 m/s and gate speed of ~62 m/s. A designed tensile testing mould was used to cast eight ASTM standard samples with a diameter of Φ6.35 mm and a gauge length of 50 mm. The main dimension of the die casting, including overflow and biscuit, is shown in Fig.3-2 (b). During casting, the mould was pre-heated by mineral oil at 250°C. The casting samples were tensile tested after being left at ambient condition for more than one day.

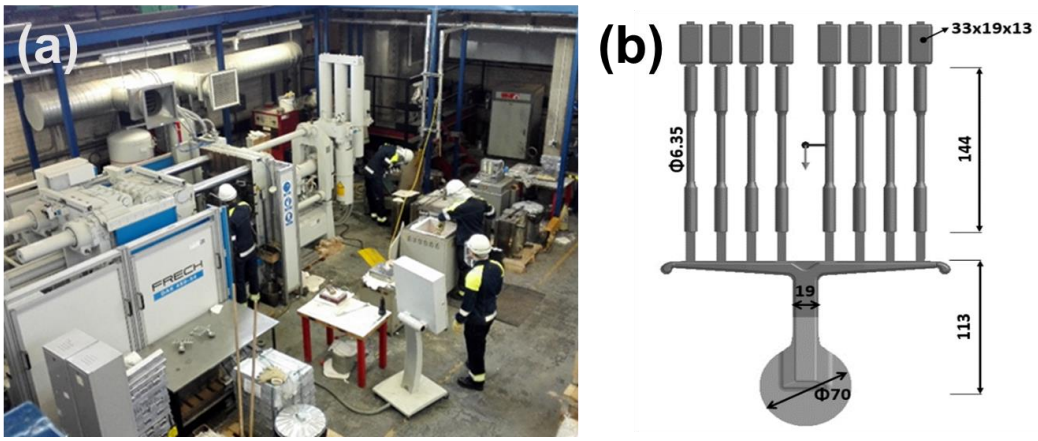

Fig.3-2 (a) High pressure die casting machine (b) the dimension of die casting with overflow and biscuit

3.2.3 Heat treatment

The solution treatment was carried out in a Carbolite electric resistance furnace with fan convection for rapid heating and cooling shown in Fig.3-3 (a). For each solution treatment, the furnace was preheated to the desired temperature and held for 2 hours before putting samples inside. The temperature of the furnace was measured using a K-type thermocouple (±2 °C), which was positioned close to the samples. After solution treatment, the samples were rapidly quenched in water at room temperature and immediately transferred to an oil bath (shown in Fig.3-3 (b)) for artificial ageing at a temperature of 170 °C for 0-48 hours. The oil bath was preheated to 170 °C and maintained for 12 hours before artificial ageing. In terms of T5 heat treatment, the as-cast samples were directly put into the oil bath oven for 0-48 hours that had been preheated at 170 °C for 12 hours. After T6 or T5 heat treatment, samples were left and cool at room temperature.

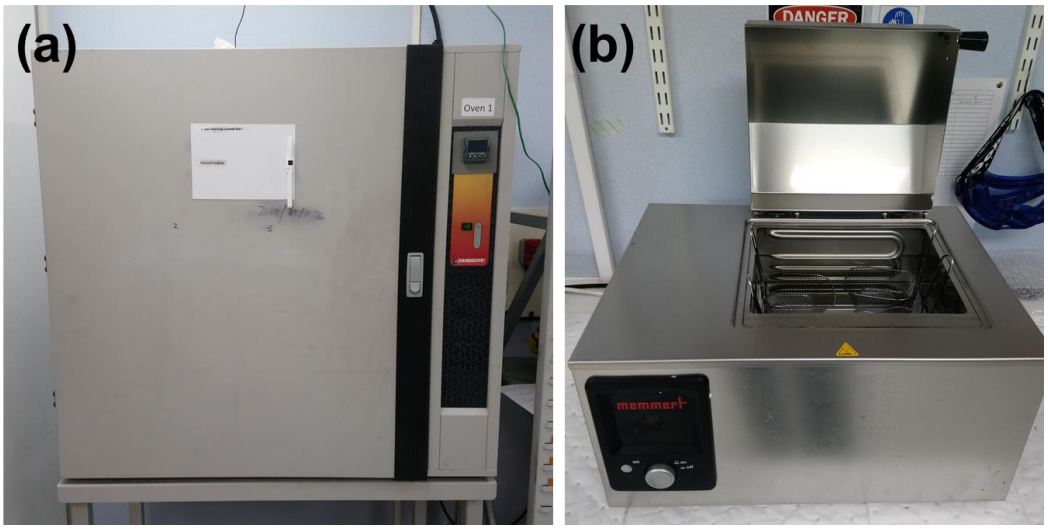

Fig.3-3 (a) Solution heat treatment oven (b) oil bath oven

3.3 Material characterisation

3.3.1 Differential scanning calorimetry (DSC)

The melting temperature and heat of fusion of both eutectic or hypoeutectic alloys were measured using a Netzch 404F1 differential scanning calorimetry (DSC) instrument (Fig.3-4) operated at a heating rate of 20K/min, in a dynamic flow of Ar at a flow rate of 50 ml/min. The DSC samples were cut from the centre of the Φ6.35 mm HPDC sample or the middle part of Φ3 mm suction rod. The weight of the sample was kept to be ~50 mg. Each sample was washed with acetone before putting into a 70 μL volume alumina crucible covered with alumina lid. Similar alumina crucible and lid were used as a reference during each DSC measurement.

Fig.3-4 Netzch 404F1 differential scanning calorimetry

3.3.2 Optical microscope (OM)

The solidified microstructures of die-cast alloys were examined by a Zeiss Axioscope optical microscope (OM) (Fig.3-5) operated at magnification ranging from 20 to 1000 times. The samples were sectioned and then cold mounted in polyester resin. Each mounted sample was ground with sandpaper, starting from #350 to #3000 grades. Each step of grinding took at least 3 min. After final grinding, the sample was polished with the nylon polishing plate using a SAPHIR 250 polishing machine operated at a polishing force of 5 N and a speed of 120 rpm for 25 min. After polishing, the polished surface was washed with alcohol and dried with electric hair drier. The volume fraction of eutectic mixtures was determined via an image analysis software known as ImageJ. The analysis was performed on at least five fields from optical micrographs taken at low magnification.

Fig.3-5 Zeiss Axioscope optical microscope

3.3.3 Scanning electron microscopy (SEM)

Fig 3-6 shows a Zeiss Supera 35 FEG SEM equipped with Energy Dispersive X-Ray Spectroscopy (EDX) used to examine the refined microstructure that was difficult to observe under an optical microscope. The samples for SEM were etched with 0.5%HF solution for 5s (light etching) or 30s (deep etching). The EDX analysis of the small regions or intermetallic compounds in samples after light etching was performed using an accelerating voltage of 20 kV and a working distance of 8.5 mm. A backscatter electron imaging mode was applied for the identification of different phases present in samples after light etching. It was performed using an accelerating voltage of 15 kV and a working distance of 8.5 mm. A secondary electron imaging mode was used to study the morphology of the phase presented in samples after deep etching. It was performed using an accelerating voltage of 5 kV and a working distance of 4.5 mm.

Fig.3-6 Zeiss Supra 35VP scanning electron microscopy

3.3.4 Electron backscatter diffraction (EBSD)

The grain size of samples was determined by electron backscatter diffraction (EBSD), before and after heat treatment. The EBSD samples were prepared with a vibratory polishing machine with a frequency of 80 Hz for 4 hours. The samples were washed with alcohol. After that, the specimens were put into the Zeiss Supera 35 FEG SEM chamber with diffraction camera. The polished surface was tilted to 70° from horizontal towards the diffraction camera. It was performed using an accelerating voltage of 20 kV and a working distance of 14 mm. The step size of EBSD scan was set to 0.4 μm, and only α-Al phase was selected for identification. OIM TSL software was used for statistical analysis of grain size. The grain tolerance angle was set to be 5°, the minimum grain size was set to be 0.8 μm, and the minimum confidence index was 0.3.

3.3.5 Focused ion beam (FIB)

The FIB (Fig.3-7) equipped with a field emission source and Gemini were used to prepare TEM specimen from a specific region in the as-cast sample. The samples for FIB were starting with a diameter of Φ3 mm and 3 mm length, and silver paste was used for the fixation of the sample onto a low profile pin stub. Initially, a Ga ion beam and the electron beam were used to deposit a 1.5 μm thick Pt protection. Subsequently, a rectangular strip of 8 μm x 8 μm x1.5 μm containing the desired region of the as-cast sample was extracted and attached to a molybdenum/copper grip with Pt deposition. The extracted sample was milled using Ga + ions operated at a voltage and current

starting from 30kV and 300pA to 3kV and 20pA until the sample was electron transparent to 3 kV in SEM imaging.

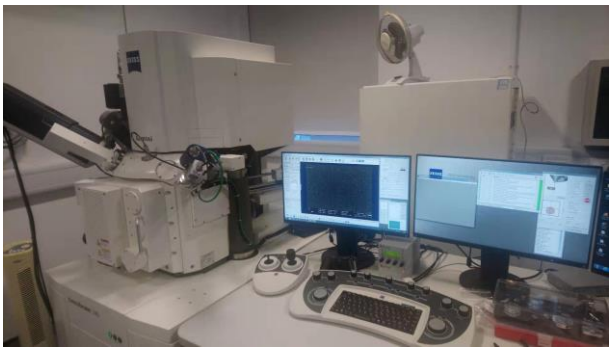

Fig.3-7 Zeiss Crossbeam Focus Ion Beam

3.3.6 Transmission electron microscope (TEM)

A JEOL 2100F transmission electron microscope (Fig.3-8) was used to characterise the nanoscaled features in the microstructure. The TEM specimens of heat-treated samples were prepared via Gatan 691 Precision Ion Polishing System (PIPS) milling. The TEM specimens of as-cast samples were prepared by milling the sample to a thickness of approximately 80 nm and applying the 'lift-out' technique in a Zeiss Auriga cross beam Focused Ion Beam (FIB) using a Mo/Cu grid with Pt deposition. The TEM studies were performed using an accelerating voltage of 200kV.

Fig.3-8 The Jeol 2100F Field Emission Gun Transmission Electron Microscope

3.3.7 Transmission Kikuchi Diffraction (TKD)

A Zeiss Auriga SEM and Oxford Instruments HKL Nordlys EBSD detector were used for TKD mapping. The accelerating voltage is set to 30 kV, and the high current mode

is was selected for probe current with a 60 µm aperture at 5.6 mm working distance. The sample for TKD was prepared by FIB 'lift-out' technique. Before putting into the SEM chamber, the sample was plasma-cleaned for 90 minutes before loading into the SEM chamber. Fig.3-9 (a,b) shows the geometry of holder, stage and detector inside the chamber. The stage was titled to 56°, and the sample was put in the 20° pre-titled holder. Thus, the sample surface was at -14° aligned to the electron beam. The diffraction patterns were collected at 75 ms exposure time with 4x4 pattern binning. The step size for acquisition is 14 nm. The TKD data was analysed with OIM TSL software.

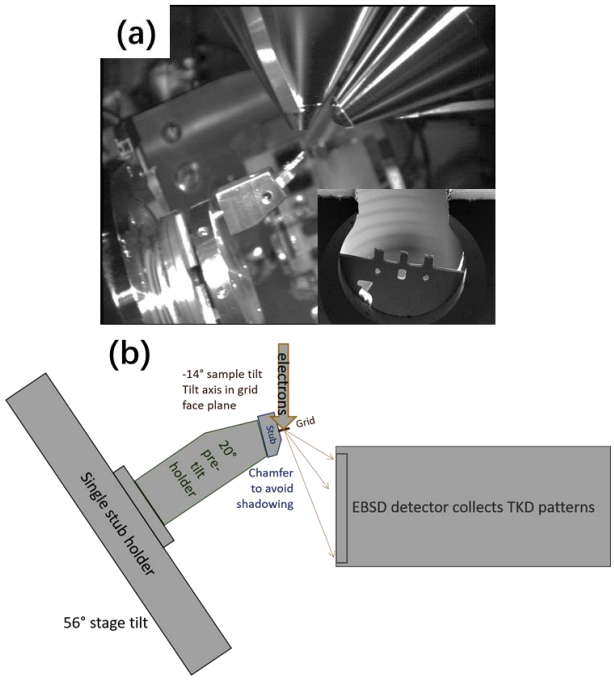

Fig.3-9 (a) TKD setup in SEM chamber (b) holder, sample and detector geometry in SEM chamber

3.3.8 X-Ray diffraction pattern (XRD)

A Bruker D8 Advanced X-ray diffractometer with Cu X-Ray radiation and Ni filter at a voltage of 40 kV and a current of 40 mA was performed on each sample to identify phases present in the samples. A step size of 0.24 degree/min and 2-theta angle between 20° and 90° were used during XRD studies.

3.4 Mechanical properties

3.4.1 Tensile test

The tensile testing was performed by an Instron 5500 machine according to ASTM B557 standard. The extensometer with 50mm gauge length was used, and the strain rate was set at 1 mm/min. Six tensile tests were performed on each alloy composition.

3.4.2 Compression test

A specimen of Φ3 mm and 6 mm length, with ends ground flat and parallel, was prepared for compression test. It was carried out at room temperature by Instron 4507 no.K8026 (20 kN load cell), in accordance with ASTM E9-19. The specimen was loaded at a rate of 0.03 mm/min. The strain measurements were taken from the corrected crosshead displacement under SEM.

3.4.3 Hardness measurement

The hardness measurement was carried out by a Vickers hardness tester (Buehler Ltd, Lake Bluff, IL) using a 5Kg load for 10 seconds. The hardness was measured on the cross-section of tensile testing specimens (50 mm gauge length). Five indentations were performed on each sample.

Chapter 4 Development of Al-Si-Mg-Mn die-cast alloys

4.1 Introduction

This chapter is concerned with the design of die-cast Al-Si-Mg-Mn multi-component alloys by the addition of Mn and Fe into Al-Si-Mg ternary eutectic and hypoeutectic alloy compositions. The choice of Mn addition is to facilitate the suppression of die soldering and detrimental β-Fe intermetallic phase formation in Al alloys, while the Fe addition is to stimulate the impurity level contributed from HPDC process [24]. Three alloys with a eutectic and two hypoeutectic (30% and 50% eutectic mixture) compositions were prepared by HPDC, and tensile testing bars were obtained for microstructure characterisation and mechanical testing. The eutectic structure formation was studied, and the effect of compositions on the resultant microstructure and tensile properties for maximum mechanical performance was understood.

4.2 Design of Al-Si-Mg-Mn multi-component alloy compositions

Pandat 8.5 CALPHAD software was used to predict the eutectic reaction (L→α-Al+Mg_2Si+Si) near the aluminium corner of the Al-Si-Mg ternary system. Fig.4-1 shows the liquidus projection showing the eutectic reaction occurred at a composition of Al13.9%Si5.55%Mg (wt%). Based on Al-Si-Mg eutectic composition, two hypoeutectic Al-Si-Mg alloys with 30% and 50% volume percentages of the eutectic mixture were determined. Initially, the solidification paths of these Al-Si-Mg-Mn alloys were predicted based on Scheil description, as shown in Fig. 4-2. 0.5wt%Mn and 0.15wt%Fe were introduced to these eutectic and hypoeutectic Al-Si-Mg compositions to make up alloys A, B and C, as shown in Table 4-1. Their effects on microstructure and properties were determined. After HPDC process, the actual compositions of the alloys were measured and shown in Table 4-2.

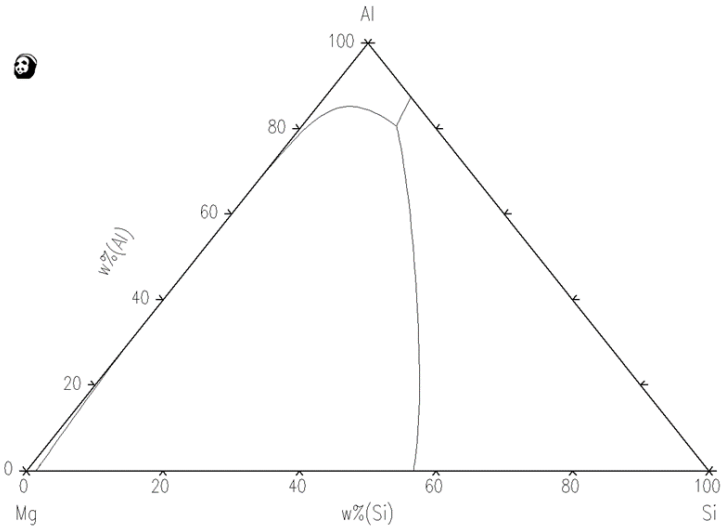

Fig.4-1 The liquidus projection of Al-Si-Mg

The solid fraction of eutectic mixture changes from ~1 to ~0.3 with different amount of Si and Mg. All three alloys have the same four-phases eutectic reaction L→α-Al+α-AlFeMnSi+Mg_2Si+Si at the same eutectic temperature of ~554 °C. There are some α-AlFeMnSi forming in near-eutectic alloy A. L→α-AlFeMnSi with a solid fraction of about 0.011 forms in alloy B prior to the reaction of L→α-AlFeMnSi+α-Al, while only one reaction (L→α-AlFeMnSi+α-Al) is found before eutectic reaction in alloy C. Both alloy B and alloy C have same ternary eutectic reaction L→α-Al+α-AlFeMnSi +Si with a solid fraction of approximate 0.03, followed by the final quaternary eutectic reaction L→α-Al+α-AlFeMnSi+Si+Mg_2Si.

Table 4-1 The calculated content of elements in the Al-Si-Mg-Mn die-cast alloys.

Alloy	Volume fraction of eutectic mixture	Alloy composition (wt.%)				
		Al	Si	Mg	Mn	Fe
A	1.0	Balance	13.9	5.55	0.5	~0.15
B	0.5	Balance	7.66	3.05	0.5	~0.15
C	0.3	Balance	5.16	2.05	0.5	~0.15

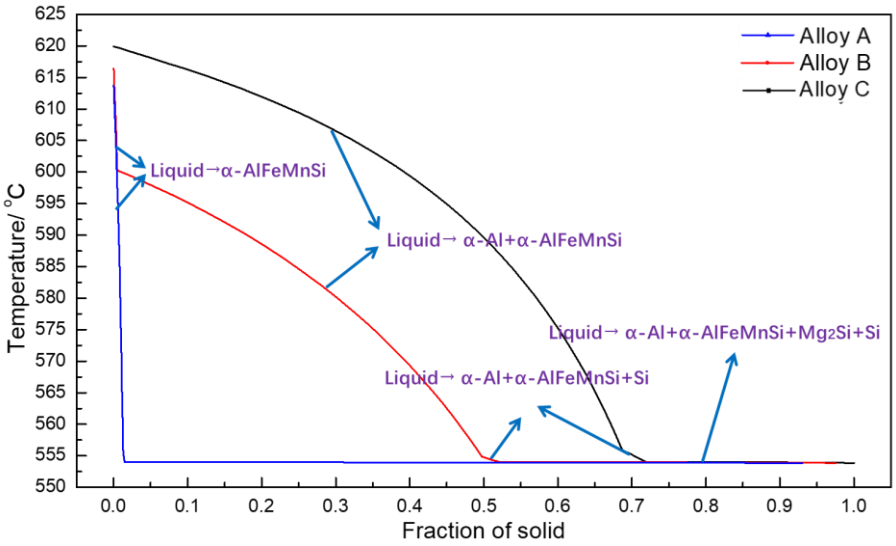

Fig. 4-2 Solidification path of Al-Si-Mg-Mn alloys calculated by the CALPHAD software Pandat 8.5

Table 4-2 Measured compositions of Al-Si-Mg-Mn alloys prepared by HPDC

Alloy	Alloy composition (wt.%)				
	Al	Si	Mg	Mn	Fe
A	Balance	13.17	5.81	0.47	0.20
B	Balance	7.48	3.55	0.52	0.18
C	Balance	5.22	2.35	0.48	0.16

4.3 Microstructure of as-cast Al-Si-Mg-Mn alloys

4.3.1 XRD analysis

Fig. 4-3 presents XRD patterns of the developed Al-Si-Mg-Mn alloys with the various volume fraction of eutectic mixtures. The main XRD peaks were identified, and they corresponded to α-Al, Si, Mg_2Si and α-AlFeMnSi phases. However, the small XRD peaks corresponded to π-AlFeMnMgSi phase, which was not predicted. It is because of the non-equilibrium solidification in HPDC and the database employed in the prediction.

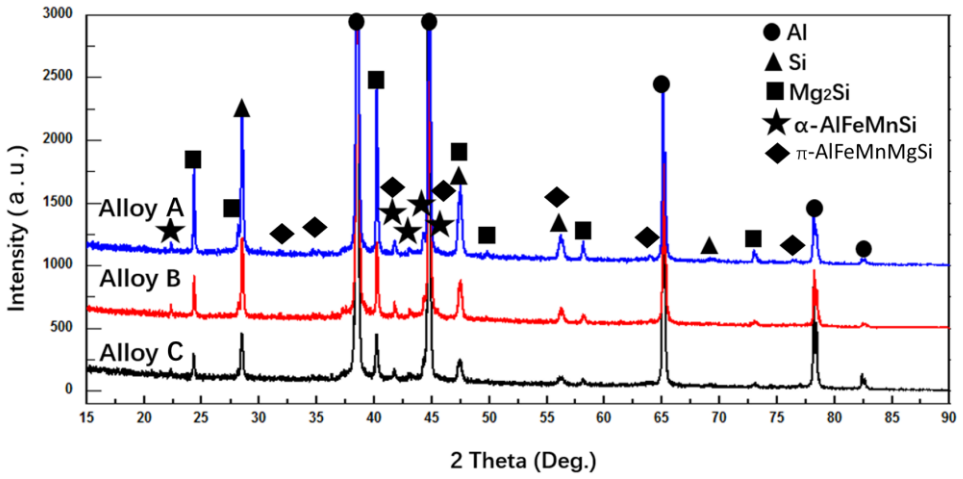

Fig. 4-3 The XRD spectrum of the Al-Si-Mg-Mn alloys

4.3.2 Optical microstructure and EBSD analysis

Alloy A exhibits a near-eutectic structure, as shown in Fig. 4-4 (a). Apart from coarse eutectic and fine eutectic matrix labelled as 'EU1' and 'EU2', some coarse Mg_2Si and compact α-AlFeMnSi particles, were found with the size of 15-40 μm and 10-30 μm, respectively. The compositions of these phases measured by SEM-EDX are listed in Table 4-3. The as-cast microstructure of alloy A is dominated by a eutectic structure, and some α-Al grains were observed with the volume fraction of ~0.11. The microstructure of eutectic Al-Si-Mg-Mn alloy has a bimodal morphology that consists of small rosette-like binary eutectic embedded within the fine quaternary eutectic matrix.

The microstructure of hypoeutetcic alloy B is shown in Fig. 4-4 (b). From the optical micrograph, there are two types of eutectic at grain boundaries (further confirmed under SEM), which are named 'Eu1' and 'Eu2', and the volume fraction of eutectic mixture was determined to be 42±7% from the image analysis. The microstructure of alloy C is similar to alloy B. The volume fraction of eutectic mixture in alloy C is found to be 24±8%, which is lower than that in alloy B.

Two types of α-Al grains were observed, which are labelled as 'α1' and 'α2' in Fig. 4-4 (b,c). α1-Al phase shows coarse fragmented morphology in both alloy B and alloy C, separated by fine α2-Al grains. The α-Al grain size distribution of alloy B and alloy C analysed by the EBSD is shown in Fig. 4-5 (a) and (b), respectively. The comparison of grain size distribution between alloy B and alloy C is shown in Fig. 4-5 (c). The average grain size of α2-Al and α1-Al are found to be 12±5 μm and 35±11 μm in alloy

C and, 9±4 μm and 30±12 μm in alloy B, respectively. The alloy B has a little finer grain size of α2-Al and α1-Al.

Table 4-3 Average compositions of intermetallic phases characterised by SEM EDX analysis.

Alloy name	Morphology	Identified compound	Al	Si	Mg	Mn	Fe
			at.%				
Alloy A	Coarse compact	$Al_{15}(Fe,Mn)_3Si_2$	71.5	12	-	12.9	3.6
	polygon	Mg_2Si	81.7	5.8	12.5	-	-
	Fine compact	$Al_{15}(Fe,Mn)_3Si_2$	71.7	11.7	-	12.9	3.7
Alloy B	Fine compact	$Al_{15}(Fe,Mn)_3Si_2$	73.1	10.9	-	12.3	3.7
Alloy C	Fine compact	$Al_{15}(Fe,Mn)_3Si_2$	72.6	11.1	-	13.6	2.7

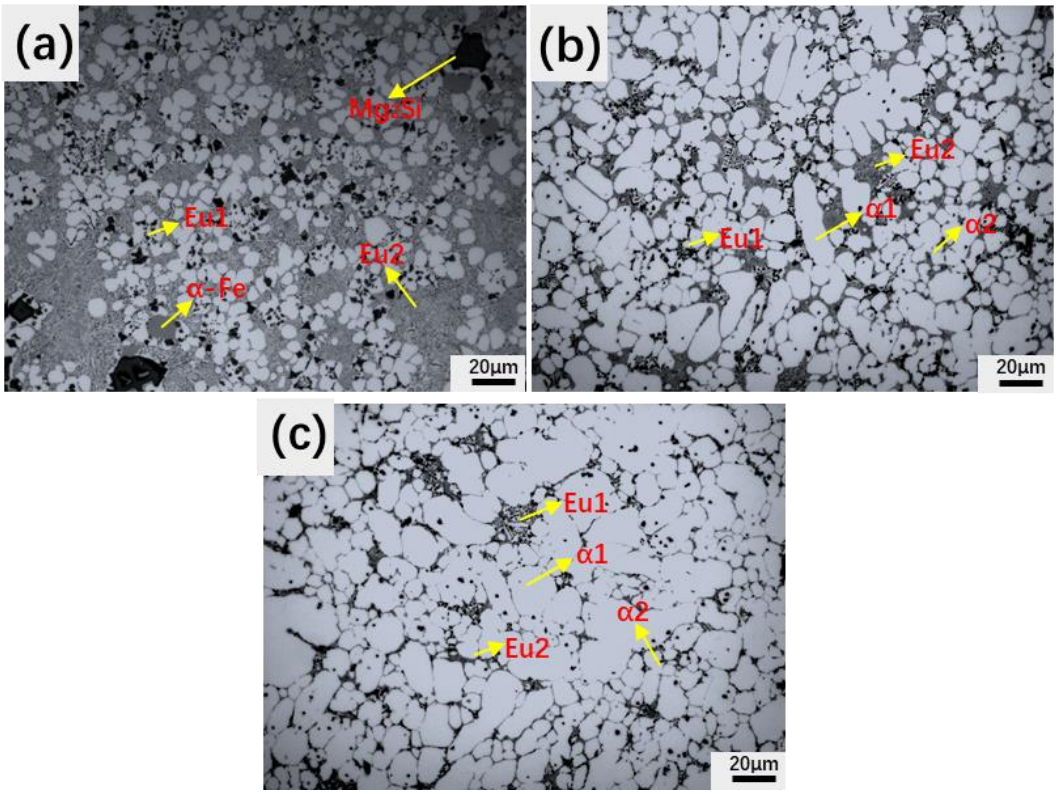

Fig.4-4 Optical micrographs showing the microstructure evolution with the decreased eutectic volume fraction in alloy A (a), alloy B (b) and alloy C (c)

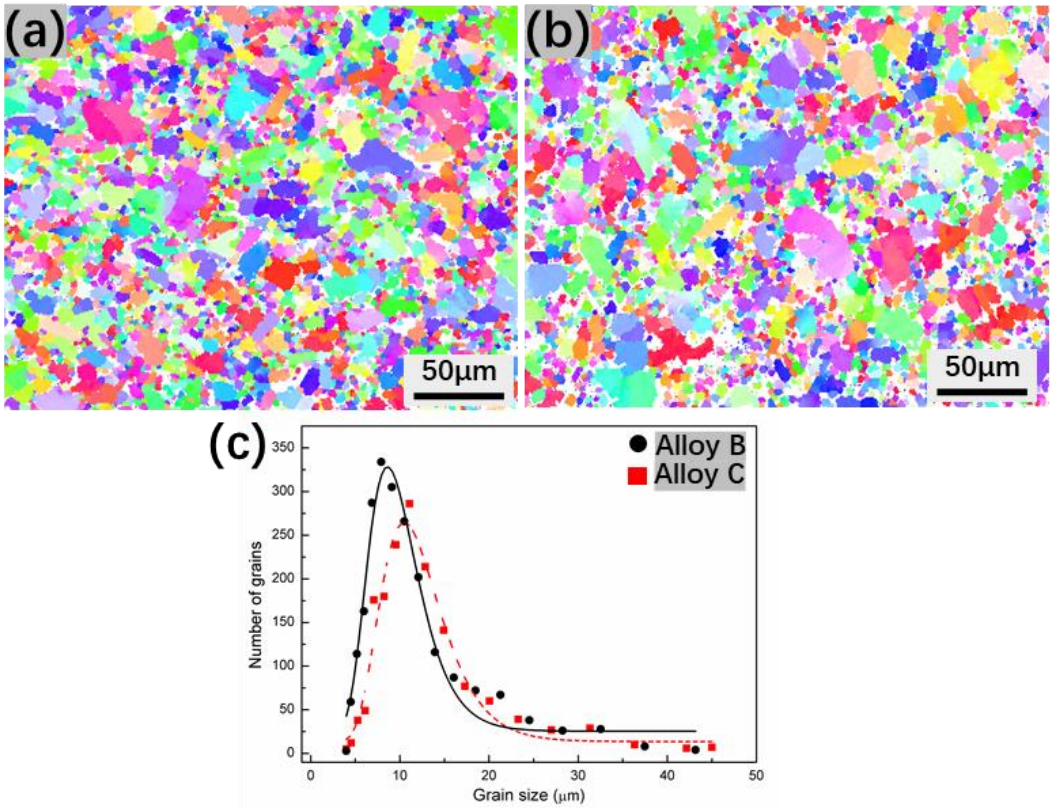

Fig.4-5 EBSD orientation map of alloy B (a), alloy C (b) and grain size distribution of alloy B and alloy C (c)

4.3.3 DSC results

From DSC curves obtained from a heating cycle, the onset temperature of the melting peak for each alloy was similar and was found to be 554 °C, which coincides with the calculated quaternary eutectic reaction temperature. Only one endothermic DSC peak with a shoulder feature was observed in alloy A. However, there are two main endothermic DSC peaks for alloy B and alloy C, which correspond to the melting of the eutectic mixture and α-Al dendrites. The shoulder feature of alloy A is associated with the multiple eutectic reactions (eg.binary and quaternary eutectic reaction) and the small volume fraction of α-Al dendrites or intermetallics, which can be inferred from optical micrographics in Fig.4-4 (a). The DSC results validate the predicted solidification paths of these alloys with a various volume fraction of eutectic mixture. From the DSC curves obtained from the cooling cycle, two large exothermic peaks are found in alloy B and alloy C, which corresponds to the formation of α-Al dendrites and eutectic mixture. However, there are some additional small exothermic peaks present in the DSC curves of these alloys as compared with those obtained from the heating cycle. It is because the cooling rate is very slow, and the solidification occurs at near-equilibrium condition while the measured composition is slightly different from

equilibrium composition. Thus some intermetallic compounds or ternary eutectic form before final eutectic reaction [212]. The alloy C has the highest solidification temperature of primary α-Al (611 °C), and the lowest temperature was found in alloy A.

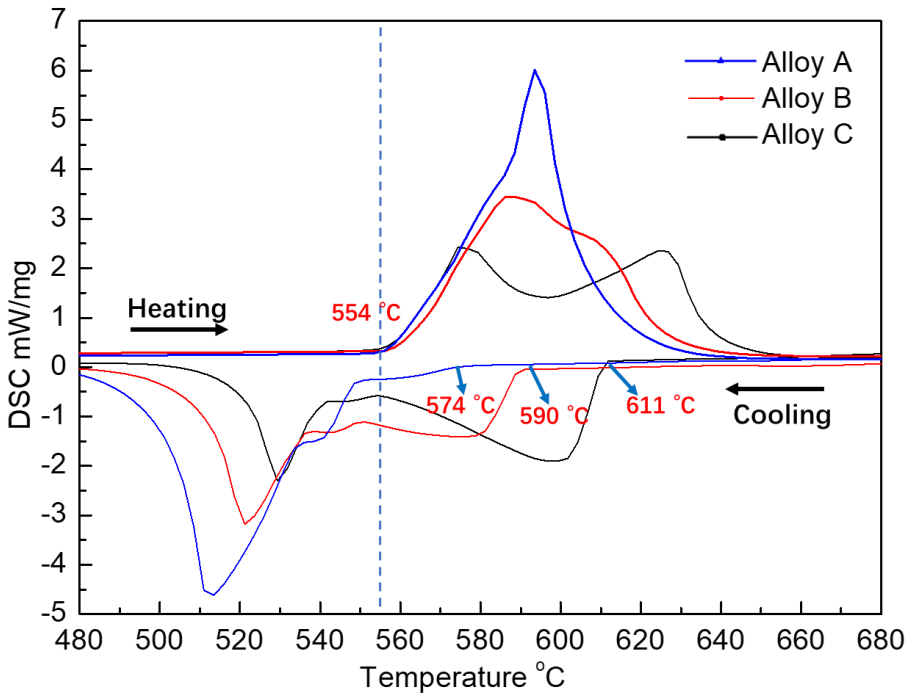

Fig. 4-6 DSC curves of alloy A, alloy B and Alloy C obtained from both heating and cooling rates of 10 K/min

4.3.4 Scanning Electron Microscopy results

The microstructure of eutectic mixture and α-AlFeMnSi particles present in these alloys was further characterised by SEM under backscattered electron imaging and in-lens mode, as shown in Fig. 4-7 (a,c,e) and (b,d,f), respectively. For near-eutectic alloy (alloy A), the as-solidified microstructure mainly consists of coarse (EU1) and fine (EU2) eutectic mixtures, as shown in Fig.4-7 (a,b). Large polygon Mg_2Si and compact α-AlFeMnSi particles with size over 10 μm were also observed. The 'EU1' eutectic mixture in alloy A consists of Mg_2Si and α-Al. The 'EU2' eutectic mixture in alloy A consisted of four phases which are Si, Mg_2Si, and α-Al, together with needle-like π-AlFeMnSiMg phases [213]. The amount of 'EU2' eutectic region (~63%) is greater than that of 'EU1' region (~20%). A small amount of fine α-AlFeMnSi particles was present in the eutectic regions with an average size of 1-2 μm, as shown in Fig. 4-7 (b).

In terms of hypoeutectic alloys with 50% (alloy B) and 30% (alloy C) eutectic mixtures shown in Fig.7 (c,d) and (e,f) respectively, the as-solidified microstructure consists of α-Al grains, α-AlFeMnSi, together with 'EU1' and 'EU2' eutectic regions. The proportion and size of α-AlFeMnSi changed from 1.4% and 1-2.5 μm for alloy B (50% eutectic mixture) to 1.2%, and 1-3.5 μm for alloy C (30% eutectic mixture). The average compositions of these intermetallic compounds were analysed and shown in Table 4-3

Fig. 4-7 (d) and (f) shows the eutectic microstructure in alloy B and alloy C under SEM in-lens mode taken at the same magnification. The 'EU1' and 'EU2' regions in alloy C show a finer microstructure compared with those in alloy B. The 'EU1' region (α-Al+Mg_2Si) has an interlamellar spacing of 0.3-0.7 μm in alloy C, while in alloy B, the interlamellar spacing is 0.5-1.3 μm. The 'EU2' eutectic region in alloy C shown in Fig. 4-7 (f) is similar to that of alloy B. The 'EU2' eutectic region in alloy C shows a finer microstructure. It can be noticed in Fig. 4-7 (f) that, apart from three types of phases (ie. Si, Mg_2Si and α-Al), the needle-like π-AlFeMnSiMg phase with higher area fraction was found in the ultrafine eutectic region in alloy C having a width of 100-400 nm and length of 2-5 μm. Further characterisation of this ultrafine eutectic region with TEM will be discussed later.

Table 4-4 Aspect ratio and equivalent diameter of Si particles in alloy A, alloy B and alloy C

Alloy	**Alloy A**	**Alloy B**	**Alloy C**
Si aspect ratio	2.43±1.59	2.44±1.37	2.55±2.02
Si average diameter (μm)	0.38±0.15	0.42±0.28	0.23±0.14

The aspect ratio and average size of eutectic Si phase in 'EU2' are shown in Table 4-4, which were characterised using in-lens SEM images (not shown here), taken at higher magnification. It can be found that the Si in these alloys has nearly the same aspect ratio. In addition, the Si particles present in alloy C has the smallest average size of 0.23±0.14 μm as compared to those present in alloy B with the largest average size of 0.42±0.28 μm. Moreover, the finer eutectic Si phase was achieved in the current Al-Si-Mg-Mn alloys, compared with binary Al-Si eutectic alloys with a similar solidification condition [136,152,214].

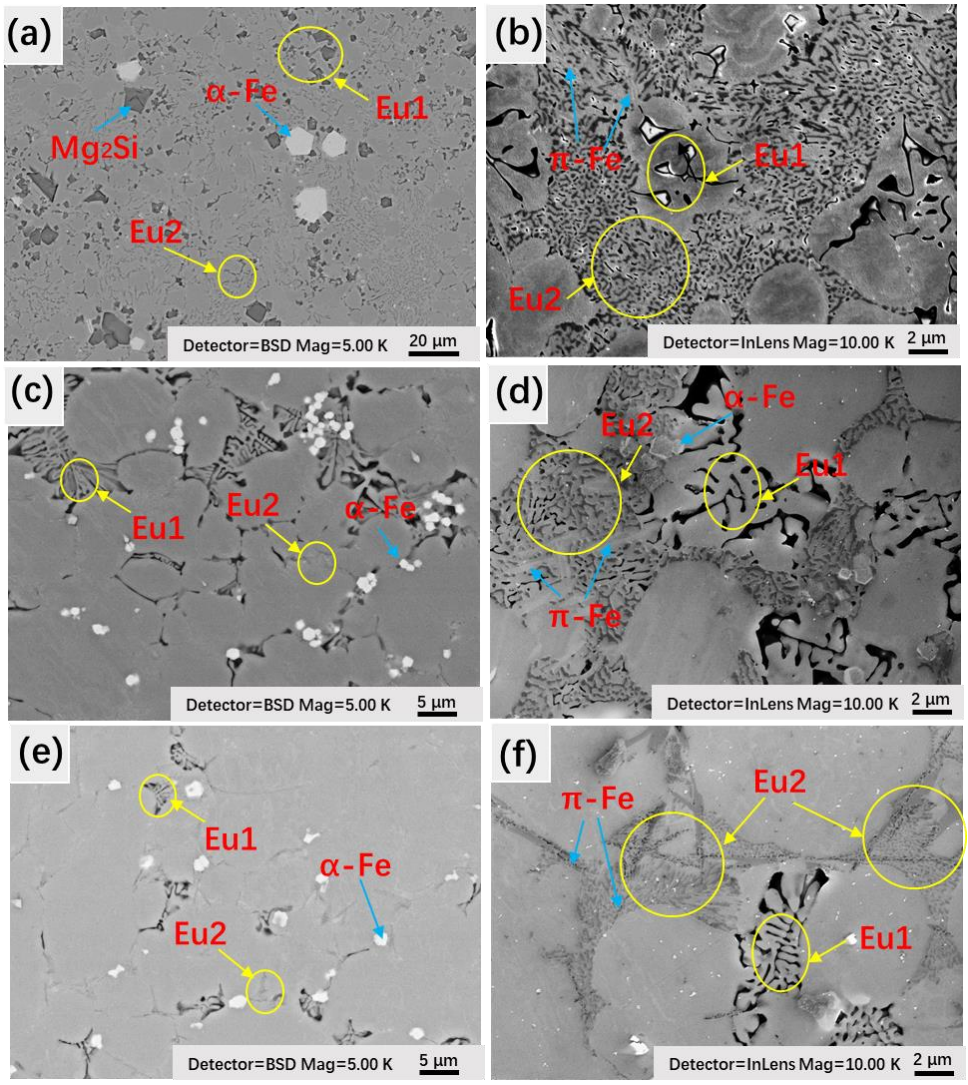

Fig. 4-7 (a, c, e) Backscattered SEM micrographs showing the microstructure of alloy A, alloy B alloy C (b, d, f) in-lens SEM micrographs with larger magnification showing the eutectic region in alloy A, alloy B and alloy C

The size distributions of α-AlFeMnSi particle present in alloy A, alloy B and alloy C are shown in Fig. 4-8 (a,b,c), respectively. Alloy A and alloy B have finer particles which have a concentrated size range between 1 and 1.5 μm, while the much broader distribution of α-AlFeMnSi particles appears in alloy C. There are a few large α-AlFeMnSi particles (over 10 μm) in alloy A with hexagonal morphology. The inserted images are backscattered electron micrographs taken at low magnification, showing the size and distribution of α-AlFeMnSi particles. Furthermore, the aspect ratio of α-AlFeMnSi particles was analysed in Fig. 4-8 (d). The α-Fe particles present in alloy A and alloy B show a lower aspect ratio.

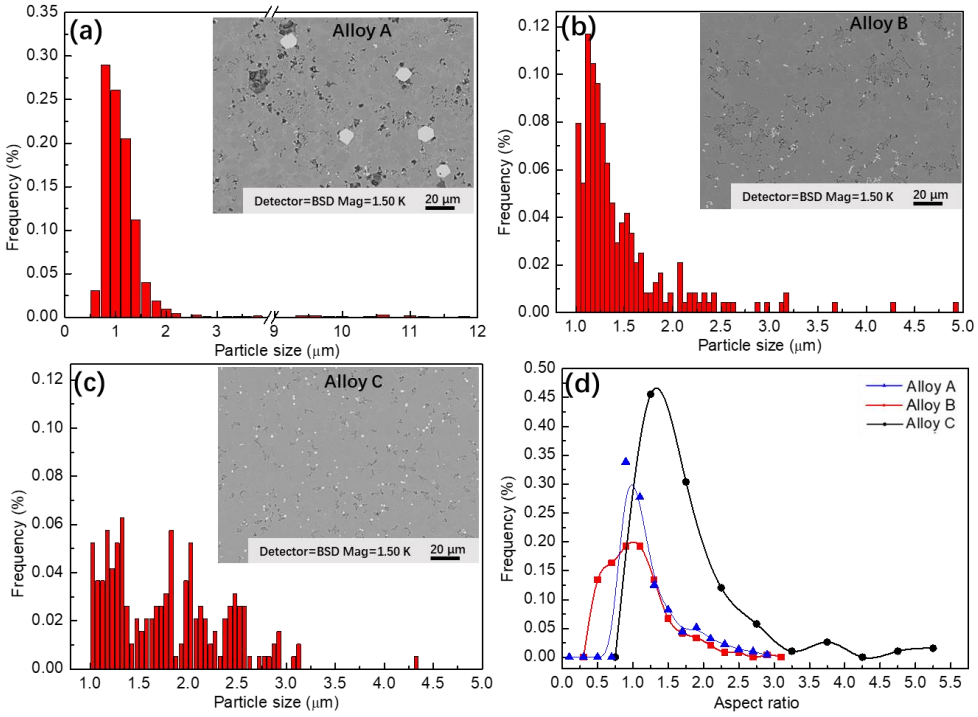

Fig. 4-8 The size distribution of α-AlFeMnSi particles present in alloy A (a), alloy B (b) and alloy C (c) together with insets of SEM micrographs of corresponding alloys and (d) the frequency of the aspect ratio

4.3.5 Transmission Electron Microscopy results

Fig. 4-9 (a) shows a bright-field TEM micrograph of the quaternary eutectic mixture present in hypoeutectic alloy C taken at [010] zone axis of π-AlFeMnSiMg phase, together with corresponding selected area diffraction patterns (SADP), as shown in Fig. 4-9 (d-g). Fig. 4-9 (b) shows BF-STEM image and elemental distributions of ultrafine eutectic regions. There are four kinds of phases co-existed within the ultrafine eutectic region of alloy C, which coincide with the microstructure characterised under SEM ('EU2' in Fig. 4-7 (f)). Mg_2Si phase has a size of ~100 nm while π-AlFeMnSiMg phase has ~250 nm width and 2-3 μm length. The Si phase in alloy A exhibits irregular and spheroidized morphology. Moreover, the high density of twins was observed in some Si particles, together with the corresponding SADP pattern, as shown in Fig. 4-9 (g). It is reported that the induced twinning in Si by the additional element or impurities is the most established growth model [215]. Herein, the high density of twinning Si may result from the absorption of the additional elements of Mg, Fe or Mn preventing further growth. The Mg_2Si phase has ultrafine particulate morphology with the size of 100-250 nm which is usually observed to be Chinese-script morphology in other solidification conditions with a lower cooling rate [216]. Fig. 4-9 (c) and (e) show the EDS spectra, together with an inset of measured composition and SADP of π-AlFeMnSiMg phase,

respectively. The extra peak was also found in Fig. 4-9 (c), which comes from the copper FIB sample grip. The substitution of Mn in π-AlFeMnMgSi phase was found as well as lower content of Fe and Mn compared with the equilibrium π-AlFeMnMgSi phase.

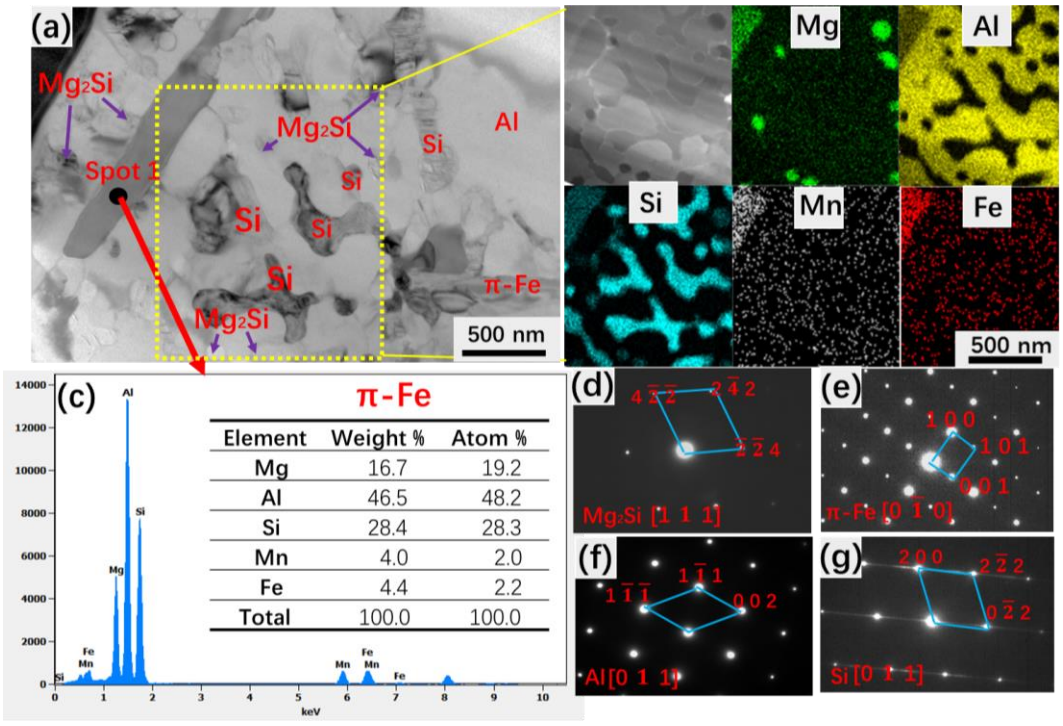

Fig. 4-9 (a) Bright-field TEM micrograph of the ultrafine eutectic region in alloy C showing the microstructure of quaternary eutectic (b) the elemental distributions inside the eutectic region (c) EDS spectra of π-AlFeMnSiMg phase, together with inset of measured composition and (d-g) SADP pattern of π-AlFeMnSiMg, Si, Mg_2Si and α-Al phases, respectively

4.4 Mechanical properties of as-cast Al-Si-Mg-Mn alloys

Fig. 4-10 (a) shows tensile stress-strain curves of these Al-Si-Mg-Mn alloys prepared by HPDC. These alloys have a yield strength above 230 MPa. However, the elongation to fracture increases with decreasing volume fraction of eutectic mixture. Fig. 4-10 (b) shows the comparison of the tensile properties of these three Al-Si-Mg alloys. Although alloy A has the highest yield strength of 285 MPa, its elongation to fracture is only limited to 0.8%. Alloy C has the highest elongation to fracture of 4.3% and yield strength of 231 MPa. The excellent yield strength of 281 MPa was achieved in alloy B with reasonable elongation to fracture of 2.3%. The yield strength of current Al-Si-Mg-Mn alloys is much higher than those of commercially available die-cast aluminium alloys, while the elongations of alloy B and alloy C are at the acceptable level. It should

be noticed that no extra elements such as Cu and Zn were added as strengthening elements to design the alloy with improved high yield strength.

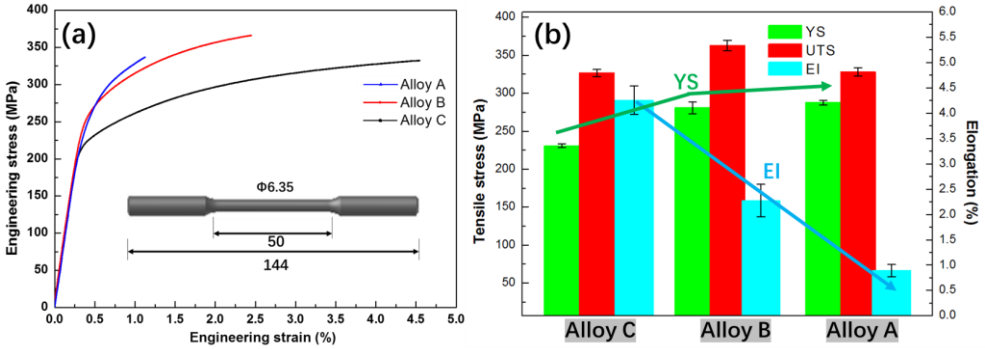

Fig. 4-10 Mechanical properties of the as-cast Al-Si-Mg-Mn alloys (a) tensile stress-strain curves, (b) average tensile properties

The cracks were found in large Mg_2Si in alloy A shown in Fig. 4-11 (a,b) and it shows cleavage features. It can be noted that the cracks initiated from large polygon Mg_2Si particles, leading to the low ductility in alloy A. Fig. 4-11 (c,e) shows the fracture surface of alloy B and alloy C, respectively, which were taken in the middle part of the sample. The fracture is a combination of eutectic region separation and cleavage fracture of α1-Al grains. It should be noted that the fracture surface was dominated by the eutectic separation, and only a few fractures of α1-Al grains were observed. The separation of the eutectic regions at grain boundaries of alloy B and alloy C were shown in Fig. 4-11 (d) and (f), respectively.

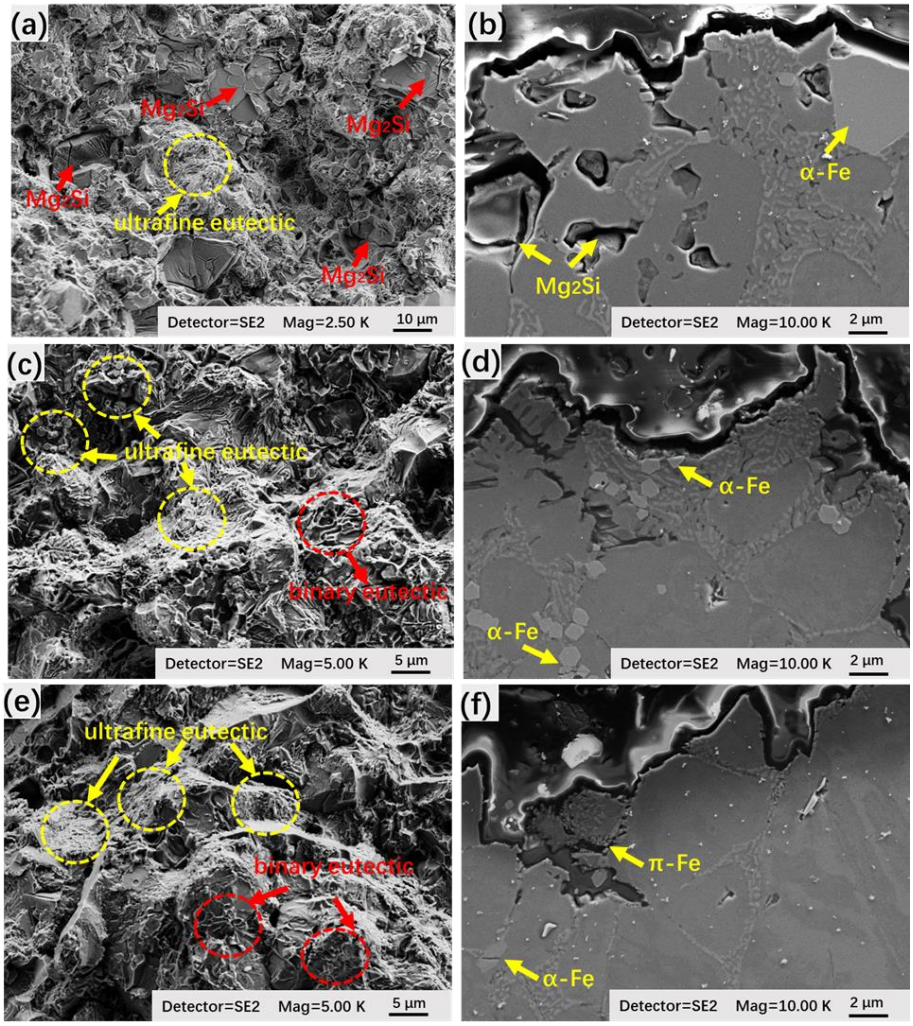

Fig. 4-11 SEM micrographs of specimens after tensile tests, showing the fractured surface of alloy A (a), alloy B (c) and alloy C (e); and crack propagation through the eutectic structure of alloy A (b), alloy B (d) and alloy C (f) (note: loading axes for (b), (d) and (f) are vertical)

Fig. 4-12 shows the dislocation pile-ups at the boundary between eutectic and α-Al grain after 3% interrupted tensile testing of hypoeutectic alloy C. The strain contrast inside α-Al grains indicates massive dislocation pile-up at the boundary which results from plastic deformation. More dislocations were found at the boundary of the ultrafine quaternary eutectic region shown in Fig. 4-12 (b).

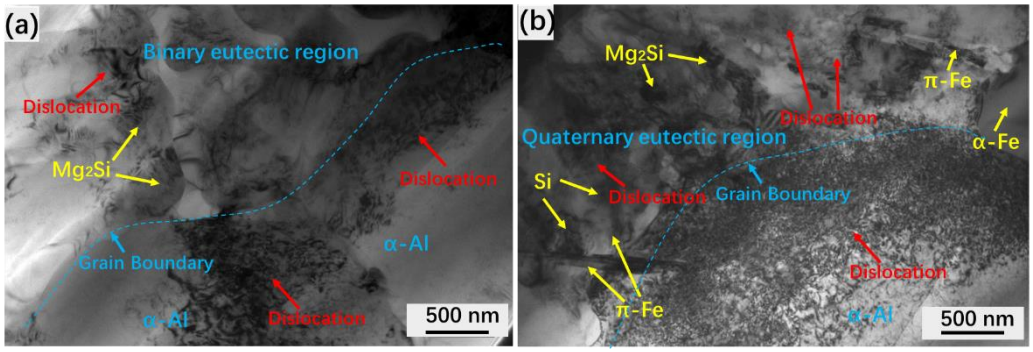

Fig. 4-12 TEM bright-field micrographs showing dislocations at the binary eutectic region (a) and the ultrafine quaternary eutectic region (b) of 3%-tensile-strained alloy C

4.5 Discussion

4.5.1 Microstructure evolution

The HPDC process is a two-stage solidification process, where some phases partially solidified in the shot sleeve at a very slow cooling rate and rest of liquid solidified in the die cavity at a very high cooling rate [217]. During the HPDC of hypoeutectic alloys, two types of α-Al phases were observed in alloy B and alloy C, and α1-Al solidified in the shot sleeve has a larger size, while much finer α2-Al forms in the die cavity. It can be found that increasing the volume fraction of the eutectic mixture can contribute to a decrease of α2-Al and α1-Al grains in size. The refined α-Al grain size with the increasing volume fraction of eutectic is due to the growth restriction mechanism [218]. At certain undercooling, the solid growth rate is affected by liquidus slope and solute contents at liquid [219]. The more addition of Si and Mg into the alloys increases the volume fraction of eutectic. In the meantime, more solutes segregate at the solid/liquid interface and more solutes diffusion in the liquid exists, restricting the growth of dendrites. Therefore, the finer α-Al grain size was achieved. Moreover, in eutectic alloy A, large polygon Mg_2Si and compact α-AlFeMnSi particles are formed without the presence of coarse α1-Al phase. From Pandat 8.5 prediction, some intermetallic compounds formed before the eutectic reactions. It should also be noted that alloy A is close to the ternary eutectic composition, which is reported to be a quasi-binary reaction and L→α-Al+Mg_2Si forms before final eutectic reaction [220]. As a result, coarse compact α-AlFeMnSi particles 0and some eutectic phase of polygon Mg_2Si formed in the shot sleeve. Some α-Al phases were also found in alloy A with an average volume fraction of 11% from edge to centre, although the composition in alloy A (eutectic composition) is close to eutectic composition. It is because HPDC process is a non-equilibrium process with two-stage solidification. Large Mg_2Si and α-AlFeMnSi

form in the shot sleeve, consuming the solute and the composition on the later solidification in die cavity is changed. Furthermore, segregation of solute distribution exists that near the surface or defect band, there is an increase of solute concentration [193]. Consequently, the composition of alloy A is close to off-eutectic composition and some α-Al grains form. In addition, the average area fraction of eutectic mixture in alloy B and alloy C is a little lower than the predicted values. There are several possible reasons. Firstly, HPDC is a non-equilibrium solidification process with a high cooling rate. Secondly, the database of Al-Si-Mg-Mn-Fe employed in the CALPHAD calculation causes somehow deviation. Lastly, the macrosegregation in the defect band region causes some deviation of volume fraction of eutectic.

The fine eutectic morphology solidified in the die cavity with submicron-scale binary eutectic and ultrafine quaternary eutectic is achieved in the Al-Si-Mg-Mn eutectic or hypo-eutectic alloys by HPDC process. The bimodal eutectic microstructure of eutectic alloys was also found and reported by Kim et al [58]. The typical bimodal eutectic microstructure in eutectic alloys consists of two types of eutectic with different length scale and the formation of this unique structure is due to the high cooling rate and additional elements which can affect the topological and crystallographic anisotropy of the liquid/solid interface, and destabilise the liquid/solid interface, resulting in shifting the couple eutectic growth zone under non-equilibrium solidification condition [221]. Thus, the homogeneous distribution of inhomogeneous structure formed in Al-Cu-Si ternary eutectic alloys. Furthermore, from XRD results, the change of volume fraction of eutectic mixture has no influence on the types of phases in the as-solidified microstructure of hypoeutectic Al-Si-Mg-Mn alloys. It should be noted that π-AlFeMnSiMg appeared in these alloys which was not predicted by Pandat 8.5. It is mainly due to the non-equilibrium solidification under HPDC process and the database employed in the current study. The binary (EU1) and quaternary (EU2) structures in alloy C are finest. Especially, the eutectic Si in alloy C is finer than some binary Al-Si die-cast alloys. It is because the multi-component recipe in the final solidification liquid can increase the constitutional undercooling and contribute to competitive growth of multiple phases, resulting in the refinement of the eutectic phases [212,222]. Moreover, The eutectic Si phase in alloy C is most exceptional among these three alloys. The alloy C with the lowest amount of quaternary eutectic fraction (alloy C) has the smallest interdendritic regions (eutectic regions), indicating less remaining liquid prior to final solidification as compared to eutectic (alloy A) and hypoeutectic (alloy B) Al-Si-Mg-Mn

compositions. Therefore much fastest heat transfer through α-Al dendrites during final eutectic solidification was obtained. As a result, ‘EU2’ has the smallest size of Si.

The addition of Mn can suppress the formation of β-Fe phase in HPDC, and similar to the development of α-Al phases, the dual size distributions of α-AlFeMnSi particles are caused by two-stage solidification as well. It was reported that the coarse α-AlFeMnSi particles solidified in the shot sleeve are below 10 μm, provided the iron content is less 0.2% [9]. Compared with alloy C, alloy B has the finer α-AlFeMnSi particles with a lower aspect ratio and the size of α-AlFeMnSi particles is below 5 μm in all these three alloys. According to the solidification sequence predicted by Pandat 8.5 in Fig.4-2, the majority of α-AlFeMnSi particles formed at a temperature ranging from 617-600 °C before α-Al formation in alloy B, while in alloy C the formation of α-AlFeMnSi particles accompanies with α-Al at the temperature ranging from 620 °C to 556 °C. Therefore, the α-AlFeMnSi particles in alloy B have less solidification time due to increased undercooling. As a result, α-AlFeMnSi particles in alloy B shows faceted hexagonal morphology with a lower aspect ratio and finer size distribution. They are distributed along grain boundaries or inside the eutectic regions. Furthermore, it can be observed that a large area fraction of large α-AlFeMnSi particles formed in alloy A, and finer α-AlFeMnSi particles formed at the eutectic regions with lower area fraction. The solidification path of alloy A involves the formation of α-AlFeMnSi particles from 615 °C to 554 °C, prior to eutectic reaction, according to Fig. 4-2. Herein, the large α-AlFeMnSi particles nucleated and grew in the short sleeve. This implies a reduced amount of Fe present in the remaining liquid, and it solidifies into a few finer α-AlFeMnSi particles near the final eutectic temperature.

The π-AlFeMnSiMg phase in alloy C is much finer compared with those in A356 and A357 alloys [223,224]. In alloy C, the formation of final quaternary eutectic reaction with a high volume fraction of refined π-AlFeMnSiMg phase is attributed to the partitioning of Fe to the remaining liquid and much faster heat transfer of the last smaller interdendritic regions under non-equilibrium solidification condition [224]. Lastly, the composition of π-AlFeMnSiMg phase is slightly different from the equilibrium composition $Al_9FeMg_3Si_5$ taking into consideration of substitution of Mn, and this results from non-equilibrium solidification process.

4.5.2 Relationship between microstructure and mechanical properties

The Al-Si-Mg-Mn alloys in the current work showed excellent mechanical properties, especially having a high yield strength in excess of 200MPa. The mechanical properties of the dendrite-ultrafine eutectic composite strongly depend on the phase selection and volume fraction of strengthening phases [122]. In another word, the elongation can be tailored by controlling the volume fraction of eutectic mixture, and at the same time, the strength can be improved via optimisation of eutectic microstructure from monolithic eutectic structure to multi-modal eutectic structure with multi-component alloy design approach. The microstructure of currently developed alloys consists of the soft α-Al primary phase, ultrafine/submicron-scale eutectic mixture, and small α-AlFeMnSi phases. The soft α-Al primary phase can act as a barrier for the crack propagation of catastrophic failure. The ultrafine/submicron-scale eutectic structure and fine iron-contained particles contribute to the high strength for these alloys. The elongation of the alloys was dominated by the volume fraction of eutectic mixture present in these alloys. Hence, the highest elongation was achieved in alloy C. However, the presence of large brittle Mg_2Si or large α-AlFeMnSi phases, together with the highest volume fraction of eutectic mixture present in alloy A is responsible for the lowest elongation to fracture of ~0.8%.

The coarse Si particles in binary Al-Si die-cast alloys playing an important role in the strength as they are the main sources of stress concentration and the crack paths preferentially go through the eutectic region. In the current work, ultrafine Si and Mg_2Si phases together with fine iron-containing multi-component phases inside the eutectic region can be more effective to suppress the crack development and α-AlFeMnSi particles formed at the grain boundary further improve the tensile stress. Moreover, based on Hall-Petch theory, higher yield strength can be achieved with much finer eutectic structure [225]. In addition, the ultrafine quaternary eutectic with much finer microstructure is more effective to inhibit the propagation of dislocation, as shown in Fig. 4-12. Some dislocations were found inside the binary eutectic regions (EU1) as well, due to the generation of dislocations within the eutectic region. No cracks were found on the eutectic phases. Therefore, the plastic deformation of ultrafine eutectic alloys was governed by dislocation slip inside the α-Al grains and the excellent yield strength is because of the interaction of dislocations between ultrafine eutectic and α-Al grains leading to better work hardening regime [226]. Hence, the alloys in the current

study have higher strength than some other die-cast aluminium alloys. It should also be noted that alloy B has higher strength than alloy C, due to much higher volume fraction of eutectic mixture. However, the highest volume fraction was obtained in alloy A, and the yield strength is similar to alloy B. The reasons are as follows. Firstly, in alloy A, a lot of coarse Mg_2Si phases which form from a binary eutectic reaction. This reduces the contribution of binary eutectic in the strength compared with that in alloy B and alloy C which have much finer binary eutectic lamellar spacings. Secondly, a large volume fraction of large compact α-AlFeMnSi phases formed prior to the final eutectic reaction in alloy A, resulting in a small quantity of fine α-AlFeMnSi phases forming in the die cavity. Therefore, the strength of alloy A is balanced by the increased volume fraction of eutectic mixtures and coarsening of α-AlFeMnSi and Mg_2Si phases. Consequently, alloy A exhibits similar yield strength with alloy B.

4.6 Conclusion

(1) High strength die-cast aluminium alloys have been developed based on the concept of multi-component alloy design approach to introduce ultrafine secondary phase and refined eutectic microstructure for enhanced strengthening mechanism. In addition, the presence of soft dendritic α-Al phase improves the ductility of this alloy system. The as-cast Al-Si-Mg-Mn alloy with 30% eutectic provides the high yield strength of 231 MPa, ultimate tensile strength of 340 MPa and elongation of 4.3%. The as-cast Al-Si-Mg-Mn alloy with 50% eutectic exhibits the super high yield strength of 281 MPa and elongation of 2.3%.

(2) Such high strength die-cast Al-Si-Mg-Mn alloys show bimodal or multi-modal microstructure, consisting of primary α-Al phase, α-AlFeMnSi, binary eutectic (Al+Mg_2Si) and ultrafine quaternary Al+Mg_2Si+Si+π-AlFeMnSiMg eutectic.

(3) The finest eutectic Si phase with an average size of 230 nm was achieved in the die-cast hypoeutectic Al-Si-Mg-Mn alloy with 30% eutectic mixture. The fine α-AlFeMnSi particles in Al-Si-Mg-Mn hypo-eutectic alloys were obtained with an average size below 2 μm.

(4) The high number density of dislocation and dislocation pile-ups observed at eutectic boundaries or inside the eutectic mixture is believed to be responsible for excellent work hardening in these multi-component alloys.

Chapter 5 Heat treatment of Al-Si-Mg-Mn die-cast alloys

5.1 Introduction

This chapter is concerned with studies of heat treatment of newly developed Al-Si-Mg-Mn alloys from Chapter 4 to optimise the solution treatment and artificial ageing conditions for maximum mechanical performance. The alloy B and alloy C were selected, due to its good mechanical properties under as-cast state. The effect of heat treatment conditions on the resultant microstructure and mechanical properties were characterised using a combination of electron microscopies, hardness and tensile test.

5.2 Microstructure of Al-Si-Mg-Mn alloys after heat treatment

5.2.1 Solution treatment of Al-Si-Mg-Mn alloys

The solidus temperature of the Al-Si-Mg-Mn alloys was 554 °C based on Pandat 8.2 calculation. A range of solution temperatures varying from 540 °C to 480 °C was chosen for this study. The composition of alloy B and alloy C can be referred in Table 4-2, which are Al7.48%Si3.55%Mg0.52%Mn0.18%Fe and Al5.22%Si2.35%Mg0.48%Mn0.16%Fe (wt%), respectively. Fig. 5-1 shows the microstructure of alloy B (a-d) and alloy C (e-h) after solution treatment at 540 °C for 10, 20, 30 and 60 mins, respectively. The defect band region can be observed from optical microscope images, which were marked in Fig. 5-1 (a,e). The mechanism of defect band formation was proposed by Gourlay et al. [227], to be due to the dilatant shear bands resulting from strain instabilities of initially solidified grains. The pore size and area percentage for each sample were quantified using ImageJ software. It can be observed that alloy B and alloy C exhibit a similar area fraction and pore size. The maximum pore size of a given solution treatment time varying from 10 to 60 minutes was approximately 47 μm, 90 μm, 102 μm and 112 μm, respectively. Here, the maximum size of pores at 540 °C for the various time was used as a measure to access the influence of solution heat treatment conditions on the quality of the sample. We introduced pore size level as a factor for the optimisation of solution treatment. It is excepted that with increasing solution treatment time, pores grow or expand and finally lead to surface blistering. The surface blisterings were only found at solution times over 30 min at 540 °C (not shown here). It can be noted that the maximum pore size in

samples with the solution treatment time of 10 min at 540 °C is almost similar to that under the as-cast state from image analysis. Therefore ‘level 1’ was defined in this solution treatment condition, representing the best quality. In addition, the ‘level 2’, ‘level 3’ and ‘level 4’ were defined based on the maximum size of pores with solution times of 20, 30 and 60 min, respectively. The area fractions of pores in different solution temperature and time are shown in Table 5-1.

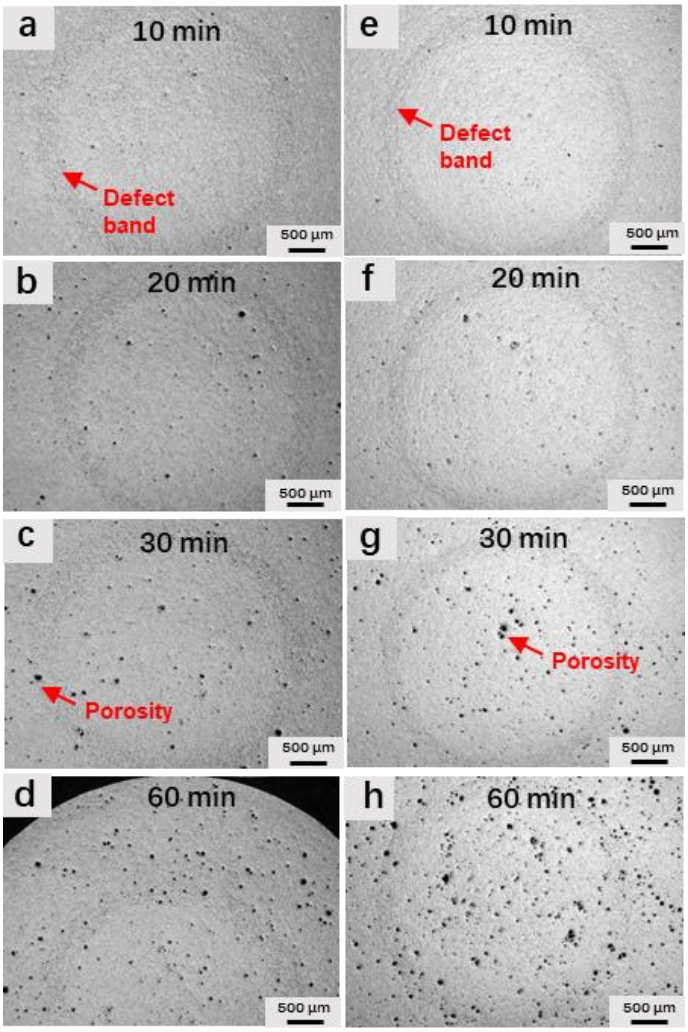

Fig. 5-1 The microstructure showing the size and distribution of porosity after solution heat treatment at 540 °C for 10, 20,30 and 60 mins of alloy B (a-d) and alloy C (e-h)

From Table 5-1, it can be found that the largest area percentage of porosity was obtained after solution treatment for 60 min at 540 °C, which is 5.83% and 4.80% for alloy C and alloy B, respectively. Alternatively, the solution treatment for 10 min at 540 °C resulted in the lowest area percentage of porosity. The decrease in solution temperature can enable longer solution treatment time without sacrificing the area

percentage porosity and maximum pore size. The pore size becomes level 2 with decreased solution treatment temperature and prolonged solution time from 520 °C for 60 min to 480 °C for 120 min, while at 540 °C it takes only 20 min for the quality of sample to become level 2. Therefore, the relationship between the solution temperature and solution times needs to be balanced. In other words, although the prolonged solution time or increased solution temperature is beneficial for the dissolution of the phases and the homogenisation of eutectic phases, it can cause the accelerated expansion of the internal pores.

Table 5-1 The area percentage of porosity and pore size level of alloy B and alloy C under different solution treatment temperature and time

T (˚C)	Time (min)	Alloy B		Alloy C	
		Area % of pores	Pore size level	Area % of pores	Pore size level
As-cast	0	0.23%	1	0.13%	1
480	30	0.38%	1	0.16%	1
	60	0.45%	1	0.18%	1
	90	1.08%	1	0.80%	1
	120	1.82%	2	1.5%	2
500	30	0.37%	1	0.48%	1
	60	0.76%	1	0.74%	1
	90	1.98%	2	1.74%	2
	120	2.5%	2	2.3%	2
520	10	0.17%	1	0.14%	1
	20	0.39%	1	0.15%	1
	30	0.47%	1	0.42%	1
	60	1.02%	2	0.8%	2
540	10	0.25%	1	0.15%	1
	20	0.52%	2	0.82%	2
	30	2.75%	3	1.05%	3
	60	4.80%	4	5.83%	4

Fig.5-2 shows a typical microstructure of alloy C after solution treatment at 480 °C for 10 min (a) and 60 min (b), and 520 °C for 10 min (c) and 30 min (d), respectively. As discussed in Chapter 4, EU1 region is the binary eutectic region (Mg_2Si+α-Al), and EU2 region is quaternary (Si+Mg_2Si+α-Al+π-AlFeMnSiMg) eutectic region. As shown in Fig. 5-2, the Mg_2Si phases exhibit black colour and Si phases have light grey colour. In the current study, solution treatment at 480 ˚C for 10 min was able to disintegrate all the eutectic Si, but some of the eutectic Mg_2Si remained and connected with high aspect ratio, as shown in Fig.5-2 (a). Similar results were found by Giulio, who reported

that solution treatment at 475 °C for 15 min was sufficient to spherodise the eutectic Si [205]. In Fig.5-2 (b), after 60 min of solution treatment, all the Mg_2Si phase was spheroidised and agglomerated as well as α-Al grains become coarsening. However, from Fig.5-2 (c), it can be seen that after solution treatment at 520 °C for 10 min, eutectic Mg_2Si and Si phases were spheroidised. However, few Mg_2Si and Si could be found in this sample, indicating the dissolution of more Si and Mg_2Si phases into the matrix. Further solution treatment for 30 min leads to the coarsening of eutectic phases and α-Al grain growth.

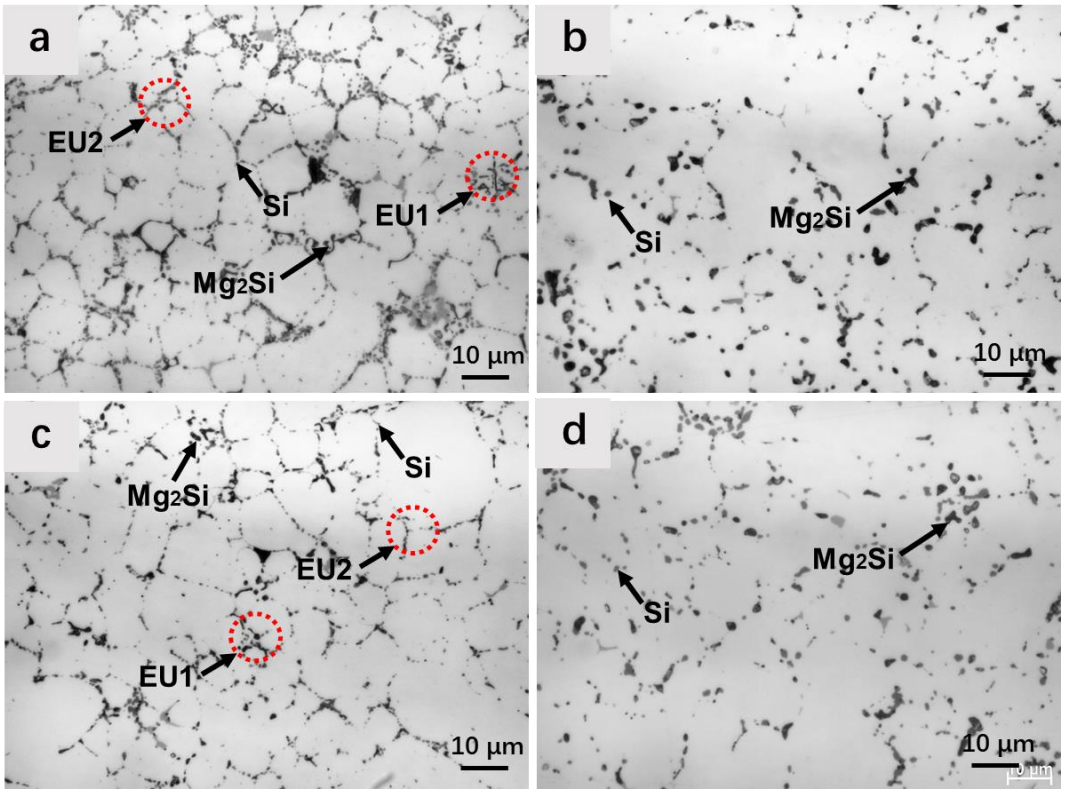

Fig.5-2 The microstructure of alloy C after solution treatment at 480 ˚C for 10 min (a) and 60 min (b), and after solution treatment at 520 ˚C for 10 min (c) and 30 min (d)

Fig.5-3 shows the microstructure of alloy B (a,b) and alloy C (c,d) after solution treatment at 540 ˚C for 10 min. From Fig.5-3 (a,c), it can be found that after 10 min of solution treatment, there is no obvious change in grain size, as compared to the as-cast state shown in Fig.4-4 (b,c). The volume fraction of Si and Mg_2Si decreased, and they have both spheroidised. From high magnification SEM images (Fig.5-3 (b,d)), it can be seen that the α1-AlFeMnSi phase remains unchanged [204], as compared to the as-cast state. But the agglomeration of Si and Mg_2Si was observed in the EU2

eutectic region. The Mg_2Si phase in EU1 region was partially dissolved and dispersed. Moreover, the needle-like π-AlFeMnSiMg (in Fig. 4-7) disappeared. Instead, some particles below 1 μm were found in EU2 region of alloy A and alloy B. These ultrafine particles were identified to be α2-AlFeMnSi particles and will be discussed later.

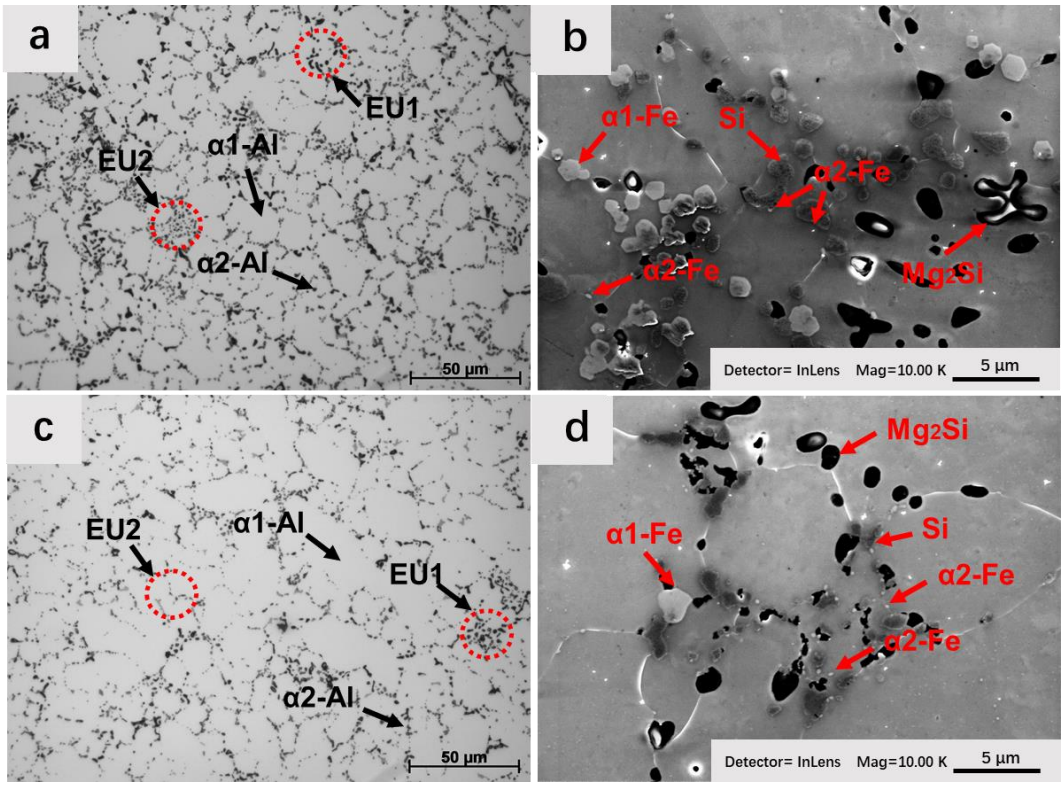

Fig.5-3 Typical microstructures of alloy B (a,b) and alloy C (c,d) after quenching from solution treatment at 540°C for 10 min, taken using optical microscope (a,b) and SEM in-lens imaging mode (c,d)

The image analysis was applied to quantify the size, volume fraction and aspect ratio of eutectic Si and Mg_2Si after solution treatment (540 °C for 10 min) from SEM in-lens images taken for each sample. From Table 5-2, the size of eutectic Si and Mg_2Si phases in alloy B and C was approximately double as compared with their as-cast counterparts. The volume fraction of Si and Mg_2Si phases in alloy B is higher than that in alloy C after solution treatment.

Table 5-2 Average particle size, volume fraction and aspect ratio of Si and Mg_2Si after solution treatment at 540 ˚C for 10 min

Alloy after solution treatment	Alloy B		Alloy C	
	Si	Mg_2Si	Si	Mg_2Si
Aspect ratio	1.68±0.82	1.9±1.2	1.73±0.58	1.9±1.6
Average diameter (μm)	1.12±0.78	1.33±0.8	0.48±0.38	0.92±0.68
Area fraction	10.2%	5.2%	4.5%	5.5%

The detailed analysis of the grain size of alloys A and B before and after quenching is shown in Fig.5-4. The EBSD evaluations of the grain size were taken at the sample cores. Fig. 5-4 (a,c) shows the EBSD mappings of α-Al grains under the as-cast state of alloy B and alloy C, respectively and their corresponding EBSD mappings after shot solution treatment are shown in Fig. 5-4 (b,e). There is no obvious coarsening of α-Al grains. The distribution of grains and average diameters are shown in Fig.5-4 (c,f). After solution treatment, the grain size of the alloys increased according to EBSD statistical analysis, although it looks similar in an optical microstructure. The average grain size of α2-Al remains almost the same after quenching, which are from 9.6 μm to 10.5 μm in alloy B and 10.6 μm to 11 μm in alloy C. As for α1-Al, there was a slight increment in both alloy B and alloy C from 30.9 μm to 32.9 μm and from 30.4 μm to 33.1 μm, respectively. It is reported that under long term solution treatment, the decreased hardness of the sample was caused dominantly by coarsening α-Al grain size and eutectic phases [228]. The highest hardness of A357 alloy was achieved after 540 °C solution treatment for around 10 min. This is because, in the early stages, α-Al was saturated on Mg and Si rapidly, without serious α-Al coarsening and dissolution of intermetallics [229]. In the current research, less growth of α-Al grains is beneficial for the yield strength.

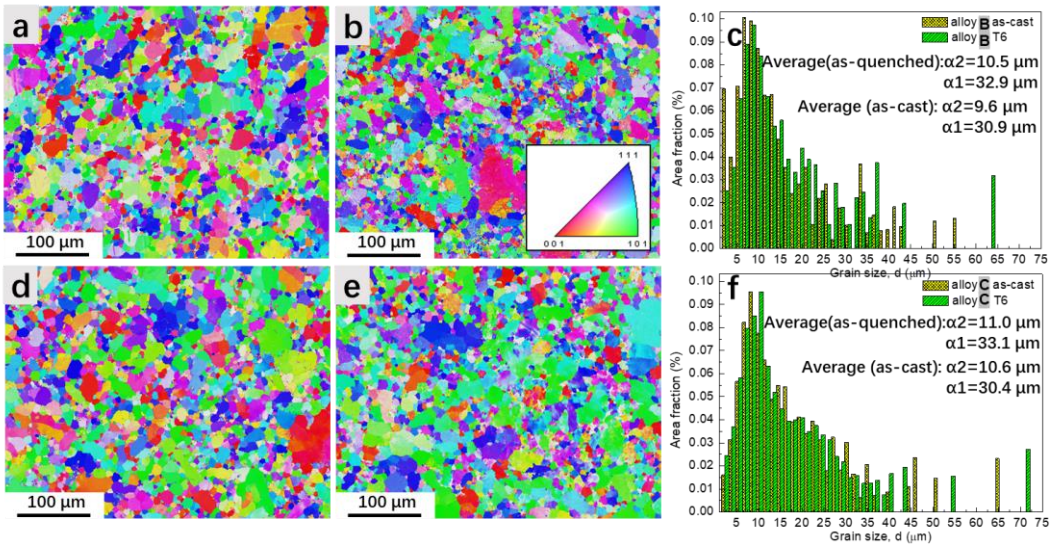

Fig.5-4 EBSD grain maps of as-cast alloy B (a), as-quenched alloy B after solution treatment at 540 °C for 10 min (b), and as-cast alloy C (d), as-quenched alloy C after solution treatment at 540 °C for 10 min (e); the grain size distribution of as-cast and as-quenched conditions for alloy B (c) and alloy C (f)

Fig.5-5 shows the eutectic region in alloy C with EDX mapping and SADP patterns after solution treatment at 540 °C for 10 min. From the bright-field images in Fig.5-5 (a), it can be seen that the π-AlFeMnSiMg has totally disappeared and fine α2-AlFeMnSi phases were found in the regions. The formula of α2-AlFeMnSi was identified to be $Al_{17.1}Fe_{3.2}Mn_{0.8}Si_{1.9}$ phase from SADP. The α2-AlFeMnSiis considered as α-AlFeMnSi with BCC structure and script-like and/or polyhedral morphology [230]. Moreover, except for a small number of α2-AlFeMnSi phases, there are some spheroidised Mg_2Si and Si particles inside the eutectic region. The EDX mapping of the eutectic region (in Fig.5-5 (b)) shows that these non-faceted α2-AlFeMnSi particles have size 150-700 nm with Al, Mn, Fe and Si four elements. The SADP patterns of these phases were shown in Fig.5-5 (c-f). This region has four phases, which are α-Al, Mg_2Si, Si and α2-AlFeMnSi.

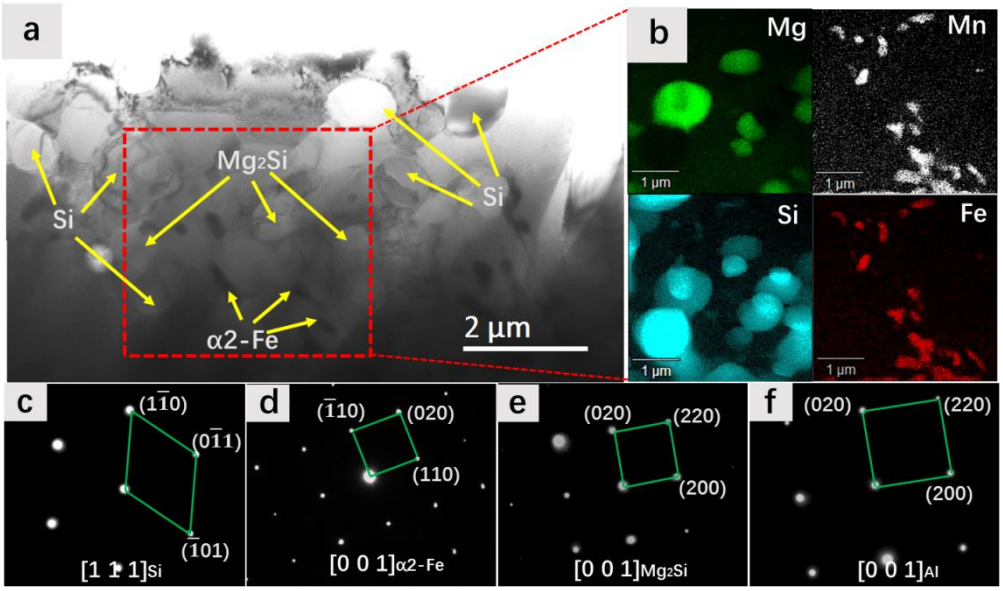

Fig.5-5 (a) TEM bright-field images of the eutectic region in alloy C after solution treatment at 540 °C for 10 min; (b) EDX maps of the selected region from Fig.5-5 (a); (c) corresponding SADP patterns of phases present in the microstructure

Fig.5-6 (a) shows the irregular and polyhedral morphology of a 300nm sized α2-AlFeMnSiphase under [001] zone axis. The particle has i. HRTEM (Fig.5-6 (b)) was used to study the crystal structure and lattice parameter of α2-AlFeMnSiphase. The α2-AlFeMnSiphase shows BCC structure with the spacing of the $\{110\}_{\alpha 2\text{-AlFeMnSi}}$ and $\{\bar{1}10\}_{\alpha 2\text{-AlFeMnSi}}$along the [001] zone axis, which are both 1.13 nm. From the EDX analysis (Fig 5-6c), the Fe/Mn ratio of α2-AlFeMnSiphase was found to be ~0.5, which is close to the composition reported by Dám et al [231].

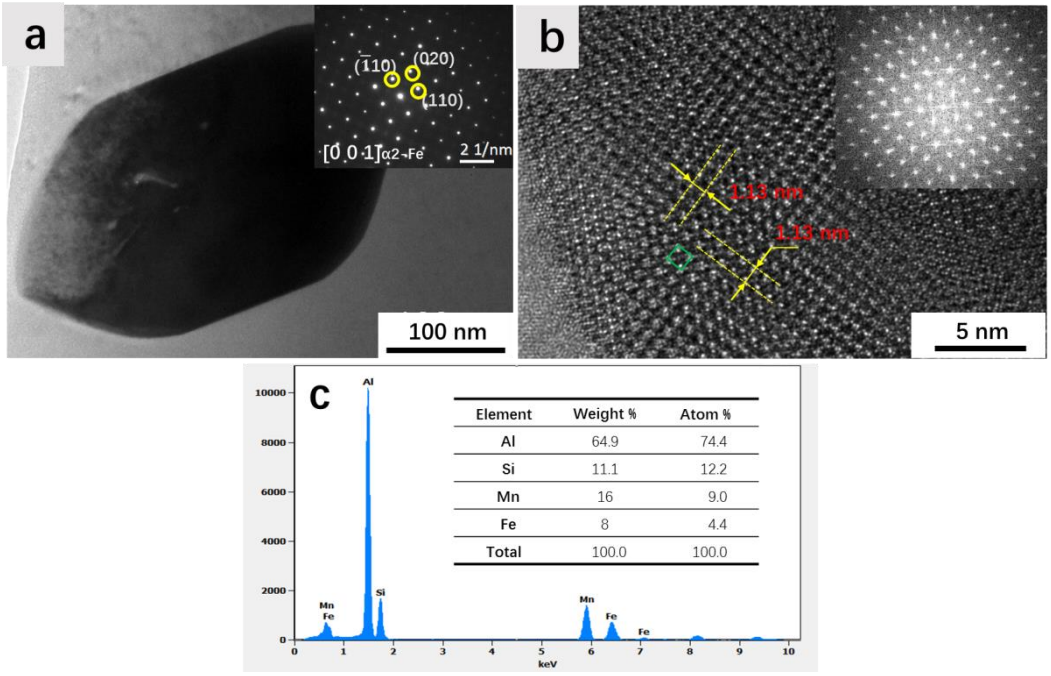

Fig.5-6 (a) TEM bright-field image of the α2-AlFeMnSiparticle with inserted SADP pattern of [001] zone axis (b) HRTEM image from the α2-AlFeMnSiparticle with corresponding FFT pattern (c) EDX spectrum collected from α2-AlFeMnSiparticle and its composition shown in the inserted table

5.2.2 Artificial ageing treatment of Al-Si-Mg-Mn alloys

Fig.5-7 shows the age-hardening curves of alloy B (a) and alloy C (b) heat treated at 170 °C after various solution treatment conditions. The highest hardness (HV) of the as-quenched sample was achieved after solution treatment at 540 °C for 10 min in both alloy B and alloy C, which gave HV values of 96 HV and 89 HV, respectively. The higher temperature can provide higher dissolution of Mg and Si in the α-Al grains prior to quenching, resulting in a higher hardness [228]. It was also found that the solution temperature has great influence on the level of hardening after ageing treatment. The peak ageing time of ~10 hours was found in both alloy B and alloy C for various solution treatment conditions. There is a slow reduction in hardness with increasing ageing time for the over-ageing condition. The highest hardness obtained at peak aged condition was achieved in alloy B and alloy C when these samples were solution treated at 540 °C for 10 min. They were found to be 135 HV and 124 HV, respectively. The increase in hardness for peak aged sample is similar for both alloys B and C, which was found to be 39 HV and 36 HV, respectively.

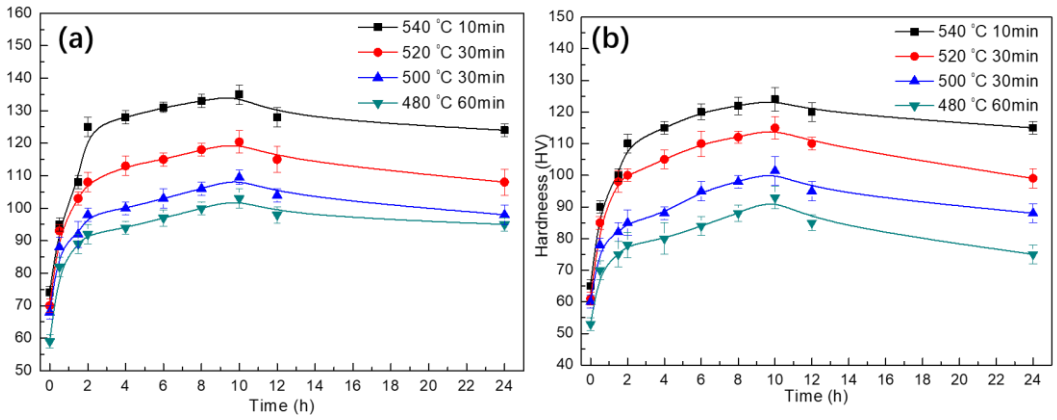

Fig.5-7 The hardness versus time curves of alloy B (a) and alloy C (b) aged at 170°C after subjected to different solution conditions

Fig. 5-8 (a-b) show the bright-field TEM images of precipitates present in alloys B and C, after peak ageing treatment at 170 °C for 10 hours, together with inserted SADP pattern taken along the $[001]_{Al}$ zone axis. It can be observed that alloys B and C share a similar diffraction pattern, which indicates that the types of precipitates are similar in both alloys. Moreover, the precipitates in alloy B and alloy C are both needle-like or granulate-shaped, with similar size and distribution. The precipitates have an average length of 30-60 nm and a diameter less than 7 nm. Fig.5-9 shows typical HRTEM images of precipitates present in alloy C aged at 170°C for 10 hours and its corresponding FFT. From Fig.5-9, the fully coherent precipitate was identified to be monoclinic β", which has orientation relationship of $[001]_{Al}//[010]_{precipitate}$ and $(200)_{precipitate}//(301)_{Al}$ [111,232].

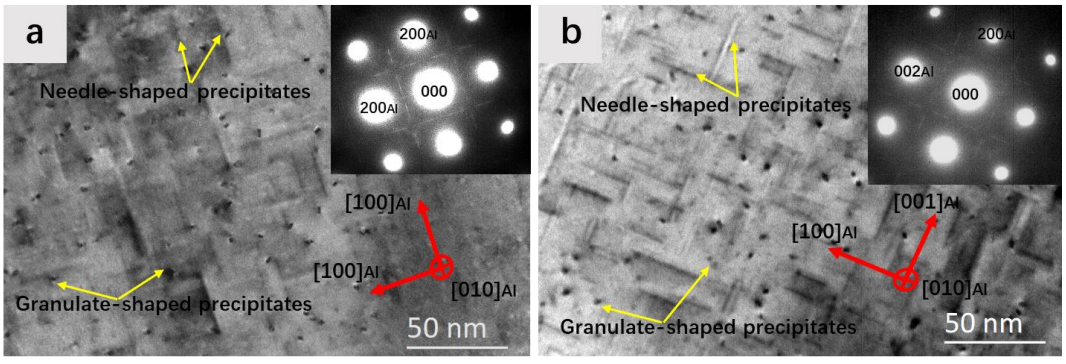

Fig.5-8 Bright-field TEM images of precipitates along [001] zone axis of the matrix alloy B (a) and alloy C (b) heat-treated at 170°C for 10 hours

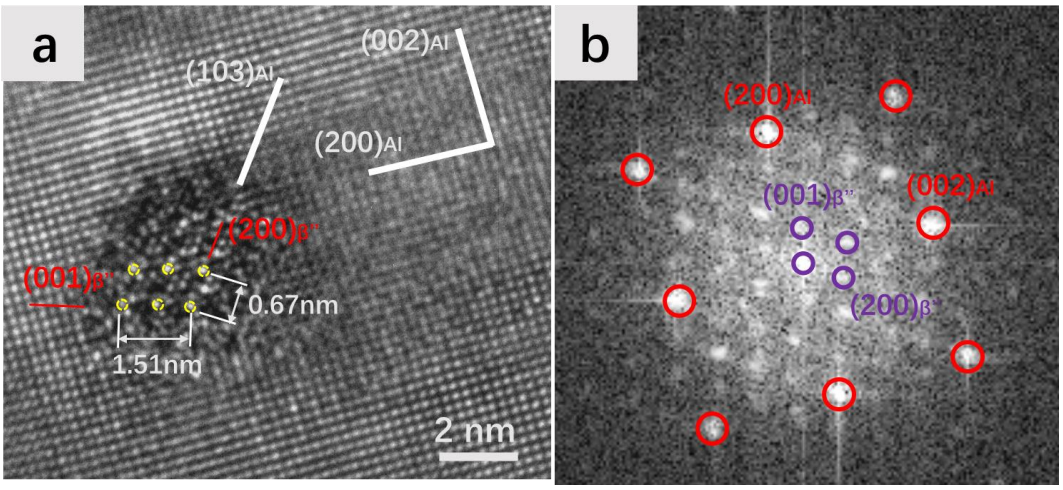

Fig.5-9 (a) β" phase in alloy A after peak ageing at 170 °C for 10 hours (b) corresponding FFT

5.2.3 Mechanical properties of Al-Si-Mg-Mn alloys after T6 heat treatment

Fig.5-10 (a) shows tensile stress-strain curves of alloy B and alloy C after T6 treatment. Alloy B has higher yield strength and ultimate tensile stress, which is 349±3 MPa and 400±7 MPa, but a lower elongation of 2.6±0.4%. The average yield strength, ultimate tensile strength and elongation of alloy C after T6 is 334±6 MPa, 391±5 MPa and 4.6±0.5%, respectively. The comparison of mechanical properties between current work and other alloys after T6 heat treatment was shown in Fig.5-10 (b). The mechanical properties in the current work exhibit better performance with short solution time during T6 treatment. Especially, alloy C with a combination of good yield strength and elongation has a great potential for industrial applications.

Fig.5-11 shows fracture surface alloy B (a,b) and alloy C (c,d) after T6 treatment. From Fig.5-11 (a,c), it can be seen that there are gas pores in both alloys with sizes of ~35 μm, due to the entrapment of gas during the high-speed injection process. Detailed fracture surfaces are shown in Fig.5-11 (b,c). There is only a small amount of cleavages of α1-Al and large number of dimples, indicating predominantly ductile fracture behaviour [175]. The particles at the fracture surface were identified to be eutectic Si or Mg_2Si. These brittle phases are the main source of stress concentration and have a high possibility of crack initiation [110].

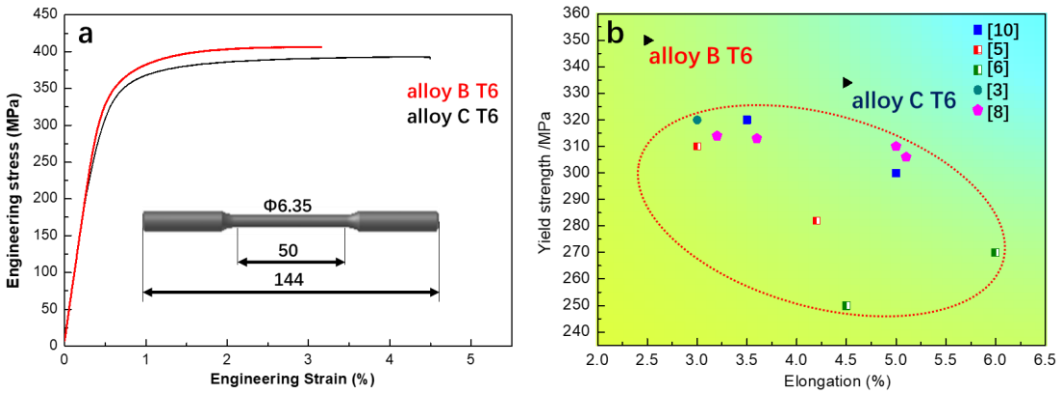

Fig.5-10 (a) Tensile stress-strain curves for alloy B and alloy C after peak ageing and (b) a comparison of Al-Si-Mg-Mn alloy with other die-cast alloys after T6 heat treatment

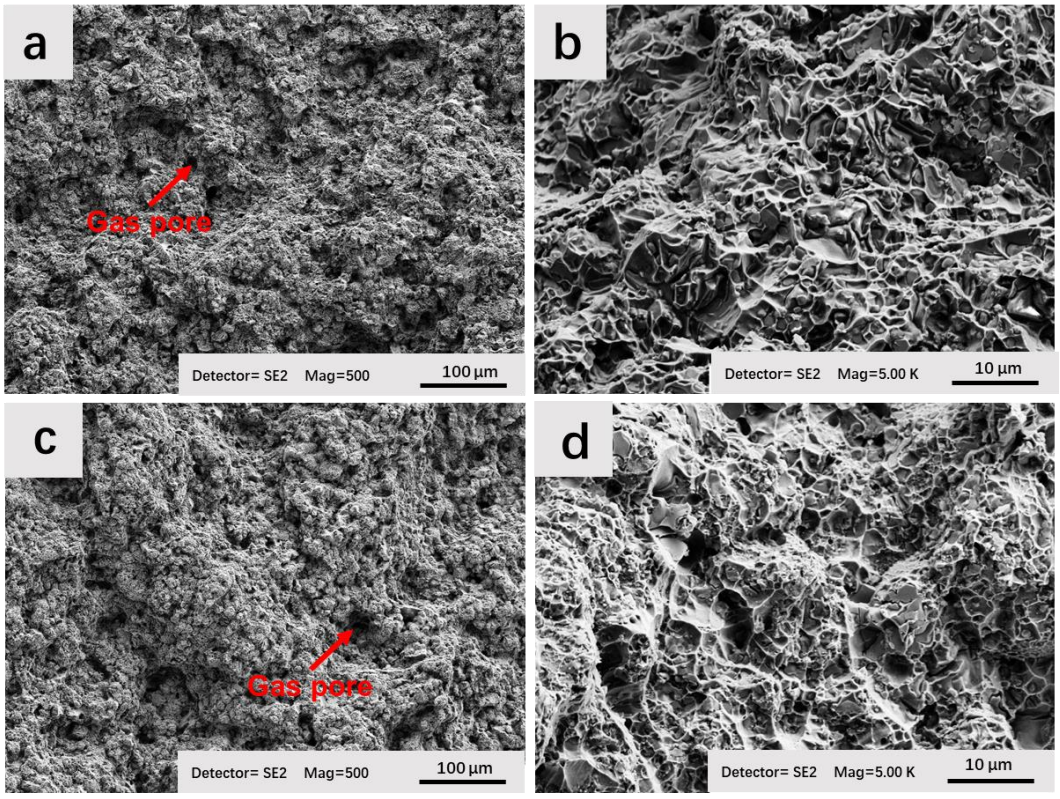

Fig.5-11 The fracture surface of alloy B (a,b) and alloy C (c,d)

5.3 Discussion

5.3.1 Microstructure evolution after heat treatment

It is well known that solution treatment at high temperature for a long period of time can lead to unavoidable surface blistering in die-cast alloys. It is because the softness

of α-Al heated at high temperature, the entrapment of the gas can expand. In order to improve the mechanical properties of die-cast alloys, several investigations have been done to optimise the heat treatment processing conditions. Yan has developed criteria to assess the quality of samples after solution treatment at various temperatures [209]. Samples with acceptable quality are those without blistering upon inspection by the naked eye, so as to determine the optimal solution time at a given solution temperature. However, it should be noted that surface blistering results from the severe growth of internal pores [199], and the initial state of pore formation and expansion cannot be seen on the surface of the sample. These pores, especially the large pores, are detrimental to the elongation of the alloys after T6 heat treatment. Here, in the current work, the assessment of solution time and temperature was developed via the combination of maximum size and area fraction of the pores, which were analysed from OM images at low magnification. From the analysis, it can be concluded that the prolonged time or increased temperature during solution treatment is detrimental for mitigating the pore expansion. The optimised solution treatment parameters of Al-Si-Mg-Mn alloys in the current study were found to be either 480 °C for 60 min or 540 °C for 10 min.

The solution heat treatment conditions (e.g. time and temperature) also affect the disintegration of eutectic phases and dissolution of primary eutectic Si and Mg_2Si phases, which is beneficial for good fracture elongation. It is reported that finer eutectic phases and higher solution temperature can shorten the solution treatment time. The disintegration time of Si or Mg_2Si can be described as [22]

$$t_{max} = \frac{32\pi^2}{9} \cdot \frac{kT}{D_s \gamma} \cdot \left(\frac{\rho}{\varphi}\right)^4 \cdot ln\frac{\rho}{\varphi} \qquad 5\text{-}1$$

where

t_{max} — disintegration time

D_s — the diffusion coefficient of Si or Mg_2Si

γ — the interfacial energy

T — the solution treatment temperature

φ — atomic diameter

ρ — the diameter of eutectic phases

It can be found that the particle size, solution temperature and diffusion coefficient have a great influence on the disintegration time. Based on calculations from equation 5-1, the disintegration time of alloys B and C under solution temperature 540 °C was

estimated to be less than 10 min. Similar results were found by Zhang, who reported that 540 °C for 1.5 min is able to fragment the Si and 5 min at 540 °C can lead to the spheriodisation of Si and the growth of Si [201]. Moreover, the solution at 540 °C for 10 min can dissolve a certain amount of Mg_2Si into the matrix, leading to a higher concentration of Mg and Si, which is similar to the results in [233]. Here, Rometsch has calculated the diffusion and homogenisation time of Mg_2Si coefficient of Mg or Si in A356 [234]. Mg_2Si with sizes below 2 μm can be dissolved at 540 °C in 3 min and homogenised in 5.1 min. Herein, the Mg_2Si present in as-cast alloys A and B has an average size below 1 μm, which was expected to require much shorter time for complete dissolution and homogenisation.

Alloy C has a finer average size of Si (0.48 μm) and Mg_2Si(0.92 μm) eutectic phases. The growth of Si or Mg_2Si can be described by Lifshitz–Slyozow–Wagner equation [205]

$$R^3 - Ro^3 = \frac{8}{9} \cdot \frac{D \cdot C_0 \gamma V^2}{R_{gas} T} t \qquad 5\text{-}2$$

where

T and t — temperature and time, respectively

R — final radius of the particle

R_0 — initial radius of the particle

R_{gas} — gas content

V — molar volume

C_0 — equilibrium concentration of structures in the matrix

D — diffusion coefficient

From this equation 5-2, the cube of final particle size (R^3) has a linear relationship to solution treatment time, at a given temperature. The growth of eutectic phases was dominated by its volume fraction, solution treatment time and temperature. It is found that the size of Si and Mg_2Si phases after solution treatment increased by 113% and 27% respectively in alloy A, while in alloy B it increased by 166% and 30%, respectively. This was induced by the different volume fraction of eutectic phases in alloy B and alloy C, and the composition of alloy B have more Si and Mg content.

π-AlFeSiMg phase ($Al_8Mg_3FeSi_6$) is usually formed on the surface of β-Fe (Al_5FeSi) in Al-Si-Mg (A356 or A357) alloys and increasing Mg leads to the formation of more π-AlFeSiMg phase, due to the peritectic reaction [235]. Moreover, the π-AlFeSiMg phase

is unstable, and after solution treatment at 540 °C, the Mg and Si in π-AlFeSiMg phases are dissolved and β-Fe (Al_5FeSi) forms [233]. It was also reported that in Al-Si-Mg alloys, π-AlFeSiMg and β-Fe remain unchanged after solution treatment at 540 °C for 5 min, and further 15 min solution treatment can lead to an overall reduction of volume fraction π-AlFeSiMg phase [228]. However, as discussed in Chapter 4, the iron-containing intermetallics in the alloys under as-cast state are α1-AlFeMnSi and π-AlFeMnSiMg, which forms before initial eutectic and at the final quaternary eutectic reaction, respectively. All the π-AlFeMnSiMg phase transforms into α2-AlFeMnSi under solution treatment at 540 °C for 10 min. The reason for this is that the HPDC process is a non-equilibrium solidification process [236] with a fast cooling rate of 500-1000 K/s. Therefore π-AlFeMnSiMg forms during the final quaternary eutectic reaction, which occurs in the small interdendritic regions with high thermal and constitutional undercooling [193]. Thus, the π-AlFeMnSiMg is the metastable phase with a composition different from the equilibrium state. After solution treatment at high temperature, the Mg and Si were easily dissolved into the matrix, and because Mn or Fe have very low solubility in aluminium, the Fe and Mn remain in the intermetallics. As a result, it transforms into nano-scale α2-AlFeMnSi phase, which consisted of only four elements including Al, Mn, Fe and Si.

It is commonly known that the precipitation sequence in Al-Si-Mg alloys is SSS→GP→β''→β'→β-Mg_2Si [237]. The peak ageing time of 10 hours at 170 °C was found in alloy B, and alloy C. Similar results were found by Sjölander et al. [238] that The peak ageing time of Al-Si-Mg alloys is 10 hours at 170 °C and 0.3 hours at 210 °C. In the first 20 min, the increment of hardness is very slow, because of the poor hardening effect of GP zones [110]. After that, there is a dramatic increase of hardness, due to the nucleation and rapid growth of coherent β'' [239]. Further ageing treatment (>10 hours) leads to the dissolution of small precipitates and the transformation of β'' to semi-coherent β' or even β-Mg_2Si precipitates which make a lower contribution of strength [110,240].

5.3.2 Relationship between the microstructure and mechanical properties

The mechanical properties of the alloys were mainly influenced by the grain size of α-Al, volume fraction and size distribution of eutectic phases, casting defects and precipitates. The yield stress can be described as [241]

$$\sigma_{YS} = \Delta\sigma_i + \Delta\sigma_{GB} + \Delta\sigma_{eutectic} + \Delta\sigma_{ss} + \Delta\sigma_{ppt} \quad 5\text{-}3$$

where

$\Delta\sigma_i$ — intrinsic strength

$\Delta\sigma_{GB}$ — grain boundary strengthening

$\Delta\sigma_{eutectic}$ — eutectic phases (volume fraction, morphology and size distribution)

$\Delta\sigma_{ss}$ — solute solution strengthening

$\Delta\sigma_{ppt}$ — precipitation hardening

In the current work, the solidification condition of the alloys is similar, having high cooling rate. The fine α-Al grains ($\Delta\sigma_{GB}$) and less coarsening eutectic phases (Si or Mg_2Si) ($\Delta\sigma_{eutectic}$) that forms during the short solution treatment is beneficial for the yield strength of the alloys, based on Hall-Petch mechanism [242] and Orowan dislocation bowing mechanism [243]. The smaller Si particles or Mg_2Si associated with decreased particle spacing, lead to higher yield strength. Moreover, the yield strength of alloy B is 15 MPa higher than that of alloy C. The precipitation hardening ($\Delta\sigma_{ppt}$) of these two alloys are similar, which can be identified from TEM images and increment of ageing hardness. The main microstructure difference between the two alloys is the volume fraction of eutectic Si and Mg_2Si ($\Delta\sigma_{eutectic}$), and similar results were found by Lados et al [244]. The T6 with short solution treatment can provide high number density of coherent needle-like β'' ($\Delta\sigma_{ppt}$), which has a higher resistance to dislocation movement than semi-coherent β' or non-coherent β, as suggested by Ahmadi et al [245]. The casting defects have little influence on the yield stress, but they affect the elongation significantly [223]. The elongation of the alloys after T6 is slightly higher than that of as-cast state and there are several factors influencing the elongation. Firstly, the short solution treatment can minimise porosity expansion and dimension stability. Secondly, the eutectic phases Si and Mg_2Si were spheroidized after the short solution treatment. Especially, the large needle-like π-AlFeMnMgSi phase, which is brittle and acts as crack initiation in the as-cast state [17], transform into nano-scale α2-AlFeMnSi particles. Lastly, the coherent smaller β'', which is usually achieved at a relatively lower ageing temperature and shorter time (below 12 hours), lead to the less sacrificing of elongation [112].

5.4 Conclusion

(1) The new T6 heat treatment (short solution treatment at 540 °C for 10 min and ageing at 170 °C for 10 hours) has been developed for the Al-Si-Mg-Mn alloys. The high yield strength of 334±6 MPa and ultimate tensile stress of 391±5 MPa

were achieved in the Al5Si2Mg0.5Mn0.5Fe(wt%) alloy with the good elongation of 4.6±0.5%.

(2) No apparent porosity expansion was found under the solution treatment at 540 °C for 10 min or at 480 °C for 90 min. But the prolonged solution time and increased solution temperature can cause porosity expansion.

(3) The π-AlFeMnSiMg phase transformed completely into the nanoscale α2-AlFeMnSiphase with a BCC crystal structure at 540 °C for 10 min, although it was reported that it transforms to β-Fe with longer solution treatment time in some other commerical Al-Si-Mg alloys.

(4) Solution temperature has significant effects on peak ageing hardening; the highest peak ageing hardness can be obtained when the samples were solution treated at 540 °C for 10 min.

(5) After peak ageing treatment, a large number of coherent β″ precipitates were formed in the Al matrix with needle-like morphology and a size of 30-60 nm. They are responsible for excellent strength enhancement in this alloy.

Chapter 6 Development of Al-Cu-Si-Mg die-cast alloys

6.1 Introduction

This chapter is concerned with the studies of the as-solidified microstructure and properties of Al-Cu-Si-Mg quaternary eutectic and hypoeutectic alloys produced by suction casting and HPDC processes respectively using a combination of SEM, TEM, XRD, DSC, compression and tensile testing methods. SEM-EBSD/TKD methods were used to determine the orientation relationship between eutectic phases derived from the inverse pole figures (IPF) analysis. The effect of copper content on the microstructure and mechanical properties of hypoeutectic quaternary alloys was studied to establish the optimum strength and ductility properties.

6.2 CALPHAD modelling of quaternary Al-Cu-Si-Mg alloys

The initial experiment is focused on the understanding of the as-solidified microstructure of Al-Cu-Si-Mg quaternary eutectic system. The equilibrium phase diagrams of quaternary Al-Cu-Si-Mg are referred in [246]. From the phase diagrams, it can be seen that there are three quaternary eutectic reactions, as shown in Fig. 6-1. They are L→Al+Al_8Mg_5+Mg_2Si+$AlCuMg_4$ (E1), L→Al+Al_2CuMg+Mg_2Si+Al_2Cu (E2) and L→Al+Si+Al_2Cu+Q($Al_5Cu_2Mg_8Si_7$) (E3). The compositions of E1, E2 and E3 are Al-2.15Cu-0.07Si-33.11Mg (wt%), Al-31.6Cu-0.9Si-7.2Mg(wt%) and Al-28Cu-6Si-2.2Mg(wt%), respectively [246,247]. E3 eutectic reaction was chosen for this study because of the ease of castability by avoiding an excessive amount of Mg.

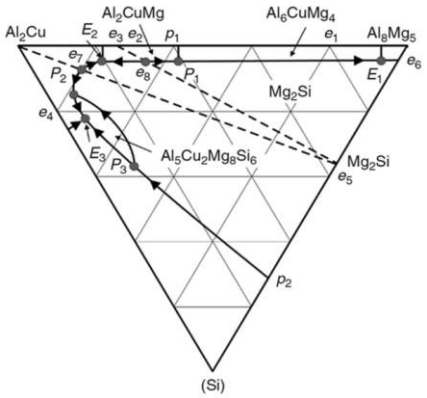

Fig. 6-1 Liquidus projection of Al-Cu-Mg-Si alloy system [248]

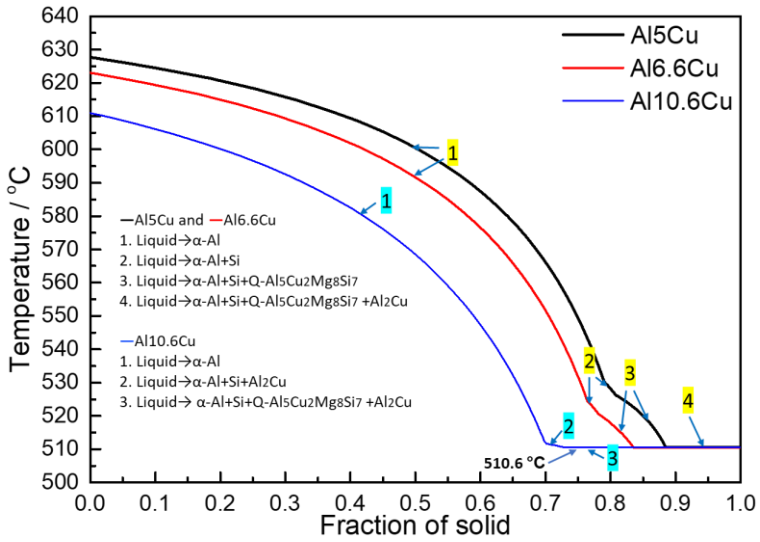

Fig. 6-2 Simulated solidification path of die-cast quaternary Al-Cu-Si-Mg alloys predicted by Pandat 8.5

Table 6-1 The predicted compositions of hypoeutectic alloys in the current study

Alloy Name	Alloy Compositions (wt%)			
	Al	Cu	Mg	Si
Al5Cu	Balance	5	1.1	2.2
Al6.6Cu	Balance	6.6	1.1	2.2
Al10.6Cu	Balance	10.6	1.1	2.2

Three quaternary hypoeutectic alloys were then designed for high pressure die casting process based on quaternary Al-Cu-Si-Mg eutectic composition (E3). Fig.6-2 shows the simulated solidification path of quaternary Al-Cu-Si-Mg hypoeutectic alloys with 20%, 25% and 30% eutectic mixture based on Scheil solidification description. The predicted compositions of the alloys with various eutectic solid fractions are shown in Table 6-1, and the three alloys were named Al5Cu, Al6.6Cu and Al10.6Cu, respectively. There are only three reactions in Al10.6Cu alloy, which are Liquid→α-Al, minor Liquid→α-Al+Si+Al_2Cu, and final Liquid→α-Al+Si+Al_2Cu+$Al_5Cu_2Mg_8Si_6$(Q) at 510.6 °C. In terms of Al5Cu and Al6.6Cu alloys, the binary and ternary eutectic reactions were observed (Liquid→α-Al+Si and Liquid→α-Al+Si+$Al_5Cu_2Mg_8Si_7$), following the reaction (Liquid→α-Al). The three alloys have all the same final quaternary reaction at 510.6 °C. The fraction of each eutectic reaction and their reaction temperature are summarised in Table 6-2. Because of die soldering during HPDC process and the formation of needle-like β-Al_5FeSi, minor Mn (0.5 wt%) and Fe (0.1 wt%) were added into the alloys [24,166]. The measured compositions of the three alloys are shown in Table 6-3.

Table 6-2 Simulated results showing temperature of formation and fraction of solid for each eutectic reaction

	Fraction of Solid	Temp. (°C)	Phase
Al5Cu	0	627.66	Liquid+α-Al
	0.79	530.24	Liquid+α-Al+Si
	0.81	526.29	Liquid+α-Al+Si+$Al_5Cu_2Mg_8Si_6$
	0.89	510.57	Liquid+α-Al+Si+$Al_5Cu_2Mg_8Si_6$+Al_2Cu
	1	510.57	α-Al+Si+$Al_5Cu_2Mg_8Si_6$+Al_2Cu
Al6.6Cu	0	623	Liquid+α-Al
	0.76	524.5	Liquid+α-Al+Si
	0.78	520.56	Liquid+α-Al+Si+$Al_5Cu_2Mg_8Si_6$
	0.84	510.57	Liquid+α-Al+Si+$Al_5Cu_2Mg_8Si_6$+Al_2Cu
	1	510.57	α-Al+Si+$Al_5Cu_2Mg_8Si_6$+Al_2Cu
Al10.6Cu	0	610.97	Liquid+α-Al
	0.701	511.66	Liquid+α-Al+Si+Al_2Cu
	0.719	510.57	Liquid+α-Al+Si+$Al_5Cu_2Mg_8Si_6$+Al_2Cu
	1	510.57	α-Al+Si+$Al_5Cu_2Mg_8Si_6$+Al_2Cu

Table 6-3 The measured compositions of the Al-Cu-Si-Mg die-cast alloys

Alloy Name	Solid fraction of eutectic mixture	Alloy composition (wt.%)					
		Al	Cu	Si	Mg	Mn	Fe
Al5Cu	~0.2	Balance	4.90	2.43	1.13	0.45	0.16
Al6.6Cu	~0.25	Balance	6.73	2.35	1.14	0.44	0.14
Al10.6Cu	~0.3	Balance	10.75	2.32	1.15	0.48	0.15

6.3 Microstructure of as-cast quaternary Al-Cu-Si-Mg alloys

6.3.1 Microstructure of quaternary Al-Cu-Si-Mg eutectic alloy

Fig.6-3(a) shows the XRD spectrum of as-cast sample. The quaternary eutectic alloy consisted of four crystalline phases, which corresponded to α-Al, Si, Al_2Cu and $Al_4Cu_2Mg_8Si_7$ (Q). The XRD result agreed with phases observed in the quaternary Al-Cu-Si-Mg eutectic alloy processed by directional solidification method [246]. Fig.6-3 (b) shows a DSC trace of quaternary alloy obtained after the heating cycle. Only one endothermic DSC peak was observed, and the onset and peak temperature were found to be 509 °C and 553 °C, respectively. This corresponds to a quaternary eutectic

reaction, which is close to the eutectic melting temperature of quaternary Al-Cu-Si-Mg eutectic, according to the equilibrium phase diagram [249]. The enthalpy of fusion(ΔH) was determined to be 209 J/g. This low melting point is favourable for the castability. Fig.6-3 (c) shows the microstructure of quaternary Al-Cu-Si-Mg alloy, which was taken from transverse section of the 3mm diameter suction cast rod at half-length. It can be seen that the quaternary eutectic alloy consisted of a bimodal microstructure, composing of lamellar eutectic cellular colonies with sizes of 5-10 μm and a fine anomalous eutectic mixture within the intercellular region. An inset in Fig.6-3 (c) shows anomalous eutectic mixture within the intercellular region taken at high magnification. It can be found that the anomalous eutectic region consisted of several eutectic phases but was devoid of any lamellar or fibrous eutectic structure. This suggests a decoupled growth of eutectic phases towards the end of the solidification process. Moreover, the sizes of Al_2Cu and α-Al phases increased from 90-150 nm in the centre of the cell to 500-800 nm at the edge of the cell. Fig.6-3 (d) shows SEM micrograph of the cellular eutectic structure, together with a composition profile taken from the centre of a cell to the intercellular region, as indicated by the black line. There was a build-up of Si content and a drop in Cu content within the anomalous eutectic region, as compared to those in the centre of the cell.

Fig.6-4 (a) shows bright-field TEM image of both cell boundary and intercellular regions of quaternary eutectic alloy taken at low magnification. It can be seen that cell boundaries are separated by a fine anomalous eutectic region. The size of Al_2Cu lamella at the cell boundary had a range of 300nm to 800 nm, which is comparable to size derived from SEM image in Fig.6-3 (c). Fig 6-4(b) shows a bright-field TEM image taken from the cell boundary at high magnification. Four phases (e.g. α-Al, Si, Al_2Cu and Q) were found to co-exist together, where α-Al and Al_2Cu phases show irregular lamellae together with fibrous Q phase and a small fraction of Si phase. The fibrous Q phase with dimensions of 100nm-150nm width and 300-500 nm length attached to the Al_2Cu lamella. Only a few Si phases exist in the cell boundary, which are trapped between Q and Al_2Cu phases. Fig.6-4 (c) shows the SADPs of α-Al, Si, Q and Al_2Cu, corresponded to <1 0 0>, <0 0 1>, <1 1 $\bar{2}$ 9> and <1 1 0> zone axes, respectively.

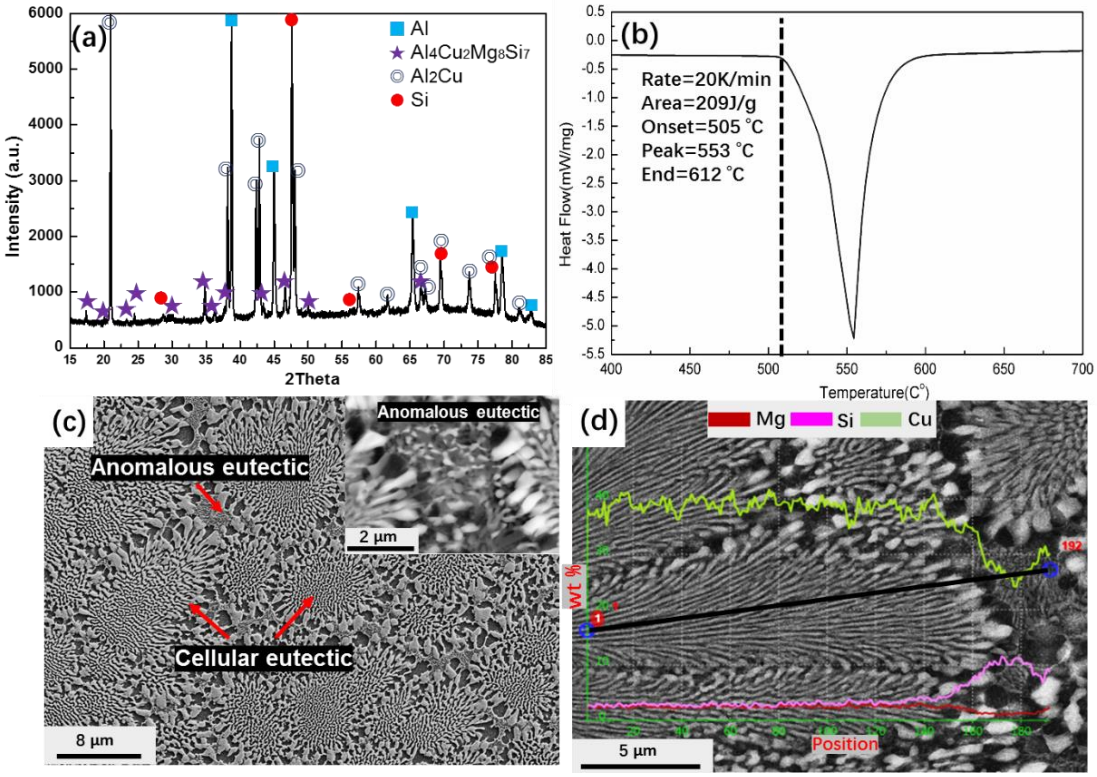

Fig.6-3 (a) XRD spectrum of quaternary eutectic alloy (b) DSC curve of quaternary eutectic alloy with a heating rate of 20 k/min (c) Secondary electron SEM images showing bimodal eutectic microstructure and inserted SEM backscattered image of anomalous eutectic region under larger magnification and (d) the eutectic cellular structure with EDX line scan from the centre of cell to intercellular region

Fig.6-4 (d) and (e) display bright-field TEM image and EELS maps of the anomalous eutectic region, respectively. Four phases (α-Al, Si, Al_2Cu and Q) also co-existed together within the anomalous eutectic region. The α-Al, Si and Al_2Cu phases exhibit an equiaxed morphology, while the Q phase has a platelet appearance. The size of Si and Al_2Cu were found to be 40-90 nm, 50-100 nm, respectively. However, the width of the Q phase was less than 100 nm, and its length was found to be 100-250 nm.

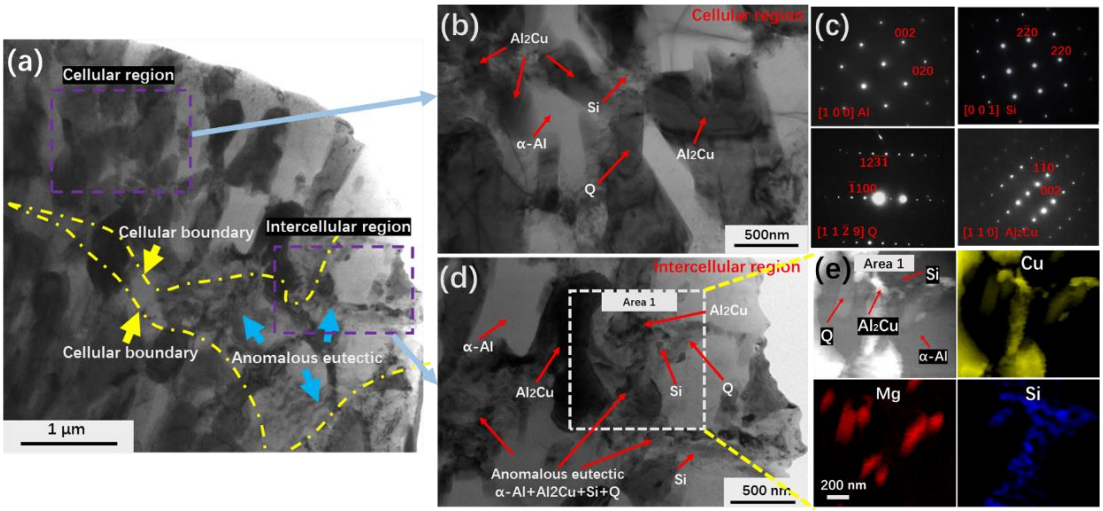

Fig.6-4 (a) TEM bright-field image taken at a low magnification showing cell boundary and intercellular regions, (b) magnified TEM bright-field image of eutectic cell boundary region and (c) corresponding SADPs, (d) magnified TEM bright-field image of the intercellular region and (e) STEM-HAADF image with EELS maps of Cu, Mg and Si

Fig.6-5 (a) shows a typical eutectic colony, which was taken from the sample prepared by FIB. Fig.6-5 (b) shows the inverse pole figure (IPF) taken from the centre of a cellular colony. The average confidence index (CI) of each point for building up the IPF figure is above 0.5. It is reported that the above CI is sufficient to index an orientation 95% of the time [250]. The identified phases from TKD include Al_2Cu, α-Al and Q phases, corresponding to previous TEM results. The average diameter of Q phases was found to be ~100 nm. In addition, the α-Al and Al_2Cu lamellar structure appeared more regular in the centre of the colony with an interlamellar spacing of 160 nm. The identified common planes and directions are shown in Fig.6-5 (c). The common directions of Al_2Cu, α-Al and Q phases were found to be $[120]_{Al2Cu}$, $[110]_{Al}$ and $[0001]_{Q}$. The common planes were found to be $(121)_{Al2Cu}$, $(111)_{Al}$ and $(31\bar{4}0)_{Q}$.

The inverse pole figure (IPF) taken from the cell boundary are shown in Fig.6-6 (b). The same types of phases, including Al_2Cu, α-Al and Q were identified at the cell boundary. The sizes of Q increased to ~200 nm in the cell boundary. The lamellar α-Al and Al_2Cu structure appeared irregular as compared with those at the centre of the cell. The pole figures of Al_2Cu, α-Al and Q phases in the cell boundary are shown in Fig.6-6 (c). The common planes of Al and Al_2Cu phases were found to be the same as those in the centre of the cell without any misorientation. However, the Q phase has a large deviation from {0001} and $\{31\bar{4}0\}$ planes, indicating the Q phases at cellular

boundary exhibited different orientations. No orientation relationships between Q and Al_2Cu, or Q and α-Al were found in the cell boundary.

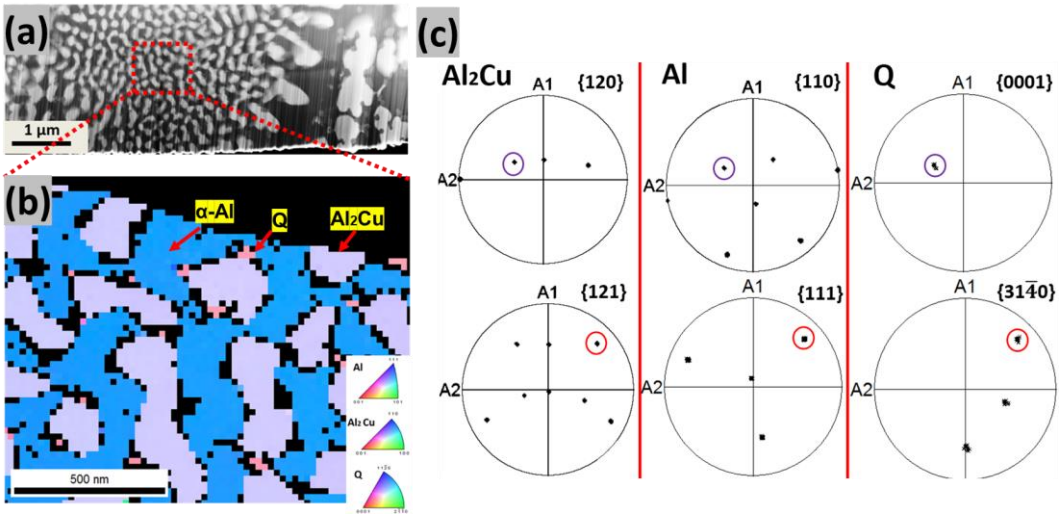

Fig.6-5 (a) SEM BSD image of the eutectic colony (b) IPF map of α-Al, Al_2Cu and Q phases from the centre of the cellular colony (c) pole figures for identification of the orientation relationship between the three phases including α-Al, Al_2Cu and Q

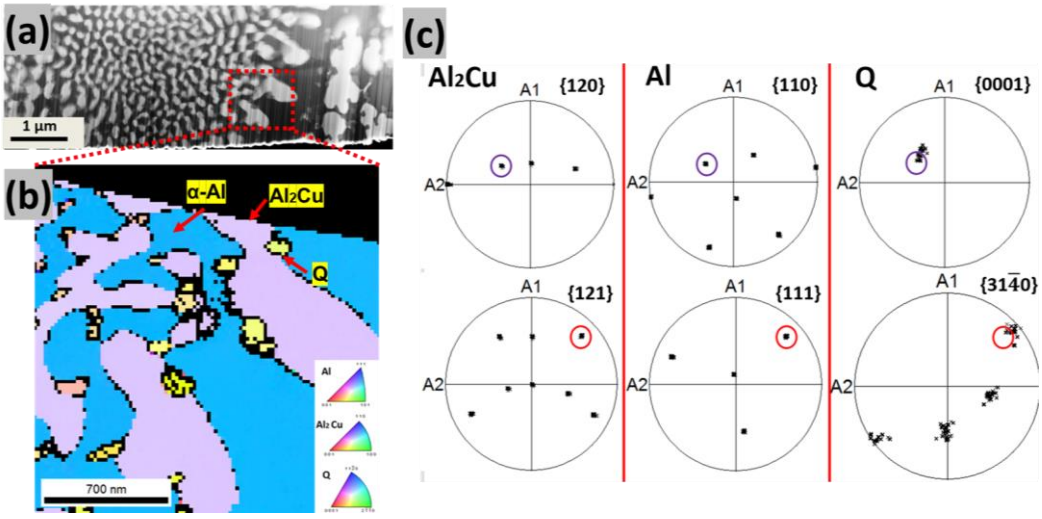

Fig.6-6 (a) SEM BSD image of the eutectic colony (b) IPF map of α-Al, Al_2Cu and Q phases at cell boundary (c) pole figures for identification of the orientation relationship between the three phases including α-Al, Al_2Cu and Q

6.3.2 Microstructure of hypoeutectic Al-Cu-Si-Mg alloys

6.3.2.1 X-Ray Diffractometry (XRD) and Differential Scanning Calorimetry (DSC) studies

Fig.6-7 (a) shows XRD spectra of these three alloys which corresponded to the equilibrium phases predicted by thermodynamic calculations. Apart from eutectic phases (α-Al, Si, Al_2Cu and $Al_5Cu_2Mg_8Si_6$), α-AlFeMnSi phase was found, due to the addition of Mn and Fe. The heating curves of these three alloys obtained by DSC are shown in Fig.6-7 (b). From the heating curves in Fig.6-7 (b), there are only two endothermic peaks in Al10.6Cu, which coincides with the melting of the quaternary eutectic mixture and primary α-Al phase. Another endothermic peaks appear in Al5Cu and Al6.6Cu following the quaternary eutectic melting peak. From the prediction in Fig.6-2, these peaks correspond to the melting of binary or ternary eutectic mixture. The temperatures at which the quaternary eutectic mixture melts for the three alloys are quite similar, at ~508 °C, as shown in the magnified inserted image in Fig.6-7 (b). The alloy is fully liquid at a temperature of Al10.6Cu is 620 °C, and in Al5Cu and Al6.6Cu, they are 629 °C and 636 °C, respectively. The experimentally determined eutectic temperatures, as well as the fully liquid temperatures, show a trend similar to that observed for the Scheil simulation result in Fig.6-2.

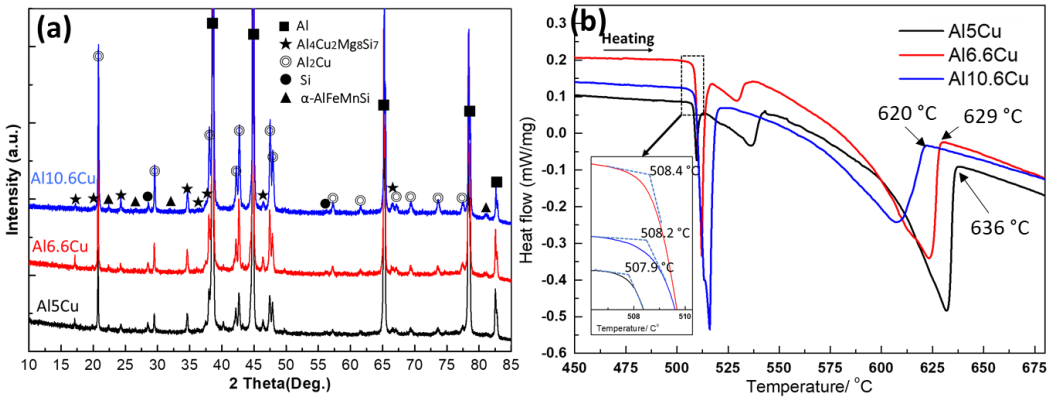

Fig.6-7 (a) XRD spectra (b) DSC heating curves of the die-cast hypoeutectic Al-Cu-Si-Mg alloys with a heating rate of 5 K/min

6.3.2.2 Scanning electron microscopy (SEM) results

Fig.6-8 (a) shows the typical microstructure of Al5Cu from the centre region of the sample. There are two types of α-Al grains labelled α1-Al and α2-Al. The α1-Al grain has a coarser size, which solidified in the shot sleeve, and finer α2-Al grain formed in

the die cavity with a much higher cooling rate [251]. Apart from Al_2Cu intermetallics at grain boundaries, there are mainly three types of eutectic structure in Al5Cu alloy shown in Fig.6-8 (a), which are called 'EU1', 'EU2' and 'EU3' regions, respectively. The microstructures of these three eutectic regions are shown in Fig.6-8 (b,c,d) taken at high magnification. From SEM image, the eutectic structure (labelled as 'Eu1') was characterised mainly to have α-Al and Al_2Cu with a lamellar spacing of 200-400nm. Another coarse eutectic structure (labelled as 'Eu2') is shown in Fig.6-8 (c), and the grey phase was identified to be $Al_5Cu_2Mg_8Si_7$(Q) phase with a lamellar spacing of 250-400nm. Fig.6-8 (d) shows the finest eutectic morphology (labelled as 'Eu3') compared with 'Eu1' and 'Eu2', indicating final quaternary eutectic reaction. The fine α-AlFeMnSi phases having a size of 0.5-3 μm were also observed at grain boundaries shown in Fig.6-8 (e). The microstructure of Al6.6Cu alloy is similar to Al5Cu, shown in Fig.6-9.

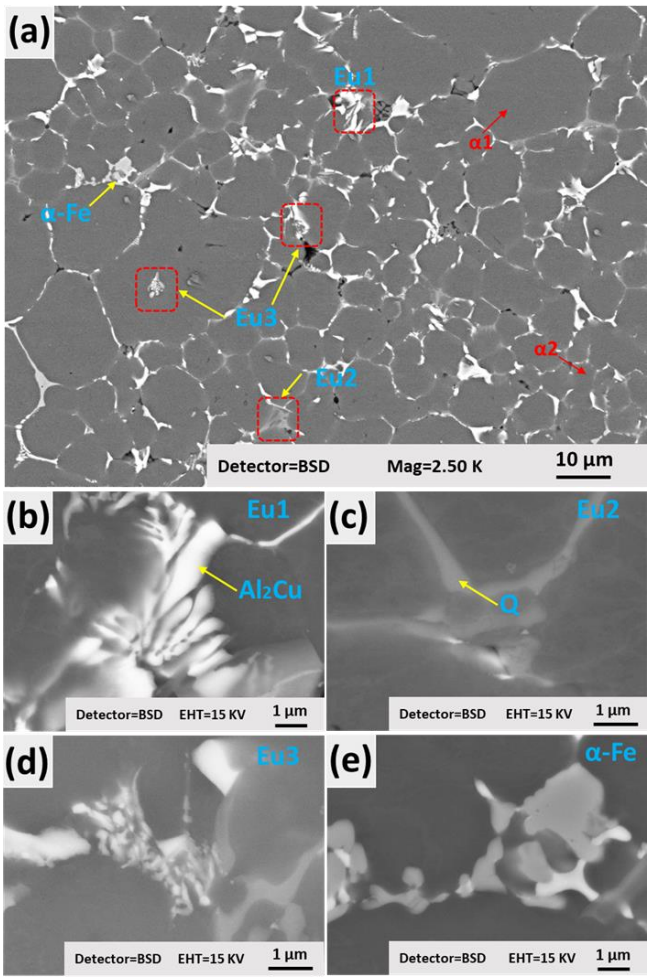

Fig.6-8 SEM Backscattered images showing (a) typical microstructure of Al5Cu taken at a low magnification (b) the microstructure of 'EU1', (c) 'EU2' and (d) 'EU3' (e) the fine compact α-AlFeMnSi intermetallics with high magnification

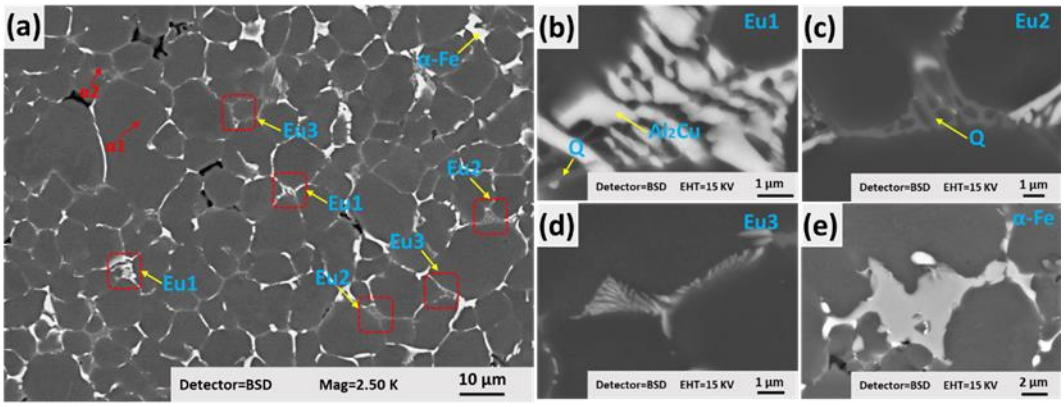

Fig.6-9 SEM Backscattered images showing (a) typical microstructure of Al6.6Cu taken at low magnification (b) the microstructure of 'EU1', (c) 'EU2' and (d) 'EU3' (e) the fine compact α-AlFeMnSi intermetallics with high magnification

Fig.6-10 (a) shows the typical microstructure of Al10.6Cu in the centre region of the sample. It can be found that the eutectic structure is more uniform. It composes of dual size of α-Al grains and ultrafine eutectic structure. The magnified image in Fig.6-10 (b) shows the structure of fine eutectic. The lamellar eutectic of α-Al-Al_2Cu was observed with an interlamellar spacing of 150-300 nm. The α-AlFeMnSi particles were observed at the boundary between the eutectic mixture and α-Al dendrites. Further characterisation with TEM of the ultrafine eutectic regions in Al10.6Cu and Al5Cu will be discussed below.

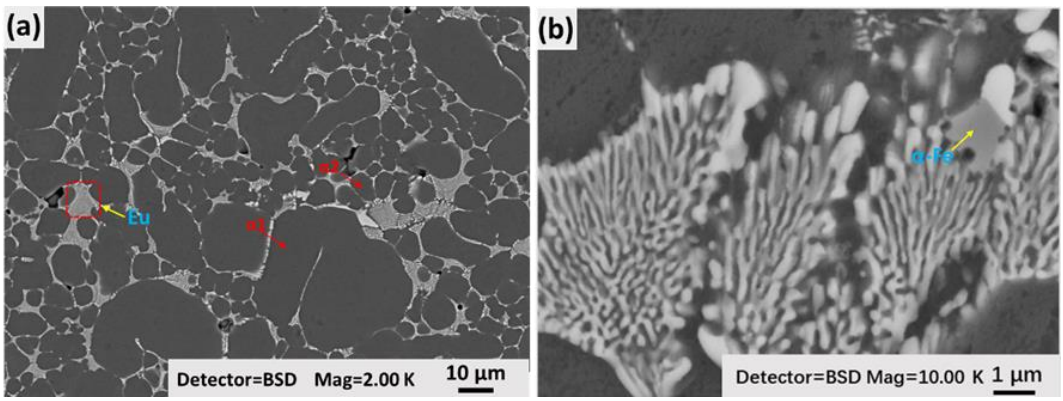

Fig.6-10 SEM Backscattered micrographs showing (a) typical microstructure of Al10.6Cu (b) the morphology of fine eutectic mixture

6.3.2.3 Electron backscatter diffraction (EBSD) studies

The grain structures of α-Al in these three alloys were obtained from EBSD analysis, in the centre region of each sample. Fig.6-11 (a-c) shows the EBSD grain-orientation in Al5Cu, Al6.6Cu and Al10.6Cu. The corresponding statistical analysis of grain size distribution and average grain size were shown in Fig.6-11 (d). The dual size distributions of α1-Al and α2-Al grain are displayed in the EBSD images. The α-Al grains show an equiaxed structure without a preferred orientation. Al10.6Cu has the finest α1 and α2 grains with an average size of 33.0 μm and 9.8 μm, respectively. The average grain sizes of α1 and α2 in Al6.6Cu are slightly finer than that of Al5Cu, which are 10.8 μm and 35.7 μm, respectively. In Al5Cu alloy, the largest sizes of α1 and α2 grains are found to be 38.8 μm and 11.0 μm.

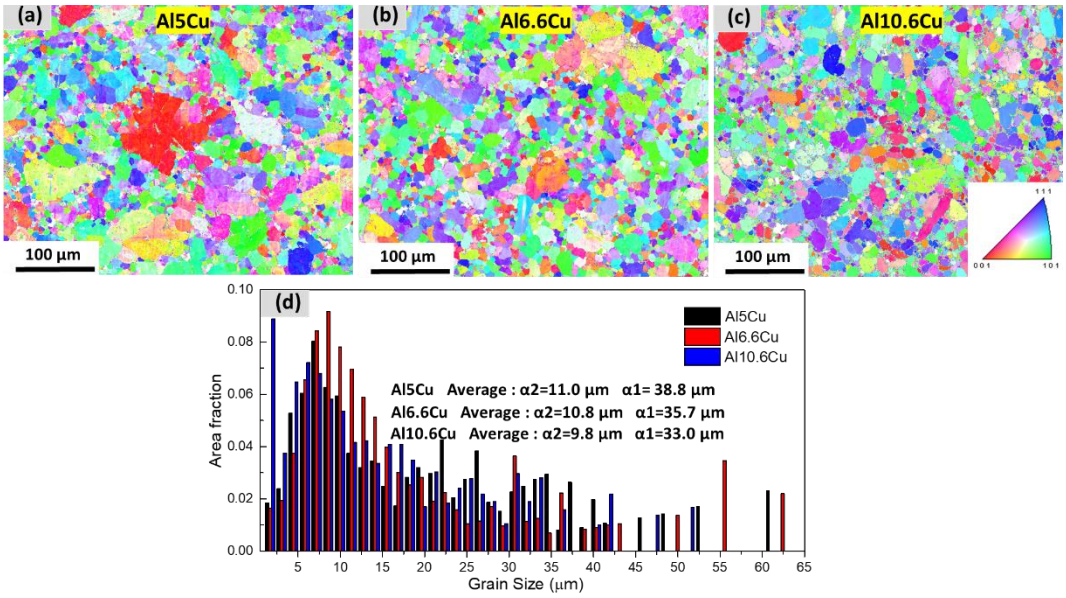

Fig.6-11 EBSD orientation map of α-Al grains in Al5Cu (a), Al6.6Cu (b), Al10.6Cu (c) and corresponding grain size distribution (d)

6.3.2.4 Transmission electron microscope (TEM) studies

Fig.6-12 shows the microstructure of the ultrafine quaternary eutectic region from Al5Cu. The ultrafine quaternary eutectic region in Al6.6Cu alloy characterised by TEM is similar to that in Al5Cu, which is not shown here. From the TEM bright-field image in Fig.6-12 (a), there are four types of phases (Al_2Cu, Si, Q and α-Al) co-existed inside this region with corresponding SADP patterns, as shown in Fig.6-12 (c-f). The HADDF-

STEM image of the region is shown in Fig.6-12 (b). It can be observed that Al_2Cu and α-Al show a lamellar structure, with a lamellar spacing of 100-250 nm, which is slightly finer than that in Al10.6Cu. Q phase (eg. what is the size) shows irregular morphology without the entrapment of Al_2Cu lamellas. Fine Si particles (eg. what is the size) were found in the ultrafine eutectic region as well, and there are no orientation relationships among these phases.

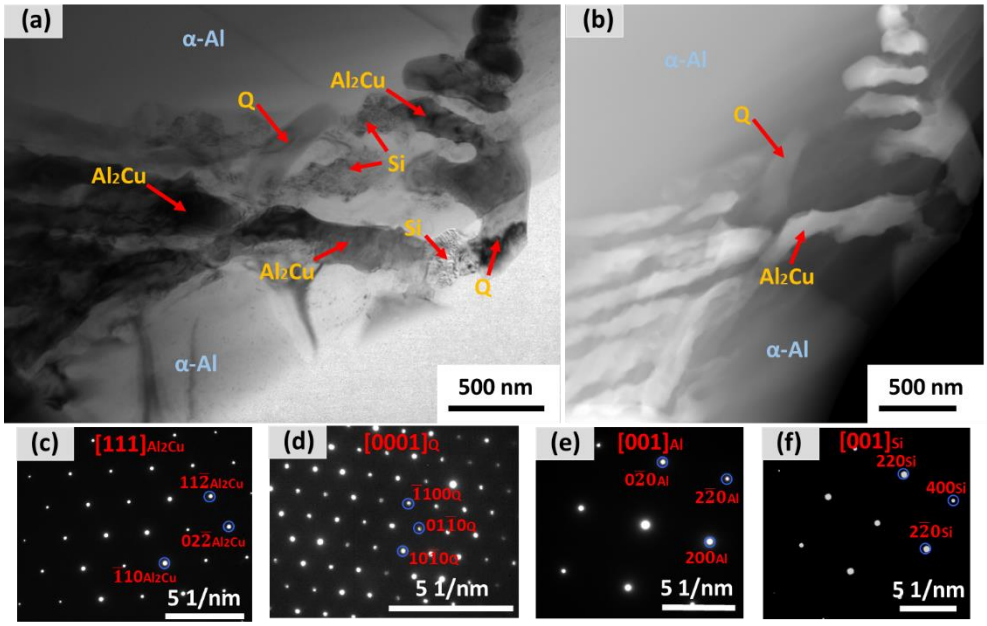

Fig.6-12 (a) TEM bright-field image (b) HAADF-STEM image showing ultrafine eutectic region in Al5Cu (c-f) SADP patterns of Al2Cu, Q, α-Al and Si

Fig.6-13 shows a TEM micrograph of Al10.6Cu taken from the ultrafine eutectic region. The TEM bright-field image shown in Fig.6-13 (a) is taken along the $[110]_{Al2Cu}$ zone axis, and the fine eutectic mixture consists of four phases (Al_2Cu, Si, Q and α-Al). The Al_2Cu and eutectic α-Al exhibits lamellar structure with a lamellar spacing between 150 to 300 nm and all Q phases attach to the lamellar Al_2Cu. There is only one particle of Si phase observed in this quaternary eutectic region, which is marked in Fig.6-13 (a). The EDX mapping of Area 1 in Fig.6-13 (a) is shown in Fig.6-13 (b). All spherical particles in Fig.6-13 (a) correspond to Q phases, and the size is in the range of 50-100 nm. The SADP patterns of Q, Al_2Cu, Si and α-Al are shown in Fig.6-13 (c-f). The 3D analysis of the morphology of eutectic phases was carried out with FIB-SEM tomography slides, as shown in the **Appendix**. From the images, the Q phase shows a fibrous morphology attaching to the Al_2Cu lamellae, while the Si phase exhibits irregular morphology with a small area fraction entrapped between the Al_2Cu lamellas.

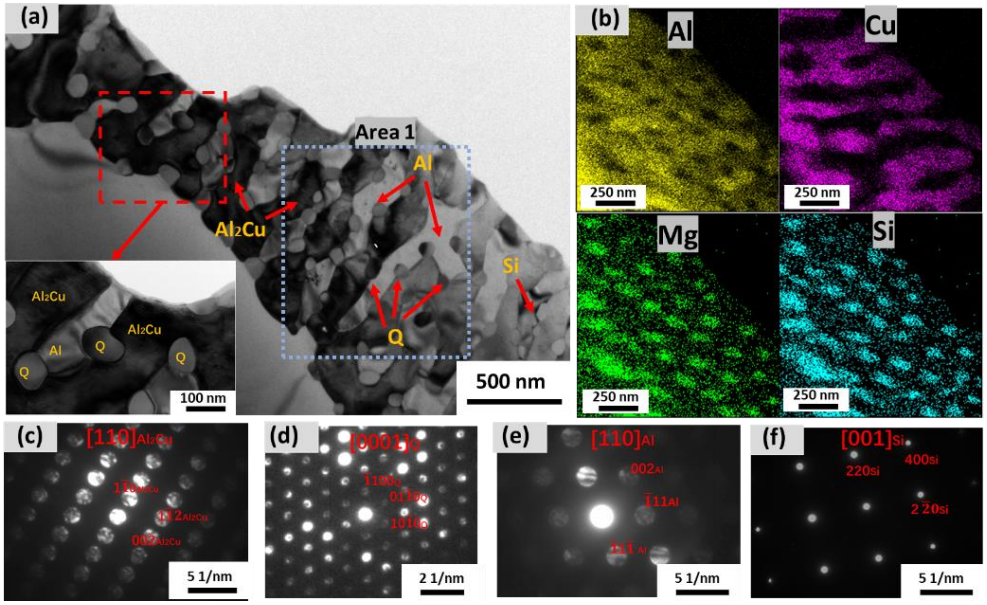

Fig.6-13 (a) TEM bright-field image with an inset of highly magnified image showing the ultrafine eutectic region in Al10.6Cu (b) corresponding EDX mapping obtained from the rectangular 'Area 1' (c-f) SADP patterns of Al_2Cu, Q, α-Al and Si phases

The orientation relationships between each of Al_2Cu, Q and α-Al phases in Al10.6Cu are determined from HRTEM images. The HRTEM images were obtained from the regions, as shown in Fig.6-13 (a). Fig.6-14 shows HRTEM images and corresponding Fast Fourier Transform (FFT), as well as one-dimensional Fourier-filtered- images of interfaces between the eutectic phases. Fig.6-14 (a) shows the interface structure between Al_2Cu and α-Al. From the corresponding FFT image in Fig.6-14 (b), the orientation relationship is $(\bar{2}20)_{Al}$~3° $from\ (00\bar{2})_{Al2Cu}$ and $[110]_{Al}//[110]_{Al2Cu}$. The HRTEM image and FFT of the interface structure between Q and α-Al are shown in Fig.6-14 (d,e), respectively. The parallel planes of Q and α-Al were identified as $(\bar{1}13)_{Al}$ and $(10\bar{1}0)_Q$ from FFT pattern. The orientation relationship of $[110]_{Al}//[0001]_Q$ and $(\bar{1}13)_{Al}//(10\bar{1}0)_Q$ was identified. The orientation relationship of Al_2Cu and Q was determined from Fig.6-14 (g) and (h). The angle between $(00\bar{2})_{Al2Cu}$ and $(\bar{1}100)_Q$ planes were found to be ~3˚ when $[110]_{Al2Cu}//[0001]_Q$. Hence, the orientation relationship of Al_2Cu, Q and α-Al was established to be:

$$\begin{cases} (\bar{2}20)_{Al}\sim 3°\ from\ (00\bar{2})_{Al2Cu},\ (\bar{1}13)_{Al}/(10\bar{1}0)_Q, (00\bar{2})_{Al2Cu}\sim 3°\ from\ (\bar{1}100)_Q \\ [110]_{Al}//[110]_{Al2Cu}//[0001]_Q \end{cases}$$

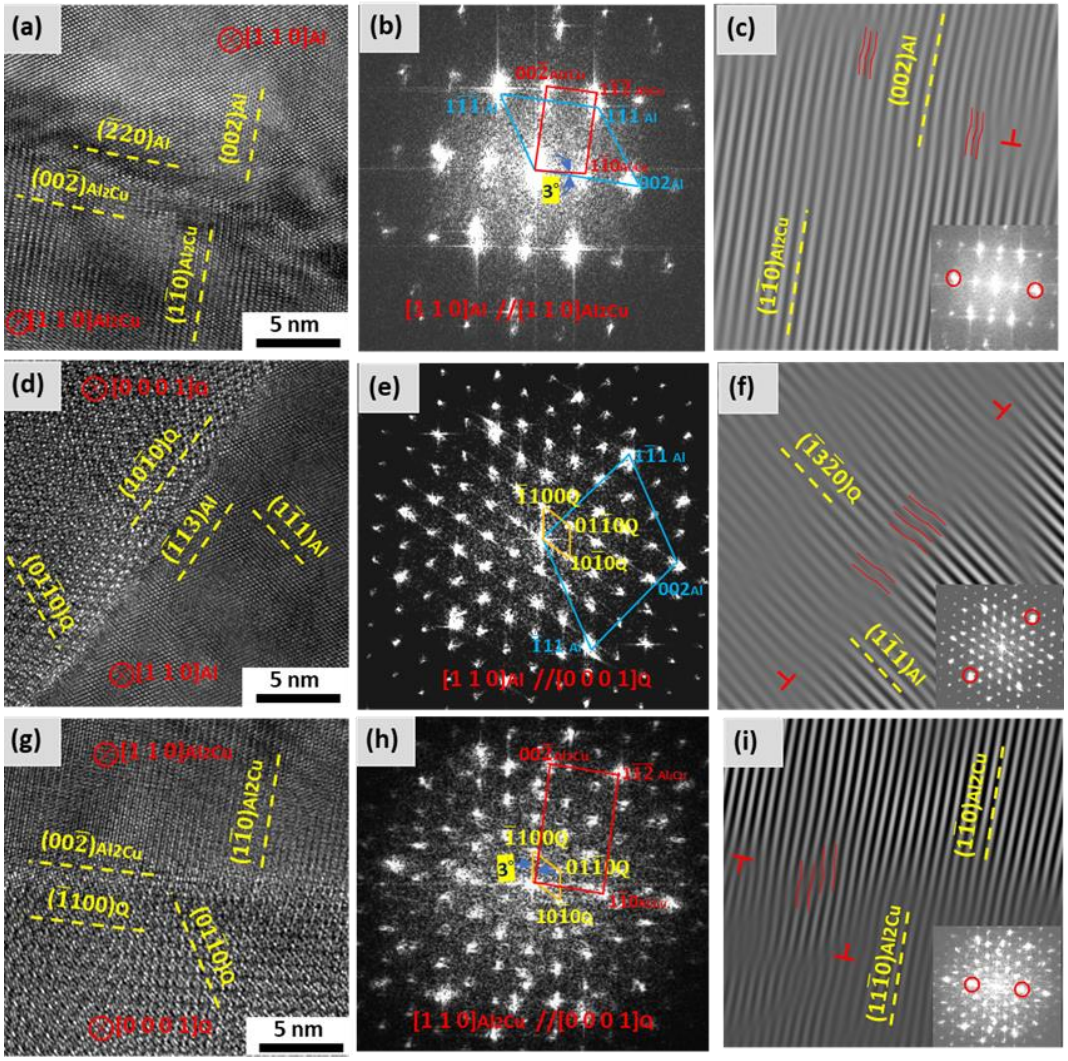

Fig.6-14 HRTEM images of Al10.6Cu showing the interface of Al and Al_2Cu, Q (a, d, g) and corresponding FFT of Al, Al_2Cu and Q (b, e, h), respectively, Fourier filtered images of the interfaces between the eutectic phases(c, f, i)

Fig.6-14 (c,f,i) shows the one-dimensional Fourier-filtered images of boundaries between the eutectic phases. The presence of dislocations on the interfaces among these three phases were observed. Only a few dislocations were found between α-Al and Al_2Cu interface, which indicates a coherent interface. Such interfaces are very stable and cannot be modified easily. However, more distortions between Q and Al_2Cu, α-Al and Q interfaces were observed, giving more edge and screw dislocations co-exist.

6.4 Mechanical properties of quaternary Al-Cu-Si-Mg alloys

6.4.1 Compression properties of quaternary Al-Cu-Si-Mg eutectic alloy

Fig.6-15 shows the typical compressive stress-strain curve of the quaternary alloy with a strain rate of $1x10^{-3}$ s^{-1}. The alloy exhibits excellent compressive properties. The fracture stress, yield stress and compressive strain were found to be ~1036 MPa, ~900 MPa and ~4.7%, respectively. An inset in Fig.6-15 shows the fractured sample after compression test. It can be seen that the maximum shear plane is inclined to the load direction by approximately 45°.

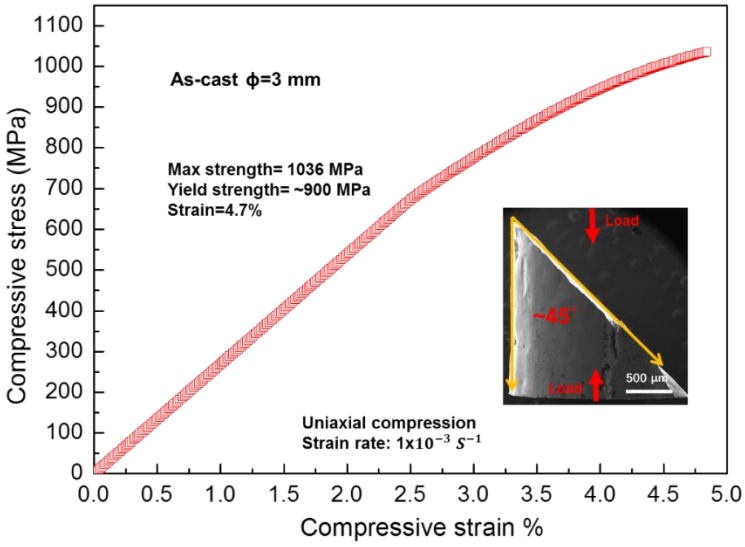

Fig.6-15 Compressive stress and strain of quaternary eutectic alloy

The fracture surface of quaternary alloy taken at low magnification is shown in Fig.6-16 (a). The shear band direction is indicated by the blue arrow. It can be seen that the fracture surface mainly comprises of flat and bumpy features, which are marked in Fig.6-16 (a). The representative regions of these two features are labelled as A and B in Fig.6-16 (a), respectively. Moreover, there are many wavy cracks which form between the two features. The magnified SEM micrographs taken from regions A and B are shown in Fig.6-16 (b,c). Fig.6-16 (b) reveals the regions of 'cup-like' concave contour with an average size of 5-10 μm that is similar to the size of eutectic cells determined from Fig.6-3 (c). It is proposed that these features are formed by the

rotational motion of the cellular colonies [128]. The microstructure of region B (Fig.6-16 (c)) contains a few wavy cracks along the boundaries of cellular colonies, indicating that the majority of the cracks in Fig.6-16 (a) are separated by the boundaries of cellular colonies. In addition, coarse Al_2Cu phase was found to fracture at the boundaries of cellular colonies, as shown in Fig.6-16 (c). This reflects that the coarse Al_2Cu phase is vulnerable to crack initiation. Meanwhile, it is clearly shown that the rotation of eutectic colonies occurs after compression deformation.

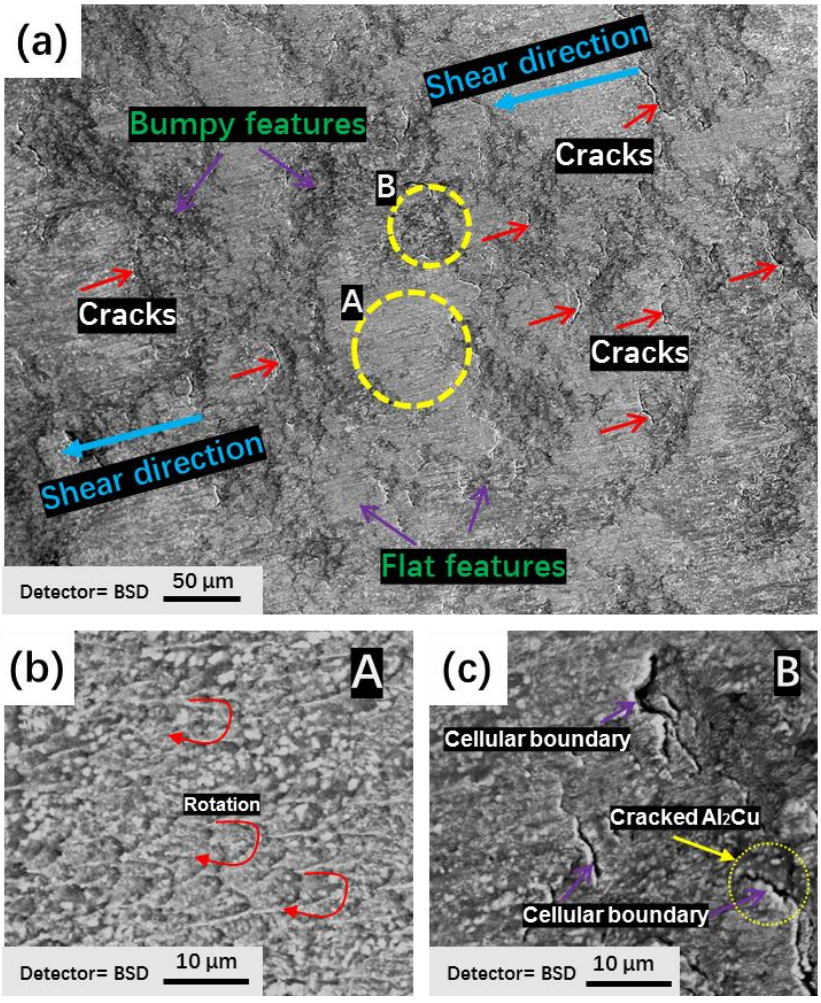

Fig.6-16 SEM backscattered images of fracture surface taken at low magnification (a), and high magnification (b,c) from regions (A, B) marked by yellow circles in (a)

To further understand the deformation of quaternary eutectic alloy, the interrupted compression with a strain of 4% was performed and the microstructure was characterised under TEM. Fig.6-17 (a) shows TEM bright-field image along $[110]_{Al}$ zone axis of α-Al lamella within one eutectic cellular colony taken at low magnification.

It can be noted from strain contrast that the orientation of α-Al is same from the centre to the boundary of the cell. A large number density of dislocation can be seen either in the eutectic cell or at the intercellular region. The nanoscale anomalous eutectic was found near cell boundaries. Fig.6-17 (b) shows the dislocations inside the cell. The dislocations were trapped inside the eutectic phases. The high magnification BF image of dislocations present in α-Al phase from anomalous eutectic and cellular eutectic regions is shown in Fig.6-17 (c). There are more dislocations present in α-Al inside the cell than α-Al inside the anomalous eutectic region. During deformation, these dislocations cannot propagate into the anomalous eutectic.

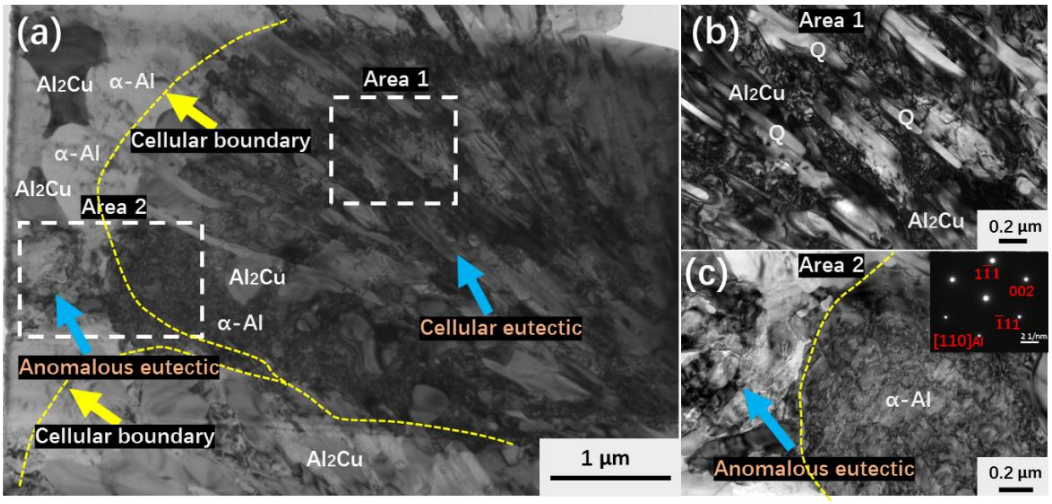

Fig.6-17 Bright-field TEM image of quaternary eutectic alloy after interrupted compression test (a) together with magnified images of cellular and intercellular regions(b,c), respectively

6.4.2 Hardness and tensile properties of hypoeutectic Al-Cu-Si-Mg alloys

Fig.6-18 shows the average hardness and area percentage of the eutectic mixture in these three alloys, measured from the edge to the centre of the mid-section of HPDC tensile sample. The area percentage of the eutectic mixture was analysed from the backscattered SEM images using ImageJ software. The centre region in each alloy has the lowest volume fraction of eutectic mixture, while the defect band region has the highest volume fraction of eutectic mixture. The cross-section of the sample with the defect band region of Al10.6Cu alloy is shown in Fig 6-18 (d). The change of the hardness with position within the cross-section in these three alloys resembles to the change in the area percentage of the eutectic mixture from the centre to the edge region. The highest average hardness in Al10.6Cu was measured to be 147 HV in the

defect band region, and the average hardness in the centre region was determined to be about 120 HV. Al5Cu alloy has the lowest average hardness of 101 HV in the centre region with the lowest area percentage of eutectic mixture of 8.9%.

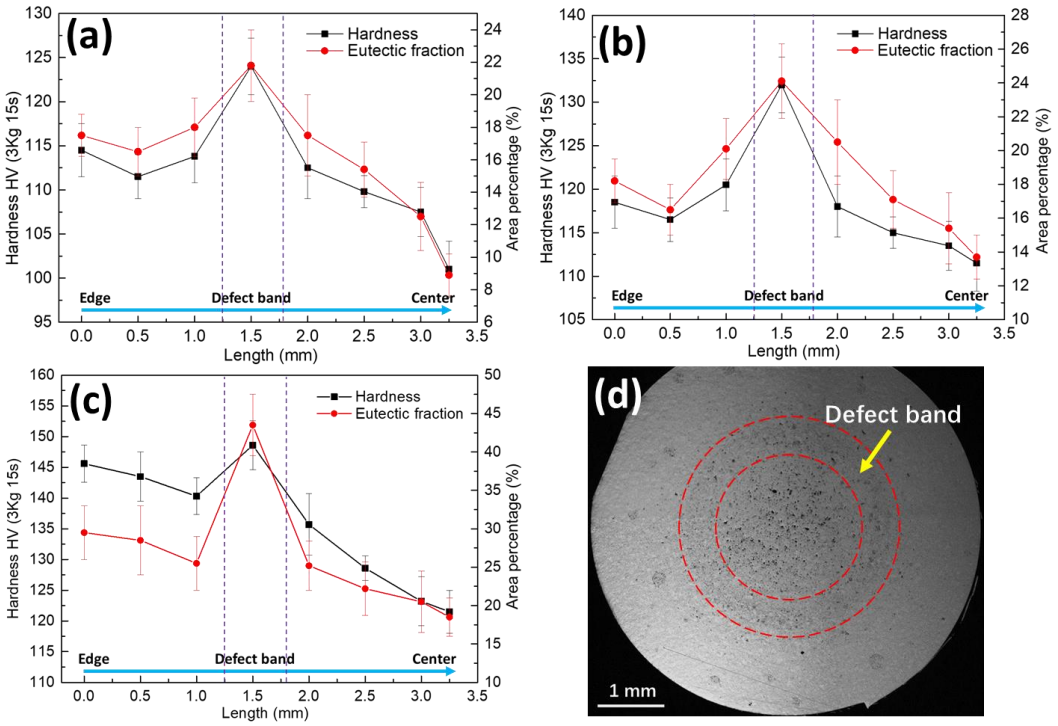

Fig.6-18 The average hardness and area percentage of eutectic mixtures from the edge to the centre of the tensile sample in: (a) Al5Cu (b) Al6.6Cu and (c) Al10.6Cu alloys; (d) cross-section of Al10.6Cu alloy showing defect band region

Fig.6-19 (a) shows tensile stress-strain curves of these three alloys with an inset showing dimensions of a standard tensile test specimen. The average tensile properties of these alloys together with some other die-cast alloys developed in recent years are shown in Table 6-4. The alloys in the current work show excellent mechanical properties. Al10.6Cu alloy has the highest yield strength of 267±5 MPa and ultimate tensile strength of 395±16 MPa, but the lowest elongation of 3.4±0.5%. Highest elongation of 7.72±1.4% was found in Al5Cu with a good yield strength of 219±3.1 MPa and ultimate tensile strength of 344.7±6.5 MPa. From Table 3, it can be found that the yield strength of most reported Al-Si and Al-Mg based die-cast alloys is below 200 MPa with elongation over 6%. Although some Al-based die-cast alloys have yield strength over 200 MPa, the elongation is near/below 2%. The mechanical properties of currently studied Al-Cu-Si-Mg based die casting alloys have yield strength over 200 MPa and good elongation which can be tailored by modification of volume fraction of eutectic mixture. Especially, the ultimate tensile strength of the reported alloys is less

than 350 MPa, while in the current alloy (Al10.6Cu) it is 395±16 MPa. The elongation as a function of yield strength is plotted in Fig.6-19 (b). The average total volume fractions of the eutectic mixture from the edge to centre in Al5Cu, Al6.6Cu and Al10.6Cu are 17.1%, 21.4% and 26.6%, respectively. It can be found that the increase of volume fraction of eutectic mixture from 21.4% in Al6.6Cu alloy to 26.6% in Al10.6Cu leads to a dramatic increase in yield strength.

Table 6-4 The mechanical properties of the recently developed die-cast alloys and the alloys in the current work

Alloy composition(wt%)		**Temper**	**Tensile Strength/MPa**	**Yield Strength /MPa**	**Elongation /%**
Al10Si1.2Cu0.8Mn [181]		As-cast	308	190	6.6
Al10Si0.4Mg0.55Fe0.2-0.85Mn [184]		As-cast	~225	~150	8-12
Al7Si0.7Mn0.3Mg [205]		As-cast	~260	~125	~10
Al9Si3Cu [197]		As-cast	~330	~140	~6
Al5.5Mg2Si0.57Mn [143]		As-cast	~320	~180	~8
Al10Mg2.8Si3.5Zn0.5Mn [192]		As-cast	~350	~250	~2.0
Al8Si3Cu1.8Zn0.86Fe [252]		As-cast	~339	~147	~5.2
Al10Si1.6Cu0.68Fe [138]		As-cast	~300	~213	~1.8
Current Work	Al5Cu	As-cast	344.7±6.5	219±3.1	7.72±1.4
	Al6.6Cu	As-cast	365±4.5	231±5.2	6.2±0.8
	Al10.6Cu	As-cast	395±16	267±5	3.4±0.5

The fracture surfaces of these three alloys are shown in Fig.6-20. From Fig.6-20, a combination of eutectic separation and cleavage fracture of large α1-Al grains as well as some porosities can be found. More eutectic separation appeared in Al10.6Cu (Fig.6-20 (c)), corresponding to the highest volume fraction of eutectic mixture. A few dimple ruptures were found in α2-Al regions in Al5Cu and Al6.6Cu, indicating the higher ductility.

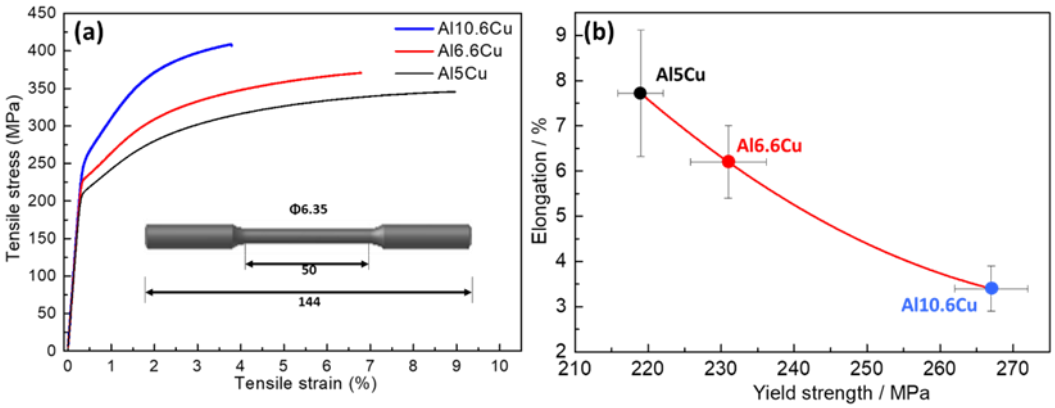

Fig.6-19 The tensile stress-strain curves of die-cast Al-Cu-Si-Mg alloys

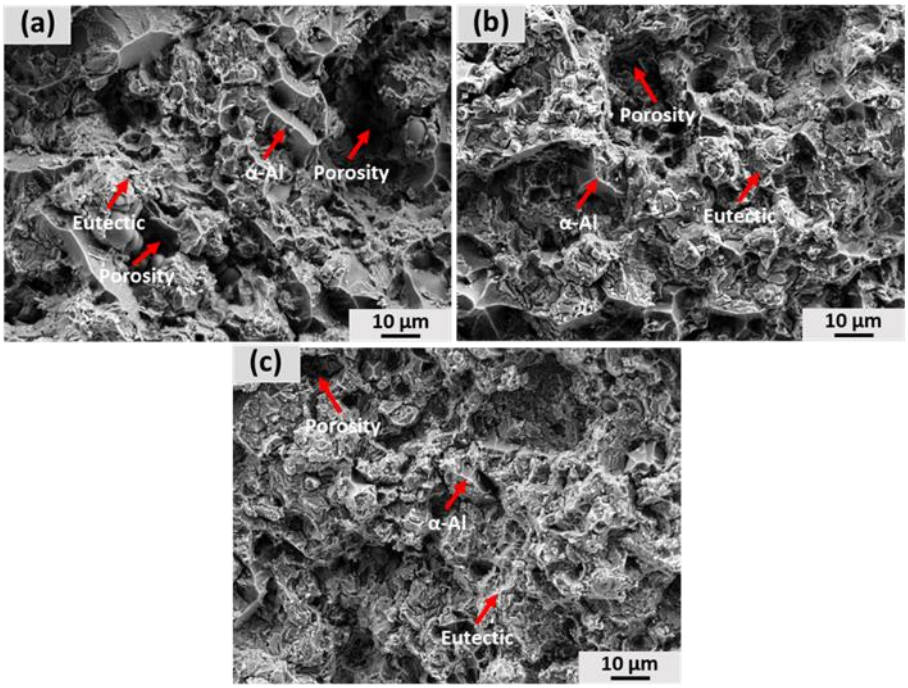

Fig.6-20 SEM micrographs showing fracture surfaces of Al5Cu (a), Al6.6Cu (b) and Al10.6Cu (c)

6.5 Discussion

6.5.1 Microstructure evolution in quaternary eutectic alloy

The solidification of eutectic alloy involves the redistribution of solute across and along the liquid/solid interface. This results in the formation of a diffusion layer ahead of solid-liquid front [88]. A short-range diffusion occurs in the highly undercooled metal-intermetallic compound eutectic system, resulting from limited diffusion under rapid solidification [253]. The lamellar eutectic growth depends on the interplay between solute diffusion and free energy. It is reported that under similar rapid solidification

condition, binary Al-Cu eutectic alloy has an interlamellar spacing of 200-300 nm, which is coarser than that of current quaternary eutectic alloy [121]. The favourable morphology of quaternary eutectic alloy is reached when each phase is in contact with other two/three phases so as to provide efficient diffusion paths in the liquid, leading to high growth rate [55,254]. Meanwhile, the α-Al and Al_2Cu lamellae in quaternary eutectic alloy both segregate Mg and Si solutes into the liquid together with the minor impurities, while they exchange Al and Cu atomic species by interlamellar diffusion. The solute rich liquid ahead of eutectic/liquid interface can lead to constitutionally undercooling [255]. The increased undercooling in the liquid ahead of solid/liquid interface affects the growth of the lamellae according to Hunt and Chilton equation, $\Delta T/\upsilon^{0.5}$ = constant, where ΔT is undercooling, υ is growth velocity. The growth rate is related to interlamellar spacing, based on Zener relationship that $\lambda^2\upsilon =$ constant [52,256], where λ is interlamellar spacing. Herein, increasing undercooling leads to increasing growth velocity, thereby resulting in the refinement of interlamellar spacing.

It is should be noted that the quaternary eutectic growth front can transform from planar to cellular morphology. Such a transformation can be explained by the solid-liquid interface stability theory [257]. The unstable eutectic growth front can lead to the development of a cellular structure, due to the presence of impurities or additional elements which change the interfacial undercooling, destabilising the solid-liquid front, resulting in the formation of cells [79,258]. Moreover, the Al_2Cu phase at the cell boundaries is much coarse. It is because the long-range solute segregation ahead of the growing solid/liquid interface can lower the solidification rate and adjust the volume fraction of the eutectic phases, leading to the development of a coarse lamellar structure on the boundaries of eutectic cells. The solutal diffusion is significantly smaller than the thermal diffusion length. Therefore, the spacing between eutectic cells is considerably larger than the lamellar spacing in the cells.

The orientation relationship is usually observed in the eutectic solidification. The orientation relationship of Al and Al_2Cu has been reported by Cantor et al. [259] to be

$$\{211\}_{Al2Cu}//\{111\}_{Al}\ and\ <120>_{Al2Cu}//<110>_{Al}$$

This orientation is usually observed in the Al-Cu alloys with various cooling rate, which is similar to those observed in the current work. The difference is that there are a lot of nanoscale Q phases adjacent to the α-Al-Al_2Cu lamellae. The orientation relationship of Al_2Cu, Q and α-Al is

$$\{211\}_{Al2Cu}//\{111\}_{Al}\ //\{31\bar{4}0\}_{Q}\ and\ <120>_{Al2Cu}//<110>_{Al}//<0001>_{Q}$$

The lattice parameters of tetragonal Al_2Cu, hexagonal Q and cubic α-Al phases are a=b=0.60671 nm and c=0.48771 nm, a=b=1.03933 nm and c=0.401736 nm, and a=b=c=0.404975 nm, respectively. The lattice parameters of Q is considerably different from Al_2Cu and α-Al. The lattice disregistries of α-Al/Q, Q/Al_2Cu and Al_2Cu/α-Al can be calculated by the method proposed by Nabarro [260], based on the TKD results in the current study. The formula can be written as follows

$$F_{x/y} = \frac{2(n_y d_x - m_x d_y)}{n_y d_x + m_x d_y} \qquad 6.5.1\text{-}1$$

Where,

$F_{x/y}$ — disregistry

d_x and d_y — d-spacing of each two eutectic phases

n_y and m_x — integers

The d-spacings of $\{211\}_{Al2Cu}$, $\{111\}_{Al,}$ and $\{31\bar{4}0\}_Q$ are 1.44164 nm, 0.701437 nm, and 0.31849 nm, respectively. It can be found that the double d-spacings of $\{111\}_{Al}$ match one d-spacing of $\{211\}_{Al2Cu}$. Therefore, n_{Al2Cu} and m_{Al} are 1 and 2, respectively. The calculated $F_{Al2Cu/Al}$ is 2.7%, meaning that the interface of α-Al and Al_2Cu is the coherent interface [261]. Similarly, the disregistry of Q and α-Al, Q and Al_2Cu were calculated to be 9.9% and 9.6%, respectively. The interfaces between Q and α-Al, Q and Al_2Cu are semicoherent interfaces [261]. The disregistries of Q and α-Al, Q and Al_2Cu are larger compared with α-Al and Al_2Cu. It should be noted that during multi-phase eutectic solidification, more interfaces generate, and the interface of each eutectic phase have different interfacial energies, following the rules that minimising the total lattice disregistry [262]. Thus, compared with binary Al-Cu eutectic alloys, the orientation remains the same in the quaternary eutectic alloy. In addition, the Q phase shows rod-like morphology between the Al_2Cu and α-Al, which has fewer interfaces, in comparison with other morphologies with similar volume fraction.

The α-Al and Al_2Cu eutectic phases continue with coupled growth from the centre to the edge of the cell. However, Q-phase initially grows in a coupled manner within the cell but changed to decoupled manner towards the cell boundary. The eutectic liquid can facilitate the coupled growth of multiple phases with various orientations at different solidification condition [263], such as additional elements or cooling rate, which affect the undercooling of the solidification. It can be observed that at the cellular boundaries, the Al_2Cu shows much coarser interlamellar spacing, indicating much lower undercooling at lateral solidification [264]. Moreover, interfaces of Q and α-Al, Q

and Al_2Cu have much higher interfacial energy. As a result, the decoupled growth occurs near the cell boundary as compared to initial coupled growth within the cell.

Lastly, the smallest solute atom in this quaternary eutectic alloy is Si, which has a very limited solid solubility in Al and dominates in the chemical segregation at the intercellular regions as compared to other solute elements. Therefore, a constitutional undercooling is expected in the intercellular region. Moreover, the regions are last solidification regions which have a higher cooling rate, owing to the positive temperature that heat can transfer through high volume fraction of lamellar structures. Therefore, high undercooling can be achieved, and the recalescence is delayed [31]. As a result, the nanoscale anomalous eutectic microstructure formed in the intercellular regions [20].

6.5.2 Microstructure evolution in quaternary hypoeutectic alloy

Solidification during HPDC process is a two-stage solidification process, which commences when the melt is poured into the shot sleeve. The relatively low temperature of the shot sleeve (250 °C) is able to cool the melt below the liquidus temperature [193]. Heterogeneous nucleation occurs in the melt and α1-Al grains formed. After passing through the narrow ingate, the fragmented or rosette α1-Al grains form. During the filling process in the die cavity, much finer α2-Al grains form, due to the high cooling rate ~1000 K/s [265]. With increase Cu content in the alloy composition, both α1-Al and α2-Al grains becomes finer. Al10.6Cu has the finest grain size, owing to the growth restriction factor that more solute in the solid/liquid front mitigates the dendritic growth as discussed in Section 4.5.1.

A defect band due to macrosegregation of alloying additions can be observed in these die-cast alloys at the location of a high area percentage of eutectic mixture. The mechanism of defect band formation was proposed by Gourlay et al. It is due to the dilatant shear bands resulting from strain instabilities of initially solidified grains [227]. In addition, the accompanied macrosegregation in the defect band region is due to the inverse segregation or exudation [266]. Thus, the highest area percentage of eutectic mixture is found in this region. The average area fraction of eutectic mixture in each alloy is a little lower than the predicted values. Apart from some reasons discussed in Section 4.5.1, the addition of minor Mn and Fe in these quaternary Al-Cu-Si-Mg alloys

can slightly affect the solid fraction of eutectic mixture, which was not considered in CALPHAD modelling.

Furthermore, the addition of Mn can suppress the formation of needle-like β-AlFeSi phase, and the small addition of Fe and high cooling rates contribute to the fine α-AlFeMnSi particles, which form prior to eutectic reactions. Most of the α-AlFeMnSi particles are distributed at the grain boundaries. The minor addition of Mn and Fe have no effects on the types of phases forming in the eutectic mixtures.

The formation of ultrafine quaternary eutectic in Al5Cu, Al6.6Cu and Al10.6Cu makes the completion of solidification in HPDC process. Al10.6Cu alloy, which was designed with quaternary hypoeutectic composition, has uniform eutectic microstructure. The decrease of Cu content can decrease the total volume fraction of eutectic mixture, and some binary or ternary eutectic structures form at high temperature with coarse morphology. The final quaternary eutectic mixture in these three alloys shows very fine microstructure. The solidification of a multi-phase quaternary eutectic mixture occurs via competitive growth and coupled/decoupled growth of eutectic phases [267]. Thus, compared with binary or ternary eutectic reactions, the diffusion in front of solid/liquid of quaternary eutectic is more complex, accompanied by high constitutional undercooling. Therefore, the lamellar thickness or spacing of multi-component eutectic alloys is usually finer than their binary counterparts.

Moreover, the coupled growth of α-Al, Q and Al_2Cu in final quaternary eutectic were found in Al10.6Cu, while in Al5Cu and Al6.6Cu, it shows different morphology without coupled growth of Q phase attached to the lamellae. There is a large variation of interfacial energy for Q/Al_2Cu and Q/α-Al interfaces, whereas the coupled growth of these three phases is very difficult and only occurs at certain undercooling. Meanwhile, the smaller interdendritic regions in Al5Cu and Al6.6Cu can lead to much higher cooling rate, which was indicated by finer lamellar spacing. It should be noted that the lamellar spacing in Al5Cu and Al6.6Cu (Fig.6-12) is finer than that in quaternary Al-Cu-Si-Mg alloy (Fig. 6-5), indicating the higher cooling rate of eutectic reaction in Al5Cu and Al6.6Cu. Consequently, the coupled growth of Q phase with α-Al and Al_2Cu disappeared from the early stage in Al5Cu and Al6.6Cu alloys.

The interfaces among α-Al, Q and Al_2Cu phases were well defined from HRTEM in Al10.6Cu. Bramfitt [261] calculated the misfit of the interfaces where lattice mismatch (δ) can be expressed as:

$$\delta = \sum_{i=1}^{3} \frac{\left|(d_{[uvw]_s^i} \cos\theta) - d_{[uvw]_n^i}\right|}{d_{[uvw]_n^i}} \times 100$$

Where $[uvw]_n^i$ is low-index direction of one phase, $[uvw]_s^i$ is low-index direction of another phase, $d_{[uvw]_s^i}$ is d-spacing along $[uvw]_s^i$ direction and $d_{[uvw]_n^i}$ is d-spacing along $[uvw]_n^i$ direction. The mismatch between the interfaces was reconstructed and simulated based on Bramfitt method. Fig.6-21 shows the atomic matching of the common planes among Al_2Cu, Q and α-Al phases. The selections of common planes and zone axis directions are based on results shown in Fig.6-14. The calculation parameters are listed in Table 6-5.

The interface between Q and Al_2Cu has the highest δ value of 7.3%, while the δ value of interface between α-Al and Al_2Cu is smallest (2.3%). Based on the authors' knowledge, this is a new orientation relationship of α-Al-Al_2Cu reported to have a coherent interface during solidification, which is different from that in binary Al-Cu or ternary Al-Cu-Ag systems [268,269]. The interfaces of Q and Al_2Cu, as well as Q and α-Al, are semi-coherent. The common interfaces usually found in the eutectic solidification, which enables to minimise the total energy of the system. The majority of interfaces are those between α-Al and Al_2Cu. The interfacial energy of Q/Al_2Cu and Q/α-Al is higher than α-Al/Al_2Cu. Firstly, the mismatch between α-Al and Al_2Cu needs to be the lowest value. The interfacial strain between Q/Al_2Cu and Q/α-Al interfaces needs to be minimised, and the orientation relationship among three phases formed based on the factors above. As a result, this unique structure formed. However, the nucleation and coupled eutectic growth mechanism of this quaternary eutectic system still need to be further systematically studied.

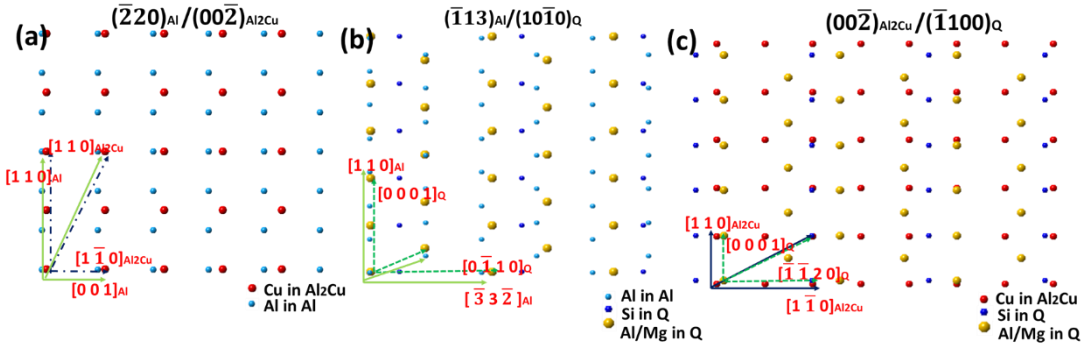

Fig.6-21 Schematic illustration of interface matching of $(\bar{2}20)_{Al}$ /$(00\bar{2})_{Al2Cu}$ (a), $(\bar{1}13)_{Al}/(10\bar{1}0)_{Q}$ (b) and $(00\bar{2})_{Al2Cu}/(\bar{1}100)_{Q}$ (c) respectively

Table 6-5 Bramfitt planar disregistry δ of Al, Al_2Cu and Q along various ORs

OR	Match planes	[uvw] Al	[uvw] Al2Cu	[uvtw] Q	θ , (°)	d[uvw]Al, nm	d[uvw]Al2Cu, nm	d[uvtw]Q, nm	δ (%)
I	$(\bar{2}20)$Al /$(00\bar{2})$Al2Cu	[1 1 0]	[1 1 0]	/	0	3x0.286	2x0.429	/	2.3
		[0 0 1]	[1 $\bar{1}$ 0]	/	0	0.405	0.429	/	
		[3 3 2]	[3 1 0]	/	1.5	0.950	0.959	/	
II	$(\bar{1}13)$Al /$(10\bar{1}0)$Q	[1 1 0]	/	[0 0 0 1]	0	3x0.286	/	2x0.402	5.8
		[$\bar{3}$ 3 2]	/	[0 $\bar{1}$ 1 0]	0	0.950	/	1.039	
		[$\bar{1}$ 2 $\bar{1}$]	/	[0 $\bar{1}$ 1 1]	7	0.496	/	0.508	
III	$(00\bar{2})$Al2Cu /$(\bar{1}100)$Q	/	[1 1 0]	[0 0 0 1]	0	/	0.429	0.402	7.3
		/	[1 $\bar{1}$ 0]	[$\overline{1\,1}$ 2 0]	0	/	2x0.429	0.789	
		/	[3 $\bar{1}$ 0]	[$\overline{3}\,\overline{3}$ 6 4]	3	/	0.959	0.885	

6.5.3 Relationship between the microstructure and the mechanical properties

6.5.3.1 The quaternary eutectic alloy

The quaternary alloy in the current study has higher compressive yield strength than some other ternary, binary alloys [58,59,121]. According to Hall-Petch equation, a fine grain size can lead to high yield strength [270]. Herein, the lamellar spacing of primary α-Al-Al_2Cu eutectic in quaternary is finer than that in Al-Cu binary or Al-Cu-Si ternary eutectic alloy [58,59]. Apart from α-Al-Al_2Cu lamellae in quaternary eutectic alloy, the presence of fine fibrous Q phases can provide additional strengthening. Thus, higher yield strength was achieved in the quaternary eutectic alloy.

It is reported that structure heterogeneity such as bimodal or multimodal eutectic is an effective approach to dissipate excessive stress via the rotation of cellular colonies [271,272]. The quaternary eutectic has a bimodal eutectic structure. At the early stage of deformation, massive dislocations were accumulated inside α-Al lamella within the cellular colonies or within the intercellular regions. Herein, the nanoscale anomalous eutectic is beneficial for the work hardening, because it can prevent the propagation of dislocation from cellular colonies into the anomalous eutectic region [58]. After further deformation, the dislocation pile-ups cause stress concentration, resulting in the generation of shear bands [127]. In the meantime, the rotational motion of cellular colonies accommodates complex plastic flows, dissipating the localisation of the shear stress [273]. Thus, a higher compressive strain can be achieved in quaternary eutectic alloy than that in Al-Cu binary eutectic alloy [121]. At the last stage of deformation, the cracks are easily initiated on the brittle coarse Al_2Cu lamella near the boundaries of

cellular colonies. Therefore, a large number of wavy cracks are observed at cellular boundaries, resulting catastrophic failure.

Although the quaternary eutectic alloy has high compressive strength, the plasticity is relatively low compared with some ternary eutectic alloys [58,59]. Further work is needed to improve its plasticity. The introduction of ductile α-Al phases and modification of nanoscale eutectic matrix such as its size, volume fraction and distribution are two effective methods to improve ductility [58,272]. Thus, the multi-component alloy concept can be tailor-made for industrial application.

6.5.3.2 The quaternary hypoeutectic alloy

The microstructure of Al-Cu-Si-Mg based hypoeutectic alloys consists of r ultrafine eutectic mixture, compact α-AlFeMnSi particles and fine α-Al grains. The fine size and morphology of α-AlFeMnSi phases with considerably low volume fraction have limited negative impact on crack initiation [184]. Moreover, the Al_2Cu phase, which is the majority intermetallic phase inside the eutectic regions, has high elasticity modulus [264] and fine lamellar spacing. Thus, a large interaction force is required for dislocation generation in the adjacent interfaces of eutectic phases [264]. In addition, some other strengthening eutectic phases such as fibrous Q and irregular Si phases with very fine morphology also contribute to the high strength of the alloys. Consequently, the alloys in the current work show more favourable mechanical properties than some other Al-based die-cast alloys.

The volume fraction of eutectic mixture plays a vital role in the elongation and strength of the alloys [274]. Okulov et al. reported that from deformation to the failure of ultrafine hypoeutectic eutectic alloys, the microstructure undergoes three stages [275]. The wave slip bands form, which is caused by dislocation pile-ups, and it is usually observed along a closed packed plane. After that, the slip bands increases and penetrate into ultrafine regions. With further deformation, some cracks form in the eutectic regions and propagate along the slip planes, resulting in final failure. With the increment of the volume fraction of eutectic mixtures, more interconnected ultrafine eutectic mixture in the alloy is able to retard the deformation of soft α-Al dendrites. Consequently, it results in excellent yield and ultimate tensile strengths, but lower elongation. Moreover, with further deformation, the dendrites cannot accommodate the stress, resulting in fast propagation of cracks along grain boundaries. The failure is through the interdendritic eutectic region.

Lastly, it can be found that the relationship between yield strength and elongation are no-linear. As shown in Fig.10 (b), the interval of volume fraction of eutectic mixture is almost the same from Al5Cu to Al10.6Cu. The increase of yield strength is much higher with a further increase in volume fraction of eutectic mixture, while the elongation is levelled over 3%. Compared with Al5Cu and Al6.6Cu, Al10.6Cu has more uniform ultrafine eutectic structure without coarse binary or ternary eutectic mixture. In the meantime, this quaternary ultrafine eutectics with fine lamellae can effectively dissipate the excessive strain in the form of multi-cracks [276]. In addition, the interfaces between α-Al and Al_2Cu are coherent, which is favourable for dislocation transmission [124]. To summerise, the approach of designing alloys with multi-phase and multi-component eutectic structures is potential for alloy development with exceptional strength.

6.6 Conclusion

(1) Quaternary Al-Cu-Si-Mg eutectic alloy was prepared by suction casting with water-cooled copper mould. The hypoeutectic Al-Cu-Si-Mg alloys with a various volume fraction of eutectic mixtures were prepared by HPDC process.

(2) The single endothermic peaks were found from DSC in quaternary eutectic alloys, and DSC curves of hypoeutectic alloys show multi-peaks, corresponding to the prediction of eutectic and hypoeutectic reactions.

(3) The microstructure of quaternary eutectic alloy shows bimodal microstructure, consisting of ultrafine cellular eutectic and nanoscaled anomalous eutectic mixture within the intercellular regions. Both cellular structure and anomalous eutectic have four types of phases, which are α-Al, Si, Al_2Cu and Q.

(4) Apart from α-Al phase, the microstructures of hypoeutectic alloys (Al5Cu and Al6.6Cu) have three types of eutectic mixtures, while Al10.6Cu hypoeutectic alloy shows almost one type of fine eutectic mixture.

(5) The coupled growth of quaternary eutectic alloy involving α-Al, Al_2Cu and Q-phase in centre of the cellular region, is found to have an orientation relationship of $\{31\bar{4}0\}_{\mathrm{Q}}$ // $\{111\}_{Al}$ // $\{211\}_{Al2Cu}$ and $< 120 >_{Al2Cu}// < 110 >_{Al}// < 0001 >_{Q}$. However, the decoupled growth of Q phase is observed at the cellular boundaries.

(6) The coupled growth of quaternary hypoeutectic alloy was studied via TEM analysis. The orientation relationship among α-Al, Al_2Cu and $Al_4Cu_2Mg_8Si_7$ (Q) phases is $[110]_{Al}$ // $[110]_{Al2Cu}$ // $[0001]_Q$ and $(\bar{2}20)_{Al}$~2° , from $(00\bar{2})_{Al2Cu}$, $(\bar{1}13)_{Al}/(10\bar{1}0)_Q$, $(00\bar{2})_{Al2Cu}$~3° from $(1\bar{1}00)_Q$. The orientation is different from that in the quaternary eutectic alloy.

(7) The excellent room temperature compressive strength and good plasticity have been achieved in quaternary Al-Cu-Si-Mg alloy, due to structural heterogeneity that contributes to strengthening via refined microstructure and the presence of multiple hard phases.

(8) The multi-component Al-Cu-Si-Mg die casting alloys with designed 20-30% ultrafine eutectic mixture show excellent yield strength of 219-267 MPa, ultimate tensile strength 344.7-395 MPa and elongation of 3.4-7.72 %.

(9) The α1-Al and α2-Al grain sizes in HPDC Al-Cu-Si-Mg alloys decreases with increasing Cu content.

(10) The defect band region has the highest volume fraction of eutectic mixtures as well as the highest hardness for a given alloy.

(11) The coupled growth of Al_2Cu, α-Al and $Al_4Cu_2Mg_8Si_7$ phases in Al10.6Cu alloy, generates coherent α-Al/Al_2Cu interface, semicoherent α-Al/Q and Al_2Cu/Q interfaces. This orientation relationship can not be found in the quaternary eutectic regions in Al5Cu and Al6.6Cu, due to different solidification condition.

Chapter 7 Heat treatment of Al-Cu-Si-Mg die-cast alloys

7.1 Introduction

This chapter is concerned with the optimisation of the solution treatment condition and the artificial ageing behaviour of quarternary Al-Cu-Si-Mg alloys. The first part is focussed on the study of heat-treated microstructure and percentage of porosity in alloys after subjected to the solution treatment at 500 °C for various holding time. The second part is concerned with the study of precipitation behaviour of the Al-Cu-Si-Mg alloys at peak ageing conditions of T5 and T6, in order to establish an understanding of the relationship between the microstructure and mechanical properties.

7.2 Effect of solution heat treatment of Al-Cu-Si-Mg die-cast alloys

The prolonged solution treatment time at a high temperature can cause unacceptable surface blistering, as discussed in Chapter 5. The increased solution temperature enables a higher peak-ageing hardness after artificial ageing. The DSC melting temperature for quaternary eutectic mixture of the Al-Cu-Mg-Si alloys is similar, which is ~508 °C, as shown in Fig. 6-7. Thus, the solution temperature of 500 °C was selected, aiming for the sufficient dissolution of Cu, Si and Mg solute elements into the matrix. All solution treated samples were quenched in water to freeze the microstructure prior to materials characterisation. Fig. 7-1 shows the microstructure of Al5Cu alloy after solution treatment at 500 °C for different holding times. Although the solution temperature is close to the quaternary eutectic temperature, no surface blistering was observed after 60 min of solution treatment. From the OM images, no apparent pore expansion was found in samples after 20 min solution treatment. After 30 min of solution treatment, some expansion of the pores appeared. The maximum size of the pore was found to be 38 μm using image analysis. Further solution treatment for 60 min, the maximum size of porosity was determined as 60 μm, and more pores were found inside the sample. After 70 min of solution treatment, large pores with a maximum size of 104 μm was found, and the surface blistering was observed (not shown here).

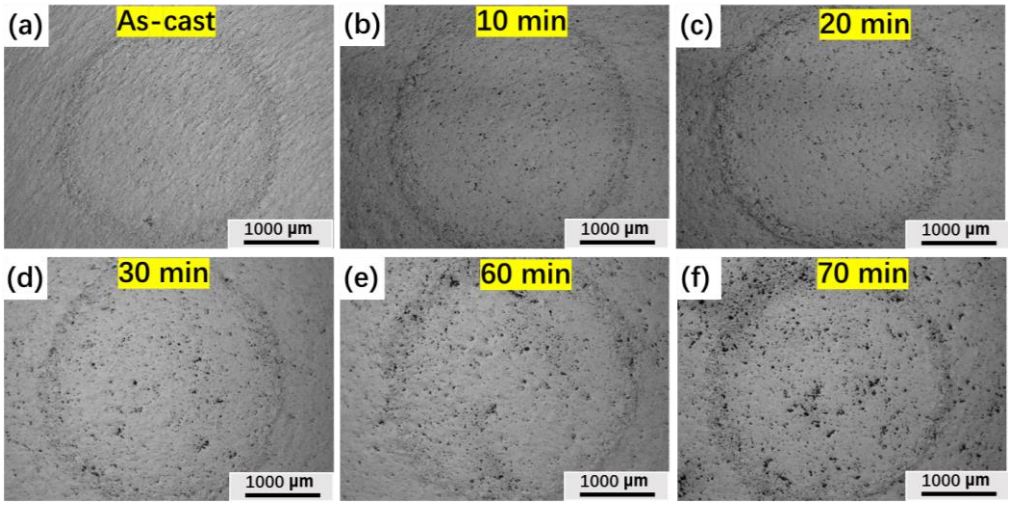

Fig.7-1 Microstructure of Al5Cu after solution treatment at 500 °C (a) as-cast/0 min (b) 10 min (c) 20 min (d) 30 min (e) 60 min (f) 70 min

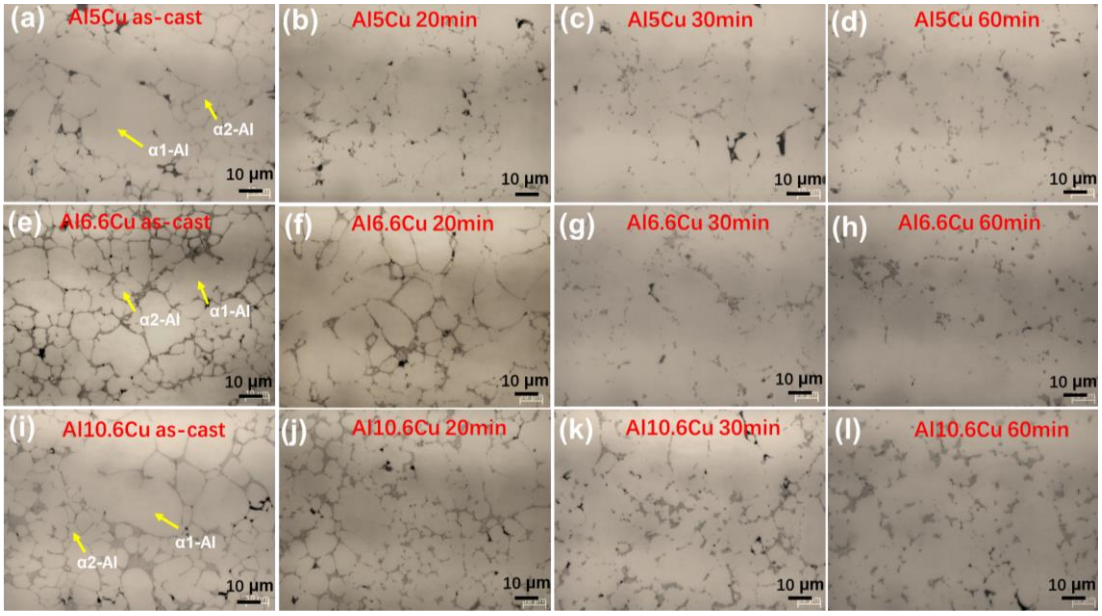

Fig.7-2 OM images showing the microstructure from as-cast sample to solution treatment at 500 °C for 60 min in Al5Cu (a-d), Al6.6Cu (e-h) and Al10.6Cu (i-l)

Table 7-1 Area percentage of porosity after solution-treatment at 500 °C for various holding times

Solution treatment at 500 °C	**Area percentage of porosity**		
	Al5Cu	Al6.6Cu	Al10.6Cu
As-cast/0 min	0.43%	0.42%	0.52%
10 min	0.5%	0.59%	0.62%
20 min	0.86%	0.82%	0.88%
30 min	1.14%	1.06%	0.98%
60 min	1.29%	1.16%	1.12%
70 min	1.83%	1.93%	2.03%

Fig. 7-1 presents the area percentages of porosity for each alloy determined from OM images. In the as-cast state, the area percentage of porosity ranges from 0.43% to 0.52% in these three alloys. A slight increase in the area percentage of porosity was found in samples heat-treated from 10 min to 60 min, while a significant increase in area percentage of porosity in samples heat-treated from 60 min to 70 min. Beyond 70 min of solution treatment, the area percentages of porosity in the alloys were found to be close or above 2%.

Fig.7-2 shows typical microstructures of these three alloys from as-cast state to solution treatment for holding time up to 60 min. For all these alloys, a similar trend in microstructural development during the solution treatment with increasing time, as observed. After 20 min of solution treatment, the microstructure consisted of α-Al grains, α-AlFeMnSi particles with slightly connected eutectic structure, and the area percentage of eutectic mixture decreased quickly as compared with that of as-cast state. No apparent coarsening of α-Al grains was found after solution treatment. After 30 min, the microstructure consisted of coarse α-Al grains with fragmented eutectic structure and spheriodised intermetallic particles. After 60 min, further coarsening of α-Al grains and intermetallic particles occurred together with a reduction in the volume fraction of intermetallic particles.

Table 7-2 SEM EDX analysis of the average chemical composition of α-Al in these alloys with various solution treatment time

Element/	**Al5Cu / Solution at 500 °C**				
(wt.%)	As-cast/0 min	10 min	20 min	30 min	60 min
Cu	0.48	1.45	2.43	2.59	2.75
Mg	1.02	0.96	0.96	0.87	0.85
Si	0.31	0.60	0.73	0.73	0.73
Element/	**Al6.6Cu / Solution at 500 °C**				
(wt.%)	As-cast/0 min	10 min	20 min	30 min	60 min
Cu	0.86	1.59	2.74	2.85	3.01
Mg	0.99	0.92	0.91	0.90	0.87
Si	0.30	0.59	0.70	0.70	0.73
Element/	**Al10.6Cu / Solution at 500 °C**				
(wt.%)	As-cast/0 min	10 min	20 min	30 min	60 min
Cu	1.41	1.88	2.97	2.99	3.21
Mg	1.10	1.07	0.87	0.88	0.86
Si	0.36	0.56	0.81	0.82	0.85

The SEM EDX analysis was used to quantify the chemical composition of the primary α-Al in these alloys. The point analysis was conducted in the centre region of each sample and (at least 30 points were measured in each alloy). Table 7-2 shows the chemical composition after solution treatment for different holding times. There was a dramatic increase in Cu and Si contents after 20 min, while the Mg content decreased slightly after solution treatment for holding time up to 60 min. The Cu and Si increased very slowly after solution treatment for holding time ranging from 20 min to 60 min in these alloys. It can be noted that in the as-cast state, the primary α-Al phase in Al5Cu and Al10.6Cu alloys contained the lowest Cu content of 0.48 wt.% and the highest Cu content of 1.41 wt.%, respectively. The Cu content of primary α-Al in Al10.6Cu was found to be the highest after solution treatment for 60 min, and the lowest content of Cu after 30 min solution treatment was found in Al5Cu alloy. There was no change in size and morphology of α-AlFeMnSi particles in these Al-Cu-Si-Mg alloys after solution treatment.

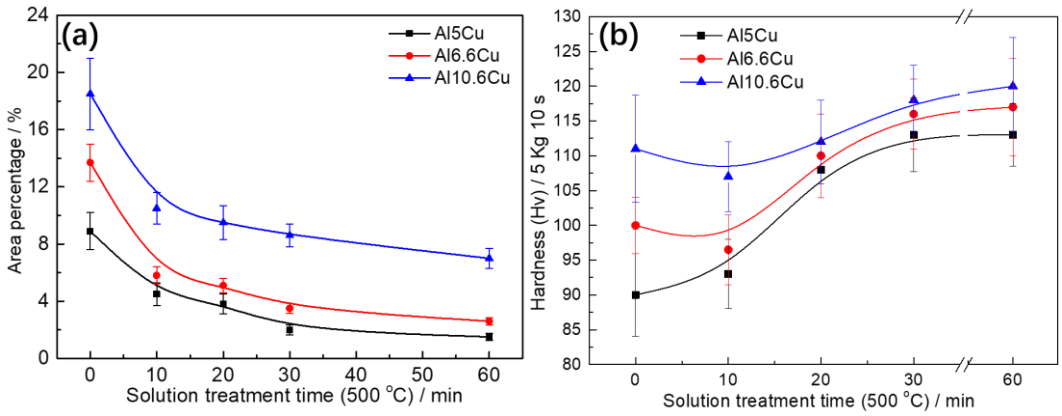

Fig.7-3 (a) Area percentage of the eutectic mixture and (b) hardness versus holding time curves of the Al-Cu-Si-Mg alloys after solution treatment at 500 °C

The image analysis was used to determine the area percentage of eutectic in these alloys. Fig. 7-3 (a) shows the area percentage of eutectic mixtures after solution treatment for various holding time. The eutectic mixture in all these alloys decreased rapidly during the first 20 min and then followed by gradual reduction with increasing time of solution treatment. The hardness of these alloys after solution treatment at 500 °C from 0 min to 60 min is shown in Fig. 7-3 (b). For the first 10 min of solution treatment at 500 °C, the hardness of Al10Cu and Al6.6Cu decreased slightly while the hardness of Al5Cu increased slightly. Further solution treatment for holding time upto 30 min, the hardness of each alloy increased with time but levelled off at 60 min.

Based on the analysis above, the solution treatment time for Al5Cu was selected to be 30 min at 500 °C, and solution treatment time for Al6.6Cu and Al10.6Cu alloys was chosen to be 60 min at 500 °C, in order to maintain a similar level of area percentage of porosity of around 1%. Thus, solution treatment of 30 min and 60 min at 500 °C was adopted, prior to subsequent artificial ageing treatment to study the age-hardening response and mechanical properties of Al5Cu, Al6.6Cu and Al10.6Cu, respectively.

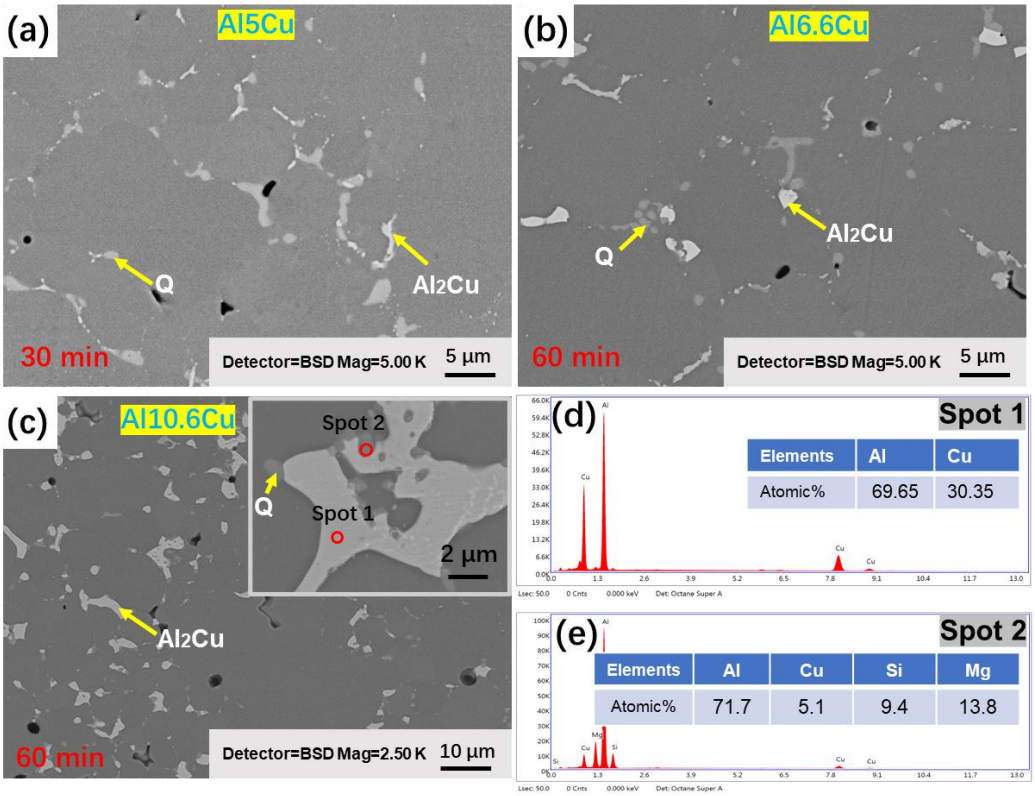

Fig.7-4 SEM back-scattered images showing the microstructure after solution treatment at 500 °C: (a) Al5Cu for 30 min; (b) Al6.6Cu for 60 min; (c) Al10.6Cu for 60 min; (d) EDX analysis of Spot 1 and (e) EDX analysis of Spot 2

Fig. 7-4 (a) shows back-scatter electron (BSE) images of the microstructure in Al5Cu alloy after solution treatment for 30 min. The images were taken from the centre of the sample. The bright and light grey phases were identified to be Al_2Cu and Q, respectively. This was confirmed by EDX analysis of Spot 1 and Spot 2 in Al10.6Cu, as shown in Fig 7-4 (d,e). The coarse Q phase distributed at the grain boundaries. The spheriodised Al_2Cu phase was observed. The microstructure of Al6.6Cu after 60 min of solution treatment is shown in Fig.7-4 (b). The Al_2Cu phase distributed at grain boundaries. The Al_2Cu particles had a size range of 1.6 µm to 0.3 µm, and Q phase is approximately 0.7-2 µm. In Al10.6Cu after 60 min solution treatment, the Q phase had a size range of 0.6 µm to 2 µm, as shown in Fig.7-4 (c). The solution treatment on these alloys led to coarsening and reduction of area percentage of Al_2Cu phase as compared with their as-cast counterparts. Apparent coarsening of α-Al primary phase in these solution treated samples were also observed. Moreover, the Q-phase was found to be embedded in the Al_2Cu lamellae, and they exhibited a size range of 300 nm to 500 nm. The morphology of Q-phase remained similar to that found in the as-cast state.

7.2.1 T5 heat treatment of Al-Cu-Si-Mg die-cast alloys

The comparison of the hardness versus time curves of hypo-eutectic Al-Cu-Si-Mg alloys after ageing treatment at 170 °C is shown in Fig. 7-5 (a). During the first 2 h, the hardness of each alloy increased significantly with time. For a longer ageing time, the hardness increased slowly and reached to a peak hardness with time. The peak-ageing time of Al10.6Cu alloy was about 10 h, but for Al5Cu and Al6.6Cu alloys, the peak-ageing time increased to 14 h. Beyond the peak-ageing time, the hardness of each alloy decreased with increasing time and reached to value of 128 HV in Al5Cu, 112 HV in Al6.6Cu and 110 HV in Al10.6Cu, respectively, after 48h ageing treatment. Fig. 7-5 (b) shows the hardness versus time curves of these three alloys aged at 210 °C. The peak-ageing times for Al5Cu and Al10.6Cu were found to be about 1.5 h and 1 h, respectively. However, the peak-ageing time for Al6.6Cu was slightly longer (about 2 h). The hardness of these alloys increased rapidly after ageing for upto 0.5 h. However, the hardness values of Al5Cu, Al6.6Cu and Al10.6Cu decreased to 110 HV, 113 HV and 120 HV, respectively after ageing for 24 h. The low ageing temperature (170 °C) condition produced higher peak hardness than the high ageing temperature (210°C) condition.

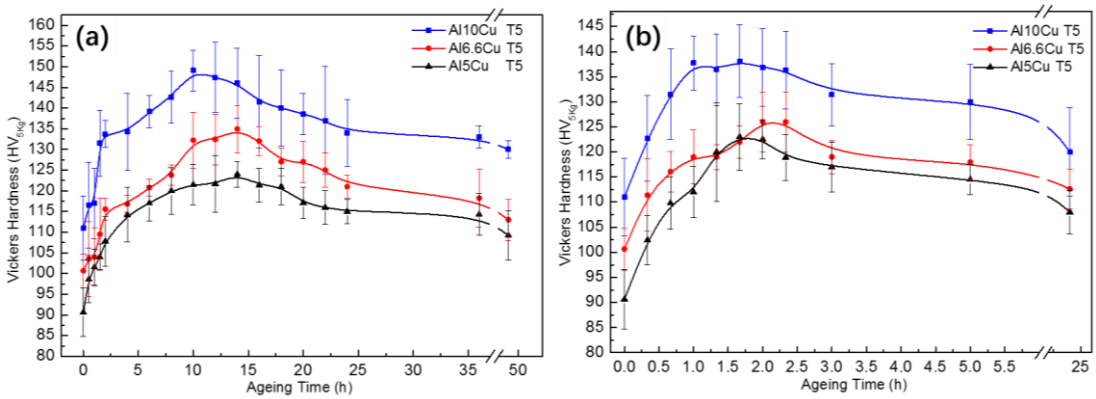

Fig.7-5 Hardness vs time curves of Al5Cu, Al6.6Cu and Al10.6Cu alloys aged at 170 °C (a) and 210 °C (b)

The TEM bright-field images and corresponding SADPs of Al5Cu, Al6.6Cu and Al10.6Cu alloys which were taken along $[001]_{Al}$ after peak ageing at 170 °C are shown in Fig. 7-6 (a,b,c), respectively. It can be seen that in Al5Cu (Fig. 7-6 (a)), there are a large number of granular-like precipitates. From the selected area electron diffraction pattern, the cruciform diffraction spots in the central positions between $(000)_{Al}$ and $(202)_{Al}$, were observed, as shown in Fig 7-6(a), indicating the existence of β'' [232].

Moreover, these rod-like precipitates with size below 5 nm were confirmed to be β'' phase by HRTEM image and its FFT, as shown in Fig.7-7 (a,b). Fig. 7-6 (b) shows precipitates in Al6.6Cu alloy heat-treated at the peak-ageing condition. Apart from some granular precipitates, more plate-like precipitates were found inside the α-Al matrix. From the HRTEM and FFT in Fig.7-7 (c,d), these plate-like precipitates corresponded to θ' phase, giving additional sets of spots in the diffraction pattern, as shown in Fig. 7-6 (b). It is reported that θ' precipitates are distributed along $(200)_{Al}$ planes [277]. The lattice parameters of the precipitates were determined as $a_{\theta'}$=0.404 nm and $c_{\theta'}$=0.58 nm, and they exhibited an orientation relationship with the α-Al according to $(200)_{Al}$|| $(002)_{\theta'}$ and $[010]_{Al}$|| $[010]_{\theta'}$, similar to those reported in the published literature [113,277,278]. Fig.7-7 (e) shows the HADDF image of the precipitates in Al6.6Cu alloy. The needle-like β'' precipitates and a few plate-like θ' are believed to be the main strengthening phases in Al6.6Cu alloy. These long and thick plate-like θ' precipitates were found with a width of ~$3c_{\theta'}$ nm and length of ~40 nm.

The TEM bright-field image of Al10.6Cu alloy heat-treated at the peak-ageing condition was shown in Fig. 7-6 (c). The peak-aged microstructure mainly consisted of granular precipitates, and plate-like phases, similar to Al6.6Cu alloy. However, the area fraction of plate-like phases was much higher than that in Al6.6Cu alloy. From the additional set of spots in the diffraction pattern, as shown in Fig. 7-6 (c) and HADDF image in Fig. 7-7 (f), these plate-like phases were identified as θ' with an average length of ~35 nm and thickness of ~3.5 $c_{\theta'}$. In addition, a bright layer on granular precipitates was observed from HADDF image (Fig. 7-7 (f)), and the precipitates were identified as Q'' with an average size of ~2 nm [117,279].

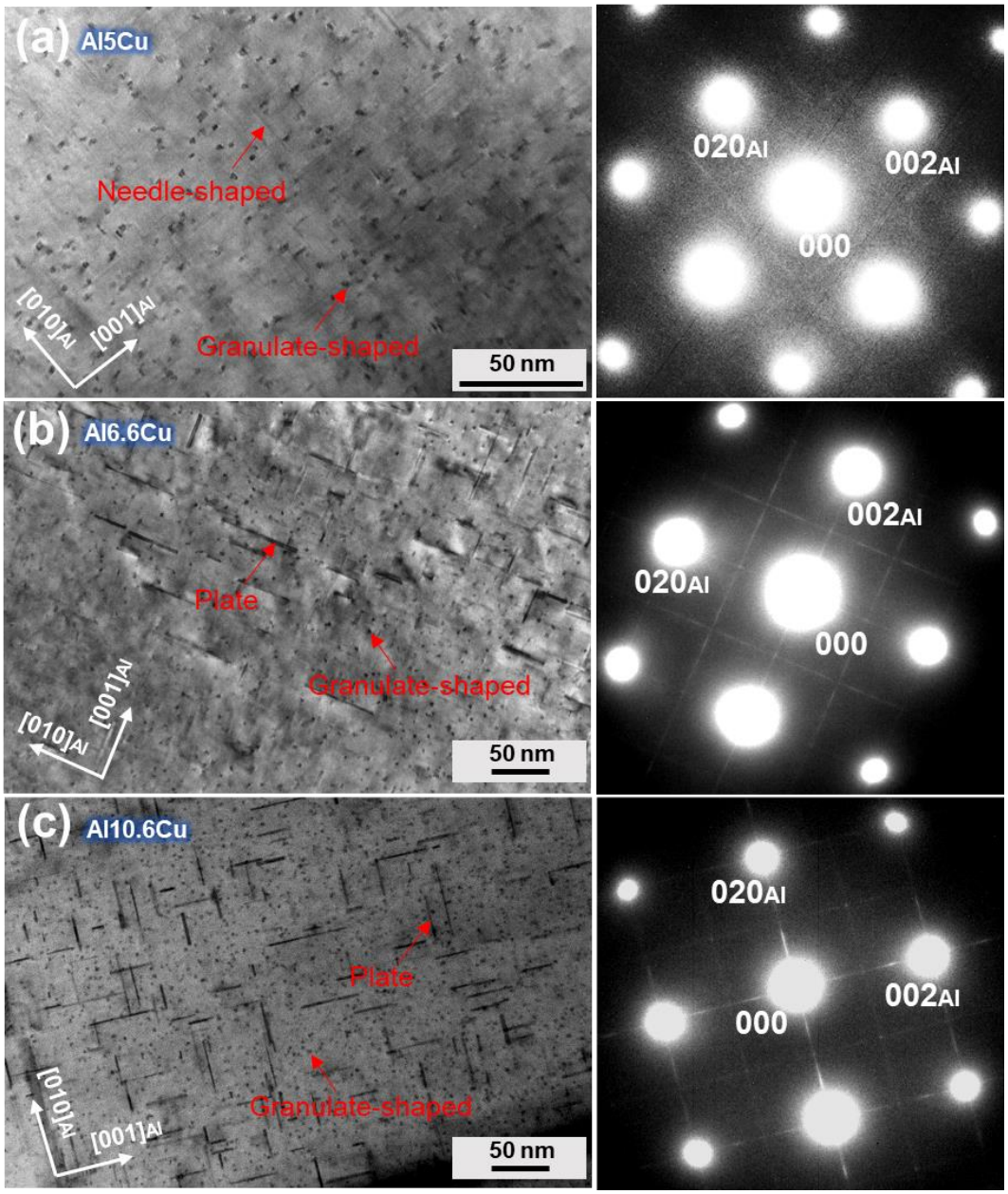

Fig. 7-6 TEM bright-field images and corresponding SADPs of Al5Cu (a), Al6.6Cu (b) and Al10.6Cu (c) after peak-ageing treatment at 170 °C

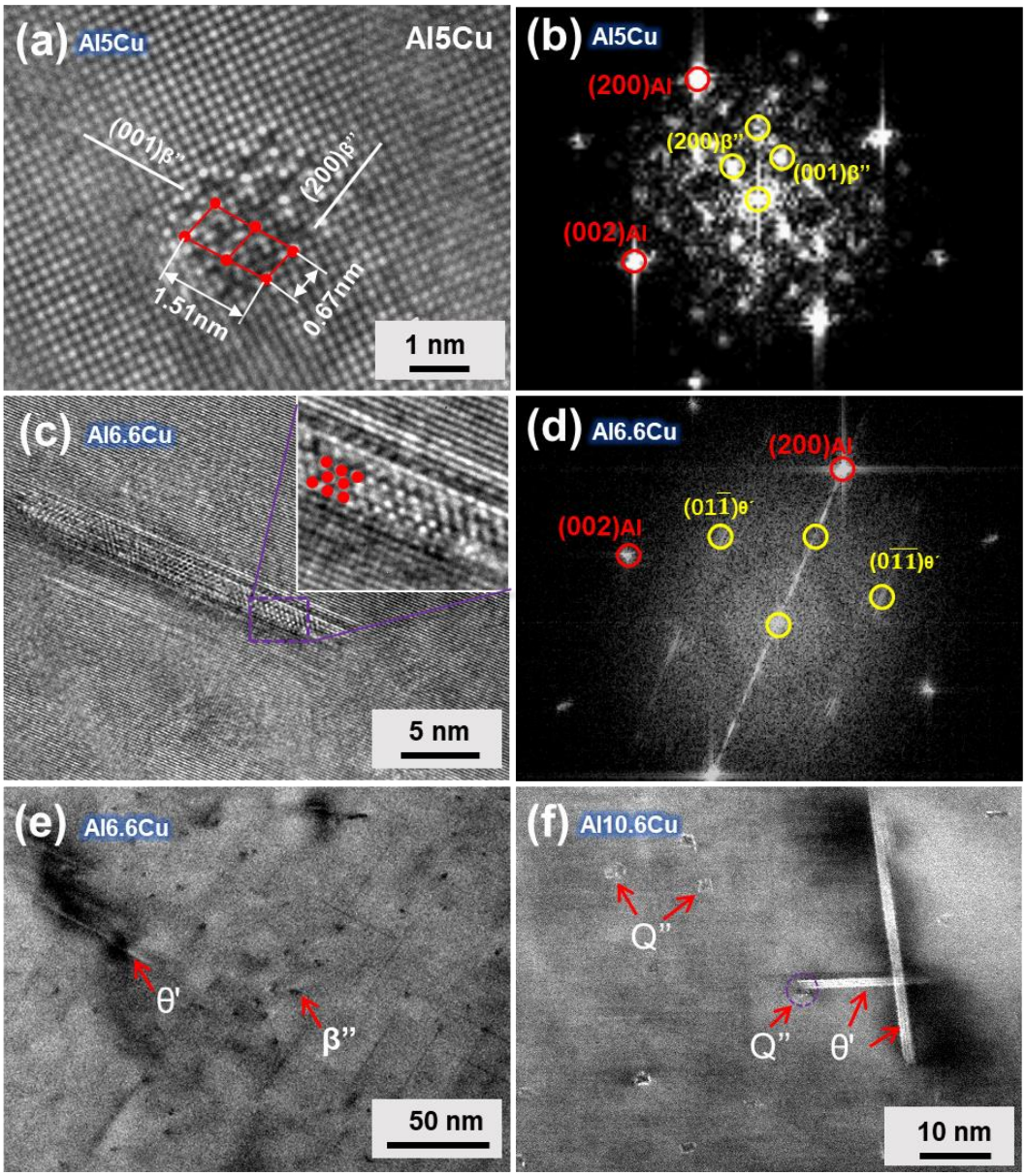

Fig. 7-7 (a) HRTEM image of β'' preciptates in Al5Cu after peak-ageing treatment at 170 °C (b) corresponding FFT; (c) HRTEM image of θ' precipitates in Al6.6Cu (d) corresponding FFT and (e) HADDF image of Al6.6Cu showing θ' and β'' precipitates after peak-ageing treatment at 170 °C; (f) HADDF image of Al10.6Cu showing coexisting of Q'' and θ' precipitates after peak-ageing treatment at 170 °C

7.2.2 T6 heat treatment of Al-Cu-Si-Mg die-cast alloys

Fig.7-8 shows the hardness versus time curves of Al5Cu, Al6.6Cu and Al10.6Cu alloys after T6 heat treatment (500 °C for 30/60 min and artificial ageing at 170 °C). The hardness of each alloy increased rapidly with increasing ageing time upto 4 h. After that, the hardness increased slightly, reaching to the peak hardness after 10h for Al5Cu 12h for Al6.6Cu and 14h for Al10.6Cu. The highest peak hardness of 155 HV was

found in Al10.6Cu. Conversely, the lowest hardness value of 143 HV was found in Al5Cu. After peak hardness was reached, the hardness decreased slowly with ageing time upto 48 h.

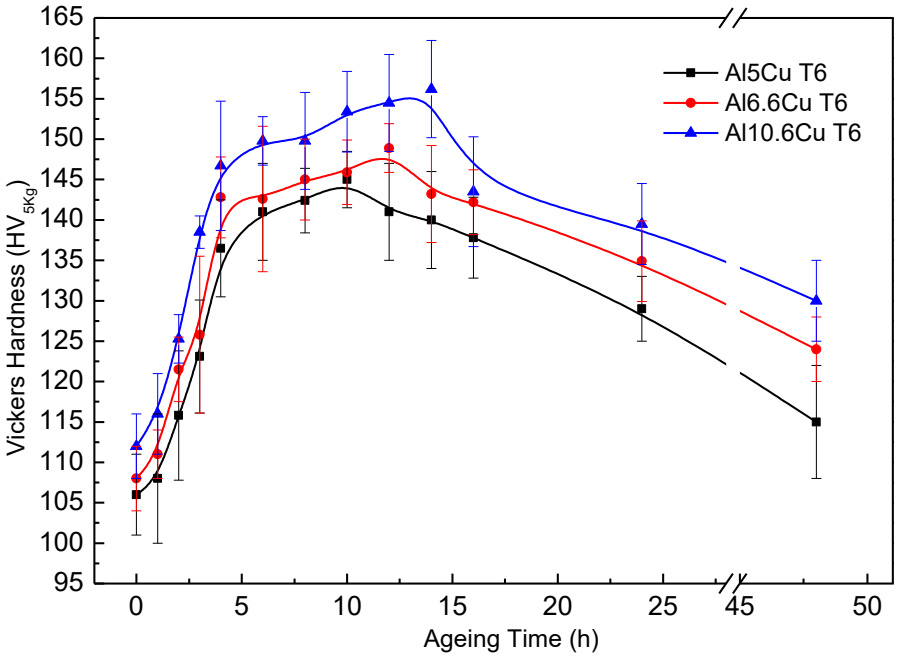

Fig. 7-8 Hardness vs time curves of Al5Cu, Al6.6Cu and Al10.6Cu alloys after solution treatment at 500 °C for 30 min (Al5Cu) or 60 min (Al6.6Cu and Al10.6Cu) followed by an artificial ageing treatment at 170 °C

Fig. 7-9 (a,c,e) show TEM bright-field images of precipitates with insets of SADPs in Al5Cu, Al6.6Cu and Al10.6Cu alloys after T6 heat treatment, respectively. The corresponding HADDF images of Al5Cu, Al6.6Cu and Al10.6Cu are shown in Fig.7-9 (b,d,f), respectively. The precipitates present in these three alloys were found to be similar. They comprised of granular Q'' and plate-like θ' densely and uniformly distributed within the α-Al matrix. From HAADF images, these θ' precipitates consisted of variable thickness, and some Q'' phase was attached to the plate-like θ' phase, thereby giving thinner and shorter morphology. The Q'' phase formed after T6 heat treatment was found to be about 1.5 nm finer than that found in T5 treatment (Fig.7-7 (f)).

The analysis of HADDF images was used to determine the area fraction and size of θ' phase. The results are shown in Table 7-3. The average thickness (i.e. 2-4.5nm) and length (i.e. 20-50nm) of θ' precipitates present in these three alloys were found to be

similar. However, the area percentage of θ’ in Al6.6Cu and Al10.6Cu was higher than that in Al5Cu.

Table 7-3 The average thickness, length and area percentage of θ’ precipitates

	Thickness of θ’ in the number of $C_{\theta'}$	**Length of θ’**	**Area percentage of θ’**
Al5Cu	3.40±1.4 $C_{\theta'}$	31±12.6 nm	5.93±1.6%
Al6.6Cu	3.34±1 $C_{\theta'}$	35±14 nm	7.02±1.4%
Al10.6Cu	3.23±1.2 $C_{\theta'}$	33.4±10 nm	7.12±1.2%

$C_{\theta'}$= 0.58 nm

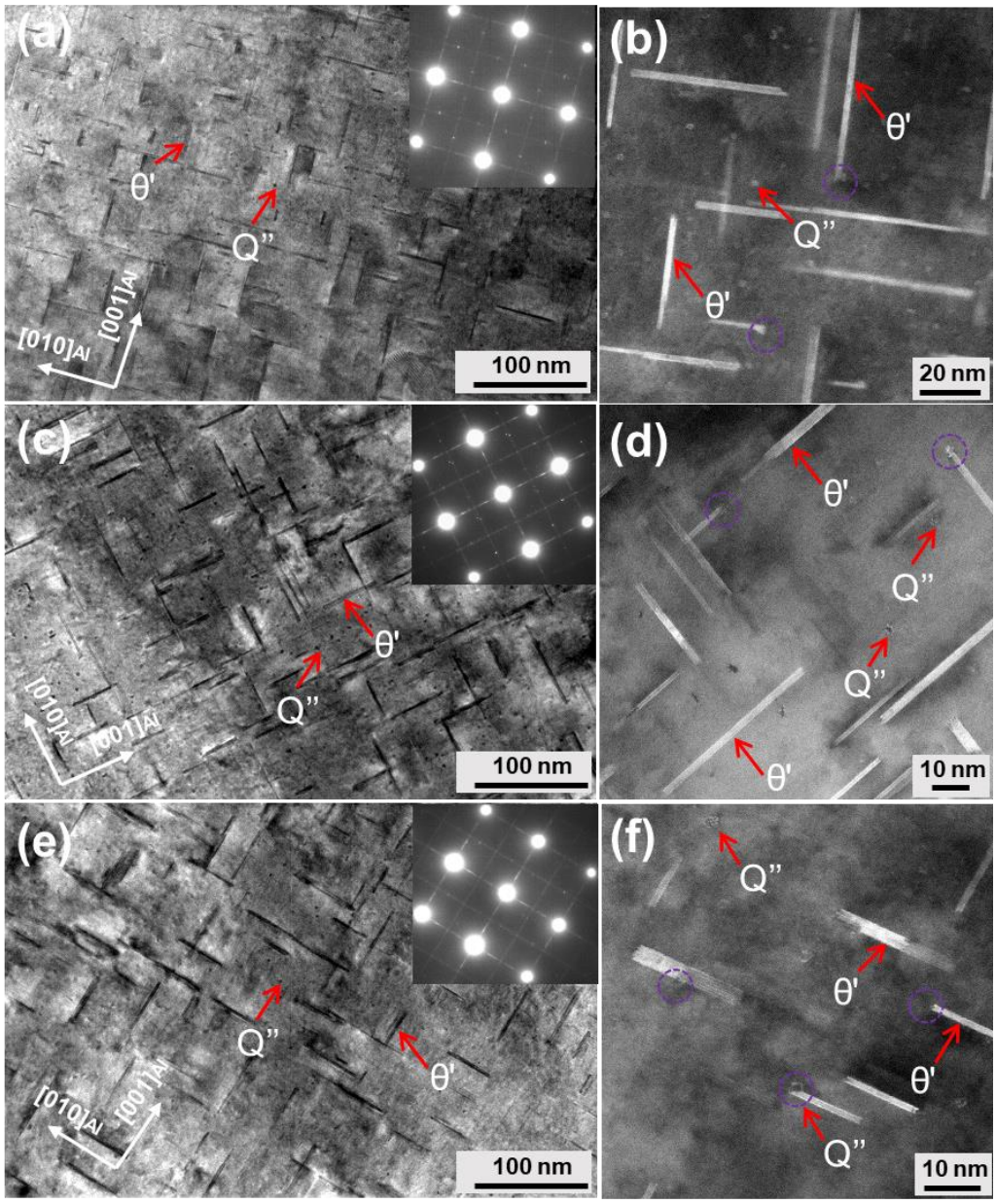

Fig. 7-9 TEM bright-field images with insets of SADPs taken from Al5Cu (a), Al6.6Cu (c) and Al10.6Cu (e) after T6 heat treatment; HADDF images show the coexistence of Q'' and θ' phases in Al5Cu (b), Al6.6Cu (d) and Al10.6Cu (f) after T6 heat treatment

7.3 Mechanical properties of Al-Cu-Si-Mg die-cast alloys

7.3.1 T5 heat treatment

The mechanical properties of the Al5Cu, Al6.6Cu and Al10.6Cu alloys after T5 heat treatment are shown in Fig. 7-10. The Al10.6Cu alloy exhibited the highest yield strength of 395±5 MPa and ultimate tensile strength of 480±8 MPa with the lowest elongation of about 1.9±0.15% as compared with other alloy compositions. The yield strength and ultimate tensile strength of Al5Cu and Al6.6Cu were determined as 351±1.5 MPa and 405±7 MPa, 362±3 MPa and 426±7 MPa, respectively. The average elongation of Al5Cu and Al6.6Cu were measured as 2.4±0.4% and 2.0±0.3%, respectively.

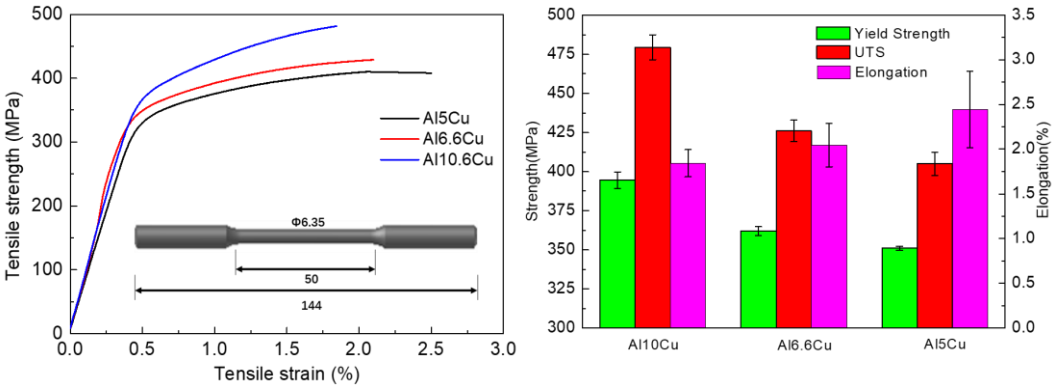

Fig. 7-10 Typical tensile stress-strain curves of Al5Cu, Al6.6Cu and Al10.6Cu alloys after T5 heat treatment (a) and bar charts of tensile mechanical properties (b)

7.3.2 T6 heat treatment

The Al5Cu, Al6.6Cu and Al10.6Cu alloys show excellent mechanical properties after T6 heat treatment. The mechanical properties of the Al5Cu, Al6.6Cu and Al10.6Cu alloys are shown in Fig. 7-11. The highest yield strength of 453±1.5 MPa was found in Al10.6Cu, with the lowest elongation of 1.32±0.15%. The Al5Cu alloy exhibited the lowest yield strength of 427±10 MPa with the highest elongation of 4.4±0.9%. The Al6.6Cu alloy showed excellent mechanical properties, with the elongation of about 4.1±1.1% and high yield strength of 444±3.4 MPa.

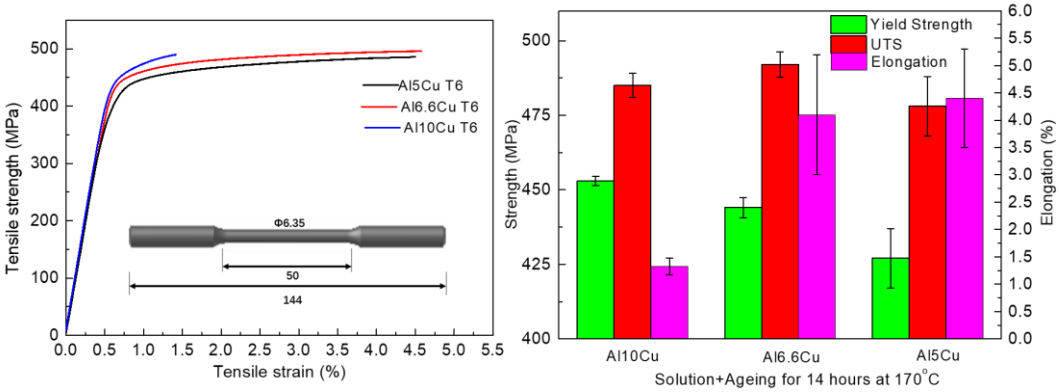

Fig. 7-11 Tensile stress-strain curves of Al5Cu, Al6.6Cu and Al10.6Cu alloys after T6 heat treatment (a) and bar charts of tensile mechanical properties (b)

The fracture surfaces of these three alloys are shown in Fig. 7-12. The fracture samples from these three alloys consisted of pores, dimples and flat surfaces. The pore size was found to be in the range of 5 μm to10 μm. The pores were developed after solution treatment, and they act as crack initiation points. With the increased addition of Cu to the alloy composition, more Cu containing intermetallic phase with a coarse morphology was found in the sample after solution treatment, as shown in Fig.7-4 (c). Thus, an increased proportion of flat surface was found in the fracture surface of Al10.6Cu. The flat surface is believed to be caused by the brittle fracture of hard phases, such as Al_2Cu and Q. Meanwhile, fewer dimples were found in fracture surface of Al10.6Cu, indicating a poor ductility property.

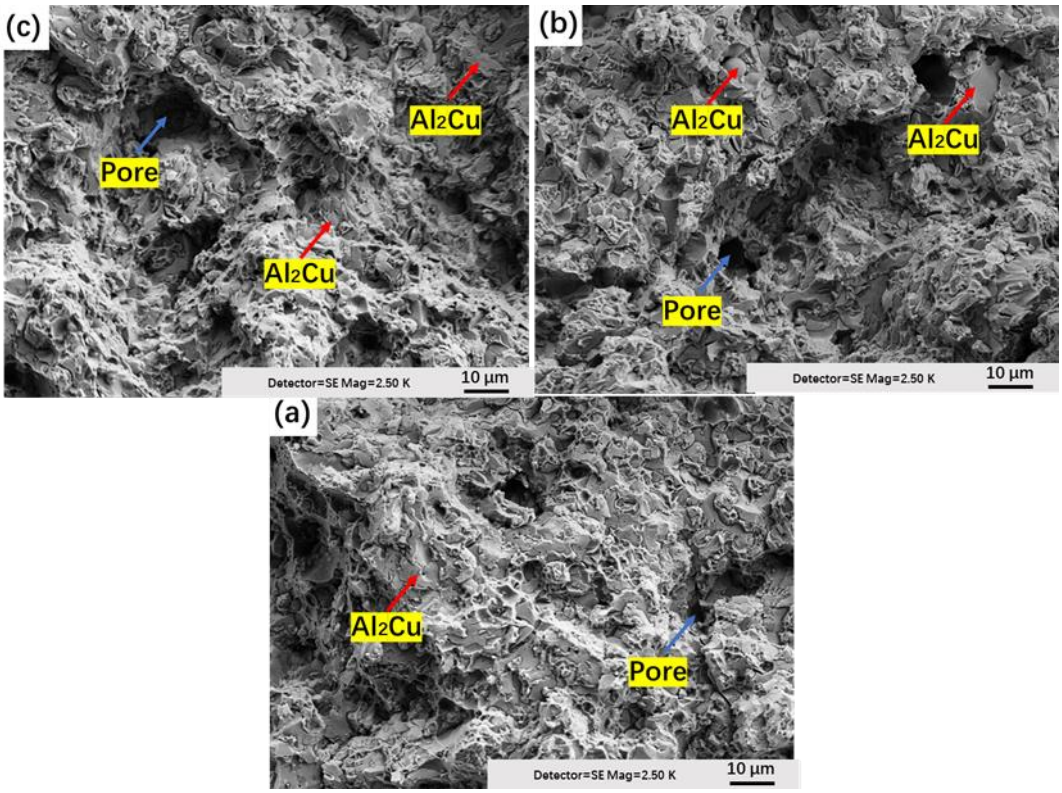

Fig. 7-12 Fracture surface of Al5Cu (a), Al6.6Cu (b) and Al10.6Cu (c) alloys after T6 heat treatment

7.4 Discussion

7.4.1 Microstructural evolution after solution treatment

Shrinkage, gas porosity and oxide inclusions are common defects present in HPDC parts. Among all the defects, porosity is the most detrimental defect to mechanical properties, especially elongation [204]. The porosity level in the as-cast state depends on the alloy composition, casting processing conditions (e.g. temperature, cooling rate etc.). The porosity level of the Al-Cu-Si-Mg alloys in the as-cast state is higher than that of Al-Si-Mg-Mn alloys which were shown in Chapter 4. The conditions (e.g. injection temperature of about 680 °C, mould temperature of 250 °C and pressure of 350 bar) used in the HPDC processing of the Al-Si-Mg-Mn and Al-Cu-Si-Mg alloy systems were similar. However, Al-Cu-Si-Mg alloys have a wider freezing range between solidus and liquidus temperatures (over 100 °C) [14], as shown in Fig 6.2. Thus, after pushing the liquid metal into the die cavity, the lack of feeding of liquid into the skeleton occurs during solidification. Consequently, there is more shrinkage than Al-Si-Mg-Mn alloys in the as-cast state. The centre of the tensile sample corresponds to the last solidification region, resulting in more porosity. The entrapment of gas resulting from the turbulence of the melt flow during the injection is the main reason

that most of the die-cast alloys are not heat treatable. In the current study, it can be noted that the surface blistering can be observed after 70 min solution treatment in the Al-Cu-Si-Mg- alloys, but in Al-Si-Mg-Mn alloys, it takes 30 min for surface blistering to occur. This is greatly affected by the solution treatment temperature. The solution temperature in Al-Cu-Si-Mg alloys is much lower (500 °C) compared with solution temperature (540 °C) used in Al-Si-Mg-Mn alloys. In addition, the area percentage of porosity in Al-Cu-Si-Mg alloys is maintained close to less than 1% after 30/60 min solution treatment, giving a maximum pore size below 40 μm.

The solution treatment plays a vital role in dissolving and spheroidising the eutectic phases. Compared with Si and Mg_2Si, the dissolution of Al_2Cu and $Al_5Cu_2Mg_8Si_7$ is much slower [280]. The dissolution of eutectic Al_2Cu and the concentration of Cu in the α-Al matrix can be described by a numerical model developed by Sjölander et al [281]. In the model, Al_2Cu spherical particle is assumed, and it predicts Cu concentration which agrees well with experimental results obtained by Sadeghi et al. [282]. From the model, the dissolution speed and increase in Cu content are related to solution treatment temperature/ time, the grain size of α-Al and Al_2Cu particle size. The finer grain size of α-Al and particle size of Al_2Cu can contribute to shorter solution treatment time [281]. In current work, the Cu concentration shows a similar trend that in the first 20 min, there is a sharp increase in Cu concentration in the α-Al matrix, while it increases very slowly after 20 min solution treatment. The reason is as follows. At the beginning of solution treatment, there are a large amount of Al_2Cu interfaces because of fine lamellar spacing of eutectic structure. As a result, those Al_2Cu phases dissolve very fast in the form of fragmentation, and the Cu content is approaching to the equilibrium state. The dissolving of the blocky Al_2Cu phase in the alloys is much slower. The further solution treatment led to a slower increment of Cu concentration, due to the coarsening of the Al_2Cu phases and decreased diffusion kinetics [173,281].

The Q phase is reported to be insoluble in the matrix with various Cu and Mg concentrations [283–285]. However, there are fine Si particles present inside the 4-phase eutectic mixture in the as-cast Al-Cu-Si-Mg alloys, which can be dissolved. Consequently, the Cu and Si contents in the α-Al matrix increase after solution treatment.

Lastly, it is found that Mg content in the α-Al matrix decreases slightly after solution treatment. This similar phenomenon has been observed by Long et al [286]. Firstly, HPDC process has a fast cooling rate, and the α-Al matrix is supersaturated with Mg.

The Q phase, which is the only magnesium-containing phase in these alloys, is not able to be dissolved into the matrix. Thus, there is no increase in Mg after solution treatment at 500 °C. Secondly, these samples contain more pores after solution treatment. It is also known that Al_2O_3 film can usually form in the internal surface of these pores [287]. Due to the strong affinity of magnesium to oxygen atoms, leading to the driving force for Mg diffusion into the oxide film at these micro-voids [286]. The Mg content in these regions will decrease. Consequently, Mg content in the α-Al grains is slightly lower than that in the as-cast state.

The hardness of each Al-Cu-Si-Mg alloy depends on the coarsening of eutectic phases and α-Al, together with the dissolution of intermetallic compounds, as well as the expansion of pores [199,228]. The hardness for samples after the first 10 min solution treatment change slightly, which is mainly because of the dissolution the eutectic phases and increase of solute content in the matrix (shown in Fig.7-3 (a)). Further solution treatment leads to a rapid increase of solute inside the matrix. Although the microstructure is coarsening, the solution strengthening makes a great contribution to the hardness. Overall, the hardness increased. There is almost no change of hardness in samples after solution treatment for time between 30 and 60 min. The reason is that the solution strengthening is offset by the strength reduction caused by an increased area percentage of porosity and coarsen α-Al or intermetallics phases.

7.4.2 Microstructure and precipitation hardening behaviour after ageing

7.4.2.1 T5 heat treatment

Due to the high cooling rate of HPDC process, the α-Al phase is saturated with Cu, Mg and Si alloying elements. Thus, the hardness is expected to increase after artificial ageing treatment, due to the formation of precipitates. It is reported that in Al-Si-Mg alloys, the precipitation sequence follows supersaturated solid solution → atomic clusters → GP zones (pre β'') → β'' → β' [112]. The β'' precipitate plays a key role in the peak hardness. Moreover, it is well known that Al-Cu alloys have excellent toughness [288] after T6 heat treatment, due to the plate-like precipitates of θ'. The precipitate sequence in Al-Cu alloy follows solid solution →GP zones →θ''→θ'→θ [289]. However, the precipitates become more complex when the α-Al matrix contains Si, Mg and Cu alloying elements together. Although there are still some other minor precipitates such as Q', Q'' or θ' after peak ageing treatment [232], the hardness of the

matrix is dominated by the major precipitates. In this study, the major precipitates are discussed. From SEM EDX analysis Table 7-2, the Si and Mg contents in the α-Al matrix, are similar in these three Al-Cu-Si-Mg alloys, and Al5Cu alloy has the lowest Cu content. As a result, after peaking ageing, the peak hardness in Al5Cu alloy is contributed by the presence of a high number density of β'' [286], as shown in Fig 7-6 (a). The prolonged ageing treatment causes coarsening of β'' or formation of semi-coherent β', resulting in a decrease in hardness. More Cu content in the matrix triggers the formation of θ' phase. Thus, in Al6.6Cu alloy, the coexisting of θ' and β'' were found, as shown in Fig 7-6 (b). In Al10.6Cu alloy which has highest Cu content under as-cast state, the β'' phase is replaced by Q'', and more θ' phase is formed, as shown in Fig 7-6 (c). It is reported that Q''-type phase is transformed from β'' phase incorporating with Cu atoms, and an outer layer of bright Cu atoms is usually observed from HADDF images [115]. Saito et al. proposed that the formation mechanism is because Cu atoms can suppress the misfit dislocations at β''/Al interface [290].

7.4.2.2 T6 heat treatment

After T6 heat treatment, precipitates observed in these three alloys are similar, which correspond to θ' and Q''. The composition of the matrix after solution treatment comprises of increased Si and Cu, as shown in Table 7-2. It is reported that the Q'' and θ' phase usually form together in the high Cu content alloys with Si and Mg [291,292]. It can be noted that θ' phase with attachment of Q'' phase is slightly thinner and shorter than those without attachment of Q'' phase. It is reported that The Q'' phase can trigger the heterogeneous nucleation of θ', due to the fact that the outer layer of Cu on Q'' phase is able to reduce the strain and interface energy [117,293]. Therefore, the growth and dimension of θ' precipitates are restricted [186,293]. The Cu content of the Al matrix in Al5Cu alloy is slightly lower than those in Al6.6Cu or Al10.6Cu alloys after solution treatment. Hence, the area fraction of θ' is slightly lower, as shown in Table 7-3, but the types of precipitates remain similar to the other two alloys after T6 heat treatment.

7.4.3 Relationship between the microstructure and mechanical properties

7.4.3.1 T5 heat treatment

The microstructure of Al-Cu-Si-Mg alloys after T5 heat treatment consists of a eutectic mixture and α-Al, which is strengthened by precipitates. The increase of yield strength

is induced by precipitation hardening ($\Delta\sigma_{ppt}$) in the α-Al phases. The β'' with needle-like morphology, exhibits a coherent interface with α-Al as shown in Fig. 7-6 (a). The increased yield strength of Al-Cu-Si-Mg alloys after artificial ageing is due to the high density of β'' precipitates, which are very effective at inhibiting the mobility of gliding dislocations [294]. Moreover, the plate-like θ' phase also has excellent shear resistance [295]. Consequently, there is a significant improvement of strength in these three Al-Cu-Si-Mg alloys.

However, it should be noted that the large increase in yield strength (~130 MPa) of the three alloys after T5 heat treatment, as compared to as-cast state, are similar, although the precipitation behaviour of these three alloys is different. The reasons are as follows. Firstly, it is reported by Nie that plate-like precipitates are the most effective for dispersion strengthening, based on Orowan theory [119]. The similar phenomenon was found by Xiao et al. [232] that the Al-Mg-Si-Cu alloys with a higher Cu content (e.g. 0.5-4.5 wt%) have a higher hardness after peak ageing, which has more plate-like θ' precipitates and fewer needle-like β'' precipitates. The contribution of different precipitates to give similar strength increment after ageing is due to the volume fraction of the precipitates within the Al matrix. Al10.6Cu alloy has the lowest fraction of α-Al (73.4%), with a large number of θ' precipitates, as shown in Fig.6-10 and Fig.7-6 (c). The limited number of θ' phases is observed in Al6.6Cu alloy with an area percentage of α-Al of 78.6%. In Al5Cu alloy, there are almost no θ' precipitates, and instead, the high number density of β'' precipitates present in the Al matrix having an area percentage of 82.9%. Finally, the increased strength of Al5Cu and Al6.6Cu is almost the same as that of Al10.6Cu, which is balanced by type and proportion of precipitates. The elongation to fracture is dominated by the area fraction of Al matrix, and the lowest elongation was found in Al10.6Cu alloy.

7.4.3.2 T6 heat treatment

After T6 heat treatment of these three alloys, the yield strength of all three alloys exceeds 420 MPa. This is due to the presence of θ' and Q'' precipitates. Generally, a high number density of θ' can lead to a high yield strength as compared with that caused by β'' precipitate because of the coherent interface and morphological nature [296,297]. The precipitates observed in these three alloys are similar, but Al5Cu has the lowest area fraction of θ' precipitates, as shown in Table 7-3. It is seen that the area fraction of intermetallics in Al5Cu at solution treatment for 30 min is almost the same as that in Al6.6Cu alloy solution treated for 60 min (shown in Fig. 7-3 (a)). Thus,

the contribution of the intermetallic phase in the eutectic mixture ($\Delta\sigma_{eutectic}$) to the strength in Al5Cu and Al6.6Cu alloys are similar. Therefore, it is believed that the higher strength in Al6.6Cu compared with Al5Cu is caused by the presence of more θ' precipitates ($\Delta\sigma_{ppt}$). However, the area fractions of θ' precipitates in Al6.6Cu and Al10.6Cu are similar, but the proportion of eutectic phases in Al10.6Cu is much higher, as shown in Fig. 7-3 (a). As a result, the contribution of an increased amount of intermetallics ($\Delta\sigma_{eutectic}$) causes highest yield strength in Al10.6Cu.

However, Al10.6Cu has the lowest elongation. This is believed to be the responsibility of very large amount of hard/brittle intermetallic eutectic phases in Al10.6Cu alloy (Fig. 7-4 (c)) which is the source of fast fracture upon tensile loading, as shown in Fig.7-12. Although the area fractions of intermetallic phase in the eutectic region between Al5Cu and Al6.6Cu alloys are similar, the Al matrix of Al5Cu has fewer θ' precipitates, leading to the highest elongation. Finally, in Al-Cu-Si-Mg alloys, although high Cu content can achieve higher strength, after solution treatment all the intermetallic phases can not be completely dissolved in the matrix, which have a negative effect on the ductility.

7.5 Conclusions

(1) The solution treatment was optimised for Al5Cu (30 min/500 °C), Al6.6Cu/ Al10.6Cu (60 min/500 °C) to maintain a low porosity level around 1% and to avoid surface blistering.

(2) The solution treatment leads to the spheriodisation of eutectic phases (Al_2Cu and Q) and break up of the intermetallic compound network. It allows a large amount of Cu and Si to be dissolved into the α-Al matrix and the coarsening of the eutectic phases (Q and Al_2Cu).

(3) After T5 heat treatment at peak-ageing condition, the precipitates in Al5Cu changes from mainly β'' to β'' and θ' in Al6.6Cu and then to θ' and Q'' in Al10.6Cu. The highest yield strength of 395±5 MPa and good elongation of 1.9±0.15% have been achieved in Al10.6Cu after peak-aged T5 condition as compared to other Al-Cu-Si-Mg alloy compositions.

(4) After T6 heat treatment at peak-ageing condition, all three Al-Cu-Si-Mg alloys produce similar Q'' and θ' precipitates at different proportions depending on the alloy composition. The lowest area fraction of θ' precipitate is found in Al5Cu.

Al10.6Cu exhibits a superior yield strength of 453±1.5 MPa, which is outperformed existing die-cast aluminium alloys.

Chapter 8 Conclusions and further work

8.1 Conclusions

1. Two multi-component systems (i.e. Al-Si-Mg-Mn and (Al-Cu-Si-Mg) have been developed for die-cast alloys with excellent tensile properties. Depending on the alloy composition, the yield strength and tensile strength of these newly developed alloys are comparable to those existing Al-based die cast alloys.

2. The as-cast microstructure of eutectic Al-Si-Mg-Mn alloy consisted of binary eutectic (α-Al+Mg_2Si) and quaternary eutectic (α-Al+Mg_2Si+Si+π-AlFeMnMgSi). However, the hypoeutectic Al-Si-Mg-Mn alloys contain additional primary α-Al phase while retaining the eutectic mixture with different proportions depending on the alloy composition.

3. The as-cast microstructure of eutectic Al-Cu-Si-Mg alloy consisted of lamellar eutectic cells with the ultrafine anomalous eutectic mixture in the intercellular region. Solidification of quaternary Al-Cu-Si-Mg alloy leads to coupled growth of eutectic phases (e.g. α-Al, Al_2Cu and Q-phase) with specific orientation relationships and non-cooperative growth of Si eutectic phase. The hypoeutectic Al-Cu-Si-Mg alloys contain additional primary α-Al phase while retaining the eutectic mixture.

4. Solution treatment for both alloy systems has been optimised for minimal porosity level, prior to artificial ageing treatment for peak strength performance. In Al-Si-Mg-Mn alloys, no apparent porosity expansion was found under the solution treatment at 540 °C for 10 min or at 480 °C for 90 min. But the prolonged solution time and increased solution temperature can cause porosity expansion.

5. After solution treatment at 540 °C for 10 min, the eutectic Si and Mg_2Si were spheriodized and the π-AlFeMnSiMg phase transformed completely into the nanoscale α2-AlFeMnSiphase with a BCC crystal structure.

6. Solution temperature has significant effects on peak ageing hardening; the highest peak ageing hardness can be obtained when the samples were solution treated at 540 °C for 10 min. The precipitates in Al-Si-Mg-Mn hypoeutectic alloys after T6 treatment are β'' which are responsible for the strengthening.

7. In Al-Cu-Si-Mg alloys, the solution treatment causes spheriodisation and dissolution of eutectic phases into α-Al matrix. The Cu content in the matrix is close to 3wt.% after solution treatment for at least 30 min at 500 °C.

8. After T5 heat treatment at peak-ageing condition, the precipitates in Al5Cu changes from mainly β'' to β'' and θ' in Al6.6Cu and then to θ' and Q'' in Al10.6Cu. The highest yield strength of 395±5 MPa and good elongation of 1.9±0.15% have been achieved in Al10.6Cu after peak-aged T5 condition as compared to other Al-Cu-Si-Mg alloy compositions.

9. The coexist of Q'' and θ' were found in Al-Cu-Si-Mg hypoeutectic alloys after T6 treatment at peak ageing condition. The lowest area fraction of θ' precipitate is found in Al5Cu. Al10.6Cu exhibits a superior yield strength of 453±1.5 MPa, which is outperformed existing die-cast aluminium alloys.

10. The exploitation of multi-component eutectic alloy system together with the introduction of ductile primary α-Al phase for the development of high strength Al die-cast alloys, has successfully demonstrated in this project.

8.2 Further work

8.2.1 The modification of Si eutectic phase in the Al-Si-Mg-Mn alloys to improve the strength and elongation

It is well known that the addition of suitable minor elements enables the modification of morphology of Si eutectic phase in the solidified microstructure. In the current work, the modification of Si eutectic phase to small size with a low aspect ratio can further improve mechanical performance (especially ductility) of the Al-Si-Mg-Mg alloys.

8.2.2 Vacuum assistant HPDC for increasing the solution treatment time

Although the shot solution treatment is approved that it can dissolve and sopherodize the eutectic phase, the prolonged solution treatment can maximise the dissolution and homogenisation of the alloys. It would be better to apply vacuum-assisted HPDC for these multi-component alloys to reduce the porosity level after heat treatment even further in the as-solidified microstructure. Hence, longer solution treatment time can be

applied to enhance the solute content in the α-Al grains, prior to artificial ageing treatment to maximise the precipitation-enhanced mechanical properties in these alloy systems.

8.2.3 Fatigue testing of multi-component alloys

Although the newly developed Al-Si-Mg-Mn and Al-Cu-Si-Mg multi-component alloys have excellent tensile properties, it is unclear how they perform under cyclic loading conditions. Therefore, the fatigue testing of these multi-component Al-Si-Mg-Mn and Al-Cu-Si-Mg alloys is essential to understand the fatigue behaviour of this material for future engineering applications in automotive industries.

8.2.4 Searching of the alternative quaternary eutectic alloy system

So far, this work has only focussed on a limited number of alloy systems. There are lots of unexplored Al-based quaternary alloy systems (e.g. Al-Cu-Si-Fe, Al-Cu-Si-Ni, Al-Cu-Si-Mn, Al-Ca-Mg-Si and Al-Cu-Si-Ag etc.) to be discovered. It is essential to understand the eutectic solidification behaviour of these less well-studied quarternary eutectic systems. This involves a combination of CALPHAD modelling of the phase constitution using Pandat/Thermocalc software and experimental studies using suction casting and materials characterisation.

8.2.5 Extend the application of hypoeutectic concept to other Al-based quarternary eutectic alloy system

The current work has demonstrated the mechanical properties of the newly developed Al die-cast alloys can be tailored for required specifications by controlling the amounts of primary α-Al and eutectic mixture in the microstructure. Hence, the application of the hypoeutectic alloy design concept can be extended to other Al-based quaternary eutectic alloys stated above to investigate their precipitation behaviour and mechanical properties in order to search for Al-based multi-component alloys with superior mechanical performance.

References

[1] F. Bonollo, N. Gramegna, G. Timelli, High-pressure die-casting: Contradictions and challenges, JOM. 67 (2015) 901–908. https://doi.org/10.1007/s11837-015-1333-8.

[2] J.W. Yeh, Alloy design strategies and future trends in high-entropy alloys, JOM. 65 (2013) 1759–1771. https://doi.org/10.1007/s11837-013-0761-6.

[3] Z.P. Chen, J.E. Gao, Y. Wu, H. Wang, X.J. Liu, Z.P. Lu, Designing novel bulk metallic glass composites with a high aluminum content, Sci. Rep. 3 (2013) 3353. https://doi.org/10.1038/srep03353.

[4] U. Hecht, L. Gránásy, T. Pusztai, B. Böttger, M. Apel, V. Witusiewicz, L. Ratke, J. De Wilde, L. Froyen, D. Camel, B. Drevet, G. Faivre, S.G. Fries, B. Legendre, S. Rex, Multiphase solidification in multicomponent alloys, Mater. Sci. Eng. R Reports. 46 (2004) 1–49. https://doi.org/10.1016/j.mser.2004.07.002.

[5] V. Vitek, G. Gutekunst, J. Mayer, M. Rühle, Atomic structure of misfit dislocations in metal-ceramic interfaces, Philos. Mag. A Phys. Condens. Matter, Struct. Defects Mech. Prop. 71 (1995) 1219–1239. https://doi.org/10.1080/01418619508244370.

[6] J. Rowe, Advanced materials in automotive engineering, Woodhead Publishing Limited, 2012. https://doi.org/10.1533/9780857095466.

[7] J.R. Davis & Associates., Aluminum and aluminum alloys, ASM International, 1993. https://books.google.co.uk/books?hl=en&lr=&id=Lskj5k3PSIcC&oi=fnd&pg=PA3&dq=Aluminum+and+aluminum+alloys&ots=Fww0de9xjV&sig=awvTN0Y9K-Mp96seQE7AxpGbXe4#v=onepage&q=Aluminum and aluminum alloys&f=false (accessed September 11, 2019).

[8] I.P. Polmear, Light Alloys - From Traditional Alloys to Nanocrystals, Elsevier/Butterworth-Heinemann, 2006. https://doi.org/10.1017/CBO9781107415324.004.

[9] T.O. Mbuya, B.O. Odera, S.P. Ng'ang'a, Influence of iron on castability

and properties of aluminium silicon alloys: Literature review, Int. J. Cast Met. Res. 16 (2003) 451–465. https://doi.org/10.1080/13640461.2003.11819622.

[10] M. Di Sabatino, L. Arnberg, Castability of aluminium alloys, in: Trans. Indian Inst. Met., Springer-Verlag, 2009: pp. 321–325. https://doi.org/10.1007/s12666-009-0049-2.

[11] M. Colombo, E. Gariboldi, A. Morri, Er addition to Al-Si-Mg-based casting alloy: Effects on microstructure, room and high temperature mechanical properties, J. Alloys Compd. 708 (2017) 1234–1244. https://doi.org/10.1016/j.jallcom.2017.03.076.

[12] S.K. Rathi, A. Sharma, M. Di Sabatino, Effect of mould temperature, grain refinement and modification on hot tearing test in Al-7Si-3Cu alloy, Eng. Fail. Anal. 79 (2017) 592–605. https://doi.org/10.1016/j.engfailanal.2017.04.037.

[13] M. De Giovanni, J.M. Warnett, M.A. Williams, P. Srirangam, 3D imaging and quantification of porosity and intermetallic particles in strontium modified Al-Si alloys, J. Alloys Compd. 727 (2017) 353–361. https://doi.org/10.1016/j.jallcom.2017.08.146.

[14] M. Li, H. Wang, Z. Wei, Z. Zhu, The effect of Y on the hot-tearing resistance of Al-5 wt.% Cu based alloy, Mater. Des. 31 (2010) 2483–2487. https://doi.org/10.1016/j.matdes.2009.11.044.

[15] D.J. Lahaie, M. Bouchard, Physical modeling of the deformation mechanisms of semisolid bodies and a mechanical criterion for hot tearing, Metall. Mater. Trans. B Process Metall. Mater. Process. Sci. 32 (2001) 697–705. https://doi.org/10.1007/s11663-001-0124-5.

[16] Y. Zhu, D. Schwam, J.F. Wallace, S. Birceanu, Evaluation of soldering, washout and thermal fatigue resistance of advanced metal materials for aluminum die-casting dies, Mater. Sci. Eng. A. 379 (2004) 420–431. https://doi.org/10.1016/j.msea.2004.03.020.

[17] C.H. Caceres, C.J. Davidson, J.R. Griffiths, Q.G. Wang, The effect of Mg on the microstructure and mechanical behavior of Al-Si-Mg casting alloys,

Metall. Mater. Trans. A. 30 (1999) 2611–2618. https://doi.org/10.1007/s11661-999-0301-8.

[18] A. Mazahery, M.O. Shabani, Modification mechanism and microstructural characteristics of eutectic si in casting Al-Si Alloys: A review on experimental and numerical studies, Jom. 66 (2014) 726–738. https://doi.org/10.1007/s11837-014-0968-1.

[19] Z.M. Shi, Q. Wang, G. Zhao, R.Y. Zhang, Effects of erbium modification on the microstructure and mechanical properties of A356 aluminum alloys, Mater. Sci. Eng. A. 626 (2015) 102–107. https://doi.org/10.1016/j.msea.2014.12.062.

[20] F. Lasagni, A. Lasagni, C. Holzapfel, F. Mücklich, H.P. Degischer, Three dimensional characterization of unmodified and Sr-modified Al-Si eutectics by FIB and FIB EDX tomography, Adv. Eng. Mater. 8 (2006) 719–723. https://doi.org/10.1002/adem.200500276.

[21] G. Ran, J.E. Zhou, Q.G. Wang, Precipitates and tensile fracture mechanism in a sand cast A356 aluminum alloy, J. Mater. Process. Technol. 207 (2008) 46–52. https://doi.org/10.1016/j.jmatprotec.2007.12.050.

[22] E. Ogris, A. Wahlen, H. Lüchinger, P.J. Uggowitzer, On the silicon spheroidization in Al-Si alloys, J. Light Met. 2 (2002) 263–269. https://doi.org/10.1016/S1471-5317(03)00010-5.

[23] J. Cho, C. Kim, Al-Si CASTING ALLOYS IN HIGH PRESSURE DIE CASTING, Int. J. Met. 8 (2014) 49–55.

[24] S. Ji, W. Yang, F. Gao, D. Watson, Z. Fan, Effect of iron on the microstructure and mechanical property of Al–Mg–Si–Mn and Al–Mg–Si diecast alloys, Mater. Sci. Eng. A. 564 (2013) 130–139. https://doi.org/10.1016/j.msea.2012.11.095.

[25] W.A. Badawy, F.M. Al-Kharafi, A.S. El-Azab, Electrochemical behaviour and corrosion inhibition of Al, Al-6061 and Al-Cu in neutral aqueous solutions, Corros. Sci. 41 (1999) 709–727. https://doi.org/10.1016/S0010-938X(98)00145-0.

[26] X. Nie, H. Zhang, H. Zhu, Z. Hu, L. Ke, X. Zeng, Effect of Zr content on formability, microstructure and mechanical properties of selective laser melted Zr modified Al-4.24Cu-1.97Mg-0.56Mn alloys, J. Alloys Compd. 764 (2018) 977–986. https://doi.org/10.1016/j.jallcom.2018.06.032.

[27] H. Li, Y. Tang, Z. Zeng, Z. Zheng, F. Zheng, Effect of ageing time on strength and microstructures of an Al-Cu-Li-Zn-Mg-Mn-Zr alloy, Mater. Sci. Eng. A. 498 (2008) 314–320. https://doi.org/10.1016/j.msea.2008.08.001.

[28] R.Y. Barkov, A. V. Pozdniakov, E. Tkachuk, V.S. Zolotorevskiy, Effect of Y on microstructure and mechanical properties of Al-Mg-Mn-Zr-Sc alloy with low Sc content, Mater. Lett. 217 (2018) 135–138. https://doi.org/10.1016/j.matlet.2018.01.076.

[29] J. Feder, K.C. Russell, J. Lothe, G.M. Pound, Homogeneous nucleation and growth of droplets in vapours, Adv. Phys. 15 (1966) 111–178. https://doi.org/10.1080/00018736600101264.

[30] D. Turnbull, Kinetics of Heterogeneous Nucleation, J. Chem. Phys. 18 (1950) 198–203. https://doi.org/10.1063/1.1747588.

[31] J.A. Spittle, Columnar to equiaxed grain transition in as solidified alloys, Int. Mater. Rev. 51 (2006) 247–269. https://doi.org/10.1179/174328006X102493.

[32] B. Chalmers, The structure of ingots, J. Aust. Inst. Met. 8 (1963) 255–263. http://www.scopus.com/inward/record.url?eid=2-s2.0-0000252668&partnerID=tZOtx3y1 (accessed June 5, 2020).

[33] W.C. Winegard, B. Chalmers, Supercooling and dendritic freezing in alloy, Trans. Am. Soc. Met. 46 (1954) 1214.

[34] OHNO A, MOTEGI T, SODA H, ORIGIN OF THE EQUIAXED CRYSTALS IN CASTINGS, Trans Iron Steel Inst Jap. 11 (1971) 18–23. https://doi.org/10.2355/isijinternational1966.11.18.

[35] G.S. Cole, G.F. Bolling, The Importance of Natural Convection in Casting, Trans. Metall. Soc. Aime. 233 (1965) 1568–1572.

[36] M.J. Bermingham, D.H. StJohn, J. Krynen, S. Tedman-Jones, M.S. Dargusch, Promoting the columnar to equiaxed transition and grain refinement of titanium alloys during additive manufacturing, Acta Mater. 168 (2019) 261–274. https://doi.org/10.1016/j.actamat.2019.02.020.

[37] S.P. Wu, D.R. Liu, J.J. Guo, Y.Q. Su, H.Z. Fu, Influence of process parameters on CET in Ti-Al alloy ingot with consideration of shrinkage cavity formation: A computer simulation, J. Alloys Compd. 441 (2007) 267–277. https://doi.org/10.1016/j.jallcom.2006.09.094.

[38] J.A. Spittle, S.G.R. Brown, Computer simulation of the effects of alloy variables on the grain structures of castings, Acta Metall. 37 (1989) 1803–1810. https://doi.org/10.1016/0001-6160(89)90065-5.

[39] B. Willers, S. Eckert, U. Michel, I. Haase, G. Zouhar, The columnar-to-equiaxed transition in Pb-Sn alloys affected by electromagnetically driven convection, Mater. Sci. Eng. A. 402 (2005) 55–65. https://doi.org/10.1016/j.msea.2005.03.108.

[40] Y.Z. Zhao, Y.H. Zhao, Q. Li, S.L. Chen, J.Y. Zhang, K.C. Chou, Effects of step size and cut-off limit of residual liquid amount on solidification simulation of Al-Mg-Zn system with Scheil model, Intermetallics. 17 (2009) 491–495. https://doi.org/10.1016/j.intermet.2008.12.006.

[41] P. Schaffnit, C. Stallybrass, J. Konrad, F. Stein, M. Weinberg, A Scheil–Gulliver model dedicated to the solidification of steel, Calphad. 48 (2015) 184–188. https://doi.org/10.1016/j.calphad.2015.01.002.

[42] C.B. Basak, M. Krishnan, Applicability of Scheil-Gulliver solidification model in real alloy: A case study with Cu-9wt%Ni-6wt%Sn alloy, Philos. Mag. Lett. 95 (2015) 376–383. https://doi.org/10.1080/09500839.2015.1074296.

[43] M.C. Schneider, C. Beckermann, A numerical study of the combined effects of microsegregation, mushy zone permeability and fllow, caused by volume contraction and thermosolutal convection, on macrosegregation and eutectic formation in binary alloy solidification, Int. J. Heat Mass Transf. 38 (1995) 3455–3473. https://doi.org/10.1016/0017-

9310(95)00054-D.

[44] Q. Chen, B. Sundman, Computation of partial equilibrium solidification with complete interstitial and negligible substitutional solute back diffusion, Mater. Trans. 43 (2002) 551–559. https://doi.org/10.2320/matertrans.43.551.

[45] B. Cantor, G.A. Chadwick, Crystallography of Al-Al3Ni, Al-Al2Cu and Al-ζ(AlAg) eutectics during nucleation and the early stages of growth, J. Cryst. Growth. 30 (1975) 101–108. https://doi.org/10.1016/0022-0248(75)90207-9.

[46] B.N. Bhat, Effect of thermotransport on directionally solidified aluminium-copper eutectic, J. Cryst. Growth. 28 (1975) 68–76. https://doi.org/10.1016/0022-0248(75)90027-5.

[47] W.T. Kim, B. Cantor, Heterogeneous nucleation of Al2Cu in Al□Cu eutectic liquid droplets embedded in an al matrix, Acta Metall. Mater. 42 (1994) 3045–3053. https://doi.org/10.1016/0956-7151(94)90401-4.

[48] S. Shankar, Y.W. Riddle, M.M. Makhlouf, Nucleation mechanism of the eutectic phases in aluminum-silicon hypoeutectic alloys, Acta Mater. 52 (2004) 4447–4460. https://doi.org/10.1016/j.actamat.2004.05.045.

[49] S. Nafisi, R. Ghomashchi, H. Vali, Eutectic nucleation in hypoeutectic Al-Si alloys, Mater. Charact. 59 (2008) 1466–1473. https://doi.org/10.1016/j.matchar.2008.01.014.

[50] M. Zarif, B. Mckay, P. Schumacher, Study of Heterogeneous Nucleation of Eutectic Si in High-Purity Al-Si Alloys with Sr Addition, Metall. Mater. Trans. A. 42 (2011) 1684–1691. https://doi.org/10.1007/s11661-010-0553-3.

[51] C. Lemaignan, M.C. Cheynet, N. Eustathopoulos, Nucleation behaviour of silver-germanium eutectic alloys, J. Cryst. Growth. 50 (1980) 720–728. https://doi.org/10.1016/0022-0248(80)90018-4.

[52] K.A. Jackson, J.D. Hunt, Lamellar and Rod Eutectic Growth, in: Dyn. Curved Front., Elsevier, 1988: pp. 363–376.

https://doi.org/10.1016/B978-0-08-092523-3.50040-X.

[53] A. Ourdjini, J. Liu, R. Elliott, Eutectic spacing selection in Al–Cu system, Mater. Sci. Technol. 10 (1994) 312–318. https://doi.org/10.1179/mst.1994.10.4.312.

[54] T. Carlberg, H. Fredriksson, On the mechanism of lamellar spacing adjustment in eutectic alloys, J. Cryst. Growth. 42 (1977) 526–535. https://doi.org/10.1016/0022-0248(77)90241-X.

[55] L.G. Gregory, D.P. Dunne, G.W. Delamore, Crystallographic orientation relationships in the tin-lead-cadmium ternary eutectic, J. Mater. Sci. 18 (1983) 51–56. https://doi.org/10.1007/BF00543809.

[56] S. Bottin-Rousseau, M. Şerefoğlu, S. Yücetürk, G. Faivre, S. Akamatsu, Stability of three-phase ternary-eutectic growth patterns in thin sample, Acta Mater. 109 (2016) 259–266. https://doi.org/10.1016/j.actamat.2016.01.065.

[57] J. Hötzer, P. Steinmetz, A. Dennstedt, A. Genau, M. Kellner, I. Sargin, B. Nestler, Influence of growth velocity variations on the pattern formation during the directional solidification of ternary eutectic Al-Ag-Cu, Acta Mater. 136 (2017) 335–346. https://doi.org/10.1016/j.actamat.2017.07.007.

[58] J.T. Kim, S.W. Lee, S.H. Hong, H.J. Park, J.Y. Park, N. Lee, Y. Seo, W.M. Wang, J.M. Park, K.B. Kim, Understanding the relationship between microstructure and mechanical properties of Al-Cu-Si ultrafine eutectic composites, Mater. Des. 92 (2016) 1038–1045. https://doi.org/10.1016/j.matdes.2015.12.080.

[59] C.S. Tiwary, S. Kashyap, K. Chattopadhyay, Development of alloys with high strength at elevated temperatures by tuning the bimodal microstructure in the Al-Cu-Ni eutectic system, Scr. Mater. 93 (2014) 20–23. https://doi.org/10.1016/j.scriptamat.2014.08.020.

[60] G.A. Song, W. Lee, N.S. Lee, K.B. Kim, J.M. Park, D.H. Kim, J. Lee, J.S. Park, Microstructural evolution and mechanical properties of Mg-Cu-Zn ultrafine eutectic composites, J. Mater. Res. 24 (2009) 2892–2898.

https://doi.org/10.1557/jmr.2009.0330.

[61] R. Goetzinger, M. Barth, D.M. Herlach, Mechanism of formation of the anomalous eutectic structure in rapidly solidified Ni-Si , Co-Sb and Ni-Al-Ti, Acta Mater. 46 (1998) 1647–1655.

[62] A.M. Mullis, C.R. Clopet, On the origin of anomalous eutectic growth from undercooled melts: Why re-melting is not a plausible explanation, Acta Mater. 145 (2018) 186–195. https://doi.org/10.1016/j.actamat.2017.12.016.

[63] X.R. Liu, C.D. Cao, B. Wei, Microstructure evolution and solidification kinetics of undercooled Co – Ge eutectic alloys, Scr. Mater. 46 (2002) 13–18.

[64] Z. Wang, X. Lin, Y. Cao, F. Liu, W. Huang, Formation of anomalous eutectic in Ni-Sn alloy by laser cladding, Opt. Laser Technol. 99 (2018) 154–159. https://doi.org/10.1016/j.optlastec.2017.08.026.

[65] L. Liu, J.F. Li, Y.H. Zhou, Solidification interface morphology pattern in the undercooled Co-24.0 at.% Sn eutectic melt, Acta Mater. 59 (2011) 5558–5567. https://doi.org/10.1016/j.actamat.2011.05.028.

[66] C. Yang, J. Gao, Y.K. Zhang, M. Kolbe, D.M. Herlach, New evidence for the dual origin of anomalous eutectic structures in undercooled Ni – Sn alloys : In situ observations and EBSD characterization, Acta Mater. 59 (2011) 3915–3926. https://doi.org/10.1016/j.actamat.2011.03.016.

[67] C.R. Clopet, R.F. Cochrane, A.M. Mullis, The origin of anomalous eutectic structures in undercooled Ag–Cu alloy, Acta Mater. 61 (2013) 6894–6902. https://doi.org/10.1016/j.actamat.2013.08.001.

[68] J.F. Li, W.Q. Jie, S. Zhao, Y.H. Zhou, Structural evidence for the transition from coupled to decoupled growth in the solidification of undercooled Ni-Sn eutectic melt, Metall. Mater. Trans. A Phys. Metall. Mater. Sci. 38 (2007) 1806–1816. https://doi.org/10.1007/s11661-007-9198-2.

[69] X.X. Wei, X. Lin, W. Xu, Q.S. Huang, M. Ferry, J.F. Li, Y.H. Zhou,

Remelting-induced anomalous eutectic formation during solidification of deeply undercooled eutectic alloy melts, Acta Mater. 95 (2015) 44–56. https://doi.org/10.1016/j.actamat.2015.05.014.

[70] B. Wei, D.M. Herlach, F. Sommer, W. Kurz, Rapid solidification of undercooled eutectic and monotectic alloys, Mater. Sci. Eng. A. 173 (1993) 355–359. https://doi.org/10.1016/0921-5093(93)90244-9.

[71] H. Wang, F. Liu, D.M. Herlach, On the solution of solute diffusion during eutectic growth, J. Cryst. Growth. 389 (2014) 68–73. https://doi.org/10.1016/j.jcrysgro.2013.11.080.

[72] R.-F. Xiao, J. Iwan, D. Alexander, F. Rosenberger, Eutectic and off-eutectic growth patterns, Mater. Sci. Eng. A. 178 (1994) 233–238. https://doi.org/10.1016/0921-5093(94)90548-7.

[73] M.S. Dargusch, M. Nave, S.D. McDonald, D.H. StJohn, The effect of aluminium content on the eutectic morphology of high pressure die cast magnesium-aluminium alloys, J. Alloys Compd. 492 (2010) L64–L68. https://doi.org/10.1016/j.jallcom.2009.11.199.

[74] C.D. Cao, W.J. Xie, B. Wei, Microstructural characterization of cobalt-antimony eutectic alloy droplets solidified in drop tube, Mater. Sci. Eng. A. 283 (2000) 86–93. https://doi.org/10.1016/S0921-5093(99)00797-2.

[75] W. Wang, F. Dai, B. Wei, Formation mechanism of primary phases and eutectic structures within undercooled Pb-Sb-Sn ternary alloys, Sci. China, Ser. G Physics, Mech. Astron. 50 (2007) 472–490. https://doi.org/10.1007/s11433-007-0046-6.

[76] J.L. Kang, W. Xu, X.X. Wei, M. Ferry, J.F. Li, Solidification behavior of Co-Sn eutectic alloy with Nb addition, J. Alloys Compd. 695 (2017) 1498–1504. https://doi.org/10.1016/j.jallcom.2016.10.289.

[77] W. Zhai, Z. Hong, B. Wei, Ternary eutectic growth of Ag-Cu-Sb alloy within ultrasonic field, Sci. China, Ser. G Physics, Mech. Astron. 50 (2007) 500–508. https://doi.org/10.1007/s11433-007-0043-9.

[78] N. Yan, D.L. Geng, Z.Y. Hong, B. Wei, Ultrasonic levitation processing

and rapid eutectic solidification of liquid Al-Ge alloys, J. Alloys Compd. 607 (2014) 258–263. https://doi.org/10.1016/j.jallcom.2014.04.006.

[79] W.H.S. Lawson, H.W. Kerr, M.H. Lewis, Cellular morphologies in rapidly solidified Al-Al2Cu and Al-Al3Ni eutectic alloys, J. Cryst. Growth. 12 (1972) 209–216. https://doi.org/10.1016/0022-0248(72)90005-X.

[80] N. Sekido, Y. Kimura, S. Miura, Y. Mishima, Microstructure development of unidirectionally solidified (Nb)/Nb3Si eutectic alloys, Mater. Sci. Eng. A. 444 (2007) 51–57. https://doi.org/10.1016/j.msea.2006.06.140.

[81] W.W. Mullins, R.F. Sekerka, Stability of a planar interface during solidification of a dilute binary alloy, J. Appl. Phys. 35 (1964) 444–451. https://doi.org/10.1063/1.1713333.

[82] Z. Shang, J. Shen, J. Zhang, L. Wang, H. Fu, Perfect cellular eutectic growth in directionally solidified NiAl–Cr(Mo) hypereutectic alloy, J. Cryst. Growth. 354 (2012) 152–156. https://doi.org/10.1016/j.jcrysgro.2012.06.005.

[83] D. Du, Y. Fautrelle, Z. Ren, R. Moreau, X. Li, Effect of a high magnetic field on the growth of ternary Al-Cu-Ag alloys during directional solidification, Acta Mater. 121 (2016) 240–256. https://doi.org/10.1016/j.actamat.2016.09.016.

[84] R. Kakitani, R. V. Reyes, A. Garcia, J.E. Spinelli, N. Cheung, Relationship between spacing of eutectic colonies and tensile properties of transient directionally solidified Al-Ni eutectic alloy, J. Alloys Compd. 733 (2018) 59–68. https://doi.org/10.1016/j.jallcom.2017.10.288.

[85] W.J. Yao, X.J. Han, B. Wei, Microstructural evolution during containerless rapid solidification of Ni-Mo eutectic alloys, J. Alloys Compd. 348 (2003) 88–99. https://doi.org/10.1016/S0925-8388(02)00803-4.

[86] W.J. Yao, N. Wang, B. Wei, Containerless rapid solidification of highly undercooled Co-Si eutectic alloys, Mater. Sci. Eng. A. 344 (2003) 10–19. https://doi.org/10.1016/S0921-5093(01)01895-0.

[87] R. Goetzinger, M. Barth, D.M. Herlach, Growth of lamellar eutectic

dendrites in undercooled melts, J. Appl. Phys. 84 (1998) 1643–1649. https://doi.org/10.1063/1.368233.

[88] J.F. Li, Y.H. Zhou, Eutectic growth in bulk undercooled melts, Acta Mater. 53 (2005) 2351–2359. https://doi.org/10.1016/j.actamat.2005.01.042.

[89] S. Zhao, J.F. Li, L. Liu, Y.H. Zhou, Cellular growth of lamellar eutectics in undercooled Ag-Cu alloy, Mater. Charact. 60 (2009) 519–524. https://doi.org/10.1016/j.matchar.2008.12.006.

[90] I.T.L. Moura, C.L.M. Silva, N. Cheung, P.R. Goulart, A. Garcia, J.E. Spinelli, Cellular to dendritic transition during transient solidification of a eutectic Sn-0.7 wt%Cu solder alloy, Mater. Chem. Phys. 132 (2012) 203–209. https://doi.org/10.1016/j.matchemphys.2011.11.033.

[91] L. Wang, C. Yao, J. Shen, Y. Zhang, T. Wang, H. Xu, L. Gao, G. Zhang, Microstructures and compressive properties of NiAl-Cr(Mo) and NiAl-Cr eutectic alloys with different Fe contents, Mater. Sci. Eng. A. 744 (2019) 593–603. https://doi.org/10.1016/j.msea.2018.12.085.

[92] S. Zhao, J. Li, L. Liu, Y. Zhou, Eutectic growth from cellular to dendritic form in the undercooled Ag–Cu eutectic alloy melt, J. Cryst. Growth. 311 (2009) 1387–1391. https://doi.org/10.1016/j.jcrysgro.2008.12.006.

[93] K.M.C.-E. W. Hume-Rothery, G. W. Mabbott, Mabbott, and KM Channel Evans, Philos. Trans. R. Soc. London, Ser.A. 233 (1934) 1–97.

[94] W. Hume-Rothery, Atomic diameters, atomic volumes and solid solubility relations in alloys, Acta Metall. 14 (1966) 17–20. https://doi.org/10.1016/0001-6160(66)90267-7.

[95] P. W. Reynolds and W. Hume-Rothery, The constitution of silver-rich antimony-silver alloys, J. Inst. Met. 60 (1937) 365–374.

[96] Y.M. Zhang, J.R.G. Evans, S. Yang, The Prediction of Solid Solubility of Alloys: Developments and Applications of Hume-Rothery′s Rules, ChemInform. 44 (2013) no-no. https://doi.org/10.1002/chin.201335198.

[97] J. Zander, R. Sandström, L. Vitos, Modelling mechanical properties for non-hardenable aluminium alloys, Comput. Mater. Sci. 41 (2007) 86–95.

https://doi.org/10.1016/j.commatsci.2007.03.013.

[98] Ø. Ryen, O. Nijs, E. Sjölander, B. Holmedal, H.E. Ekström, E. Nes, Strengthening mechanisms in solid solution aluminum alloys, Metall. Mater. Trans. A Phys. Metall. Mater. Sci. 37 (2006) 1999–2006. https://doi.org/10.1007/s11661-006-0142-7.

[99] E.O. Hall, The deformation and ageing of mild steel: III Discussion of results, Proc. Phys. Soc. Sect. B. 64 (1951) 747–753. https://doi.org/10.1088/0370-1301/64/9/303.

[100] M. Furukawa, Z. Horita, M. Nemoto, R.Z. Valiev, T.G. Langdon, Microhardness measurements and the hall-petch relationship in an Al-Mg alloy with submicrometer grain size, Acta Mater. 44 (1996) 4619–4629. https://doi.org/10.1016/1359-6454(96)00105-X.

[101] C. Carlton, P.J. Ferreira, What is behind the inverse Hall-Petch behavior in nanocrystalline materials?, in: Mater. Res. Soc. Symp. Proc., 2006: pp. 19–24. https://doi.org/10.1016/j.actamat.2007.02.021.

[102] T. Gladman, Precipitation hardening in metals, Mater. Sci. Technol. 15 (1999) 30–36. https://doi.org/10.1179/026708399773002782.

[103] R.O. Scattergood, D.J. Bacon, The Orowan mechanism in anisotropic crystals, Philos. Mag. 31 (1975) 179–198. https://doi.org/10.1080/14786437508229295.

[104] G. Monnet, S. Naamane, B. Devincre, Orowan strengthening at low temperatures in bcc materials studied by dislocation dynamics simulations, Acta Mater. 59 (2011) 451–461. https://doi.org/10.1016/j.actamat.2010.09.039.

[105] I.P. Polmear, Light Alloys - From Traditional Alloys to Nanocrystals, Light Alloy. 2 (2006) 273–277. https://doi.org/10.1017/CBO9781107415324.004.

[106] S.J. Andersen, H.W. Zandbergen, J. Jansen, C. Træholt, U. Tundal, O. Reiso, The crystal structure of the β″ phase in Al-Mg-Si Alloys, Acta Mater. 46 (1998) 3283–3298. https://doi.org/10.1016/S1359-6454(97)00493-X.

[107] N. Maruyama, R. Uemori, N. Hashimoto, M. Saga, M. Kikuchi, Effect of silicon addition on the composition and structure of fine-scale precipitates in Al-Mg-Si alloys, Scr. Mater. 36 (1997) 89–93. https://doi.org/10.1016/S1359-6462(96)00358-2.

[108] L. Bourgeois, C. Dwyer, M. Weyland, J.-F. Nie, B.C. Muddle, Structure and energetics of the coherent interface between the θ′ precipitate phase and aluminium in Al–Cu, Acta Mater. 59 (2011) 7043–7050. https://doi.org/10.1016/j.actamat.2011.07.059.

[109] S. HU, M. BASKES, M. STAN, L. CHEN, Atomistic calculations of interfacial energies, nucleus shape and size of θ′ precipitates in Al–Cu alloys, Acta Mater. 54 (2006) 4699–4707. https://doi.org/10.1016/j.actamat.2006.06.010.

[110] R. Chen, Q. Xu, H. Guo, Z. Xia, Q. Wu, B. Liu, Correlation of solidification microstructure refining scale, Mg composition and heat treatment conditions with mechanical properties in Al-7Si-Mg cast aluminum alloys, Mater. Sci. Eng. A. 685 (2017) 391–402. https://doi.org/10.1016/j.msea.2016.12.051.

[111] N. Chomsaeng, M. Haruta, T. Chairuangsri, H. Kurata, S. Isoda, M. Shiojiri, HRTEM and ADF-STEM of precipitates at peak-ageing in cast A356 aluminium alloy, J. Alloys Compd. 496 (2010) 478–487. https://doi.org/10.1016/j.jallcom.2010.02.084.

[112] G.A. Edwards, K. Stiller, G.L. Dunlop, M.J. Couper, The precipitation sequence in Al-Mg-Si alloys, Acta Mater. 46 (1998) 3893–3904. https://doi.org/10.1016/S1359-6454(98)00059-7.

[113] C. Liu, Z. Ma, P. Ma, L. Zhan, M. Huang, Multiple precipitation reactions and formation of θ'-phase in a pre-deformed Al–Cu alloy, Mater. Sci. Eng. A. 733 (2018) 28–38. https://doi.org/10.1016/j.msea.2018.07.039.

[114] P. Ouellet, F.H. Samuel, Effect of Mg on the ageing behaviour of Al-Si-Cu 319 type aluminium casting alloys, J. Mater. Sci. 34 (1999) 4671–4697. https://doi.org/10.1023/A:1004645928886.

[115] L. Ding, Z. Jia, J.F. Nie, Y. Weng, L. Cao, H. Chen, X. Wu, Q. Liu, The

structural and compositional evolution of precipitates in Al-Mg-Si-Cu alloy, Acta Mater. 145 (2018) 437–450. https://doi.org/10.1016/j.actamat.2017.12.036.

[116] W.F. Miao, D.E. Laughlin, Effects of Cu content and preaging on precipitation characteristics in aluminum alloy 6022, Metall. Mater. Trans. A Phys. Metall. Mater. Sci. 31 (2000) 361–371. https://doi.org/10.1007/s11661-000-0272-2.

[117] L. Liu, J.H. Chen, S.B. Wang, C.H. Liu, S.S. Yang, C.L. Wu, The effect of Si on precipitation in Al-Cu-Mg alloy with a high Cu/Mg ratio, Mater. Sci. Eng. A. 606 (2014) 187–195. https://doi.org/10.1016/j.msea.2014.03.079.

[118] H. Li, Y. Tang, Z. Zeng, Z. Zheng, F. Zheng, Effect of ageing time on strength and microstructures of an Al-Cu-Li-Zn-Mg-Mn-Zr alloy, Mater. Sci. Eng. A. 498 (2008) 314–320. https://doi.org/10.1016/j.msea.2008.08.001.

[119] J.F. Nie, Effects of precipitate shape and orientation on dispersion strengthening in magnesium alloys, Scr. Mater. 48 (2003) 1009–1015. https://doi.org/10.1016/S1359-6462(02)00497-9.

[120] R.M. Srivastava, J. Eckert, W. Löser, B.K. Dhindaw, L. Schultz, Cooling Rate Evaluation for Bulk Amorphous Alloys from Eutectic Microstructures in Casting Processes., Mater. Trans. 43 (2002) 1670–1675. https://doi.org/10.2320/matertrans.43.1670.

[121] J.M. Park, K.B. Kim, D.H. Kim, N. Mattern, R. Li, G. Liu, J. Eckert, Multi-phase Al-based ultrafine composite with multi-scale microstructure, Intermetallics. 18 (2010) 1829–1833. https://doi.org/10.1016/j.intermet.2010.02.042.

[122] I. V. Okulov, M. Bönisch, A.S. Volegov, H.S. Shahabi, H. Wendrock, T. Gemming, J. Eckert, Micro-to-nano-scale deformation mechanism of a Ti-based dendritic-ultrafine eutectic alloy exhibiting large tensile ductility, Mater. Sci. Eng. A. 682 (2017) 673–678. https://doi.org/10.1016/j.msea.2016.11.082.

[123] R. Li, G. Liu, M. Stoica, J. Eckert, FeCo-based multiphase composites

with high strength and large plastic deformation, Intermetallics. 18 (2010) 134–139. https://doi.org/10.1016/j.intermet.2009.07.003.

[124] L.M. Kang, C. Yang, F. Wang, X.X. Li, D.Z. Zhu, W.W. Zhang, W.P. Chen, Y. Huan, Designing ultrafine lamellar eutectic structure in bimodal titanium alloys by semi-solid sintering, J. Alloys Compd. 702 (2017) 51–59. https://doi.org/10.1016/j.jallcom.2017.01.257.

[125] L.H. Liu, C. Yang, Z.Y. Liu, L.C. Zhang, W.W. Zhang, X.S. Huang, L.J. He, P.J. Li, Ultrahigh strength and large plasticity of nanostructured Ti62Nb12.2Fe13.6Co6.4Al5.8 alloy obtained by selectively controlled micrometer-sized phases, Mater. Charact. 124 (2017) 260–265. https://doi.org/10.1016/j.matchar.2017.01.009.

[126] J.F. Löffler, Bulk metallic glasses, Intermetallics. 11 (2003) 529–540. https://doi.org/10.1016/S0966-9795(03)00046-3.

[127] Z.F. Zhang, G. He, H. Zhang, J. Eckert, Rotation mechanism of shear fracture induced by high plasticity in Ti-based nano-structured composites containing ductile dendrites, Scr. Mater. 52 (2005) 945–949. https://doi.org/10.1016/j.scriptamat.2004.12.014.

[128] J.H. Han, K.B. Kim, S. Yi, J.M. Park, D.H. Kim, S. Pauly, J. Eckert, Influence of a bimodal eutectic structure on the plasticity of a (Ti 70.5 Fe29.5)91 Sn9 ultrafine composite, Appl. Phys. Lett. 93 (2008) 1–4. https://doi.org/10.1063/1.3029745.

[129] Y.S. Kim, H.J. Park, J.T. Kim, S.H. Hong, G.H. Park, J.M. Park, J.Y. Suh, K.B. Kim, Influence of Nb on microstructure and mechanical properties of Ti-Sn ultrafine eutectic alloy, Met. Mater. Int. 23 (2017) 20–25. https://doi.org/10.1007/s12540-017-6263-2.

[130] R. Li, S. Pang, M. Stoica, J.M. Park, U. Kühn, T. Zhang, J. Eckert, Mechanical properties of rapidly solidified Fe-Al-B ternary alloys, J. Alloys Compd. 504 (2010) S472–S475. https://doi.org/10.1016/j.jallcom.2010.02.082.

[131] J.M. Park, K.B. Kim, W.T. Kim, M.H. Lee, J. Eckert, D.H. Kim, High strength ultrafine eutectic Fe-Nb-Al composites with enhanced plasticity,

Intermetallics. 16 (2008) 642–650. https://doi.org/10.1016/j.intermet.2008.01.005.

[132] T. Maity, J. Das, High strength Ni-Zr-(Al) nanoeutectic composites with large plasticity, Intermetallics. 63 (2015) 51–58. https://doi.org/10.1016/j.intermet.2015.04.002.

[133] E.M. Park, G.A. Song, J.H. Han, Y. Seo, J.Y. Park, K.B. Kim, Solid-state phase transformation-induced heterogeneous duplex structure in Ti-Sn-Fe alloys, J. Alloys Compd. 515 (2012) 86–89. https://doi.org/10.1016/j.jallcom.2011.11.078.

[134] L. Wang, M. Makhlouf, D. Apelian, Aluminium die casting alloys: Alloy composition, microstructure, and properties-performance relationships, Int. Mater. Rev. 40 (1995) 221–238. https://doi.org/10.1179/imr.1995.40.6.221.

[135] M.C. Santos, A.R. Machado, W.F. Sales, M.A.S. Barrozo, E.O. Ezugwu, Machining of aluminum alloys: a review, Int. J. Adv. Manuf. Technol. 86 (2016) 3067–3080. https://doi.org/10.1007/s00170-016-8431-9.

[136] X. Dong, X. Zhu, S. Ji, Effect of super vacuum assisted high pressure die casting on the repeatability of mechanical properties of Al-Si-Mg-Mn die-cast alloys, J. Mater. Process. Technol. 266 (2019) 105–113. https://doi.org/10.1016/J.JMATPROTEC.2018.10.030.

[137] P. Zhang, Z. Li, B. Liu, W. Ding, Tensile Properties and Deformation Behaviors of a New Aluminum Alloy for High Pressure Die Casting, J. Mater. Sci. Technol. 33 (2017) 367–378. https://doi.org/10.1016/j.jmst.2016.02.013.

[138] Y. Sui, Q. Wang, B. Ye, L. Zhang, H. Jiang, W. Ding, Effect of solidification sequence on the microstructure and mechanical properties of die-cast Al-11Si-2Cu-Fe alloy, J. Alloys Compd. 649 (2015) 679–686. https://doi.org/10.1016/j.jallcom.2015.07.187.

[139] L. Wang, P. Turnley, G. Savage, Gas content in high pressure die castings, J. Mater. Process. Technol. 211 (2011) 1510–1515. https://doi.org/10.1016/j.jmatprotec.2011.03.024.

[140] G. Dour, M. Dargusch, C. Davidson, A. Nef, Development of a non-intrusive heat transfer coefficient gauge and its application to high pressure die casting: Effect of the process parameters, J. Mater. Process. Technol. 169 (2005) 223–233. https://doi.org/10.1016/j.jmatprotec.2005.03.026.

[141] H. Gao, B. Zhao, Z. Zhao, C. Liu, A cluster of inclusions on Al-Si-Cu die casting cylinder block, Eng. Fail. Anal. 55 (2015) 370–375. https://doi.org/10.1016/j.engfailanal.2015.07.015.

[142] X.P. Niu, B.H. Hu, I. Pinwill, H. Li, Vacuum assisted high pressure die casting of aluminium alloys, J. Mater. Process. Technol. 105 (2000) 119–127. https://doi.org/10.1016/S0924-0136(00)00545-8.

[143] Z. Hu, L. Wan, S. Wu, H. Wu, X. Liu, Microstructure and mechanical properties of high strength die-casting Al–Mg–Si–Mn alloy, Mater. Des. 46 (2013) 451–456. https://doi.org/10.1016/j.matdes.2012.10.020.

[144] A.R. Adamane, L. Arnberg, E. Fiorese, G. Timelli, F. Bonollo, INFLUENCE OF INJECTION PARAMETERS ON THE POROSITY AND TENSILE PROPERTIES OF HIGH-PRESSURE DIE CAST Al-Si ALLOYS : A REVIEW, 9 (2015) 43–53.

[145] Z.W. Chen, M.Z. Jahedi, The effect of temperature on soldering and the sequence of formation of the soldered layer during high pressure die casting of Al-11Si-3Cu alloy, Int. J. Cast Met. Res. 11 (1998) 129–138. https://doi.org/10.1080/13640461.1998.11819267.

[146] I. Outmani, L. Fouilland-Paille, J. Isselin, M. El Mansori, Effect of Si, Cu and processing parameters on Al-Si-Cu HPDC castings, J. Mater. Process. Technol. 249 (2017) 559–569. https://doi.org/10.1016/j.jmatprotec.2017.06.043.

[147] W. Yang, X. Yang, S. Ji, Melt superheating on the microstructure and mechanical properties of diecast Al-Mg-Si-Mn alloy, Met. Mater. Int. 21 (2015) 382–390. https://doi.org/10.1007/s12540-015-4215-2.

[148] J. Hernández, J. López, F. Faura, P. Gómez, Analysis of the Flow in a High-Pressure Die Casting Injection Chamber, J. Fluids Eng. 125 (2003)

315. https://doi.org/10.1115/1.1538627.

[149] F. Faura, J. López, J. Hernández, On the optimum plunger acceleration law in the slow shot phase of pressure die casting machines, Int. J. Mach. Tools Manuf. 41 (2001) 173–191. https://doi.org/10.1016/S0890-6955(00)00079-1.

[150] D.R. Gunasegaram, M. Givord, R.G. O'Donnell, B.R. Finnin, Improvements engineered in UTS and elongation of aluminum alloy high pressure die castings through the alteration of runner geometry and plunger velocity, Mater. Sci. Eng. A. 559 (2013) 276–286. https://doi.org/10.1016/j.msea.2012.08.098.

[151] G.O. Verran, R.P.K. Mendes, L.V.O.D. Valentina, DOE applied to optimization of aluminum alloy die castings, J. Mater. Process. Technol. 200 (2008) 120–125. https://doi.org/10.1016/j.jmatprotec.2007.08.084.

[152] K.-T. Chiang, N.-M. Liu, T.-C. Tsai, Modeling and analysis of the effects of processing parameters on the performance characteristics in the high pressure die casting process of Al–SI alloys, Int. J. Adv. Manuf. Technol. 41 (2009) 1076–1084. https://doi.org/10.1007/s00170-008-1559-5.

[153] G.P. Syrcos, Die casting process optimization using Taguchi methods, J. Mater. Process. Technol. 135 (2002) 68–74. https://doi.org/10.1016/S0924-0136(02)01036-1.

[154] L.X. Kong, F.H. She, W.M. Gao, S. Nahavandi, P.D. Hodgson, Integrated optimization system for high pressure die casting processes, J. Mater. Process. Technol. 201 (2008) 629–634. https://doi.org/10.1016/j.jmatprotec.2007.11.250.

[155] S. Otarawanna, C.M. Gourlay, H.I. Laukli, A.K. Dahle, Microstructure Formation in AlSi4MgMn and AlMg5Si2Mn High-Pressure Die Castings, Metall. Mater. Trans. A. 40 (2009) 1645–1659. https://doi.org/10.1007/s11661-009-9841-1.

[156] P.A. Hogan, Die Solder Prediction and Reduction, MSc thesis, (2008) 117.

[157] M.A. Easton, M.A. Gibson, S. Zhu, T.B. Abbott, An a priori hot-tearing

indicator applied to die-cast magnesium-rare earth alloys, Metall. Mater. Trans. A Phys. Metall. Mater. Sci. 45 (2014) 3586–3595. https://doi.org/10.1007/s11661-014-2272-7.

[158] M. Rappaz, J.-M. Drezet, M. Gremaud, A new hot-tearing criterion, Metall. Mater. Trans. A. 30 (1999) 449–455. https://doi.org/10.1007/s11661-999-0334-z.

[159] P.R. Rios, G.S. Fonseca, Geometrical models for grain, grain boundary and grain edge average curvature in an Al-1mass%Mn alloy, Scr. Mater. 52 (2005) 893–897. https://doi.org/10.1016/j.scriptamat.2005.01.001.

[160] R. Kimura, H. Hatayama, K. Shinozaki, I. Murashima, J. Asada, M. Yoshida, Effect of grain refiner and grain size on the susceptibility of Al-Mg die casting alloy to cracking during solidification, J. Mater. Process. Technol. 209 (2009) 210–219. https://doi.org/10.1016/j.jmatprotec.2008.01.053.

[161] O. Zak, B. Tonn, A. Baesgen, L. Kallien, New wear resistant hypereutectic AlSi14cu4FeCrMn alloys for high pressure die casting, Int. J. Met. 9 (2015) 49–57. https://doi.org/10.1007/BF03356040.

[162] L. Bichler, A. Elsayed, K. Lee, C. Ravindran, Influence of mold and pouring temperatures on hot tearing susceptibility of AZ91D magnesium alloy, Int. J. Met. 2 (2008) 43–54.

[163] J.I.E. Song, X. Wang, T. Denouden, Q. Han, Evolution of Intermetallic Phases in Soldering of the Die Casting of Aluminum Alloys, 47 (2016) 2609–2615. https://doi.org/10.1007/s11661-016-3454-2.

[164] H. Zhang, EFFECT OF IRON ON THE MICROSTRUCTURE AND MECHANICAL PROPERTIES OF Al-Si, J. Mater. Sci. Lett. 7 (2007) 775–780.

[165] A. Fabrizi, S. Ferraro, G. Timelli, The influence of Sr, Mg and Cu addition on the microstructural properties of a secondary AlSi9Cu3(Fe) die casting alloy, Mater. Charact. 85 (2013) 13–25. https://doi.org/10.1016/j.matchar.2013.08.012.

[166] H. Zhu, J. Guo, J. Jia, Experimental study and theoretical analysis on die soldering in aluminum die casting, J. Mater. Process. Technol. 123 (2002) 229–235. https://doi.org/10.1016/S0924-0136(01)01174-8.

[167] S. Shankar, D. Apelian, Die soldering: Mechanism of the interface reaction between molten aluminum alloy and tool steel, Metall. Mater. Trans. B. 33 (2002) 465–476. https://doi.org/10.1007/s11663-002-0057-7.

[168] Z.W. Chen, Formation and progression of die soldering during high pressure die casting, Mater. Sci. Eng. A. 397 (2005) 356–369. https://doi.org/10.1016/j.msea.2005.02.057.

[169] Q. Han, S. Viswanathan, Analysis of the mechanism of die soldering in aluminum die casting, Metall. Mater. Trans. A. 34 (2003) 139–146. https://doi.org/10.1007/s11661-003-0215-9.

[170] B. Level, R.A. Harding, Solidification Defects in Castings, (1994).

[171] A.R. GmbH, Primary Aluminium Casting Alloys Foundry Planet, (2012). http://www.foundry-planet.com/fileadmin/redakteur/Material/08-03-10-Leporello_engl.pdf.

[172] H. Yang, D. Watson, Y. Wang, S. Ji, Effect of nickel on the microstructure and mechanical property of die-cast Al–Mg–Si–Mn alloy, J. Mater. Sci. 49 (2014) 8412–8422. https://doi.org/10.1007/s10853-014-8551-2.

[173] E. Sjölander, S. Seifeddine, The heat treatment of Al-Si-Cu-Mg casting alloys, J. Mater. Process. Technol. 210 (2010) 1249–1259. https://doi.org/10.1016/j.jmatprotec.2010.03.020.

[174] L. Zuo, B. Ye, J. Feng, X. Kong, H. Jiang, W. Ding, Effect of Q-Al5Cu2Mg8Si6 phase on mechanical properties of Al-Si-Cu-Mg alloy at elevated temperature, Mater. Sci. Eng. A. 693 (2017) 26–32. https://doi.org/10.1016/j.msea.2017.03.087.

[175] X. Dong, H. Yang, X. Zhu, S. Ji, High strength and ductility aluminium alloy processed by high pressure die casting, J. Alloys Compd. 773 (2019) 86–96. https://doi.org/10.1016/j.jallcom.2018.09.260.

[176] S. Shankar, Y.W. Riddle, M.M. Makhlouf, Eutectic solidification of aluminum-silicon alloys, Metall. Mater. Trans. A. 35 (2004) 3038–3043. https://doi.org/10.1007/s11661-004-0048-1.

[177] Y. Wang, H.T. Li, Z. Fan, Oxidation of aluminium alloy melts and inoculation by oxide particles, in: Trans. Indian Inst. Met., 2012: pp. 653–661. https://doi.org/10.1007/s12666-012-0194-x.

[178] A.M.A. Mohamed, A.M. Samuel, F.H. Samuel, H.W. Doty, Influence of additives on the microstructure and tensile properties of near-eutectic Al-10.8%Si cast alloy, Mater. Des. 30 (2009) 3943–3957. https://doi.org/10.1016/j.matdes.2009.05.042.

[179] S.G. Shabestari, The effect of iron and manganese on the formation of intermetallic compounds in aluminum-silicon alloys, Mater. Sci. Eng. A. 383 (2004) 289–298. https://doi.org/10.1016/j.msea.2004.06.022.

[180] H.F. El-Labban, E.R.I. Mahmoud, Modification of microstructures for hypoeutectic, eutectic and hypereutectic Al–Cu binary alloys, Int. J. Cast Met. Res. 28 (2015) 81–88. https://doi.org/10.1179/1743133614Y.0000000136.

[181] P. Zhang, Z. Li, B. Liu, W. Ding, Effect of chemical compositions on tensile behaviors of high pressure die-casting alloys Al-10Si-yCu-xMn-zFe, Mater. Sci. Eng. A. 661 (2016) 198–210. https://doi.org/10.1016/j.msea.2016.03.032.

[182] S.G. Shabestari, H. Moemeni, Effect of copper and solidification conditions on the microstructure and mechanical properties of Al–Si–Mg alloys, J. Mater. Process. Technol. 153–154 (2004) 193–198. https://doi.org/10.1016/j.jmatprotec.2004.04.302.

[183] A. Fabrizi, S. Ferraro, G. Timelli, The influence of Sr, Mg and Cu addition on the microstructural properties of a secondary AlSi9Cu3(Fe) die casting alloy, Mater. Charact. 85 (2013) 13–25. https://doi.org/10.1016/j.matchar.2013.08.012.

[184] D. Bösch, S. Pogatscher, M. Hummel, W. Fragner, P.J. Uggowitzer, M. Göken, H.W. Höppel, Secondary Al-Si-Mg High-pressure Die Casting

Alloys with Enhanced Ductility, Metall. Mater. Trans. A Phys. Metall. Mater. Sci. 46 (2015) 1035–1045. https://doi.org/10.1007/s11661-014-2700-8.

[185] S.K. Shaha, F. Czerwinski, W. Kasprzak, J. Friedman, D.L. Chen, Improving High-Temperature Tensile and Low-Cycle Fatigue Behavior of Al-Si-Cu-Mg Alloys Through Micro-additions of Ti, V, and Zr, Metall. Mater. Trans. A Phys. Metall. Mater. Sci. 46 (2015) 3063–3078. https://doi.org/10.1007/s11661-015-2880-x.

[186] H. Yang, S. Ji, W. Yang, Y. Wang, Z. Fan, Effect of Mg level on the microstructure and mechanical properties of die-cast Al-Si-Cu alloys, Mater. Sci. Eng. A. 642 (2015) 340–350. https://doi.org/10.1016/j.msea.2015.07.008.

[187] V. Dao, S. Zhao, W. Lin, C. Zhang, Effect of process parameters on microstructure and mechanical properties in AlSi9Mg connecting-rod fabricated by semi-solid squeeze casting, Mater. Sci. Eng. A. 558 (2012) 95–102. https://doi.org/10.1016/j.msea.2012.07.084.

[188] X. Zhu, H. Yang, X. Dong, S. Ji, The effects of varying Mg and Si levels on the microstructural inhomogeneity and eutectic Mg2Si morphology in die-cast Al–Mg–Si alloys, J. Mater. Sci. 54 (2019) 5773–5787. https://doi.org/10.1007/s10853-018-03198-6.

[189] O. Prach, O. Trudonoshyn, P. Randelzhofer, C. Körner, K. Durst, Effect of Zr, Cr and Sc on the Al–Mg–Si–Mn high-pressure die casting alloys, Mater. Sci. Eng. A. 759 (2019) 603–612. https://doi.org/10.1016/j.msea.2019.05.038.

[190] D.R. Gunasegaram, M. Givord, R.G.O. Donnell, B.R. Finnin, Improvements engineered in UTS and elongation of aluminum alloy high pressure die castings through the alteration of runner geometry and plunger velocity, Mater. Sci. Eng. A. 559 (2013) 276–286. https://doi.org/10.1016/j.msea.2012.08.098.

[191] P. Zhang, Z. Li, B. Liu, W. Ding, L. Peng, Improved tensile properties of a new aluminum alloy for high pressure die casting, Mater. Sci. Eng. A.

651 (2016) 376–390. https://doi.org/10.1016/j.msea.2015.10.127.

[192] S. Ji, F. Yan, Z. Fan, Development of a high strength Al–Mg2Si–Mg–Zn based alloy for high pressure die casting, Mater. Sci. Eng. A. 626 (2015) 165–174. https://doi.org/10.1016/j.msea.2014.12.019.

[193] S. Ji, Y. Wang, D. Watson, Z. Fan, Microstructural Evolution and Solidification Behavior of Al-Mg-Si Alloy in High-Pressure Die Casting, Metall. Mater. Trans. A. 44 (2013) 3185–3197. https://doi.org/10.1007/s11661-013-1663-5.

[194] A.M. Samuel, F.H. Samuel, Effect of alloying elements and dendrite arm spacing on the microstructure and hardness of an Al-Si-Cu-Mg-Fe-Mn (380) aluminium die-casting alloy, J. Mater. Sci. 30 (1995) 1698–1708. https://doi.org/10.1007/BF00351598.

[195] E. Taghaddos, M.M. Hejazi, R. Taghiabadi, S.G. Shabestari, Effect of iron-intermetallics on the fluidity of 413 aluminum alloy, J. Alloys Compd. 468 (2009) 539–545. https://doi.org/10.1016/j.jallcom.2008.01.079.

[196] S. Zhu, J.Y. Yao, L. Sweet, M. Easton, J. Taylor, P. Robinson, N. Parson, Influences of nickel and vanadium impurities on microstructure of aluminum alloys, JOM. 65 (2013) 584–592. https://doi.org/10.1007/s11837-013-0572-9.

[197] G. Timelli, F. Bonollo, The influence of Cr content on the microstructure and mechanical properties of AlSi9Cu3(Fe) die-casting alloys, Mater. Sci. Eng. A. 528 (2010) 273–282. https://doi.org/10.1016/j.msea.2010.08.079.

[198] S. Shin, K. Lim, I. Park, Characteristics and microstructure of newly designed Al-Zn based alloys for the die-casting process, J. Alloys Compd. 671 (2016) 517–526. https://doi.org/10.1016/j.jallcom.2016.02.127.

[199] R.N. Lumley, R.G. O'Donnell, D.R. Gunasegaram, M. Givord, Heat Treatment of High-Pressure Die Castings, Metall. Mater. Trans. A. 38 (2007) 2564–2574. https://doi.org/10.1007/s11661-007-9285-4.

[200] R. Lumley, The Development of High Strength and Ductility in High-Pressure Die-Cast Al-Si-Mg Alloys from Secondary Sources, JOM. 71

(2019) 382–390. https://doi.org/10.1007/s11837-018-3121-8.

[201] D.L. Zhang, L.H. Zheng, D.H. StJohn, Effect of a short solution treatment time on microstructure and mechanical properties of modified Al-7wt.%Si-0.3wt.%Mg alloy, J. Light Met. 2 (2002) 27–36. https://doi.org/10.1016/S1471-5317(02)00010-X.

[202] R.N. Lumley, I.J. Polmear, P.R. Curtis, Rapid Heat Treatment of Aluminum High-Pressure Diecastings, Metall. Mater. Trans. A. 40 (2009) 1716–1726. https://doi.org/10.1007/s11661-009-9836-y.

[203] W. Yang, L. Liu, J. Zhang, S. Ji, Insight into the partial solutionisation of a high pressure die-cast Al-Mg-Zn-Si alloy for mechanical property enhancement, Mater. Sci. Eng. A. 682 (2017) 85–89. https://doi.org/10.1016/j.msea.2016.11.028.

[204] A. Niklas, S. Orden, A. Bakedano, M. Silva, E. Nogués, A.I. Fernández-calvo, Effect of solution heat treatment on gas porosity and mechanical properties in a die cast step test part manufactured with a new AlSi10MnMg (Fe) secondary alloy, Mater. Sci. Eng. A. 667 (2016) 376–382. https://doi.org/10.1016/j.msea.2016.05.024.

[205] G. Timelli, O. Lohne, L. Arnberg, H.I. Laukli, Effect of Solution Heat Treatments on the Microstructure and Mechanical Properties of a Die-Cast AlSi7MgMn Alloy, Metall. Mater. Trans. A. 39 (2008) 1747–1758. https://doi.org/10.1007/s11661-008-9527-0.

[206] M.C. Srivastava, O. Lohne, ENERGY ABSORPTION CHARACTERISTICS OF DUCTILE AlSi4MgMn AND AlSi9MgMn DIE-CASTINGS INVESTIGATED BY SHEAR BOLT TESTING, Int. J. Met. (2016). https://doi.org/10.1007/s40962-016-0073-z.

[207] W. Kasprzak, H. Kurita, G. Birsan, B.S. Amirkhiz, Hardness control of Al-Si HPDC casting alloy via microstructure refinement and tempering parameters, Mater. Des. 103 (2016) 365–376. https://doi.org/10.1016/j.matdes.2016.03.093.

[208] M.A. Moustafa, F.H. Samuel, H.W. Doty, Effect of solution heat treatment and additives.pdf, J. Mater. Sci. 8 (2003) 4507–4522.

https://doi.org/10.1023/A:1027333602276.

[209] F. Yan, W. Yang, S. Ji, Z. Fan, Effect of solutionising and ageing on the microstructure and mechanical properties of a high strength die-cast Al–Mg–Zn–Si alloy, Mater. Chem. Phys. 167 (2015) 88–96. https://doi.org/10.1016/j.matchemphys.2015.10.014.

[210] H. Ye, An Overview of the Development of Al-Si-Alloy Based Material for Engine Applications, J. Mater. Eng. Perform. 12 (2003) 288–297. https://doi.org/10.1361/105994903770343132.

[211] M.F. Ibrahim, E. Samuel, A.M. Samuel, A.M.A. Al-Ahmari, F.H. Samuel, Metallurgical parameters controlling the microstructure and hardness of Al-Si-Cu-Mg base alloys, Mater. Des. 32 (2011) 2130–2142. https://doi.org/10.1016/j.matdes.2010.11.040.

[212] Z. Lu, L. Zhang, Thermodynamic description of the quaternary Al-Si-Mg-Sc system and its application to the design of novel Sc-additional A356 alloys, Mater. Des. 116 (2017) 427–437. https://doi.org/10.1016/j.matdes.2016.12.034.

[213] C.R. Barbosa, J.O.M. de Lima, G.M.H. Machado, H.A.M. de Azevedo, F.S. Rocha, A.S. Barros, O.F.L. da Rocha, Relationship Between Aluminum-Rich/Intermetallic Phases and Microhardness of a Horizontally Solidified AlSiMgFe Alloy, Mater. Res. 22 (2018). https://doi.org/10.1590/1980-5373-mr-2018-0365.

[214] G. Timelli, A. Fabrizi, The Effects of Microstructure Heterogeneities and Casting Defects on the Mechanical Properties of High-Pressure Die-Cast AlSi9Cu3(Fe) Alloys, Metall. Mater. Trans. A Phys. Metall. Mater. Sci. 45 (2014) 5486–5498. https://doi.org/10.1007/s11661-014-2515-7.

[215] J.H. Li, M. Albu, F. Hofer, P. Schumacher, Solute adsorption and entrapment during eutectic Si growth in A-Si-based alloys, Acta Mater. 83 (2015) 187–202. https://doi.org/10.1016/j.actamat.2014.09.040.

[216] Y.L. Liu, S.B. Kang, H.W. Kim, The complex microstructures in an as-cast Al-Mg-Si alloy, Mater. Lett. 41 (1999) 267–272. www.elsevier.comrlocatermatlet (accessed February 23, 2019).

[217] W. bo Yu, S. Liang, Y. you Cao, X. bo Li, Z. peng Guo, S. mei Xiong, Interfacial heat transfer behavior at metal/die in finger-plated casting during high pressure die casting process, China Foundry. 14 (2017) 258–264. https://doi.org/10.1007/s41230-017-6066-6.

[218] A.M. Mitrašinović, F.C. Robles Hernández, Determination of the growth restriction factor and grain size for aluminum alloys by a quasi-binary equivalent method, Mater. Sci. Eng. A. 540 (2012) 63–69. https://doi.org/10.1016/j.msea.2012.01.072.

[219] T.E. Quested, A.T. Dinsdale, A.L. Greer, Thermodynamic modelling of growth-restriction effects in aluminium alloys, Acta Mater. 53 (2005) 1323–1334. https://doi.org/10.1016/j.actamat.2004.11.024.

[220] Y. Kaygisiz, N. Maraşli, Microstructural, mechanical and electrical characterization of directionally solidified Al-Si-Mg eutectic alloy, J. Alloys Compd. 618 (2015) 197–203. https://doi.org/10.1016/j.jallcom.2014.08.056.

[221] J.M. Park, N. Mattern, U. Kühn, J. Eckert, K.B. Kim, W.T. Kim, K. Chattopadhyay, D.H. Kim, High-strength bulk Al-based bimodal ultrafine eutectic composite with enhanced plasticity, J. Mater. Res. 24 (2011) 2605–2609. https://doi.org/10.1557/jmr.2009.0297.

[222] H. Eckert, G. He, J. Das, W. Loser, Nanostructured composites in multicomponent alloy systems, Mater. Trans. 44 (2003) 1999–2006. https://doi.org/10.2320/matertrans.44.1999.

[223] R. Chen, Q. Xu, H. Guo, Z. Xia, Q. Wu, B. Liu, Correlation of solidification microstructure refining scale, Mg composition and heat treatment conditions with mechanical properties in Al-7Si-Mg cast aluminum alloys, Mater. Sci. Eng. A. 685 (2017) 391–402. https://doi.org/10.1016/j.msea.2016.12.051.

[224] C.R. Barbosa, G.H. Machado, H.M. Azevedo, F.S. Rocha, J.C. Filho, A. A. Pereira, O.L. Rocha, Tailoring of Processing Parameters, Dendritic Microstructure, Si/Intermetallic Particles and Microhardness in As-cast and Heat-Treated Samples of Al7Si0.3Mg Alloy, Met. Mater. Int. (2019)

1–14. https://doi.org/10.1007/s12540-019-00334-y.

[225] B. Gwalani, S. Gorsse, D. Choudhuri, Y. Zheng, R.S. Mishra, R. Banerjee, Tensile yield strength of a single bulk Al 0.3 CoCrFeNi high entropy alloy can be tuned from 160 MPa to 1800 MPa, Scr. Mater. 162 (2019) 18–23. https://doi.org/10.1016/j.scriptamat.2018.10.023.

[226] L.M. Kang, C. Yang, Y.J. Zhao, X.X. Li, S.G. Qu, W.W. Zhang, Y. Long, Z.Y. Xiao, Bimodal eutectic titanium alloys: Microstructure evolution, mechanical behavior and strengthening mechanism, Mater. Sci. Eng. A. 700 (2017) 10–18. https://doi.org/10.1016/j.msea.2017.05.102.

[227] C.M. Gourlay, A.K. Dahle, Dilatant shear bands in solidifying metals, Nature. 445 (2007) 70–73. https://doi.org/10.1038/nature05426.

[228] S. Menargues, E. Martín, M.T. Baile, J.A. Picas, New short T6 heat treatments for aluminium silicon alloys obtained by semisolid forming, Mater. Sci. Eng. A. 621 (2015) 236–242. https://doi.org/10.1016/j.msea.2014.10.078.

[229] L. Pedersen, L. Arnberg, The effect of solution heat treatment and quenching rates on mechanical properties and microstructures in AlSiMg foundry alloys, Metall. Mater. Trans. A. 32 (2001) 525–532. https://doi.org/10.1007/s11661-001-0069-y.

[230] Y.J. Li, A.M.F. Muggerud, A. Olsen, T. Furu, Precipitation of partially coherent α-Al(Mn,Fe)Si dispersoids and their strengthening effect in AA 3003 alloy, Acta Mater. 60 (2012) 1004–1014. https://doi.org/10.1016/j.actamat.2011.11.003.

[231] K. Dám, F. Průša, D. Vojtěch, Structural and mechanical characteristics of the Al-23Si-8Fe-5Mn alloy prepared by combination of centrifugal spraying and hot die forging, Mater. Sci. Eng. A. 610 (2014) 197–202. https://doi.org/10.1016/j.msea.2014.05.045.

[232] Q. Xiao, H. Liu, D. Yi, D. Yin, Y. Chen, Y. Zhang, B. Wang, Effect of Cu content on precipitation and age-hardening behavior in Al-Mg-Si-xCu alloys, J. Alloys Compd. 695 (2017) 1005–1013. https://doi.org/10.1016/j.jallcom.2016.10.221.

[233] E. Sjölander, S. Seifeddine, Optimization of Solution Treatment of Cast Al-7Si-0.3Mg and Al-8Si-3Cu-0.5Mg Alloys, Metall. Mater. Trans. A. 45 (2014) 1916–1927. https://doi.org/10.1007/s11661-013-2141-9.

[234] P.A. Rometsch, L. Arnberg, D.L. Zhang, Modelling dissolution of Mg 2 Si and homogenisation in Al-Si-Mg casting alloys, Int. J. Cast Met. Res. 12 (1999) 1–8. https://doi.org/10.1080/13640461.1999.11819338.

[235] Q.G. Wang, Microstructural effects on the tensile and fracture behavior of aluminum casting alloys A356/357, Metall. Mater. Trans. A. 34 (2003) 2887–2899. https://doi.org/10.1007/s11661-003-0189-7.

[236] K.N. Braszczyńska-Malik, Effect of high-pressure die casting on structure and properties of Mg-5Al-0.4Mn-xRE (x = 1, 3 and 5 wt%) experimental alloys, J. Alloys Compd. 694 (2017) 841–847. https://doi.org/10.1016/j.jallcom.2016.10.033.

[237] C. Ravi, C. Wolverton, First-principles study of crystal structure and stability of Al-Mg-Si-(Cu) precipitates, Acta Mater. 52 (2004) 4213–4227. https://doi.org/10.1016/j.actamat.2004.05.037.

[238] E. Sjölander, S. Seifeddine, Artificial ageing of Al-Si-Cu-Mg casting alloys, Mater. Sci. Eng. A. 528 (2011) 7402–7409. https://doi.org/10.1016/j.msea.2011.06.036.

[239] B. Rinderer, M. Couper, X.Y. Xiong, S.X. Gao, J.F. Nie, Precipitation Sequence in an Al-Si-Mg Foundry Alloy, Mater. Sci. Forum. 654–656 (2010) 590–595. https://doi.org/10.4028/www.scientific.net/MSF.654-656.590.

[240] S.J. Andersen, C.D. Marioara, A. Frøseth, R. Vissers, H.W. Zandbergen, Crystal structure of the orthorhombic U2-Al4Mg4 Si4 precipitate in the Al-Mg-Si alloy system and its relation to the β′ and β″ phases, Mater. Sci. Eng. A. 390 (2005) 127–138. https://doi.org/10.1016/j.msea.2004.09.019.

[241] R. Chen, Q. Xu, H. Guo, Z. Xia, Q. Wu, B. Liu, Modeling the precipitation kinetics and tensile properties in Al-7Si-Mg cast aluminum alloys, Mater. Sci. Eng. A. 685 (2017) 403–416. https://doi.org/10.1016/j.msea.2016.12.042.

[242] N.J. Petch, The cleavage strength of polycrystals, Journal of Iron and Steel Institute, J. Iron Steel Inst. 174 (1953) 25–28. https://ci.nii.ac.jp/naid/10019881123 (accessed July 1, 2020).

[243] N. Haghdadi, A. Zarei-Hanzaki, A.A. Roostaei, A.R. Hemmati, Evaluating the mechanical properties of a thermomechanically processed unmodified A356 Al alloy employing shear punch testing method, Mater. Des. 43 (2013) 419–425. https://doi.org/10.1016/J.MATDES.2012.07.001.

[244] D.A. Lados, D. Apelian, L. Wang, Solution Treatment Effects on Microstructure and Mechanical Properties of Al-(1 to 13 pct)Si-Mg Cast Alloys, Metall. Mater. Trans. B. 42 (2011) 171–180. https://doi.org/10.1007/s11663-010-9437-6.

[245] M.R. Ahmadi, E. Povoden-Karadeniz, B. Sonderegger, K.I. Öksüz, A. Falahati, E. Kozeschnik, A model for coherency strengthening of large precipitates, Scr. Mater. 84–85 (2014) 47–50. https://doi.org/10.1016/j.scriptamat.2014.04.019.

[246] Y. Kayg, N. Maras, Directional solidification of Al-Cu-Si-Mg quaternary eutectic alloy, J. Alloys Compd. 721 (2017) 764–771. https://doi.org/10.1016/j.jallcom.2017.06.027.

[247] S. Cui, I.H. Jung, Thermodynamic modeling of the quaternary Al-Cu-Mg-Si system, Calphad Comput. Coupling Phase Diagrams Thermochem. 57 (2017) 1–27. https://doi.org/10.1016/j.calphad.2017.02.002.

[248] L. Mondolfo, Aluminum alloys: structure and properties, 1976. https://books.google.com/books?hl=en&lr=&id=Xf4kBQAAQBAJ&oi=fnd&pg=PP1&ots=Q56x2sJxob&sig=Ukp_TcIkCN_xw7t-_NV4M3qJlQA (accessed July 16, 2020).

[249] L. Mondolfo, Aluminum alloys: structure and properties, 1976. https://books.google.com/books?hl=en&lr=&id=Xf4kBQAAQBAJ&oi=fnd&pg=PP1&ots=Q53C1mJusd&sig=TidoDSJe5iRLCNZRLSjHxO53ZUU (accessed September 29, 2019).

[250] D.P. Field, Recent advances in the application of orientation imaging,

Ultramicroscopy. 67 (1997) 1–9. https://doi.org/10.1016/S0304-3991(96)00104-0.

[251] A.R. Adamane, L. Arnberg, E. Fiorese, G. Timelli, F. Bonollo, Influence of injection parameters on the porosity and tensile properties of high-pressure die cast Al-Si alloys: A review, Int. J. Met. 9 (2015) 43–52. https://doi.org/10.1007/bf03355601.

[252] Y. Zhang, S. Wang, E. Lordan, Y. Wang, Z. Fan, Improve mechanical properties of high pressure die cast Al9Si3Cu alloy via dislocation enhanced precipitation, J. Alloys Compd. 785 (2019) 1015–1022. https://doi.org/10.1016/j.jallcom.2019.01.278.

[253] J. Pu, W.J. Feng, J.Z. Xiao, Z.H. Gan, H.Y. Yi, K. Cui, Non-equilibrium solidification of bulk undercooled Ni – P eutectic alloys, J. Cryst. Growth. 256 (2003) 139–145. https://doi.org/10.1016/S0022-0248(03)01299-5.

[254] M.A. Ruggiero, J.W. Rutter, Origin of microstructure in the 332 K eutectic of the Bi-In-Sn system, Mater. Sci. Technol. 13 (1997) 5–11. https://doi.org/10.1179/mst.1997.13.1.5.

[255] G. He, J. Eckert, W. Löser, M. Hagiwara, Composition dependence of the microstructure and the mechanical properties of nano/ultrafine-structured Ti–Cu–Ni–Sn–Nb alloys, Acta Mater. 52 (2004) 3035–3046. https://doi.org/10.1016/j.actamat.2004.03.006.

[256] W. Kurz, D.J. Fisher, Dendrite growth in eutectic alloys: The coupled zone, Int. Met. Rev. 24 (1979) 177–204. https://doi.org/10.1179/imtr.1979.24.1.177.

[257] W.W. Mullins, R.F. Sekerka, Stability of a planar interface during solidification of a dilute binary alloy, J. Appl. Phys. 35 (1964) 444–451. https://doi.org/10.1063/1.1713333.

[258] T. Himemiya, Growth models of two-phase eutectic cell in a ternary eutectic system: A phase selection map, Mater. Trans. JIM. 40 (1999) 675–684. https://doi.org/10.2320/matertrans1989.40.675.

[259] B. Cantor, G.A. Chadwick, The tensile deformation of unidirectionally

solidified Al-Al3Ni and Al-Al2Cu eutectics, J. Mater. Sci. 10 (1975) 578–588. https://linkinghub.elsevier.com/retrieve/pii/0022024874900359 (accessed November 18, 2019).

[260] F.R.N. (Frank R.N. Nabarro, M.S. Duesbery, J.P. Hirth, Dislocations in solids, North-Holland Pub. Co, 1979.

[261] BRUCE L. BRAMFITT, The Effect of Carbide and Nitride Additions on the Heterogeneous Nucleation Behavior of Liquid Iron, Metall. Trans. 1 (1970) 1987–1995.

[262] X. Wang, Y. Zhong, Q. Sun, Y. Li, W. Zhang, D. Qi, D. Wang, B. Jiang, Crystallography and interfacial structure in a directionally solidified Al2O3/Y3Al5O12/ZrO2 eutectic crystal, Scr. Mater. 145 (2018) 23–27. https://doi.org/10.1016/j.scriptamat.2017.10.008.

[263] D. Du, Y. Fautrelle, A. Dong, D. Shu, G. Zhu, B. Sun, X. Li, Effect of Ag Content on the Microstructure and Crystallization of Coupled Eutectic Growth in Directionally Solidified Al-Cu-Ag Alloys, Metall. Mater. Trans. A. 49 (2018) 4735–4747. https://doi.org/10.1007/s11661-018-4799-5.

[264] Q. Lei, B.P. Ramakrishnan, S. Wang, Y. Wang, J. Mazumder, A. Misra, Structural refinement and nanomechanical response of laser remelted Al-Al2Cu lamellar eutectic, Mater. Sci. Eng. A. 706 (2017) 115–125. https://doi.org/10.1016/j.msea.2017.08.105.

[265] Z.-P. Guo, S.-M. Xiong, B.-C. Liu, M. Li, J. Allison, Effect of Process Parameters, Casting Thickness, and Alloys on the Interfacial Heat-Transfer Coefficient in the High-Pressure Die-Casting Process, Metall. Mater. Trans. A. 39 (2008) 2896–2905. https://doi.org/10.1007/s11661-008-9640-0.

[266] C.M. Gourlay, H.I. Laukli, A.K. Dahle, Defect band characteristics in Mg-Al and Al-Si high-pressure die castings, Metall. Mater. Trans. A Phys. Metall. Mater. Sci. 38 (2007) 1833–1844. https://doi.org/10.1007/s11661-007-9243-1.

[267] B. Chanda, G. Potnis, P.P. Jana, J. Das, A review on nano-/ultrafine advanced eutectic alloys, J. Alloys Compd. 827 (2020) 154226.

https://doi.org/10.1016/j.jallcom.2020.154226.

[268] P. Steinmetz, A. Dennstedt, M. Şerefoğlu, I. Sargin, A. Genau, U. Hecht, Crystal orientation relationships in ternary eutectic Al-Al2Cu-Ag2Al, Acta Mater. 157 (2018) 96–105. https://doi.org/10.1016/j.actamat.2018.07.016.

[269] S.J. Wang, G. Liu, J. Wang, A. Misra, Characteristic orientation relationships in nanoscale Al-Al2Cu Eutectic, Mater. Charact. 142 (2018) 170–178. https://doi.org/10.1016/j.matchar.2018.05.037.

[270] W.L.R. Santos, C.B. Cruz, J.E. Spinelli, N. Cheung, A. Garcia, Tailoring microstructure, tensile properties and fracture process via transient directional solidification of Zn-Sn alloys, Mater. Sci. Eng. A. 712 (2018) 127–132. https://doi.org/10.1016/j.msea.2017.11.039.

[271] J.M. Park, D.H. Kim, K.B. Kim, W.T. Kim, Deformation-induced rotational eutectic colonies containing length-scale heterogeneity in an ultrafine eutectic Fe83 Ti7 Zr6 B4 alloy, Appl. Phys. Lett. 91 (2007) 1–4. https://doi.org/10.1063/1.2793189.

[272] J.T. Kim, S.H. Hong, J.M. Park, J. Eckert, K.B. Kim, Microstructure and mechanical properties of hierarchical multi-phase composites based on Al-Ni-type intermetallic compounds in the Al-Ni-Cu-Si alloy system, J. Alloys Compd. 749 (2018) 205–210. https://doi.org/10.1016/j.jallcom.2018.03.313.

[273] J.M. Park, D.H. Kim, K.B. Kim, W.T. Kim, Deformation-induced rotational eutectic colonies containing length-scale heterogeneity in an ultrafine eutectic Fe83 Ti7 Zr6 B4 alloy, Appl. Phys. Lett. 91 (2007) 1–4. https://doi.org/10.1063/1.2793189.

[274] Q. Cai, C.L. Mendis, I.T.H. Chang, Z. Fan, Microstructure evolution and mechanical properties of new die-cast Al-Si-Mg-Mn alloys, Mater. Des. 187 (2020) 108394. https://doi.org/10.1016/j.matdes.2019.108394.

[275] I. V. Okulov, M. Bönisch, U. Kühn, W. Skrotzki, J. Eckert, Significant tensile ductility and toughness in an ultrafine-structured Ti68.8Nb13.6Co6Cu5.1Al6.5 bi-modal alloy, Mater. Sci. Eng. A. 615

(2014) 457–463. https://doi.org/10.1016/j.msea.2014.07.108.

[276] I. V. Okulov, S. Pauly, U. Kühn, P. Gargarella, T. Marr, J. Freudenberger, L. Schultz, J. Scharnweber, C.G. Oertel, W. Skrotzki, J. Eckert, Effect of microstructure on the mechanical properties of as-cast Ti-Nb-Al-Cu-Ni alloys for biomedical application, Mater. Sci. Eng. C. 33 (2013) 4795–4801. https://doi.org/10.1016/j.msec.2013.07.042.

[277] Z. Shen, Q. Ding, C. Liu, J. Wang, H. Tian, J. Li, Z. Zhang, Atomic-scale mechanism of the θ″ → θ′ phase transformation in Al-Cu alloys, J. Mater. Sci. Technol. 33 (2017) 1159–1164. https://doi.org/10.1016/j.jmst.2016.08.031.

[278] L. Bourgeois, C. Dwyer, M. Weyland, J.F. Nie, B.C. Muddle, Structure and energetics of the coherent interface between the θ′ precipitate phase and aluminium in Al-Cu, Acta Mater. 59 (2011) 7043–7050. https://doi.org/10.1016/j.actamat.2011.07.059.

[279] J.K. Sunde, C.D. Marioara, R. Holmestad, The effect of low Cu additions on precipitate crystal structures in overaged Al-Mg-Si(-Cu) alloys, Mater. Charact. 160 (2020) 110087. https://doi.org/10.1016/j.matchar.2019.110087.

[280] P. Ouellet, F.H. Samuel, Effect of Mg on the ageing behaviour of Al-Si-Cu 319 type aluminium casting alloys, J. Mater. Sci. 34 (1999) 4671–4697. https://doi.org/10.1023/A:1004645928886.

[281] E. Sjölander, S. Seifeddine, Optimisation of solution treatment of cast Al-Si-Cu alloys, Mater. Des. 31 (2010). https://doi.org/10.1016/j.matdes.2009.10.035.

[282] I. Sadeghi, M.A. Wells, S. Esmaeili, Effect of particle shape and size distribution on the dissolution behavior of Al 2 Cu particles during homogenization in aluminum casting alloy Al-Si-Cu-Mg, J. Mater. Process. Technol. 251 (2018) 232–240. https://doi.org/10.1016/j.jmatprotec.2017.08.042.

[283] L. Lasa, J.M. Rodriguez-Ibabe, Evolution of the main intermetallic phases in Al-Si-Cu-Mg casting alloys during solution treatment, J. Mater. Sci. 39

(2004) 1343–1355. https://doi.org/10.1023/B:JMSC.0000013895.72084.c9.

[284] A.K. Gupta, A.K. Jena, M.C. Chaturvedi, Insoluble phase in Al-1·52Cu-0·75Mg alloys containing silicon, Mater. Sci. Technol. (United Kingdom). 3 (1987) 1012–1018. https://doi.org/10.1179/mst.1987.3.12.1012.

[285] L. Lasa, J.M. Rodriguez-Ibabe, Characterization of the dissolution of the Al2Cu phase in two Al-Si-Cu-Mg casting alloys using calorimetry, Mater. Charact. 48 (2002) 371–378. https://doi.org/10.1016/S1044-5803(02)00283-8.

[286] H.C. Long, J.H. Chen, C.H. Liu, D.Z. Li, Y.Y. Li, The negative effect of solution treatment on the age hardening of A356 alloy, Mater. Sci. Eng. A. 566 (2013) 112–118. https://doi.org/10.1016/j.msea.2012.12.093.

[287] Q.G. Wang, C.J. Davidson, J.R. Griffiths, P.N. Crepeau, Oxide films, pores and the fatigue lives of cast aluminum alloys, Metall. Mater. Trans. B Process Metall. Mater. Process. Sci. 37 (2006) 887–895. https://doi.org/10.1007/BF02735010.

[288] M. Zeren, Effect of copper and silicon content on mechanical properties in Al-Cu-Si-Mg alloys, J. Mater. Process. Technol. 169 (2005) 292–298. https://doi.org/10.1016/j.jmatprotec.2005.03.009.

[289] A. Guinier, Heterogeneities in Solid Solutions, Solid State Phys. - Adv. Res. Appl. 9 (1959) 293–398. https://doi.org/10.1016/S0081-1947(08)60568-8.

[290] T. Saito, F.J.H. Ehlers, W. Lefebvre, D. Hernandez-Maldonado, R. Bjørge, C.D. Marioara, S.J. Andersen, E.A. Mørtsell, R. Holmestad, Cu atoms suppress misfit dislocations at the β″/Al interface in Al–Mg–Si alloys, Scr. Mater. 110 (2016) 6–9. https://doi.org/10.1016/j.scriptamat.2015.07.033.

[291] A.R. Farkoosh, M. Pekguleryuz, Enhanced mechanical properties of an Al-Si-Cu-Mg alloy at 300°C: Effects of Mg and the Q-precipitate phase, Mater. Sci. Eng. A. 621 (2015) 277–286. https://doi.org/10.1016/j.msea.2014.10.080.

[292] A. Bobel, K. Kim, C. Wolverton, M. Walker, G.B. Olson, Equilibrium composition variation of Q-phase precipitates in aluminum alloys, Acta Mater. 138 (2017) 150–160. https://doi.org/10.1016/j.actamat.2017.07.048.

[293] M. Gazizov, C.D. Marioara, J. Friis, S. Wenner, R. Holmestad, R. Kaibyshev, Precipitation behavior in an Al–Cu–Mg–Si alloy during ageing, Mater. Sci. Eng. A. 767 (2019) 138369. https://doi.org/10.1016/j.msea.2019.138369.

[294] J. Buha, R.N. Lumley, A.G. Crosky, Microstructural development and mechanical properties of interrupted aged Al-Mg-Si-Cu alloy, Metall. Mater. Trans. A Phys. Metall. Mater. Sci. 37 (2006) 3119–3130. https://doi.org/10.1007/s11661-006-0192-x.

[295] T. Saito, F.J.H. Ehlers, W. Lefebvre, D. Hernandez-Maldonado, R. Bjørge, C.D. Marioara, S.J. Andersen, E.A. Mørtsell, R. Holmestad, Cu atoms suppress misfit dislocations at the β″/Al interface in Al-Mg-Si alloys, Scr. Mater. 110 (2016) 6–9. https://doi.org/10.1016/j.scriptamat.2015.07.033.

[296] J.H. Jang, D.G. Nam, Y.H. Park, I.M. Park, Effect of solution treatment and artificial aging on microstructure and mechanical properties of Al-Cu alloy, Trans. Nonferrous Met. Soc. China (English Ed. 23 (2013) 631–635. https://doi.org/10.1016/S1003-6326(13)62509-1.

[297] L. Jiang, J.K. Li, G. Liu, R.H. Wang, B.A. Chen, J.Y. Zhang, J. Sun, M.X. Yang, G. Yang, J. Yang, X.Z. Cao, Length-scale dependent microalloying effects on precipitation behaviors and mechanical properties of Al-Cu alloys with minor Sc addition, Mater. Sci. Eng. A. 637 (2015) 139–154. https://doi.org/10.1016/j.msea.2015.04.035.

Appendix

The 3D morphology of ultrafine Al-Cu-Si-Mg eutectic region in Al10.6Cu alloy was obtained via FIB-SEM tomography slices, which are provided as images numbered from 1 to 8 below. The 50% mixed backscattered and secondary electron mode was used to get the most information from each image.